

ACTA

UNIVERSITATIS OULUENSIS

Alberto Rabbachin

LOW COMPLEXITY UWB RECEIVERS WITH RANGING CAPABILITIES

FACULTY OF TECHNOLOGY,
DEPARTMENT OF ELECTRICAL AND INFORMATION ENGINEERING,
CENTRE FOR WIRELESS COMMUNICATIONS,
UNIVERSITY OF OULU

C
TECHNICAL



ACTA UNIVERSITATIS OULUENSIS
C Technica 298

ALBERTO RABBACHIN

**LOW COMPLEXITY UWB RECEIVERS
WITH RANGING CAPABILITIES**

Academic dissertation to be presented, with the assent of
the Faculty of Technology of the University of Oulu, for
public defence in Auditorium IT116 (Tietotalo II),
Linnanmaa, on May 26th, 2008, at 12 noon

OULUN YLIOPISTO, OULU 2008

Copyright © 2008
Acta Univ. Oul. C 298, 2008

Supervised by
Doctor Ian Oppermann
Professor Matti Latva-aho

Reviewed by
Doctor Mischa Dohler
Professor Arne Svensson

ISBN 978-951-42-8799-2 (Paperback)
ISBN 978-951-42-8800-5 (PDF)
<http://herkules.oulu.fi/isbn9789514288005/>
ISSN 0355-3213 (Printed)
ISSN 1796-2226 (Online)
<http://herkules.oulu.fi/issn03553213/>

Cover design
Raimo Ahonen

OULU UNIVERSITY PRESS
OULU 2008

Rabbachin, Alberto, Low complexity UWB receivers with ranging capabilities

Faculty of Technology, University of Oulu, P.O.Box 4000, FI-90014 University of Oulu, Finland, Department of Electrical and Information Engineering, Centre for Wireless Communications, University of Oulu, P.O. Box 4500, FI-90014 University of Oulu, Finland
Acta Univ. Oul. C 298, 2008
Oulu, Finland

Abstract

This Thesis examines low complexity receiver structures for impulse-radio (IR) ultra-wideband (UWB) systems to be used in wireless sensor network applications. Such applications require radio communication solutions characterized by low cost, low complexity hardware and low power consumption to provide very long battery life.

Analysis of several auto-correlation receiver (AcR) structures is performed in the presence of additive white Gaussian noise to identify receiver structures that offer a good compromise between implementation complexity and data communication performance.

The classes of receiver that demonstrate the best complexity/performance trade-off are shown to be the AcR utilising transmitted-reference with binary pulse amplitude modulation signaling, and the energy detector (ED) utilising binary pulse position modulation. The analysis of these two schemes is extended to consider multipath fading channels. Numerically integrable bit error rate probability (BER) expressions are derived in order to evaluate the receivers' performance in the presence of fading distributions characterized by closed form characteristic functions. Simulations utilising widely accepted UWB channel models are then used to evaluate the BER in different indoor environments.

Since UWB systems share frequency spectrum with many narrowband (NB) systems, and need to coexist with other UWB systems, the performance of low complexity receivers can be seriously affected by interference. In the presence of NB interference, two cases have been considered: 1) single NB interference, where the interfering node is located at a fixed distance from the receiver, and 2) multiple NB interference, where the interfering nodes are scattered according to a spatial Poisson process. When considering UWB interference, the case of multiple sources of interference has been considered. For both the multiple NB and the multiple UWB interference cases, the model derived considers several interference parameters, which can be integrated into BER formulations for quick performance evaluations. The framework is sufficiently simple to allow tractable analysis and can serve as a guideline for the design of heterogeneous networks where coexistence between UWB systems and NB systems is of importance.

The very large bandwidth of UWB signals offers an unprecedented possibility for accurate ranging operations. Signal leading-edge estimation algorithms based on average maximum likelihood estimators are derived considering different multipath channel fading distributions. Suboptimal solutions are proposed and investigated in order to support ranging capabilities in low complexity receiver structures. The ability to identify line-of-sight and non-line-of-sight conditions with the ED-based receiver is also addressed.

An example of an IR-UWB low complexity transceiver based on ED for sensor network applications is proposed in this Thesis. Ad-hoc solutions for pulse transmission, synchronization and data detection are developed.

Keywords: auto-correlation receiver, detection, energy detector, estimation, impulse radio, interference, UWB

To my family

Preface

The research work presented in this Thesis, carried out at the Centre for Wireless Communications (CWC), University of Oulu, Finland, during the years 2003-2007, has been possible thanks to the support of many people. Some of them should be acknowledged personally.

Ian, I can very well remember my first face-to-face meeting with you at CWC. It's still puzzling to me that you accepted to be my supervisor on that occasion, considering that I understood very little of what you told me in your fantastic Australian accent during that memorable first chat! One thing was clear though: working with you would be challenging and exciting. I was right. During these past few years, not only did you guide me in my research work but you also introduced me to the worldwide research community. Your always-positive life attitude helped me a lot in the most difficult moments of my PhD.

Matti, thanks a lot for the help you gave me during the redaction of my Thesis. Without your support I would probably still be messing up with the table of contents. I am grateful also for the opportunity you gave me to be your teaching assistant.

My eternal gratitude goes to you Moe: your enthusiasm and contagious passion for your subject flow from you to me every time we meet. Thank you for having made my sojourns in Boston unforgettable (how many lobsters did we eat?), and for letting me work with your incredible team. Thanks also to you, Snow, for welcoming me in your house as part of the family.

My fascination for wireless communications dates from a fabulous course called *Trasmissione Numerica*, which I attended as a master student at Bologna University. Giovanni, I am immensely grateful to you for having aroused in me a good deal of passion in this field thanks to your extraordinary teaching skills.

Two widely recognized scientists contributed to the revision of this Thesis. I wish to thank Prof. Arne Svensson from Chalmers University, Sweden and Dr. Mischa Dohler from CTTC, Spain, whose detailed comments significantly improved the quality of this Thesis.

The development of the UWB chip was a really challenging and thrilling period. I will never forget the long hours spent to discuss with my colleagues Lucian and Sakari. Thanks a lot guys for the knowledge related to chip design I have learnt from you. Many

thanks also to Jari, Matti H. and Raffaello, who helped me move my first steps in the UWB technology.

Working to achieve a PhD has its ups and downs. Special thanks to my friends Jussi, for sharing the office and the PhD “pain”, and Leonardo for his unbeatable sense of humor. I wish you all the best for your PhD, guys. I hope you will get rid of it soon!

Most of the work presented here was conducted in the European funded projects PULSERS I and PULSESRS II and in the CWC founded projects URFA and UWEN. I would like to thank Infoetech Oulu Graduate School, as well as Nokia Foundation and Elisa Foundation, for their financial support during the last months of my doctoral studies.

Some of the work presented in this Thesis has been carried out together with some researchers from other institutes. In this regard I would like to mention the great help I got from Tony and Pedro at MIT, and from Benôit and Samuel at CEA-Leti. I am constantly picking up new knowledge from you guys - keep dropping it!

In a foreign country you sometimes have to find ways to survive bureaucracy. I would like to thank all the administrative personnel at CWC and Telecommunication Laboratory for their help and their patience with my inexistent Finnish skills.

Leaving my family to spend a few months in Grenoble was a hard decision, but I was very lucky to meet you, Ben and Sam. Thank you for making me feel at home and for letting me discover the pleasures of fondue and Chartreuse! I am sure our friendship will last forever.

Luckily, I did not spend all of my time in the lab! I relieved stress playing with the Multilats basketball team all over Northern Finland. Running behind the ball with you guys has kept me feeling young inside and quite in good shape. For the wonderful lunches, dinners, trips and for all the special moments we have spent together, many thanks to Sandra, Mika, Antonio, Veronica, Mehdi, Alicia, Davide, Giorgio, Sandrine, Stefano and Seamus. Last but not least, thank you Luca and Liisa for being there since the beginning.

Home sweet home has always been on my mind. Thank you my friends Marco and Massimo for a whole life spent together and for making every return of mine back to Italy always a special occasion. I hope our aperitif sessions in the shadow of “Il Campanile” will never end.

Mamma e papà, grazie per aver compreso la mia volontà di andare all'estero e per la pazienza e l'amore inesauribili con cui mi avete sempre seguito negli studi e nella vita.

Anna e Mario, la vostra casa è un porto sicuro, dove sono sempre accolto a braccia aperte e da dove ogni volta sono pronto a salpare verso nuove avventure insieme a Sara, carico di entusiasmo e di consigli preziosi. Grazie di cuore di tutto!

Se questa straordinaria odissea ha avuto un inizio e una fine devo ringraziare te, Sara, che hai coraggiosamente deciso di imbarcarti con me in questa avventura donandomi in ogni istante il tuo amore e la tua fiducia di sempre. Grazie per la pazienza quotidiana dimostratami ogni volta che l'umore non era quello giusto e, nei giri di boa della nostra vita, grazie per indicarmi sempre la via più difficile che alla fine si rivela essere la più entusiasmante.

Mio piccolo Leonardo, grazie per i tuoi sorrisi raggianti e per l'energia vulcanica che mi trasmetti senza sosta da quando sei nato. Infine a te piccolino che scalci nel pancione della mamma, grazie per aver reso ancora più emozionante questo sprint finale.

List of symbol and abbreviations

$(\cdot)^I$	super-script I is used to identify parameters related to the multiple UWB interferers
$a_j^{(k)}$	j th element of a bipolar random sequence of the k th user
A	stable distributed random variable
B_f	fractional bandwidth
$c_j^{(k)}$	j th element of a TH random sequence of the k th user
d	radio link distance
$d_i^{(k)}$	i th transmitted data symbol of the k th user
$e_i^{(n)}$	i th transmitted data symbol of the n th interferer
E_b	energy per bit
E'_b	integrated energy per bit
E_p	energy per pulse
f_c	UWB signal central frequency
f_H	3 dB upper end of the signal bandwidth
f_L	3 dB lower end of the signal bandwidth
f_j	NB signal central frequency
g_m	reference modulation parameter
\mathbf{G}	complex Gaussian random variable
G	Gaussian random variable
$G_{RX}(f)$	frequency-dependent receiver antenna gain
$G_{TX}(f)$	frequency-dependent transmitter antenna gain
h_l	multipath channel component
I	transmitted power of each NB interferer
J	average received NB interference power (single interferer case)
L_1	path loss at 1 meter
L_2	path loss at 10 meter
k_v	shape parameter of a Gamma distribution
m	fading parameter in the presence of Nakagami fading
$\tilde{n}(t)$	noise signal at the output of the BPZF
n_i or $n_{i,j}$	samples of a band-limited AWGN process
N_0	noise spectral density

N_{0bit}	averaged noise spectral density
N_{h}	maximum allowable integer shift
N_{p}	number of pulses per symbol
NF	noise figure
$p(t)$	transmitted UWB pulse
\mathbf{p}_n	complex value of the n th sample phase component
$\hat{P}(f)$	magnitude of the frequency response of $p(t)$ at the frequency f
P_{e}	error probability function
$P_{\text{e}}^{(\text{NBI})}$	error probability function in the presence of a single NB interferer
$P_{\text{e}}^{(\text{NBIs})}$	error probability function in the presence of multiple NB interferers
$P_{\text{e}}^{(\text{UWB})}$	error probability function in the presence of multiple UWB interferers
P_{fa}	probability of false alarm
P^{I}	transmitted power of each UWB interferer
$P_{\text{RX}}(f)$	frequency-dependent received power
$P_{\text{TX}}(f)$	frequency-dependent transmitted power
$q^{(\text{ED})}$	degrees of freedom of the Chi-squared distributed decision variable for the ED
$q^{(\text{TR})}$	degrees of freedom of the Chi-squared distributed decision variable for the AcR
$\tilde{r}(t)$	received signal at the output of the BPZFF
\mathbf{r}_n	complex value of the n th received signal sample
R_{d}	data rate
$R_{f(t)}(\tau)$	auto-correlation function of the function $f(t)$
$R^{(n)}$	distance between the n th NB transmitter and the UWB receiver
R_{s}	radius of a circle
$s(t)$	transmitted signal
$\mathcal{S}(\alpha, \beta, \gamma)$	alpha-stable distribution
$\mathcal{S}_{\text{c}}(\alpha, \beta, \gamma)$	complex alpha-stable distribution
T	integration time
T_{d}	channel excess delay
T_{f}	pulse repetition period
T_{f}^{ED}	average pulse repetition period for ED
T_{f}^{TR}	average pulse repetition period for AcR
T_{g}	duration of the received signal
T_{i}	integration time

T_o	observation time
T_p	pulse duration
T_r	delay between the reference pulse and the modulated pulse
T_{small}	integration time for the threshold-crossing and maximum selection algorithm for time-of-arrival estimation
T_u	uncertainty time
$\bar{\mathbf{v}}_{1,j}^{(n)}$	vector composed by the samples of the n th received UWB interference signal
$\mathbf{v}_{1,j,m}^{(n)}$	m th component of the vector $\bar{\mathbf{v}}_{1,j}^{(n)}$
$w(t)$	output of the channel impulse response filter
W	signal bandwidth
$\mathbf{X}^{(n)}$	circularly symmetric random variable
α	characteristic exponent of the unidimensional alpha stable random variable
α_j	amplitude of the fading associated with the single NB interferer
α_n	amplitude of the fading associated with the n th interferer
β	skewness parameter of the unidimensional alpha stable random variable
γ	dispersion parameter of the unidimensional alpha stable random variable
γ_{UWB}	dispersion parameter of the unidimensional random variable representing the aggregate interference in the presence of multiple UWB interferers
$\Gamma(\cdot)$	Gamma function
$\delta(\cdot)$	Diract function
δ_{toa}	integer part of Δ_{toa}/T_p
$\bar{\delta}_{\text{toa}}$	estimate of δ_{toa}
δ_p	fractional part of Δ_{toa}/T_p
Δ	modulation delay for the PPM
Δ_{toa}	delay of the received signal
ε	decay factor of the power delay profile
θ_n	phase of the fading associated with the n th interferer
λ	spatial density of the interferers
$\Lambda^G(\cdot)$	averaged maximum likelihood estimator function in the presence of complex Gaussian fading
$\Lambda_{\text{flat}}^G(\cdot)$	suboptimal averaged maximum likelihood estimator function in the pres-

	ence of complex Gaussian fading
$\Lambda_s^G(\cdot)$	suboptimal averaged maximum likelihood estimator function in the presence of complex Gaussian fading
$\Lambda_{\text{snrest}}^G(\cdot)$	suboptimal averaged maximum likelihood estimator function in the presence of complex Gaussian fading
$\Lambda_{\text{snrest,flat}}^G(\cdot)$	suboptimal averaged maximum likelihood estimator function in the presence of complex Gaussian fading
$\Lambda^{\text{GML}}(\cdot)$	generalized maximum likelihood estimator function
$\Lambda^{\text{IGML}}(\cdot)$	improved generalized maximum likelihood estimator function
$\Lambda^{\text{N}}(\cdot)$	averaged maximum likelihood estimator function in the presence of Nakagami fading
$\Lambda^{\text{L}}(\cdot)$	averaged maximum likelihood estimator function in the presence of Log-normal fading
Ω_i	average power of the i th multipath component in the presence of Nakagami fading
Ω_v	shape parameter of a Gamma distribution
μ	location parameter of the unidimensional alpha stable random variable
$\mu_{Y_{\text{ED},1}}^{(\text{NBI})}$	non-centrality parameter of the a Chi-squared distributed random variable $Y_{\text{ED},1}$ in the presence of a single NB interferer
$\mu_{Y_{\text{ED},2}}^{(\text{NBI})}$	non-centrality parameter of the a Chi-squared distributed random variable $Y_{\text{ED},2}$ in the presence of a single NB interferer
$\mu_{Y_{\text{TR},1}}^{(\text{NBI})}$	non-centrality parameter of the a Chi-squared distributed random variable $Y_{\text{TR},1}$ in the presence of a single NB interferer
$\mu_{Y_{\text{TR},2}}^{(\text{NBI})}$	non-centrality parameter of the a Chi-squared distributed random variable $Y_{\text{TR},2}$ in the presence of a single NB interferer
$\mu_{Y_{\text{ED},1}}^{(\text{NBIs})}$	non-centrality parameter of the a Chi-squared distributed random variable $Y_{\text{ED},1}$ in the presence of multiple NB interferers
$\mu_{Y_{\text{ED},2}}^{(\text{NBIs})}$	non-centrality parameter of the a Chi-squared distributed random variable $Y_{\text{ED},2}$ in the presence of multiple NB interferers
$\mu_{Y_{\text{TR},1}}^{(\text{NBIs})}$	non-centrality parameter of the a Chi-squared distributed random variable $Y_{\text{TR},1}$ in the presence of multiple NB interferers
$\mu_{Y_{\text{TR},2}}^{(\text{NBIs})}$	non-centrality parameter of the a Chi-squared distributed random variable $Y_{\text{TR},2}$ in the presence of multiple NB interferers
$\mu_{Y_{\text{ED},1}}^{(\text{UWB})}$	non-centrality parameter of the a Chi-squared distributed random variable $Y_{\text{ED},1}$ in the presence of multiple UWB interferers

$\mu_{Y_{ED,2}}^{(UWB)}$	non-centrality parameter of the a Chi-squared distributed random variable $Y_{ED,2}$ in the presence of multiple UWB interferers
$\mu_{Y_{TR,1}}^{(UWB)}$	non-centrality parameter of the a Chi-squared distributed random variable $Y_{TR,1}$ in the presence of multiple UWB interferers
$\mu_{Y_{TR,2}}^{(UWB)}$	non-centrality parameter of the a Chi-squared distributed random variable $Y_{TR,2}$ in the presence of multiple UWB interferers
τ_l	time delay of the l th multipath component
τ_i	delay of the i th interferer
τ_n	random variable which accounts for the asynchronism between the interferers
ν	amplitude decay factor
$\xi_n(\delta_{toa})$	signal energy in the n th integration interval as a function of δ_{toa}
$\tilde{\xi}_n(\delta_{toa})$	estimate of the signal energy in the n th integration interval as a function of the j th hypothesis
$\tilde{\xi}_p$	estimate of the total received signal energy
$\tilde{\sigma}_0^2$	estimated noise variance
σ_L	standard deviation of the variable's logarithm in the presence of Log-normal fading
σ_I	shadowing parameter of the interferer
σ_r	CRLB of the signal timing estimation variance
$\tilde{\Sigma}$	cross-correlation matrix
ϕ_l	random phase
$\psi(\nu)$	characteristic function
$\zeta(t)$	aggregate interference signal
$\zeta(t)^{(n)}$	n th interference signal at the UWB receiver
$\tilde{\zeta}_{1,j}$	complex vector composed by the samples of the aggregate interference taken over a single time frame of the received signal
$\bar{\zeta}_{1,j}$	vector composed by the samples of the aggregate interference taken over a single time frame of the received signal
$\zeta_{1,j,m}$	m th element of the vector $\bar{\zeta}_{1,j}$
$\tilde{\zeta}$	vector composed by the samples of the aggregate interference taken over an entire symbol of the received signal
A/D	analogue to digital
AcR	auto-correlation receiver
ALT	alternate transmission scheme

AML	average maximum likelihood
ASIC	application-specific integrated circuit
AWGN	additive white gaussian noise
BiCMOS	bipolar complementary metal oxide semiconductor
BEP	bit error probability
BPAM	binary pulse amplitude modulation
BPPM	binary pulse position modulation
BPZF	bandpass zonal filter
CDMA	code division multiple access
CF	characteristic function
CM1	IEEE 802.15.4a channel model 1
CM2	IEEE 802.15.4a channel model 2
CM3	IEEE 802.15.4a channel model 3
CM4	IEEE 802.15.4a channel model 4
CMOS	complementary metal oxide semiconductor
CRLB	Cramer-Rao lower bound
DB	doublet based transmission scheme
DAA	detection and avoidance
DLL	digital locked loop
DS-CDMA	direct sequence code division multiple access
EC	European Commission
ED	energy detector
FCC	Federal Communication Commission
GPS	global positioning system
GSM	Global System for Mobile communications
HDR	high data rate
HDTV	high definition television
IEEE	institute of electrical and electronics engineer
GML	generalized maximum likelihood
IGML	improved generalized maximum likelihood
IPI	inter-pulse interference (also called intra-symbol interference)
IR	impulse radio
IR-UWB	impulse radio ultra-wideband
isi	called intra-symbol interference
LDR	low-data-rate

LGW	locally generated waveform
LNA	low noise amplifier
MAX	maximum selection
MB	multi-band
mTR	modulated transmitted reference
ML	maximum likelihood
NB	narrowband
NBI	narrowband interference
NLOS	non-line of sight
OFDM	orthogonal frequency multiplexing
OOK	on-off keying
PDA	personal digital assistant
PAM	pulse amplitude modulation
PPM	pulse position modulation
RF	radio frequency
SIR	signal-to-interference ratio
SIR _T	signal-to-interference ratio defined by the ratio between the received UWB signal power and the interference transmitted power
<i>SNR</i>	signal-to-noise ratio
SR	single reference transmission scheme
SW	sliding window
TC	threshold crossing
TDMA	time division multiple access
TH	time hopping
ToA	time-of-arrival
TR	transmitted reference
RF	radio frequency
UMTS	Universal Mobile Telecommunications System
UWB	ultra-wideband
VGA	variable gain amplifier
WB	wideband
WCDMA	wideband code division multiple access
WLAN	wireless local area network
WPAN	wireless personal area network
$\mathbb{E}\{\cdot\}$	expectation

$\Re\{\cdot\}$	real part
$\Im\{\cdot\}$	imaginary part
$\log(\cdot)$	logarithmic function
\triangleq	defined as
\approx	approximately equal to
\simeq	similar to

Contents

Abstract	
Preface	7
List of symbol and abbreviations	18
1 Introduction	23
1.1 UWB history	23
1.2 Motivation	27
1.3 Author's contribution	28
1.4 Outline of the thesis	29
2 Prior and parallel work on IR-UWB	31
2.1 Data detection and synchronization	32
2.2 Coexistence and interference	34
2.3 Ranging estimation	36
2.4 Conclusions	37
3 Data detection for UWB low complexity receivers	39
3.1 Introduction	39
3.2 System model for AcR	40
3.2.1 Transmitted signals	40
3.2.2 Receiver structures	42
3.3 Signal-to-noise ratio derivations	47
3.4 Numerical results in the AWGN channel	51
3.5 System and channel models for BEP analysis of non-coherent UWB receivers in fading channel	56
3.5.1 Transmitted Signals	57
3.5.1.1 BPPM	57
3.5.1.2 TR-BPAM	57
3.5.2 Channel model	58
3.5.3 Energy detector (ED)	59
3.5.4 Auto-correlation receiver (AcR)	60
3.6 BEP analysis of non-coherent UWB receivers in fading channel	61
3.6.1 Energy detector (ED) with BPPM signaling	61
3.6.2 Auto-correlation (AcR) with TR-BPAM signaling	63
	19

3.7	Numerical and simulation results	65
3.7.1	Numerical results in Nakagami fading channels	65
3.7.2	Simulation results in IEEE 802.15.4a channel models	68
3.7.3	Pulse compression technique	72
3.8	Conclusions	75
4	Coexistence and interference	77
4.1	Introduction	77
4.2	Overview of stable distributions	78
4.2.1	Univariate stable distribution	78
4.2.2	Multivariate stable distribution	79
4.3	BEP analysis in the presence of narrowband interference	82
4.3.1	BEP analysis in the presence of a single NB interferer	82
4.3.1.1	Auto-correlation receiver (AcR)	83
4.3.1.2	Energy detector (ED)	85
4.3.2	BEP analysis in the presence of multiple NB interferers	87
4.3.2.1	Auto-correlation receiver (AcR) in the presence of multiple NB interferers	89
4.3.2.2	Energy detector (ED) in the presence of multiple NB interferers	92
4.3.3	Numerical and simulation results	92
4.3.3.1	Performance with a single NB interferer	93
4.3.3.2	Performance with multiple NB interferers	96
4.4	UWB interference	101
4.4.1	Multiple UWB interferers	101
4.4.2	Received signals in the presence of UWB interference	103
4.4.2.1	Auto-correlation receiver (AcR)	103
4.4.2.2	Energy detector (ED)	104
4.4.3	Statistical characterization of the aggregate interference	104
4.4.4	BEP analysis in the presence of multiple UWB interferers	111
4.4.4.1	Energy detector (ED) performance in the presence of Type 1 interference	112
4.4.4.2	Energy detector (ED) performance in the presence of Type 2 interference	114
4.4.4.3	Auto-correlation receiver (AcR) performance in the presence of Type 1 interference	116

4.4.4.4	Auto-correlation receiver (AcR) performance in the presence of Type 2 interference	118
4.4.5	Numerical results	119
4.4.5.1	Type 1 interference	119
4.4.5.2	Type 2 interference	123
4.5	Conclusions	127
5	Time of arrival estimation	129
5.1	Leading edge estimation problem	129
5.2	Signal model for ToA	130
5.3	Threshold crossing and maximum selection algorithm	132
5.4	Averaged maximum-likelihood (AML) and generalized maximum-likelihood (GML) estimators	133
5.4.1	Averaged maximum-likelihood estimators (AML)	134
5.4.2	Suboptimal AML estimators	137
5.4.3	Generalized maximum-likelihood estimator (GML)	139
5.4.4	Improved generalized maximum likelihood estimator (IGML)	141
5.5	Channel model identification	142
5.6	Simulation results	146
5.6.1	AML estimators	146
5.6.2	Simulation results for sub-optimal estimators in 802.15.4a channel models	150
5.6.3	Simulation results for improved GML estimators	155
5.7	Conclusions	159
6	A practical implementation of a low-complexity transceiver for IR-UWB systems	161
6.1	Introduction	161
6.2	UWB physical layer system model	161
6.2.1	Transmitted signal	161
6.2.2	Synchronization and data detection	162
6.2.3	Preamble detection and frame synchronization	168
6.2.4	Time-of-arrival	170
6.2.5	Link budget	170
6.3	Transceiver design and power consumption	172
6.3.1	Transmitter	172
6.3.2	Receiver	173

6.3.3	Transceiver complexity	175
6.4	Conclusions	176
7	Conclusions and future work	177
7.1	Summary and conclusions	177
7.2	Future work	178
	References	180
	Appendices	190

1 Introduction

1.1 UWB history

Wireless connectivity has enabled a new mobile lifestyle with significant enhanced convenience for mobile computing users. Consumers will soon demand the same convenience throughout their digital home, connecting their PCs, personal digital recorders and players, digital camcorders and digital cameras, high-definition TVs (HDTVs), gaming systems, personal digital assistants (PDAs), and cell phones to each other in a wireless personal area network (WPAN)[1]. But today's wireless local area network (WLAN) and WPAN technologies cannot meet the needs of tomorrow's connectivity with a host of emerging consumer electronic devices that require high bandwidth. New technologies are required to meet the needs of high-speed WPANs. Due to the natural development of communications technology, the lower regions of the frequency spectrum are the most heavily used by existing wireless systems. In order to find new available spectrum, wireless carrier based systems such as wideband code-division-multiple-access (WCDMA) and wireless local-area-network (WLAN) have moved to even higher frequencies requiring the use of high frequency oscillators that are able to provide periodic signals of the order of several gigahertz. These oscillators no longer present a challenge from the design and the implementation point of view; however, the power consumption required by the radio-frequency (RF) components of such carrier based communication systems cannot be considered trivial for portable devices. Issues related to power consumption and low complexity (cost) are even more crucial for the emerging wireless application of sensor networks. If sensor networks need to operate in spectrum regions above 3 GHz, the power consumption of carrier based systems would make their implementation very difficult.

Ultra-wideband (UWB) systems based on impulse-radio (IR) transmission offer a solution for the bandwidth, cost, power consumption, and physical size requirements of next-generation consumer electronic devices. UWB can provide wireless connectivity with consistently high data rates across multiple devices within the digital home and the office thanks to the very large bandwidth. The use of short pulses of the order of a few nanoseconds produces a baseband signal which can occupy significant parts of the spectrum in the 1-10 GHz region depending on the pulse shape. The baseband

nature of the IR signal allows reduced complexity of the RF stage of both transmitter and receiver since up-conversion and down-conversion of the signal are not required. This translates to reduced complexity of the transceiver and also a significant saving in power consumption. The combination of low-power and very large bandwidth also means that it is possible to have transmission with very low spectral density, with levels at or below the noise floor. The extremely low power spectral density of UWB systems supports operation in a spectral overlay fashion with other systems where the UWB systems represent a very small interference power.

One of the first examples of a wireless system demonstrated by Guglielmo Marconi in 1897 can be considered to be based on UWB signaling since Marconi's earliest spark-gap transmitters occupied a large portion of spectrum, from very low frequencies up to a relatively high-frequency band. However, the benefits of large bandwidth and the capability of implementing multi-user systems provided by electromagnetic pulses were not considered at that time. The impulse concept was first introduced in 1963 by Ross [2] who described a linear time invariant system by its response to an impulsive excitation (as also proposed by Papoulis in 1962 [3]). However, signals with bandwidth of the order of several gigahertz found their application when the IR technique was introduced for the first time in radar applications [4]. The use of radio signals with very short temporal duration are particularly suited to radar systems since they can provide extremely fine accuracy for the estimate of target distance and for the shape of the targeted object [5–7]. The use of IR techniques in radio communication was introduced by Fullerton who carried out experiments and filed the first patent applications for communication systems based on time modulated radio impulses in 1987 [8]. Fullerton was also the founder of Time Domain Corporation which was the first company to produce a UWB chipset in 1999. In the academic community, Scholtz was the first to demonstrate the potential of this technique. In the introduction of [9] written in 1993 when almost all research attention was directed toward code-division multiple-access (CDMA) systems, Scholtz states: *“The current emphasis on constant-envelope spread-spectrum modulations has caused engineers to ignore one design which has considerable potential, namely time-hopping. The technology for generating and receiving pulses of the order of a nanosecond or less in width, similar in shape to one cycle of a sine wave, is available. These monocycles can be received by correlation detection virtually at the antenna terminals, making a relatively low-cost receiver possible.”* Three years later, two new works were published by Win dealing with multi-user capacity of the time-hopping-IR (TH-IR) technique [10] and with the analogue/digital implementation of IR

based systems [11]. From this point, UWB was no longer exclusively the domain of academia with interest increasing from industry. The needs of regulation for this type of carrier-less transmission prompted the U.S. Federal Communications Commission (FCC) to release the First Report and Order in 2002 covering commercial use of UWB [12]. In the FCC report, the definition of a UWB signal is related to the fractional bandwidth of the signal which is expressed as

$$B_f = 2 \frac{f_H - f_L}{f_H + f_L}, \quad (1)$$

where f_L and f_H are the lower and upper end (3 dB points) of the signal spectrum, respectively. UWB signals are those that have a fractional bandwidth greater than 20 percent. The spectral mask defined by the FCC for commercial use of UWB essentially provides two separate spectral regions which may be used for UWB transmission, one in the lower part of the spectrum in the range of 0-900 MHz and the other in the range of 3.1-10.6 GHz with a maximum power spectral density of -41.3 dBm/MHz. The European Commission Committee (ECC) published the first draft of a European UWB spectral mask [13] in February 2007 allowing unlicensed UWB transmission with a power spectral density of -41.3 dBm/MHz from 6 to 10 GHz. More strict rules are imposed for transmission in the lower band of 4.2-4.8 GHz where only time limited transmissions are allowed and detection-and-avoidance (DDA) techniques are required in UWB transmitters in order to permit transmission only when no other systems are using the spectrum (starting in 2010). It should be noted that the FCC considers UWB transmission to be those radio signals with a minimum bandwidth of 500 MHz, while for the ECC the minimum bandwidth is 50 MHz. Both the FCC and ECC spectral masks are presented in Fig. 1.

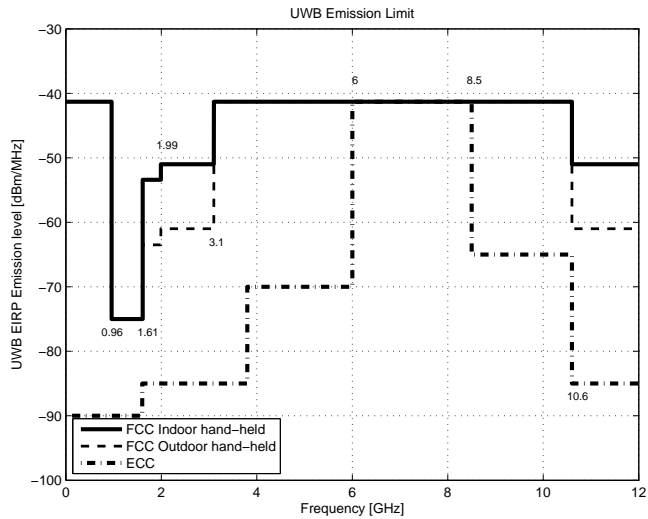


Fig. 1. UWB emission limit.

The IR technique is not the only means to generate signals which satisfy the UWB definition. Multi-band (MB) techniques can readily be used to create UWB signals. Thanks to the maturity of orthogonal frequency division multiplexing (OFDM) technology, the MB-OFDM technique proposed by the WiMedia Alliance [14] lead to rapid commercialization with initial applications targeting replacement of the USB cables with UWB wireless USB. The IR and MB-OFDM approaches represented the main candidate proposals in the IEEE 802.15.3a standardization group. The failure of the standardization group to endorse a single UWB technology signalled a defeat for high-data-rate (HDR) application based on IR.

Where IR techniques seem to have more chance to succeed is in low-data-rate (LDR) applications since OFDM-based systems require intensive signal processing and consequently are not suitable for low power consumption applications. In the advanced work being performed by IEEE 802.15 Low Rate Alternative PHY Task Group (TG4a) for WPANs [15], the IR technique has been chosen as one possible air interface. The principal interest of this task group is in providing communications and high precision ranging / location capability (1 metre accuracy or better), high aggregate throughput, as well as adding scalability to data rates, longer range, and lower power consumption

and cost [16]. A multitude of applications can benefit from such a physical layer. Other than WPAN, possible scenarios include sensor positioning and identification networks, wireless outdoor sensor networks, wireless body area networks, and wireless indoor tags networks.

1.2 Motivation

The initial interest in exploiting UWB systems can be summarized by two well known formulas. The first is the Shannon capacity formula expressed as

$$C = W \log_2(1 + SNR), \quad (2)$$

where the capacity increases logarithmically with the SNR and linearly with the bandwidth W . The second formula is the Cramer-Rao lower bound (CRLB) which expresses the lower bound of the signal timing estimation variance as

$$\sigma_t = \frac{1}{2W\sqrt{SNR}}. \quad (3)$$

The high capacity provided by UWB signals can offer a solution to high data rate applications such as HDTV. The very high temporal accuracy can offer high precision in location and tracking capabilities, and can find application particularly in indoor environments where GPS is less reliable. Other appealing characteristics inherent to the IR-UWB technique are the possibility to have low cost and low power consumption devices. These characteristics arise from the essentially baseband nature of the signal transmission. Unlike conventional radio systems, the UWB transmitter produces a very short time domain pulse that is able to propagate without the need for an additional RF mixing stage. The very wide bandwidth of the UWB signal implies that the signal spans frequencies commonly used as carrier frequencies. The signal propagates well without the need for additional up-conversion. This also means that a local oscillator can be omitted from the receiver chain. In order to exploit the potential of UWB expressed by the two formulas above, high complexity receivers are required if common digital signal processing techniques are employed. However, the advantages in the RF design offered by IR-UWB have promoted research into sub-optimal receiver algorithms with reduced complexity for relatively low data rate solutions. Among the most common sub-optimal solutions, the implementation of non-coherent receivers which do not perform channel estimation has attracted wide interest. Performance of low complexity

non-coherent receivers is limited by the noise enhancement typical of this type of receiver; however, they remain interesting solutions for several scenarios, especially in sensor network applications and LDR personal area networks where cost and power consumption of each terminal are required to be very low.

Thanks to the very large bandwidth of UWB signals, the power spectral density of the transmitted signals are very low with correspondingly low interference to other systems sharing part of the UWB spectrum. This characteristic convinced the regulatory institutions in a number of countries to allow unlicensed UWB transmission under certain power limitations. Consequently, wide proliferation of low-cost UWB devices is expected, leading to the need of UWB devices to coexist with narrowband (NB) systems and other UWB devices belonging to uncoordinated networks (for example in WBAN).

The motivation of this Thesis is to provide a framework to allow analysis of different low complexity IR-UWB solutions in typical UWB channel conditions and account for the presence of geographically distributed interferers. Ranging issues are also addressed within the scope of estimation algorithms which can be implemented in the analogue domain. Most of the work presented in this Thesis has been driven by the need to develop a physical layer for low data rate communication systems with ranging capabilities, based on low complexity and low power consumption transceivers.

1.3 Author's contribution

Original work by the author addresses several aspects of the UWB communication systems and is captured in a number of publications referenced in this section. Low-complexity receiver structures and algorithms for data detection and signal delay estimation are proposed and analyzed in typical UWB channel conditions. Furthermore, a model for the interference arising from both narrowband (NB) and UWB systems is proposed and the impact on non-coherent UWB receivers is performed. Within the larger development framework leading to the development of an energy detection based UWB ASIC at the Centre for Wireless Communication (CWC), the author focussed on solutions for signal transmission, synchronization and delay estimation.

In the area of data detection, the focus was on first identifying low complexity receiver solutions particularly reviewing different implementations of the auto-correlation receiver (AcR). The performance of the different types of AcR structures were analyzed by the derivation of signal-to-noise ratio at the decision block in the presence of an AWGN channel. The performance of the candidate solutions which can be char-

acterized as non-coherent, is then compared in the presence of channel fading using closed-form BEP expressions and numerically integrable BEP formulas [17, 18].

In order to address the interference problem, the author focussed on the derivation of an appropriate interference model which takes into account several interference parameters and which can also be integrated into BEP formulations. The framework is simple enough to allow tractable analysis and can serve as a guideline for the design of heterogeneous networks where coexistence between UWB systems and NB systems is of importance [19–21].

The large bandwidth offered by UWB signal can potentially offer very high temporal resolution which offers unprecedented possibilities in terms of ranging estimation. The author derives several averaged maximum likelihood estimators of the received signal leading edge operating in different types of channel fading and proposes sub-optimal solutions which, beside their low-complexity, can provide good accuracy [22, 23].

In the area of synchronization procedure, the author focussed on an ad-hoc solution which was implemented in a low-complexity UWB CMOS ASIC with a receiver based on energy detection [24–28]. The synchronization operates on a periodic transmission of a burst of radio impulses composed of a sequence of pulses very close to each other [29].

1.4 Outline of the thesis

This Thesis is organized as follows: Chapter 2 presents a comprehensive overview of previous and parallel work related to UWB systems which relate to the discussion developed in later chapters; in Chapter 3, the data detection problem is analyzed by comparing the performance of targeted low complexity receiver solutions. The analysis is then extended to fading channels using closed form BEP expressions and numerically integrable BEP formulas. In this chapter, a pulse compression technique is also introduced and its benefits in terms of BEP are shown. Chapter 4 focuses on time-of-arrival estimation with low complexity receivers. An initial statistical foundation of the proposed techniques is derived within a simplified signal model. Then the performance of several low complexity solutions are compared considering the IEEE 802.15.4a channel models. Due to its importance in ranging and in providing a measure of the confidence of the measured distance, a LOS/NLOS identification algorithm based on the temporal distribution of the signal energy is proposed. Chapter 5 focusses on deriving closed

form expressions for BEP considering NB and UWB interference. For both cases, the statistical model is based on an alpha-stable distribution which assumes interference is generated by multiple interferers spatially distributed according to a Poisson point process. The beginning of this chapter offers a short review of univariate and multivariate stable distributions. Chapter 6 presents the design of an UWB sensor network system based on an UWB CMOS ASIC developed at the CWC. The physical layer of the UWB system is based on the pulse compression technique and on an energy detection receiver structure. Chapter 7 concludes the Thesis with a summary of the results and a discussion of potential areas for future work.

2 Prior and parallel work on IR-UWB

During the past few years, UWB has been one of the most attractive topics for the wireless research community. After the pioneering studies related to radar application based on radio impulses [30], the first patent application [8] of Fullerton and the theoretical work of Scholtz [9] introduced the use of IR for communications purposes. In the paper by Scholtz, it is clear to see how UWB benefits from earlier research into spread spectrum. The use of very narrow pulses allows the application of the CDMA technique at the time domain level through the time-hopping technique. The interest in applications of UWB grew thanks to the work of Win [11, 31–34]. These studies provided the basic understanding of the effect of time hopping and scrambling of pulses on the frequency spectrum of the IR based signal and they underlined the potential offered by the degree of diversity provided by the channel impulse response of UWB signals. Starting from this theoretical basis, research on IR technology focussed on channel modeling, on the coexistence of UWB with other systems and on defining receiver architectures for high data rate (HDR) and low data rate (LDR) systems with ranging capabilities. The extremely wide bandwidth of UWB signals offered new challenges for modeling the propagation channel. In [35], Molish gives a general overview of UWB signal propagation is offered. The author shows how the frequency selectivity of the propagation process causes fundamental differences between UWB channels and "conventional" (wideband) channels. The first "standard" channel models available where those developed by the IEEE 802.15.3a group dedicated to higher speed physical layer extension for high rate wireless personal area networks (WPAN) [36]. These channel models are a modified version of the pre-existing wideband indoor channel models of Saleh and Valunzuela [37] developed to address communication ranges up to 10 meters. Within another working group, the IEEE 802.15.4a, dedicated to low data rate communications, several channel models [38] have been proposed in order to cover communication ranges up to 30 meters in different indoor and outdoor environments. These quickly became widely accepted among researchers. However, they are characterized by log-normal fading of the amplitude of each multipath component and so are not easy to handle mathematically. In [39], the authors show that Nakagami fading offers a good fit to the fading of each UWB channel component. The importance of this work lays in the fact that the Nakagami distribution is more mathematically tractable.

Other significant works related to IR channel modeling are: [40] where a UWB space-variant multipath channel model for indoor communications is proposed; [41], where the authors investigate the value of the time decay constant of the channel power delay profile; and [42], where a second order auto-regressive model with random parameters is proposed in order to approximate the UWB channel frequency response obtained from a wide measurement campaign. Another issue raised by the use of UWB signals is the path-loss model which describes the signal power attenuation as a function of distance. In [43, 44], the authors focus on path-loss and time dispersion parameters proposing a statistical model for the path-loss exponent. A new dual slope path-loss model for UWB signals is presented in [45, 46]. In these papers, the path-loss model is derived considering different power loss coefficients for each multipath component in order to account for the extra attenuation due to the reflections experienced by the multipath components traveling more than the line-of-sight.

2.1 Data detection and synchronization

Accurate time synchronization is a particularly challenging issue for UWB communication due to the high number of multipath components and the low duty cycle of the signal which characterizes time-hopping (TH) based systems. Early studies focused on the synchronization of HDR devices based on DS-SS [47]. An interesting framework for code acquisition was developed by Homier [48–50] who proposes new search algorithms for code acquisition. A theoretical framework for code acquisition in the presence of multipath has been developed by Suwansantisuk and presented in [51]. In [52], a chip-level post detection integration technique previously proposed for DS-SS system was applied to TH-IR based systems. An interesting framework deriving the Cramer-Rao-lower-bound for the synchronization of UWB signals in AWGN and multipath channels is presented in [53]. More recent studies focused on synchronization techniques for non-coherent receivers. In [54], the authors emphasize the robustness of differential and auto-correlation UWB receivers to synchronization errors when compared to coherent receivers. The authors of [55] propose a transmission protocol which allows blind synchronization with low-complexity receivers (i.e. energy detector). A synchronization stage based on intuitive arguments for an energy detector is proposed in [56]. Synchronization algorithms based on noisy templates for auto-correlation receivers are presented in [57]. These algorithms reduce the severe loss of the received energy available for data detection compared with receiver structures which make use

of the typical transmitted reference signaling to perform the correlation. However they have the drawback that very long delay lines are required at the receiver in order to perform the correlation.

The first studies on the achievable BEP performances of UWB wireless systems focussed on HDR systems based on locally generated waveform (LGW) techniques [58–60]. The authors of these studies showed the fading robustness offered by the huge bandwidth diversity provided by UWB and began to identify the challenges of implementing LGW receivers. The performance of digital RAKE receiver structures with different levels of complexity and different sampling rates in the IEEE 802.15.3a UWB channel models are investigated in [61]. The paper showed that serious degradation is observed if the sampling rate is less than the chip rate. In [62], the authors point out one of the main challenges related to IR signal detection based on LGW, considering the effects of timing jitter and tracking on the performance of UWB communications. The result of this study showed that the performance of IR coherent receivers are very sensitive to timing jitter and signal tracking errors. The reduced RF complexity and other implementation advantages offered by IR are somewhat offset by more stringent timing tolerances. These timing issues were already known from the implementation of IR for radar applications. A possible solution to this problem, with the drawback of sub-optimal performance, is based on the principle of differential detection where a delayed copy of the received signal is used in the correlation instead of the locally generated waveform [7]. Receivers using this technique are also known as auto-correlation receivers. When this technique is used, the tracking operation is no longer required. This type of receiver requires the transmitted signal to be opportunely designed in order to offer a reference signal for correlation. This type of signaling, also known as transmitted-reference, was first applied to IR communication systems by Hoctor and Tomlinson. In [63], the authors resume the transmitted reference (TR) scheme proposed 40 years earlier by Pierce [64] adding multiuser capability by using TH modulation. When applied to UWB signals, the auto-correlation receiver has another advantage given by the fact that the reference signal offers an estimate (although noisy) of the propagation channel. As expected by the large bandwidth and as described by several channel measurement campaigns [11, 65–67], the UWB channel impulse response is very rich in multipath components. The channel estimation then requires very long temporal scanning, greatly increasing the power consumption and the receiver complexity. The long channel estimation also requires an overhead which can increase dramatically when compared with NB or wideband (WB) systems. Another solution for limiting the timing and channel estimation

issues is the energy detector also known as the radiometer [68]. The first application of a radiometer for the detection of IR based transmission was proposed in [69] where the authors quantified the “covertness” of IR based transmission for military purposes. The use of the energy detector was proposed for low complexity and low power consumption UWB communication systems by Weisenhorn in 2004 [70]. Several studies related to low complexity receivers then followed. Related to auto-correlation receivers, several works have been published by Quek which focused on analytical studies evaluating the performance of these receivers in the presence of channel fading [71, 72] and in the presence of single tone narrowband interference [73]. Other contributions on auto-correlation receivers came from the work of Witrisal [74], Pausini and Romme [75, 76]. Witrisal showed that auto-correlation UWB systems are accurately modeled by second-order discrete-time Volterra systems. Through these systems, optimal and sub-optimal receivers for differential UWB communications systems affected by inter-symbol interference (ISI) can be derived. Pausini and Romme focused on studying the effect of intra-symbol interference and inter-symbol interference for auto-correlation receivers and the possible counter measures. For energy detector based receivers, there was less interest before the first IEEE 802.15.4a standard draft was produced. The modulation technique which can be supported by energy detection are based on PPM [70] and on On-Off keying (OOK) modulation [77, 78]. In [79], Weisenhorn developed a ML energy detector receiver based on partial channel state information which was similarly proposed on auto-correlation receivers in [80]. Doubuloz focused on evaluating the performance of energy detectors in the IEEE 802.15.4a channel models [81]. An improved energy detector for On-Off keying was also proposed in [82]. Another interesting low complexity solution for UWB systems was proposed by the CEA-LETI group in [83] where the receiver is digital and performs coherent demodulation of the data based on 1 bit A/D conversion with a moderately high speed sampling of the received signal.

2.2 Coexistence and interference

The ability to transmit radio signals using an unlicensed bandwidth of several gigahertz is one of the most appealing characteristics of UWB, however, this was also the reason why UWB faced hostility when initially proposed for widespread adoption. Proponents of narrowband or wideband systems using licensed spectrum expressed concern related to the potential electromagnetic interference from widespread UWB devices. This skepticism led to many studies related to the coexistence of Global Positioning System

(GPS), Global System for Mobile communications (GSM), Universal Mobile Telecommunications System (UMTS), WLAN and other systems with UWB systems. Major contributions on this topic came from simulations and experiments carried out at the Centre for Wireless Communication at Oulu University [84–87], and from computer simulations presented in [88–90]. The performance of the UMTS systems measured in the presence of UWB interference is published in [91]. Coexistence results based on physical layer analysis of WLAN and UWB systems are reported in [92]. Models for the UWB interference on NB systems are given in [93] and in [94]. This extensive investigation demonstrated that the impact of UWB transmission is minimal and it can be further decreased by properly selecting the pulse waveform used and using spectrum smoothing techniques (i.e. pseudo random polarity codes). On the other hand, UWB systems are affected by the interference from several existing systems which use a portion of the UWB spectrum. The effect of narrowband interference on UWB signals has been considered first in radar application [95] and then in communication systems [96, 97] where the authors studied the degradation of the performance of LGW based systems. In [98], the authors show that TH UWB systems are more robust to NB interference than direct-sequence spread-spectrum systems thanks to the reduced duty cycle of the signal. The authors of [99] showed that the NB interference can be mitigated by opportunely shaping the waveform. Frequency nulls in the spectrum of the UWB signal are obtained by using a signal waveform composed of two pulses. The nulls in the spectrum are positioned according to the time interval between the two pulses. However this mitigation technique has the drawback that very high precision in the design of the waveform is required. The effect of a single NB interferer on auto-correlation receivers has been considered in [71, 73] where the authors analyzed the performance of TR and differential TR schemes. In [100], the authors propose an ad-hoc pseudo random amplitude code to reduce the NBI effect on the auto-correlation receiver. Of particular interest is the work done by Win and Pinto in [101] where the authors consider the effect of the NBI on UWB coherent receivers and in [102] where the UWB interference effect on NB coherent receivers is considered. The authors use an interference model proposed for the first time by Sousa in [103] for CDMA systems as an alternative to the Gaussian approximation which takes into account the spatial distribution of multiple NB interference sources. This model makes use of the alpha-stable distribution which is widely applied to economic studies but which also has attracted the attention of wireless researchers in order to model the statistics of shot-noise and co-channel interference in radar and data communication systems[104–106]. A less ac-

curate statistical modeling of the aggregate UWB interference received by a NB system based on the shot-noise theory is presented in [107].

2.3 Ranging estimation

One of the major benefits of UWB communications is the fine temporal accuracy provided by the very large bandwidth. This leads to UWB systems being used in radar applications since they could provide fine resolution on the shape of the target and also high accuracy on the distance of the target. UWB signals are also suitable for localization systems in indoor environments [108]. The first theoretical study which investigated the ranging capability was done by Lee in [109]. A ranging technique based on the power delay profile and high sampling frequency is proposed in [110]. Other studies on the potential accuracy of UWB ranging are presented in [111, 112]. Ranging capabilities have most commonly been associated with LDR devices since these devices provide longer communication ranges than HDR devices and are more suitable for applications with requirements for location awareness. In [113, 114], Dardari studies the performance of time-of-arrival (ToA) estimation using threshold crossing based algorithms and also gives lower bounds on the ranging estimation in realistic UWB channels. A Cramer Lower Bound formulation considering typical UWB channel parameters is given in [115]. Since LDR devices are often required to be low complexity and have low power consumption, there have been many studies into solutions for ToA estimation based on low sampling rate (low complexity) and non-coherent reception. Extensive investigation on time-of-arrival estimation for low complexity receivers is given in [116–119]. Time-of-arrival estimation in non-line of sight (NLOS) conditions is crucial for ranging purposes. This situation has been investigated in [120]. The recognition of the NLOS condition is also important since it can offer a confidence level for the ToA estimator, as in [121], a correction on the estimation of the ToA can be applied. Similar to what Pahlavan proposed in [122] where the author gives an overview of the technical aspects of different technologies for wireless indoor location systems, a way to avoid the ranging estimation for localization purposes is the geo-regioning technique using UWB signals proposed by Althaus in [123]. With this technique, the localization of a target is performed by comparing several stored channel impulse responses, where each one corresponds to a particular region, with the received channel impulse response and choosing the most likely one. The challenge with this algorithm is to distinguish location with similar signatures and to build a signature database. A possible alternative to

low complexity time domain processing is presented by Maravic [124, 125] in which the receiver operates in the frequency domain. This has the advantage of low RF complexity since it is based on low sampling rate. Recent work in this direction has also been presented in [126] where simplified algorithms based on Nyquist sub-sampling are proposed. Several attempts at implementing and designing a ASIC and system with ranging and positioning capabilities have been already presented in [24, 27, 127].

2.4 Conclusions

This chapter has presented a review of the earliest studies of IR-UWB and highlighted the main contributions present in the literature focusing on low complexity IR-UWB systems. The first studies and application of IR techniques to radar systems have been presented together with the efforts to derive a statistical model to describe the complex propagation characteristics of UWB signals.

Synchronization procedures with different complexity have been reviewed as well as several analytical works related to the BEP performance of low complexity receivers. The major challenges imposed by the IR technique in designing coherent receivers have been highlighted through the results of publications which focussed on different coherent receiver structures.

Prior and parallel works to this thesis on auto-correlation and energy detection receivers showed that such solutions can be interesting for sensor network applications and can be used also for ranging applications.

Several coexistence studies mainly regarding UWB interference on NB systems have been introduced. Fewer published work have addressed the effect of NB and UWB interference on UWB non-coherent systems.

3 Data detection for UWB low complexity receivers

3.1 Introduction

One of the goals of this thesis is to identify and evaluate possible solutions for low complexity receivers which support the low power consumption and low cost requirements of sensor networks. This chapter presents and compares different low complexity receiver solutions through the analysis of their signal-to-noise ratio (SNR) at the decision stage in an AWGN channel and bit-error-probability (BEP) in multipath fading channels. It is worth specifying the meaning of low complexity and the implication related to power consumption. The transmission of signals with bandwidth up to several GHz offers several advantages but also brings some disadvantages mainly related to implementation complexity. For instance, the large bandwidth of the UWB channel leads to a large number of resolvable multipath components. In theory, this implies reduced channel fading. The complexity of the channel impulse distortion of the received signal is difficult to predict and reproduce at the receiver in order to fully exploit the diversity. For instance, if we consider the implementation of a Rake receiver which is based on the knowledge of the received signal waveform, issues of power consumption and complexity arise immediately. Due to the complexity of the Rake receiver, a fully digital implementation is required since the signal processing required to extrapolate the channel information would be difficult to implement in the analogue domain. A fully digital solution would require sampling rates of the order of several GHz. Such a solution could not be low power with the technology available today. Furthermore, since the received energy is spread over several multipath components, in order to have sufficient observed signal energy, a large number of components need to be selected, processed and combined.

Aside from these difficulties, the advantage that more than others moved into the development of UWB systems was the fact that no high frequency oscillators are required to up and down convert the signal leading to possible low-cost transceivers.

A trade-off can then be found by reducing the performance of the receiver from that of the optimal structure and considering only low-complexity designs. These low complexity receiver structures are almost all characterized by largely analogue imple-

mentations, requiring only relatively low sampling rates (of the order of the symbol rate) without requiring any channel estimation.

3.2 System model for AcR

A class of receivers which can be implemented almost entirely using analogue techniques is the auto-correlation receiver (AcR). The AcR can be considered as a sub-optimal differential detector and utilizes a delayed version of the received signal to perform the correlation avoiding the need to produce a local replica of the received signal and to provide any channel estimation. The AcR requires a delay line which provides a delayed replica of the received signal to perform the correlation. In order to use this type of receiver, the transmitted signal needs to be opportunely designed. Among the AcR class of receivers, the energy detector (ED) is a special case where the delay between the signal and its replica is zero.

3.2.1 Transmitted signals

The AcR class of receivers requires a carefully designed transmitted signal in order to provide the reference signal to perform the correlation. For impulse radio based UWB, the transmitted signal is composed of one or more reference pulses and one or more modulation pulses which carry the information. The type of modulation schemes considered in this chapter are pulse position modulations (PPM) and pulse amplitude modulation (PAM). Since many modulation/receiver schemes are investigated in the next section, we limit the analysis to binary PPM (BPPM) and binary PAM (BPAM).

Based on the way the pulses are combined at the receiver to perform the correlation, we can distinguish the single reference (SR) structures, where a single pulse is used as a reference for $N_p - 1$ received pulses to generate $N_p - 1$ correlation values; the doublet (DB) based structures, where $N_p/2$ references are used respectively for $N_p/2$ correlation operations; and the alternate (ALT) structures where alternatively each pulse acts as a reference and as a modulated signal. This last structure is similar to differential modulation. In the following structures, we will consider two possible implementation choices for the BPPM. We have the TR choice where two lines with different delays are implemented at the receiver to produce the required observation variables, and the modulated TR (mTR) choice where the reference is also modulated in order to use the same delay line for both decision variables (the position modulation also affects the reference

pulses). A summary of the receiver structures examined and modulations scheme used is given in Fig. 2. Schemes 1, 2 and 3 are related to the SR, the schemes 4, 5 and 6 represents the DB structures and schemes 7 and 8 are for the ALT structures. The ED is not numbered since its performance are equivalent to the DB with BPAM modulation.

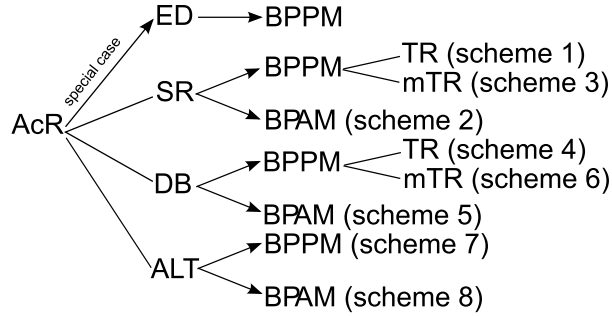


Fig. 2. Receiver structures/modulations tree.

For SR and DB structures, we use a notation which includes both TR and mTR, and both BPPM and BPAM. The transmitted signal for SR structures is defined as

$$s_{SR}(t) = \sum_i \sqrt{\frac{E_b}{N_p T_p}} p(t - g_m d_i \Delta - iT_s) + \sum_{j=0}^{N_p-2} \sqrt{\frac{E_b}{N_p T_p}} a_i p(t - (j+1)T_f - d_i \Delta - iT_s), \quad (4)$$

while for the DB structures it is given by

$$s_{DB}(t) = \sum_i \sum_{j=0}^{\frac{N_p}{2}-1} \sqrt{\frac{E_b}{N_p T_p}} p(t - jT_f - g_m d_i \Delta - iT_s) + \sqrt{\frac{E_b}{N_p T_p}} a_i p(t - jT_f - T_r - d^{(k)} \Delta - iT_s). \quad (5)$$

For the ALT structures, for both BPAM and BPPM, the transmitted signal can be represented as

$$s_{ALT}(t) = \sum_i \sum_{j=0}^{N_p-1} \sqrt{\frac{E_b}{N_p T_p}} a_{i,j} p(t - jT_f - d_i \Delta - iT_s). \quad (6)$$

As mentioned before, the ED receiver is a special implementation of the AcR and the transmitted signal for BPPM can be expressed as¹

$$s_{\text{ED}}(t) = \sum_i \sum_{j=0}^{N_p/2-1} \sqrt{\frac{2E_b}{N_p T_p}} p(t - jT_f - d_i \Delta - iT_s). \quad (7)$$

In equations (4)-(7), $p(t)$ is the bandpass pulse of bandwidth W , duration T_p , centered at the frequency f_c , and with $1/T_p \int_0^{T_p} p^2(t) dt = 1$. The value N_p represents the total number of transmitted pulses, E_b is the energy per symbol, $d_i \in \{0, 1\}$ and $a_i \in \{-1, 1\}$ are the i th transmitted symbols respectively for BPPM and BPAM, while $a_{i,0} \in \{-1, 1\}$ and $a_{i,j} = a_{i,0}^{j+1}$ for $j \neq 0$ are used for the ALT case with BPAM. When BPPM is used $a_i = 1$ and $a_{i,0} = 1$, while if BPAM is used $d_i = 0$. The term T_f is the pulse repetition period, Δ is the modulation delay used to distinguish bit "0" and bit "1". When BPPM is considered, $\Delta < T_f$, T_r is the minimum distance between the two pulses composing the doublet and $T_r < T_f$. T_f and Δ might assume different values in the proposed schemes, but they are always set to avoid inter-pulse interference (IPI) and inter-symbol interference (ISI). The variable g_m is used to distinguish a scheme with modulated reference receiver ($g_m = 1$) from a scheme with non-modulated reference ($g_m = 0$). For all the transmitted signal structures represented by equations (4)-(7), the symbol energy is equally spread over the pulses composing a symbol. For all the proposed structures, the received signal can be expressed as

$$r^{(k)}(t) = w^{(k)}(t) + n(t), \quad (8)$$

where $w^{(k)}(t) = s^{(k)}(t) * h(t)$ and $n(t)$ is a white Gaussian process with two-sided power spectral density $\sigma_0^2 = \frac{N_0}{2}$. The function $h(t)$ is the impulse response of the channel with maximum excess delay T_d . Since the purpose of this chapter is to compare the performance of the different pulse repetition structures, only the AWGN case is considered. Assuming no IPI and no ISI, the presence of multipath will affect the performance of all the receivers in the same way without modifying the relationship between them.

3.2.2 Receiver structures

With correlation based receivers, the correlation of the received signal with a locally generated waveform reduces the noise bandwidth to the signal bandwidth. When the

¹Another modulation which is supported by the ED is On-Off Keying. However, detection of On-Off Keying modulated signal requires the setting of a threshold which is not included in our studies. It cannot be considered as a low-complexity solution since noise and signal strength estimations are required.

receiver does not make use of locally generated waveform, the filtering operation after the antenna is essential to limit the noise contribution. In order to limit the noise power, an ideal band-pass zonal filter (BPZF) is considered in this chapter. The filter is characterized by a bandwidth W , which is considered sufficiently large to ensure that the spectrum of the filtered signal $\tilde{r}(t)$ is undistorted and, consequently, ISI and IPI caused by filtering will be negligible.

In order to proceed in the analysis with a simplified notation, we define for BPPM the decision variable for the $i = 0$ received bit as

$$Y = Y_1 - Y_2, \quad (9)$$

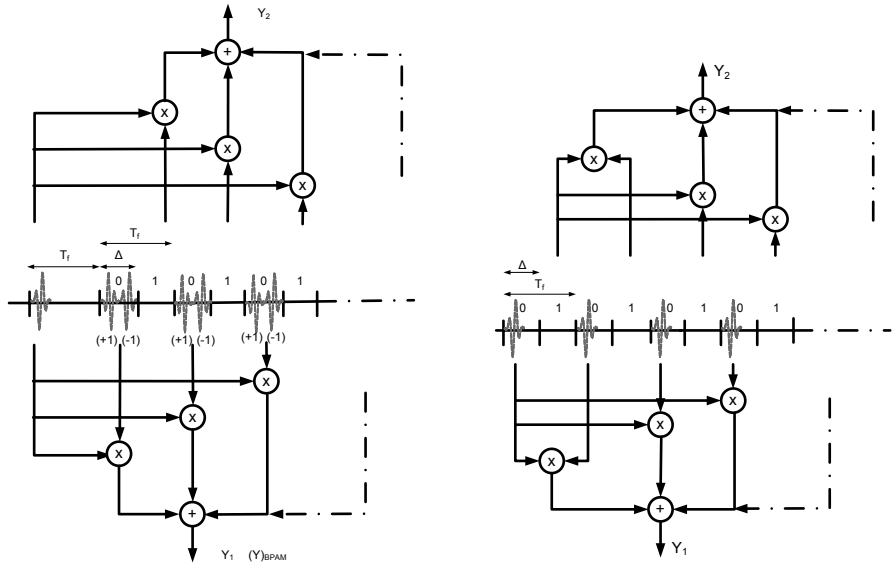
where Y_1 and Y_2 are the observed variables defined by the outputs of the correlators (integrators for the ED).

For SR structures in the case of BPPM, as shown in Figures 3(a) and 3(b) in the cases without and with modulated reference respectively, the decision variable obtained by adding the results of $N_p - 1$ correlations can be expressed as

$$\begin{aligned} Y^{\text{SR-BPPM}} &= \sum_{j=0}^{N_p-2} \int_0^T \tilde{r}(t) \tilde{r}(t + (j+1)T_f) dt \\ &- \sum_{j=0}^{N_p-2} \int_0^T \tilde{r}(t + g_m \Delta) \tilde{r}(t + (j+1)T_f + \Delta) dt, \end{aligned} \quad (10)$$

and in the case of BPAM, as shown in Figures 3(a), the decision variable can be expressed as

$$Y^{\text{SR-BPAM}} = \sum_{j=0}^{N_p-2} \int_0^T \tilde{r}(t) \tilde{r}(t + (j+1)T_f) dt. \quad (11)$$



(a) TR with BPPM (scheme 1) and TR with BPAM (scheme 3)

(b) mTR with BPPM (scheme 2)

Fig. 3. SR structures.

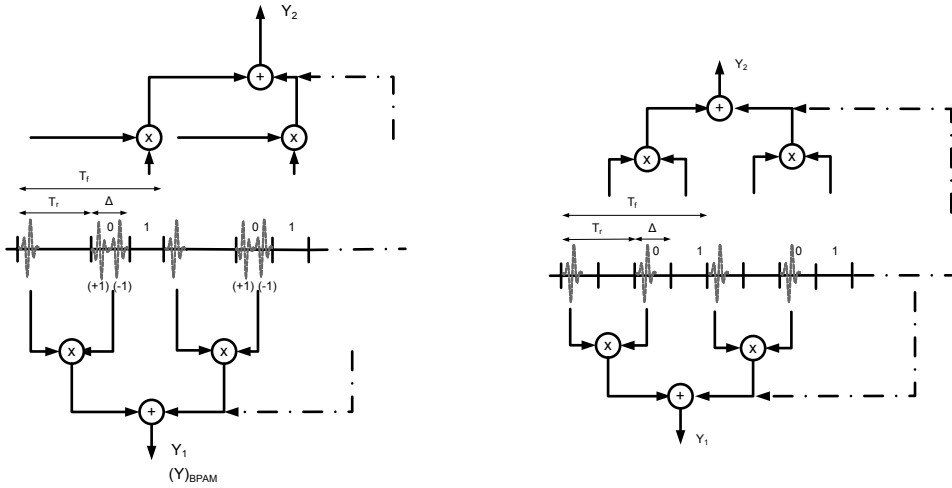
Now considering DB structures and considering BPPM, as shown in Figures 4(a) and 4(b) in the cases without and with modulated reference respectively, the decision variable obtained by adding the result of $\frac{N_p}{2}$ correlations, can be expressed as

$$\begin{aligned}
 Y^{DB-BPPM} & \quad (12) \\
 & = \sum_{j=0}^{\frac{N_p}{2}-1} \int_0^T \tilde{r}(t + jT_f) \tilde{r}(t + jT_f + T_r) dt \\
 & \quad - \sum_{j=0}^{\frac{N_p}{2}-1} \int_0^T \tilde{r}(t + jT_f + g_m \Delta) \tilde{r}(t + jT_f + T_r + \Delta) dt,
 \end{aligned}$$

and in the case of BPAM, as shown in Fig. 4(a), the decision variable can be expressed

as

$$Y^{\text{DB-BPAM}} = \sum_{j=0}^{\frac{N_p}{2}-1} \int_0^T \tilde{r}(t + jT_f) \tilde{r}(t + jT_f + T_r) dt. \quad (13)$$



(a) TR with BPPM (scheme 4) and TR with BPAM (scheme 6)

(b) mTR with BPPM (scheme 5)

Fig. 4. DB structures.

Considering the ALT structures (Fig. 5) and considering the case of BPPM, the decision variable obtained by adding the result of $N_p - 1$ correlations can be expressed as

$$\begin{aligned}
Y^{\text{ALT-BPPM}} &= \sum_{j=0}^{N_p-2} \int_0^T \tilde{r}(t + jT_f) \tilde{r}(t + (j+1)T_f) dt \\
&\quad - \sum_{j=0}^{N_p-2} \int_0^T \tilde{r}(t + jT_f + \Delta) \tilde{r}(t + (j+1)T_f + \Delta) dt,
\end{aligned} \tag{14}$$

and in the case of BPAM the decision variable can be expressed as

$$Y^{\text{ALT-BPAM}} = \sum_{j=0}^{N_p-2} \int_0^T \tilde{r}(t + jT_f) \tilde{r}(t + (j+1)T_f) dt.$$

For the ED receiver with BPPM signaling, the decision variable can be written as

$$Y^{\text{ED-BPPM}} = \sum_{j=0}^{\frac{N_p}{2}-1} \int_0^T \tilde{r}(t + jT_f)^2 dt - \sum_{j=0}^{\frac{N_p}{2}-1} \int_0^T \tilde{r}(t + jT_f + \Delta)^2 dt. \tag{15}$$

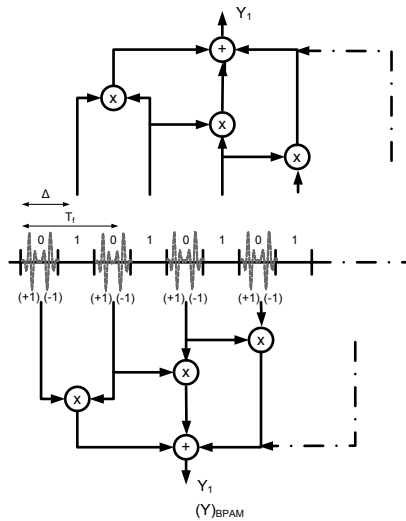


Fig. 5. ALT structures with BPPM (scheme 7) and with BPAM (scheme 8).

In all the receiver schemes presented in this section, the integration time T determines the number of multipath components (or equivalently, the amount of energy) captured by the receiver as well as the amount of noise. Note that the decision on the received data ($\{0, 1\}$ in the BPPM case and $\{-1, 1\}$ in the BPAM case), is based on the rule

$$Y \begin{matrix} 1(-) \\ \geq \\ 0(+1) \end{matrix} 0. \quad (16)$$

3.3 Signal-to-noise ratio derivations

Following the sampling expansion approach, a low pass-band signal $\tilde{f}(t)$ with limited bandwidth $W/2$ is completely determined by an infinite series of complex samples of the signal spaced $1/W$ seconds apart. Similarly, a real-valued pass band signal $\tilde{f}(t)$ of bandwidth W is completely determined by an infinite series of samples of its low-pass

equivalent signal spaced $1/W$ seconds apart [128]. The received waveform can be then represented in the limited integration time T by a limited series of independent samples [68]

$$\tilde{r}(t) \approx \sum_{m=1}^{2WT} \frac{1}{\sqrt{2W}} \tilde{r}\left(\frac{m}{W}\right) \frac{\sin(2\pi Wt - m)}{2\pi Wt - m}. \quad (17)$$

Now, considering the correlation between two bandwidth-limited signals as is the case for correlation based receivers, equation (10) and (11) can be rewritten for $d_0 = 0$ and $a_0 = 1$ respectively as

$$Y_{|d_0=0}^{\text{SR-BPPM}} = \frac{1}{2W} \sum_{j=0}^{N_p-2} \left[\sum_{m=1}^{2WT} \left(\sqrt{\frac{E_b}{N_p T_p}} w_{1,m} + n_{1,m} \right) \left(\sqrt{\frac{E_b}{N_p T_p}} w_{j,m} + n_{3,j,m} \right) - \left((1-g_m) \left(\sqrt{\frac{E_b}{N_p T_p}} w_{1,m} + n_{1,m} \right) + g_m n_{1,m} \right) n_{4,j,m} \right], \quad (18)$$

and

$$Y_{|a_0=1}^{\text{SR-BPAM}} = \frac{1}{2W} \sum_{j=0}^{N_p-2} \left[\sum_{m=1}^{2WT} \left(\sqrt{\frac{E_b}{N_p T_p}} w_{1,m} + n_{1,m} \right) \left(\sqrt{\frac{E_b}{N_p T_p}} w_{j,m} + n_{3,j,m} \right) \right], \quad (19)$$

where $w_{1,m}$, $w_{j,m}$, $n_{1,m}$, $n_{2,m}$, $n_{3,j,m}$ and $n_{4,j,m}$ are for odd (even m) real (imaginary) parts of the equivalent low-pass version samples of the signals $w(t)$, $w(t + (j+1)T_f)$, $n(t)$, $n(t + \Delta)$, $n(t + (j+1)T_f)$ and $n(t + (j+1)T_f + \Delta)$ in the interval $[0, T]$ respectively.

Similarly, equation (12) and (13) can be rewritten respectively as

$$Y_{|d_0=0}^{\text{DB-BPPM}} = \frac{1}{2W} \sum_{j=0}^{\frac{N_p}{2}-1} \left[\sum_{m=1}^{2WT} \left(\sqrt{\frac{E_b}{N_p T_p}} w_{j,m} + n_{1,j,m} \right) (w_{j,m} + n_{2,j,m}) - \left((1-g_m) \left(\sqrt{\frac{E_b}{N_p T_p}} w_{j,m} + n_{1,j,m} \right) + g_m n_{2,j,m} \right) n_{4,j,m} \right], \quad (20)$$

and

$$Y_{|a_0=1}^{\text{DB-BPAM}} = \frac{1}{2W} \sum_{j=0}^{\frac{N_p}{2}-1} \left[\sum_{m=1}^{2WT} \left(\sqrt{\frac{E_b}{N_p T_p}} w_{j,m} + n_{1,j,m} \right) \left(\sqrt{\frac{E_b}{N_p T_p}} w_{j,m} + n_{2,j,m} \right) \right], \quad (21)$$

where $w_{j,m}$, $n_{1,m}$, $n_{2,j,m}$, $n_{3,j,m}$ and $n_{4,j,m}$ are for odd (even m) real (imaginary) parts of the equivalent low-pass version samples of the signals $w(t + jT_f)$, $n(t + jT_f)$, $n(t + jT_f + \Delta)$, $n(t + jT_f + T_r)$ and $n(t + jT_f + T_r + \Delta)$ in the interval $[0, T]$ respectively.

Equation (14) and (15) can be rewritten as

$$Y_{|d_0=0}^{\text{ALT-BPPM}} = \frac{1}{2W} \sum_{j=0}^{N_p-2} \left[\sum_{m=1}^{2WT} \left(\sqrt{\frac{E_b}{N_p T_p}} w_{j,m} + n_{1,j,m} \right) \left(\sqrt{\frac{E_b}{N_p T_p}} w_{j+1,m} + n_{1,j+1,m} \right) - n_{2,j,m} n_{2,j+1,m} \right], \quad (22)$$

and

$$Y_{|a_0=1}^{\text{ALT-BPAM}} = \frac{1}{2W} \sum_{j=0}^{N_p-2} \left[\sum_{m=1}^{2WT} \left(\sqrt{\frac{E_b}{N_p T_p}} w_{j,m} + n_{1,j,m} \right) \left(\sqrt{\frac{E_b}{N_p T_p}} w_{j+1,m} + n_{1,j+1,m} \right) \right], \quad (23)$$

where $w_{j,m}$, $n_{1,m}$ and $n_{2,j,m}$ are for odd (even m) real (imaginary) parts of the equivalent low-pass version samples of the signals $w(t + jT_f)$, $n(t + jT_f)$ and $n(t + jT_f + \Delta)$, in the interval $[0, T]$ respectively. Finally the decision variable for the ED case can be rewritten as

$$Y_{|d_0=0}^{\text{ED-BPPM}} = \frac{1}{2W} \sum_{j=0}^{\frac{N_p}{2}-1} \left[\sum_{m=1}^{2WT} \left(\sqrt{\frac{E_b}{N_p T_p}} w_{j,m} + n_{1,j,m} \right)^2 - \left(\sqrt{\frac{E_b}{N_p T_p}} w_{j,m} + n_{2,j,m} \right)^2 \right], \quad (24)$$

where $w_{j,m}$, $n_{1,j,m}$ and $n_{2,j,m}$ are for odd (even m) are real (imaginary) parts of the equivalent low-pass version samples of the signals $w(t + jT_f)$, $n(t + mT_f)$ and $n(t + jT_f + \Delta)$ in the interval $[0, T]$ respectively. Conditioned on the channel impulse response,² Y_{d_0} is a sum of deterministic variables plus several zero mean r.v.s. If the number $N_p WT$ of r.v.s contributing to the decision variable is sufficiently large, the decision variables given in (18)-(23) can be considered as Gaussian distributed. The goodness of the Gaussian approximation has been empirically proven in [129] and used to evaluate the performance of some AcR schemes in [130, 131]. The use of the Gaussian approximation means that for all the receiver structures proposed, the same error probability function $Q(\cdot)$ can be applied. The signal-to-noise ratio at the decision device (SNR_d) is then used to compare the performance of the proposed receiver schemes. The SNR_d can be defined

²Note that this is trivial for the AWGN channel.

as follows:

$$\text{SNR}_d = \frac{E\{Y\}^2}{\text{Var}\{Y\}}. \quad (25)$$

The derivation of the following SNR_d terms can be found in detail in Appendix 1. For the SR structures based on TR and mTR, it is shown that in the case of BPPM, the signal-to-noise ratio at the decision device can be expressed as

$$(\text{SNR}_d)_{\text{SR-BPPM}} = \frac{\frac{(N_p-1)}{N_p} \frac{2E'_b}{N_0}}{\left(N_p + 1 - g_m + 2N_p TW \frac{N_0}{E'_b}\right)}. \quad (26)$$

and for the BPAM case as

$$(\text{SNR}_d)_{\text{SR-BPAM}} = \frac{\frac{(N_p-1)}{N_p} \frac{2E'_b}{N_0}}{\left(N_p + N_p TW \frac{N_0}{E'_b}\right)}. \quad (27)$$

For the DB structures based on TR and mTR it is shown that in the case of BPPM the signal-to-noise ratio at the decision device can be expressed as

$$(\text{SNR}_d)_{\text{DB-BPPM}} = \frac{\frac{2E'_b}{N_0}}{\left(6 - 2g_m + 2N_p TW \frac{N_0}{E'_b}\right)}, \quad (28)$$

and for the BPAM case as

$$(\text{SNR}_d)_{\text{DB-BPAM}} = \frac{\frac{2E'_b}{N_0}}{\left(4 + 2N_p TW \frac{N_0}{E'_b}\right)}. \quad (29)$$

For the ALT structure with BPPM it can be shown that SNR_d is defined as

$$(\text{SNR}_d)_{\text{ALT-BPPM}} = \frac{\frac{(N_p-1)}{N_p} \frac{2E'_b}{N_0}}{\left(4 \frac{N_p}{N_p-1} - \frac{6}{N_p-1} + N_p TW \frac{N_0}{E'_b}\right)}, \quad (30)$$

and for the ALT structure with BPAM

$$(\text{SNR}_d)_{\text{ALT-BPAM}} = \frac{\frac{(N_p-1)}{N_p} \frac{2E'_b}{N_0}}{\left(4 \frac{N_p}{N_p-1} - \frac{6}{N_p-1} + N_p TW \frac{N_0}{E'_b}\right)}. \quad (31)$$

Finally, for the ED structure, the SNR_d is

$$(\text{SNR}_d)_{\text{ED-BPPM}} = \frac{\frac{2E'_b}{N_0}}{\left(4 + N_p TW \frac{N_0}{E'_b}\right)}. \quad (32)$$

Note that E'_b is the integrated signal energy for an integration interval of duration T .³

3.4 Numerical results in the AWGN channel

The use of equations (27) - (31) in the $Q()$ function to determine the BEP is based on a Gaussian approximation of the decision variables. Due to the approximation, the BEP results might not be extremely precise in terms of BEP; however, they can be used for a quick performance comparison among the different receiver structures. For the results presented in this section, we consider the simple case of the AWGN channel. Frequency selective channel fading affects the BEP performance; however, the performance comparison among the different schemes is independent of the channel fading. Note that we consider here $E'_b = E_b$. Figures 6(a) and 6(b) show the performance of the proposed structures versus the E_b/N_0 . For high E_b/N_0 , the performance of the different schemes are related to the capacity to recover the transmitted energy and to the noise variance from the signal-noise cross terms while the contribution of the pure noise terms to the variance tends to be negligible. Although the SR schemes suffer a small signal energy overhead using a single reference pulse, the performances of the SR schemes are compromised by the repeated injection of the same noise components in the decision variable which increases the variance of the observed variable. For low E_b/N_0 values, the ALT scheme provides the best performance when BPAM is used. The performance of the DB with TR signaling approaches the best performance when the E_b/N_0 rises. In this case the 3 dB energy loss associated with the presence of the reference pulses is compensated by a minor noise enhancement compared with the ALT schemes.

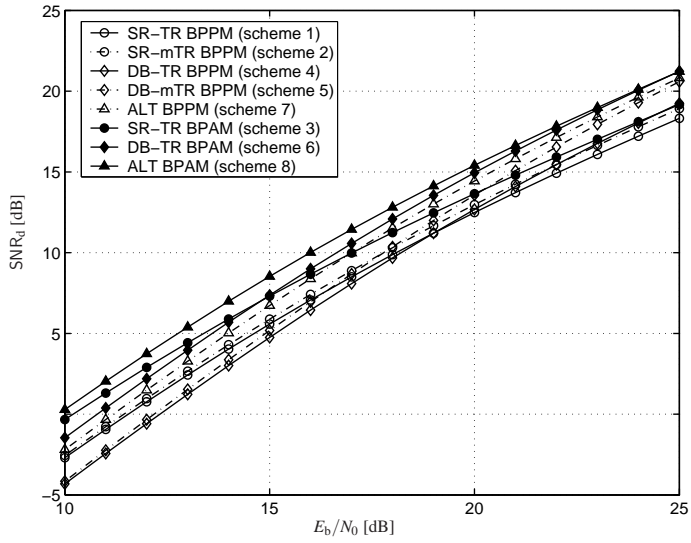
The ED receiver performance is not reported in the figures; however, equations (29) and (32) show that ED with BPPM and DB-TR with BPAM have equal performance. Equations (29) and (32) show also that if compared to optimal coherent receivers, these two schemes are affected by a minimum of 3 and 6 dB loss respectively.⁴

Figures 7(a) and 7(b) show the SNR_d versus the time bandwidth product WT . These figures provide a comparison of the performance of the different schemes which account for the delay spread of the channel. As known from the literature, antipodal modulation in low E_b/N_0 region performs better than orthogonal modulation, since fewer noise

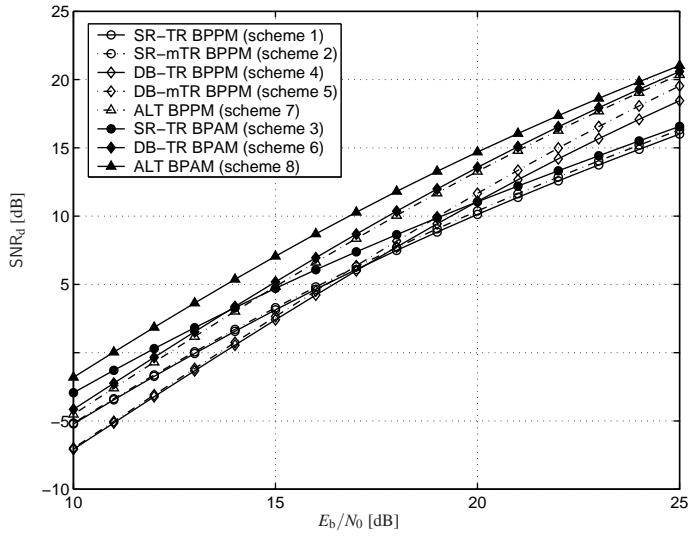
³In the presence of a multipath channel the integration time T effects the integrated signal energy so that $E'_b \leq E_b$.

⁴The minimum loss is for very high E_b/N_0 . In this case, the third term at the denominator of the SNR_d s can be considered negligible.

components are involved in the decision variable. This makes the BPAM modulated structures less sensitive to the integration time and bandwidth product increase. However, the ALT with BPPM structure outperforms the SR and DB with BPAM structures for small WT values due to the good usage of the transmitted signal energy. The DB structures with BPPM experience the greatest degradation in performance with an increase of WT .

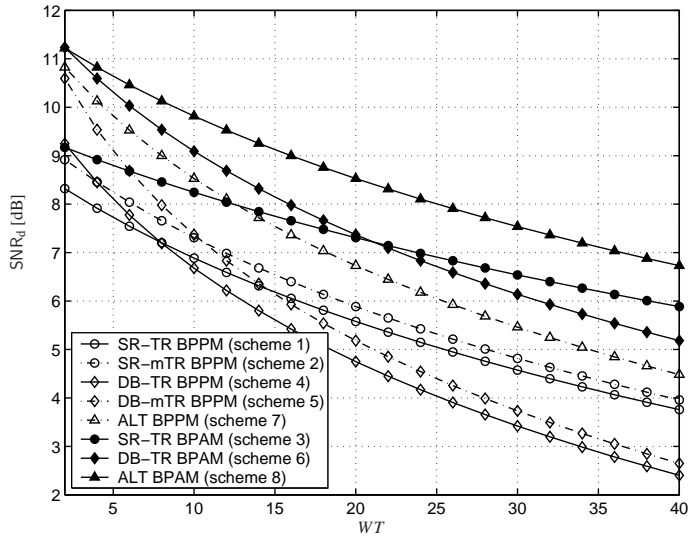


(a) $N_p = 6$

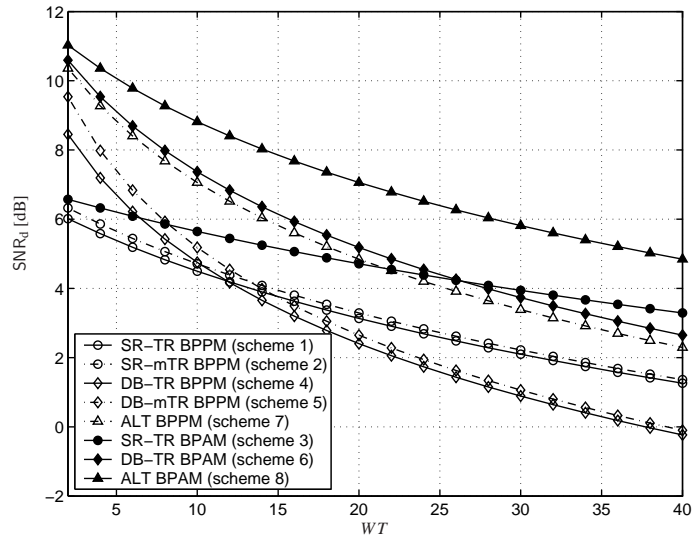


(b) $N_p = 12$

Fig. 6. SNR_d for different E_b/N_0 values, integration time and bandwidth product $WT = 20$.

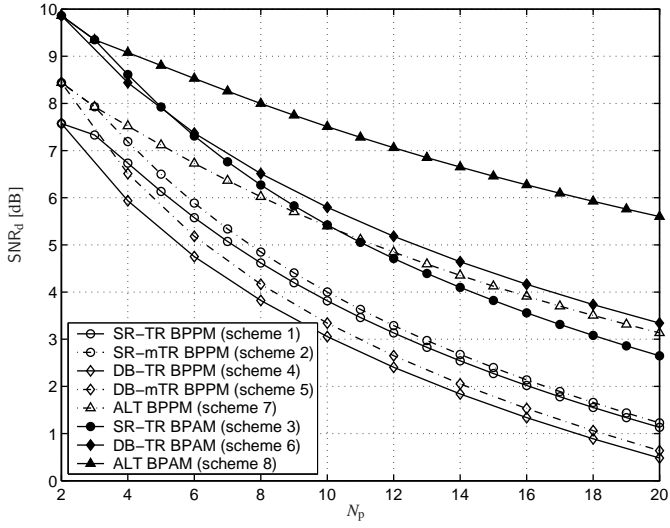


(a) $N_p = 6$

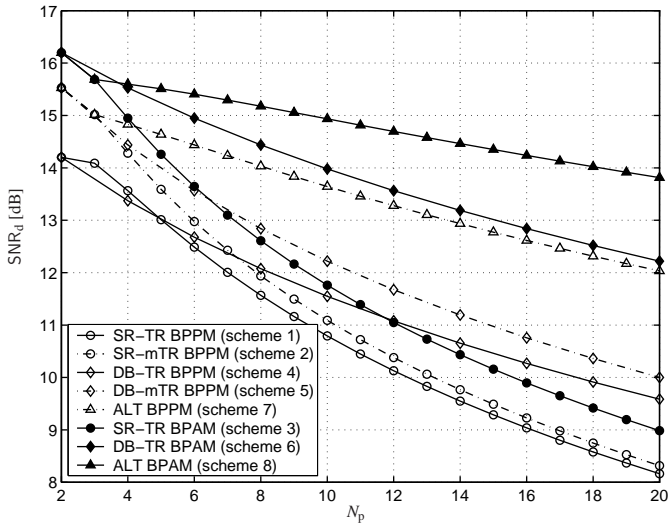


(b) $N_p = 12$

Fig. 7. SNR_d for different integration time and bandwidth product values WT and $E_b/N_0 = 15$ dB.



(a) $E_b/N_0 = 15$ dB



(b) $E_b/N_0 = 20$ dB

Fig. 8. SNR_d for different pulses per symbol values N_p , integration time and bandwidth product $WT = 20$.

In Figures 8(a) and 8(b), the dependence of SNR_d on N_p is shown. Here again the ALT structure provides the best performance. The performance of all the other schemes tend to diverge from the ALT scheme when N_p increases. The ALT scheme with BPPM tends to approach the performance of the DB-TR scheme with BPAM for high N_p values. The impact of increasing the number of pulses for SR schemes is a strong increase in the variance of the signal-noise cross terms produced by the noise present in the single reference as can be seen in equations (26) and (27). While for lower E_b/N_0 values, pulse repetition has less effect on SR schemes than DB schemes for higher E_b/N_0 , the increase of number of pulse affects the SR schemes more than the others schemes. In high E_b/N_0 conditions, the signal-noise cross terms are dominant in the contribution to the variance of the decision variable. For this reason the SR structure is the more penalized since the same noise term related to the reference is amplified $N_p - 1$ times. These figures show that the mTR schemes slightly outperforms the TR schemes, especially for low values of N_p and WT , and high values of E_b/N_0 .

3.5 System and channel models for BEP analysis of non-coherent UWB receivers in fading channel

Directly looking at the SNR's formulation and at the numerical results presented in the previous section, we can reduce the choice of solutions which provide reasonable performance with the lowest complexity. Among the schemes proposed, the ALT structure with BPAM showed the best performance; however, its implementation forbids the use of a hopping code sequence and requires a despreading operation at the receiver in order to perform the detection. Reaching similar conclusions as the IEEE 802.15.4a LDR UWB working group, the choice is then in favour of the ED with BPPM and the auto-correlation receiver with DB-TR signaling and BPAM which we now simply write as TR-BPAM. As can be understood by the SNR expressions, these two schemes perform equally. In this section we focus on the derivation of closed form expressions of the BEP for the ED receiver with BPPM signaling and the AcR with TR-BPAM signaling which includes the effect of channel fading. We first briefly redefine the signaling models for the two schemes we will focus on in the reminder of the Thesis.

3.5.1 Transmitted Signals

3.5.1.1 BPPM

First considering the BPPM signaling shown in Fig. 9, the transmitted signal for user k can be expressed as

$$s_{\text{BPPM}}^{(k)}(t) = \sum_i \left[(1 - d_i^{(k)}) b_1^{(k)}(t - iT_s) + d_i^{(k)} b_2^{(k)}(t - iT_s) \right], \quad (33)$$

where $d_i^{(k)} \in \{0, 1\}$ is the i th data symbol and $T_s = \frac{N_s}{2} T_f^{\text{ED}}$ is the symbol duration with N_s and T_f^{ED} the number of pulses per symbol and the average pulse repetition period, respectively. The transmitted signal for $d_i^{(k)} = 0$ and $d_i^{(k)} = 1$ can be written, respectively, as

$$\begin{aligned} b_1^{(k)}(t) &= \sum_{j=0}^{\frac{N_s}{2}-1} \sqrt{\frac{E_p^{\text{ED}}}{T_p}} a_j^{(k)} p(t - jT_f^{\text{ED}} - c_j^{(k)} T_p), \\ b_2^{(k)}(t) &= \sum_{j=0}^{\frac{N_s}{2}-1} \sqrt{\frac{E_p^{\text{ED}}}{T_p}} a_j^{(k)} p(t - jT_f^{\text{ED}} - c_j^{(k)} T_p - \Delta), \end{aligned} \quad (34)$$

where the parameter Δ is the time shift between two different data bits. In TH signaling, $\{c_j^{(k)}\}$ is the pseudo-random sequence of the k th user, where $c_j^{(k)}$ is an integer in the range $0 \leq c_j^{(k)} < N_h$, and N_h is the maximum allowable integer shift. The bipolar random amplitude sequence $\{a_j^{(k)}\}$ is used here only for spectrum smoothing purposes while the TH sequence is used to mitigate interference and to support multiple access. The term $p(t)$ is a bandpass pulse of duration T_p , center frequency f_c , and with $1/T_p \int_0^{T_p} p^2(t) dt = 1$. For BPPM with non-coherent receivers, the bipolar random amplitude sequence $\{a_j^{(k)}\}$ can only serve the purpose of spectrum smoothing. The energy of the transmitted pulse is then $E_p^{\text{ED}} = \frac{2E_s^{\text{ED}}}{N_s}$, where E_s^{ED} is the symbol energy associated with BPPM. To preclude intra-symbol interference (isi) and ISI, we assume $\Delta \geq T_g$ and $(N_h - 1)T_p + \Delta + T_g \leq T_f^{\text{ED}}$.

3.5.1.2 TR-BPAM

Considering the TR signaling shown in Fig. 9, the transmitted signal for user k can be decomposed into a reference signal component $b_r^{(k)}(t)$ and a data modulated signal

$b_d^{(k)}(t)$ as follows:

$$s_{\text{TR}}^{(k)}(t) = \sum_i b_r^{(k)}(t - iT_s) + d_i^{(k)} b_d^{(k)}(t - iT_s), \quad (35)$$

where $d_i^{(k)} \in \{-1, 1\}$ is the i th data symbol, and $T_s = N_s T_f^{\text{TR}}$ is the symbol duration with N_s and T_f^{TR} the number of pulses per symbol and the average pulse repetition period, respectively [132].⁵ The reference and data modulated signals can be written as

$$\begin{aligned} b_r^{(k)}(t) &= \sum_{j=0}^{\frac{N_s}{2}-1} \sqrt{\frac{E_p^{\text{TR}}}{T_p}} a_j^{(k)} p(t - j2T_f^{\text{TR}} - c_j^{(k)} T_p), \\ b_d^{(k)}(t) &= \sum_{j=0}^{\frac{N_s}{2}-1} \sqrt{\frac{E_p^{\text{TR}}}{T_p}} a_j^{(k)} p(t - j2T_f^{\text{TR}} - c_j^{(k)} T_p - T_r), \end{aligned} \quad (36)$$

where $b_d^{(k)}(t)$ is equal to a version of $b_r^{(k)}(t)$ delayed by T_r , and the rest of the terms in (36) are defined similarly as in (34). The energy of the transmitted pulse is $E_p^{\text{TR}} = E_s^{\text{TR}}/N_s$ where E_s^{TR} is the symbol energy associated with TR signaling. Note that the transmitted energy is equally allocated among $N_s/2$ reference pulses and $N_s/2$ modulated pulses. The differences between the BPPM case and the TR case are the position modulation and the transmitted energy allocated among $N_s/2$ modulated pulses. The duration of the received UWB pulse is $T_g = T_p + T_d$, where T_d is the maximum excess delay of the channel. We consider $T_r \geq T_g$ and $(N_h - 1)T_p + T_r + T_g \leq 2T_f^{\text{TR}}$ to preclude isi and ISI respectively. Note T_r is the time separation between each pair of data and reference pulses.

3.5.2 Channel model

The received signal can be expressed as

$$r(t) = h(t) * s(t) + n(t), \quad (37)$$

where $s(t)$ is the transmitted signal and $h(t)$ is the channel impulse response which can be written as

$$h(t) = \sum_{l=1}^L h_l \delta(t - \tau_l), \quad (38)$$

⁵Note that $T_f^{\text{TR}} = \frac{T_f^{\text{FD}}}{2}$ such that the symbol duration of the two signaling schemes is the same.

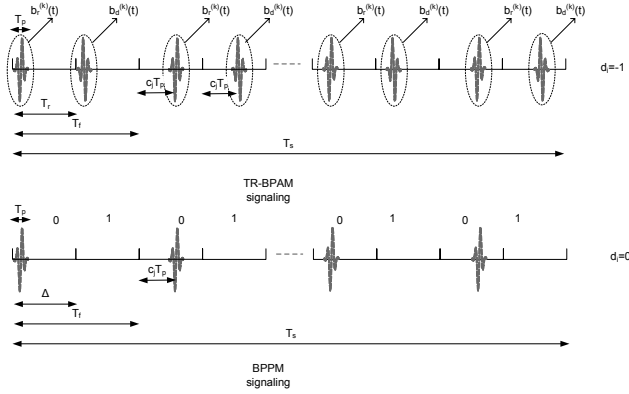


Fig. 9. Signaling schemes.

where h_l and τ_l are the amplitude and the arrival time of the l th channel multipath component. The term $n(t)$ is zero-mean, white Gaussian noise with two-sided power spectral density $N_0/2$. We consider the resolvable dense multipath channel case, i.e., $|\tau_l - \tau_j| \geq T_p, \forall l \neq j$, where $\tau_l = \tau_1 + (l-1)T_p$, and $\{h_l\}$ are assumed to be statistically independent random variables (r.v.s). We can express $h_l = |h_l| \exp(j\phi_l)$, where $\phi_l = 0$ or π_l with equal probability.

3.5.3 Energy detector (ED)

As mentioned in the previous section, the energy detection can be seen as a special case of the AcR where the delay between the reference pulse and the information pulse is zero. This changes the statistics of the integrator outputs if compared with the AcR case. The two receiver schemes are illustrated in Fig. 10. For a single user case, the signal after the BPZF can be represented as

$$\begin{aligned} \tilde{r}_{\text{BPPM}}(t) &= \sum_i \sum_{j=0}^{\frac{N_s}{2}-1} \sum_{l=1}^L \sqrt{\frac{E_P^{\text{ED}}}{T_p}} h_l a_j \left[(1-d_i) p(t - jT_f - c_j^k T_p - \tau_l) \right. \\ &\quad \left. + (d_i) p(t - jT_f - c_j^k T_p - \Delta - \tau_l) \right] + \tilde{n}(t), \end{aligned} \quad (39)$$

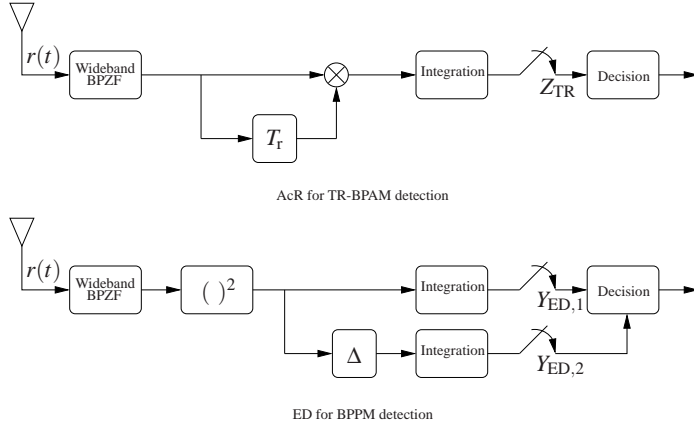


Fig. 10. Receiver structures for UWB non-coherent schemes.

where $\tilde{n}(t)$ represents the noise process after the band pass filter (BPZF).⁶

Note that in the case of Gaussian noise, the samples taken with $1/W$ interval are statistically independent since the auto-correlation function of the BPZF is

$$R_{h_{\text{BPZF}}(t)}(\tau) = W \text{sinc}(W\tau) \cos(2\pi f_c \tau). \quad (40)$$

The decision on the received data is based on the difference of the observed integration outputs that can be expressed as

$$Z_{\text{ED}} = \underbrace{\sum_{j=0}^{\frac{N_s}{2}-1} \int_{jT_f+c_jT_p}^{jT_f+c_jT_p+T} (\tilde{r}_{\text{BPPM}}(t))^2 dt}_{Z_{\text{ED},1}} - \underbrace{\sum_{j=0}^{\frac{N_s}{2}-1} \int_{jT_f+c_jT_p+\Delta}^{jT_f+c_jT_p+T+\Delta} (\tilde{r}_{\text{BPPM}}(t))^2 dt}_{Z_{\text{ED},2}}. \quad (41)$$

The integration interval T determines the number of multipath components (or equivalently, the amount of energy) captured by the receiver as well as the amount of noise. An optimal integration interval, which depends on the power delay profile and on the signal-to-noise ratio, is therefore desirable.

3.5.4 Auto-correlation receiver (AcR)

As mentioned in the previous section, the AcR offers quite good performance in rich multipath channels where the signal is heavily distorted and the channel is difficult to

⁶The effect of the BPZF on $p(t)$ is considered negligible, consequently no distortion is considered.

estimate.

The output of the BPZF for TR signaling can be expressed as

$$\begin{aligned}
& \tilde{r}_{\text{TR}}(t) \\
&= \sum_i \sum_{j=0}^{\frac{N_s}{2}-1} \sum_{l=1}^L \left[\sqrt{\frac{E_p^{\text{TR}}}{T_p}} h_l a_j p(t - iN_s T_f - j2T_f - c_j T_p - \tau_l) \right. \\
&\quad \left. + \sqrt{\frac{E_p^{\text{TR}}}{T_p}} h_l a_j d_i p(t - iN_s T_f - j2T_f - c_j T_p - T_f - \tau_l) \right] \\
&+ \tilde{n}(t). \tag{42}
\end{aligned}$$

The correlation output of the AcR can be expressed as

$$Z_{\text{TR}} = \sum_{j=0}^{\frac{N_s}{2}-1} \int_{j2T_f+T_f+c_jT_p}^{j2T_f+T_f+c_jT_p+T} \tilde{r}_{\text{TR}}(t) \tilde{r}_{\text{TR}}(t - T_f) dt, \tag{43}$$

where the integration time T determines the amount of integrated signal energy.

3.6 BEP analysis of non-coherent UWB receivers in fading channel

In order to derive and compare the performance of the AcR and the ED receivers, the sampling expansion is used [128, 132–134].

3.6.1 Energy detector (ED) with BPPM signaling

The observed variables in (41) corresponding to the energy of the received signals over the two observation intervals can be written as

$$\begin{aligned}
Z_{\text{ED},1} &= \sum_{j=0}^{\frac{N_s}{2}-1} \int_0^T (w_{1,j}(t) + \eta_{1,j}(t))^2 dt, \\
Z_{\text{ED},2} &= \sum_{j=0}^{\frac{N_s}{2}-1} \int_0^T (w_{2,j}(t) + \eta_{2,j}(t))^2 dt, \tag{44}
\end{aligned}$$

where $w_{1,j}(t) \triangleq (1 - d_0) \check{b}_1(t + jT_f^{\text{ED}} + c_j T_p)$, $w_{2,j}(t) \triangleq d_0 \check{b}_2(t + jT_f^{\text{ED}} + c_j T_p + \Delta)$, $\eta_{1,j}(t) \triangleq \tilde{n}(t + jT_f^{\text{ED}} + c_j T_p)$ and $\eta_{2,j}(t) \triangleq \tilde{n}(t + jT_f^{\text{ED}} + c_j T_p + \Delta)$. Note that $\check{b}_1(t) \triangleq$

$(b_1 * h * h_{ZF})(t)$ and $\check{b}_2(t) \triangleq (b_2 * h * h_{ZF})(t)$. For analytical convenience, we normalized the observed variables in (44). By using the sampling expansion, the normalized observed variables, $Z_{ED,1}$ and $Z_{ED,2}$ in the case of $d_0 = 0$ become⁷

$$\begin{aligned} Y_{ED,1} &\triangleq \frac{1}{2\sigma_{ED}^2} \sum_{j=0}^{\frac{N_s}{2}-1} \sum_{m=1}^{2WT} \frac{(w_{1,j,m} + \eta_{1,j,m})^2}{2W}, \\ Y_{ED,2} &\triangleq \frac{1}{2\sigma_{ED}^2} \sum_{j=0}^{\frac{N_s}{2}-1} \sum_{m=1}^{2WT} \frac{\eta_{2,j,m}^2}{2W}, \end{aligned} \quad (45)$$

where $w_{1,j,m}$, $\eta_{1,j,m}$, $w_{2,j,m}$, and $\eta_{2,j,m}$, for odd m (even m) are the real (imaginary) parts of the samples of the equivalent low-pass version of $w_{1,j}(t)$, $\eta_{1,j}(t)$, $w_{2,j}(t)$, and $\eta_{2,j}(t)$ respectively, sampled at Nyquist rate W over the interval $[0, T]$. The noise samples $\frac{\eta_{1,j,m}}{\sqrt{2W}}$ and $\frac{\eta_{2,j,m}}{\sqrt{2W}}$ in (45) are statistically independent with equal variance $\sigma_{ED}^2 = N_0/2$. Conditioned on $\{h_l\}$, the observed variables $Y_{ED,1}$ and $Y_{ED,2}$ are respectively non-central and central chi-square distributed with $q_{ED} = N_s WT$ degrees of freedom. The non-centrality parameter of $Y_{ED,1}$, for $d_0 = 0$, can be expressed as

$$\mu_{ED} = \frac{1}{2\sigma_{ED}^2} \sum_{j=0}^{\frac{N_s}{2}-1} \int_0^T w_{1,j}^2(t) dt = \frac{E_s}{N_0} \sum_{l=1}^{L_{CAP}} h_l^2, \quad (46)$$

where $L_{CAP} \triangleq \lceil \min\{WT, WT_g\} \rceil$ denotes the actual number of multipath components integrated. The BEP is then given by the solution of the double integral

$$\begin{aligned} P_{e,ED|\mu_{ED},d_0=0} &= \int_0^\infty \int_0^{y_1} e^{-(y_1+\mu_{ED})} \left(\frac{y_1}{\mu_{ED}} \right)^{\frac{(q-1)}{2}} \\ &\quad \times I_{q-1}(2\sqrt{y_1\mu_{ED}}) \frac{y_2^{(q-1)}}{(q-1)!} \exp(-y_2) dy_1 dy_2. \end{aligned} \quad (47)$$

This integral has been solved in a closed-form in [135, 136]. Considering the symmetry of $Y_{ED,1}$ and $Y_{ED,2}$ with respect to d_0 , the error probability can be expressed as

$$\begin{aligned} P_{e,ED} &= \mathbb{E}_{\mu_{ED}} \{ \mathbb{P} \{ Z_{ED,1} < Z_{ED,2} | d_0 = 0 \} \} \\ &= \frac{1}{2^{q_{ED}}} \left[\sum_{n=0}^{q_{ED}-1} \binom{(-j)^n}{n!} \mathbb{E} \left\{ e^{-\frac{\mu_{ED}(jv)}{2}} \left(\frac{\mu_{ED}(jv)}{2} \right)^n \right\} \right]_{jv=-1} \\ &\quad \times \sum_{k=n}^{q_{ED}-1} \frac{1}{2^k} \frac{(k+q_{ED}-1)!}{(k-n)!(q_{ED}+n-1)!}, \end{aligned} \quad (48)$$

⁷Due to the statistical symmetry of Z_{ED} with respect to d_0 , we simply need to consider the BEP conditioned on $d_0 = 0$.

where $n!$ represents the factorial of n . It can be noticed that $\mathbb{E} \left\{ e^{-\frac{\mu_{\text{ED}}(j\nu)}{2}} \left(\frac{\mu_{\text{ED}}(j\nu)}{2} \right)^n \right\} = \frac{d^n}{d\nu^n} \psi_{\mu_{\text{ED}}}(j\nu)$ where $\psi_{\mu_{\text{ED}}}(j\nu)$ is the CF of μ_{ED} . If the CF of μ_{ED} is known, equation (48) provides the error probability of the energy detector in the presence of a fading channel. The BEP can be then defined as

$$P_{e,\text{ED}} \triangleq P_e(\psi_{\gamma_{\text{ED}}}(j\nu), q_{\text{ED}}). \quad (49)$$

3.6.2 Auto-correlation (AcR) with TR-BPAM signaling

We recall here the work performed in [137–139]. The decision statistics for AcR with TR-BPAM conditioned on d_0 and $a_j = +1$ can be expressed as

$$U_{j|d_0=+1} = \sum_{m=1}^{2WT} \left[\left(\frac{1}{\sqrt{2W}} w_{j,m} + \beta_{1,j,m} \right)^2 - \beta_{2,j,m}^2 \right], \quad (50)$$

$$U_{j|d_0=-1} = \sum_{m=1}^{2WT} \left[- \left(\frac{1}{\sqrt{2W}} w_{j,m} - \beta_{2,j,m} \right)^2 + \beta_{1,j,m}^2 \right], \quad (51)$$

where $\beta_{1,j,m} = \frac{1}{2\sqrt{2W}} (\eta_{2,j,m} + \eta_{1,j,m})$ and $\beta_{2,j,m} = \frac{1}{2\sqrt{2W}} (\eta_{2,j,m} - \eta_{1,j,m})$ are statistically independent Gaussian r.v.s with variance $\sigma_{\text{TR}}^2 = \frac{N_0}{4}$. Due to the statistical symmetry of U_j with respect to d_0 and $\{a_j\}$, we simply need to calculate the BEP conditioned on $d_0 = +1$ and $a_j = +1$.⁸ For notational simplicity, we define the normalized r.v.s Y_1 , Y_2 , Y_3 , and Y_4 as

$$\begin{aligned} Y_1 &\triangleq \frac{1}{2\sigma_{\text{TR}}^2} \sum_{j=0}^{\frac{N_s}{2}-1} \sum_{m=1}^{2WT} \left(\frac{1}{\sqrt{2W}} w_{j,m} + \beta_{1,j,m} \right)^2, \\ Y_2 &\triangleq \frac{1}{2\sigma_{\text{TR}}^2} \sum_{j=0}^{\frac{N_s}{2}-1} \sum_{m=1}^{2WT} \beta_{2,j,m}^2, \\ Y_3 &\triangleq \frac{1}{2\sigma_{\text{TR}}^2} \sum_{j=0}^{\frac{N_s}{2}-1} \sum_{m=1}^{2WT} \left(\frac{1}{\sqrt{2W}} w_{j,m} - \beta_{2,j,m} \right)^2, \\ Y_4 &\triangleq \frac{1}{2\sigma_{\text{TR}}^2} \sum_{j=0}^{\frac{N_s}{2}-1} \sum_{m=1}^{2WT} \beta_{1,j,m}^2. \end{aligned} \quad (52)$$

Conditioned on the channel, Y_1 and Y_3 are non-central chi-squared r.v.s, whereas Y_2 and Y_4 are central chi-squared r.v.s all having $N_s WT$ degrees of freedom as for the variables

⁸With statistical symmetry we intend that $U_{j|d_0=+1}$ and $U_{j|d_0=-1}$ are identically distributed.

in the ED case defined in equation (45). Both Y_1 and Y_3 have the same non-centrality parameter given by

$$\mu_{\text{TR}} = \frac{1}{2\sigma_{\text{TR}}^2} \sum_{j=0}^{\frac{M_s}{2}-1} \int_0^T w_j^2(t) dt = \frac{E_s}{N_0} \sum_{l=1}^{L_{\text{CAP}}} h_l^2. \quad (53)$$

Note that, when conditioned on the channel, the r.v.s $Y_{\text{ED},1}$ and $Y_{\text{ED},2}$ have the same distribution as $Y_{\text{TR},1}$ and $Y_{\text{TR},2}$ in (52). The parameters q_{ED} and q_{TR} are also the same. This proves, without using any Gaussian approximation, that the two systems perform equally. While the TR system has a 3dB penalty due to the splitting of the symbol energy over both reference pulse and modulated pulse, the ED system has a 3dB penalty due to the more severe noise enhancement from the squaring operation.

In the presence of a channel impulse response characterized by a long channel delay spread (several multipath components) with an exponential power delay profile (PDP), the evaluation of (48) can present some difficulties related to the evaluation of the high order derivatives of the characteristic function (CF) $\psi_{Y_{\text{ED}}}(j\nu)$.

In order to overcome this issue, another way to derive the BEP of those systems is based on the CF of the difference of two chi-squared distributed variables.

Considering that the CF of the difference between two non-central chi-squared r.v.s (X_1 and X_2) with the same degrees of freedom q is given by [140]

$$\psi(j\nu) = \left(\frac{1}{1+\nu^2} \right)^q \exp\left(\frac{-j\nu\mu_{X_1}}{1+j\nu} + \frac{j\nu\mu_{X_2}}{1-j\nu} \right), \quad (54)$$

where μ_{X_1} and μ_{X_2} are the non-centrality parameters of X_1 and X_2 , respectively. Using the inversion theorem [141], we can derive the probability that $X_1 - X_2 < 0$ as

$$\mathbb{P}\{X_1 - X_2 < 0\} = \frac{1}{2} + \frac{1}{\pi} \int_0^\infty \left(\frac{1}{1+\nu^2} \right)^q \mathfrak{Re} \left\{ \frac{\exp\left(\frac{-j\nu\mu_{X_1}}{1+j\nu} + \frac{j\nu\mu_{X_2}}{1-j\nu} \right)}{j\nu} \right\} d\nu. \quad (55)$$

Letting $q = q_{\text{TR}}(q_{\text{ED}})$, $X_1 = Y_{\text{TR},1}(Y_{\text{ED},1})$, $X_2 = Y_{\text{TR},2}(Y_{\text{ED},2})$, $\mu_{X_1} = \mu_{\text{TR}}(\mu_{\text{ED}})$, and $\mu_{X_2} = 0$ in (55), and by further averaging with respect to $\mu_{\text{TR}}(\mu_{\text{ED}})$, the BEP of the AcR for detecting TR signaling with BPAM is given by

$$P_{e,\text{TR}} \triangleq P_e(\psi_{\mu_{\text{TR}}}(j\nu), q_{\text{TR}}) = \frac{1}{2} + \frac{1}{\pi} \int_0^\infty \left(\frac{1}{1+\nu^2} \right)^{q_{\text{TR}}} \mathfrak{Re} \left\{ \frac{\psi_{\mu_{Y_{\text{TR}}}}\left(\frac{-j\nu}{1+j\nu} \right)}{j\nu} \right\} d\nu, \quad (56)$$

and the BEP of the ED for detecting BPPM is given by

$$P_{e,ED} \triangleq P_e(\Psi_{\mu_{ED}}(j\nu), q_{ED}) = \frac{1}{2} + \frac{1}{\pi} \int_0^\infty \left(\frac{1}{1+\nu^2} \right)^{q_{ED}} \Re \left\{ \frac{\Psi_{\mu_{ED}} \left(\frac{-j\nu}{1+j\nu} \right)}{j\nu} \right\} d\nu. \quad (57)$$

This formulation of the BEP will be very useful when we analyze the effect of NB and UWB interference on the ED and the AcR.

3.7 Numerical and simulation results

In the previous sections, the equivalence among the ED with BPPM signaling, and the AcR with TR-BPAM in terms of BEP has been shown with and without a Gaussian approximation of the observed variables. In this section the performances of these two non-coherent receiver structures are evaluated considering different types of channel fading. We first consider a generic dense resolvable multipath channel, where each multipath component is Nakagami distributed according to [142] and then extend the result considering the IEEE 802.15.4a channel models.

3.7.1 Numerical results in Nakagami fading channels

For the generic dense resolvable multipath channel with Nakagami fading, m represents the fading severity index and $\mathbb{E}\{h_l^2\}$ is the average power of each component, where $\mathbb{E}\{h_l^2\} = \mathbb{E}\{h_1^2\} \exp[-\varepsilon(l-1)]$, for $l = 1, \dots, L$, are normalized such that $\sum_{l=1}^L \mathbb{E}\{h_l^2\} = 1$. For simplicity, the fading severity index m is assumed to be identical for all paths. The average power of the first arriving multipath component is given by $\mathbb{E}\{h_1^2\}$, and ε is the channel power decay factor. The power of the a Nakagami distributed signal amplitude varies according to the Gamma distribution which has a closed form CF given by

$$\Psi_{|h_i|^2}(j\nu) = \left(\frac{1}{1 - j\nu \frac{\varepsilon}{m}} \right)^m, \quad (58)$$

where γ_i is the SNR of h_i . With this fading model, the CFs of the non-centrality parameters μ_{ED} and μ_{TR} are

$$\Psi_{\mu_{ED}}(j\nu) = \Psi_{\mu_{TR}}(j\nu) = \prod_{i=1}^{L_{CAP}} \Psi_{|h_i|^2}(j\nu). \quad (59)$$

As shown in Fig. 11, for a flat PDP the BEP reduces if the integration time increases up to the maximum excess delay of the channel. After this point, the integrated signal is composed only of noise and consequently the error probability increases. Fig. 12 and Fig. 13 represent the BEP as a function of the integration time in the case of an exponential PDP. It can be noticed that there is an optimal integration point within the interval $[0, T_g]$. If we consider the function $E(T)$ which represents the integrated signal energy for the interval $[0, T]$ we can rewrite SNR_d defined in (29) as

$$\text{SNR}_d(T) = \frac{E^2(T)}{N_0(4E(T) + 2N_p W T N_0)}. \quad (60)$$

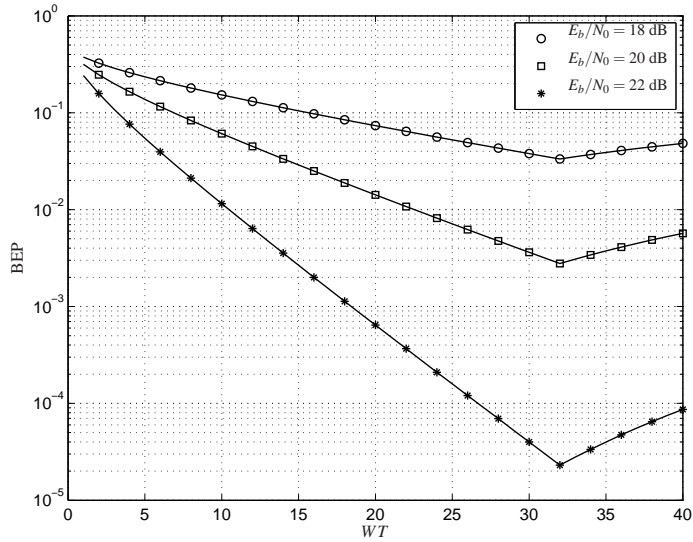


Fig. 11. BEP of the ED and of the AcR for different integration time and bandwidth product values WT , $N_s = 32$ (16 pulses for BPPM and 32 pulses for TR-BPAM), in the presence of a Nakagami channel fading with $L = 32$ multipath components, channel power decay factor $\varepsilon = 0$, and fading parameter $m = 3$.

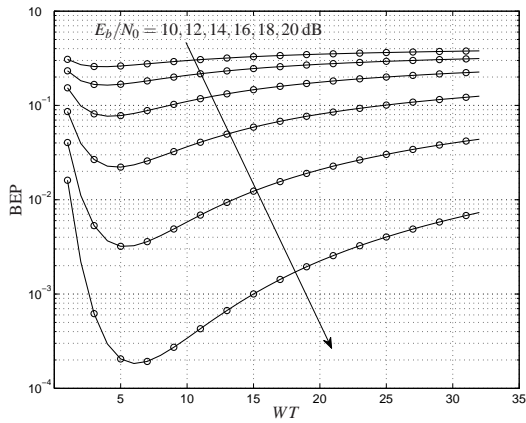


Fig. 12. BEP of the ED and of the AcR for different integration time and bandwidth product values WT , $N_s = 32$ (16 pulses for BPPM and 32 pulses for TR-BPAM), in the presence of a Nakagami channel fading with $L = 32$ multipath components, channel power decay factor $\varepsilon = 0.4$, and fading parameter $m = 3$.

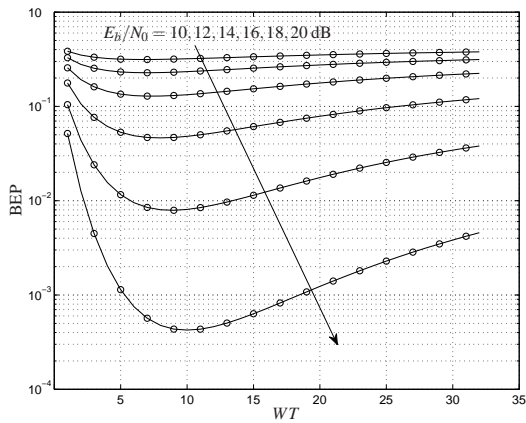


Fig. 13. BEP of the ED and of the AcR for different integration time and bandwidth product values WT , $N_s = 32$ (16 pulses for BPPM and 32 pulses for TR-BPAM). The numerical results are obtained in the presence of a Nakagami channel fading with $L = 50$ multipath components, channel power decay factor $\varepsilon = 0.2$, and fading parameter $m = 3$.

For flat PDP the integrated signal energy function can be expressed as $E(T) = E_b \frac{T}{T_g}$ for $T \leq T_g$ and $E(T) = E_b$ for $T > T_g$, while for an exponential PDP we have $E(T) = \frac{E_b(1-\exp(-\varepsilon T))}{(1-\exp(-\varepsilon T_g))}$ for $T \leq T_g$ and $E(T) = E_b$ for $T > T_g$. In the case of flat PDP, it is easy to show that the function $\text{SNR}_d(T)$ increases and decreases monotonically for $T \leq T_g$ and $T \geq T_g$ respectively. For an exponential PDP, it can be shown graphically that the function $\text{SNR}_d(T)$ is to be convex with a maximum within the interval $[0, T_g]$. We cannot algebraically derive the position of the maximum but we can see that the maximum position depends on the E_b/N_0 , on the number of pulses N_p , on the maximum excess delay of the channel T_g , and on the channel power decay factor ε . From the BEP curves we can notice that it is better to overestimate the optimal integration time since an excess of integrated noise is less harmful than a reduced integrated signal energy.

3.7.2 Simulation results in IEEE 802.15.4a channel models

The results presented in the previous section depicted some peculiar behavior of the non-coherent receivers. In those results we implicitly considered perfect time synchronization of the receiver, meaning perfect knowledge of the position of the first multipath component which defines the integration starting point of the received signal. What we present hereafter are BEP obtained considering 1000 realizations of IEEE802.15.4a channel models. These channel models consider both LOS and NLOS conditions and in general are characterized by hundreds of components, leading to considerable changes in PDP from one realization to another. We briefly list here some of the key features of the models:

- arrival paths in clusters
- mixed Poisson distribution for ray arrivals times
- possible delay dependence of cluster decay times
- Nakagami distribution of small scale fading with different m -factors for different components

The channel impulse response of these models is given in general as

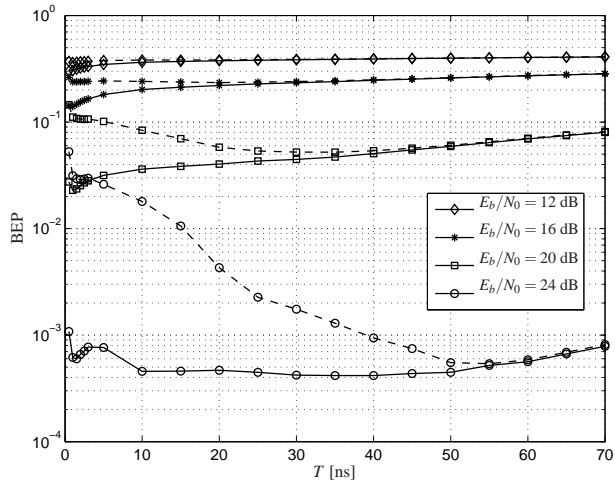
$$h(t) = \sum_{l=0}^L \sum_{c=0}^K h_{c,l} \exp(j\phi_{c,l}) \delta(t - T_l - \tau_{c,l}), \quad (61)$$

where $h_{k,l}$ is the tap weight of the k th component in the l th cluster, T_l is the delay of the l th cluster, and $\tau_{k,l}$ is the delay of the k th multipath component relative to the l th cluster

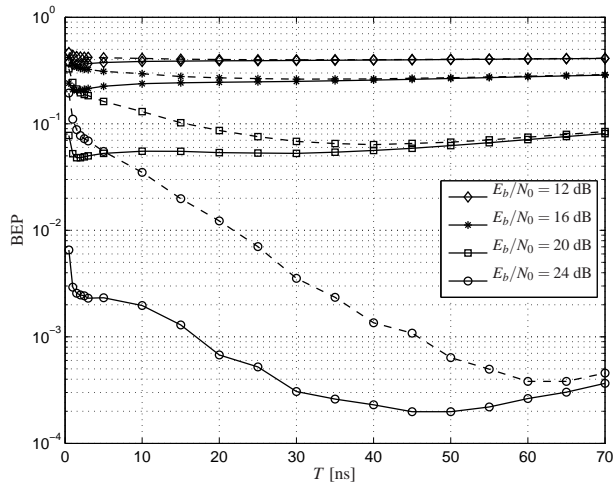
arrival time T_l . The phases $\phi_{k,l}$ are uniformly distributed in the range $[0, 2\pi)$. Details of the channel models proposed in the standard can be found in [38].

Since the type of receivers investigated, at least in their most simple implementations, cannot perform a selection of the multipath components, it is interesting to consider the effect of the synchronization procedure on the BEP performance. We consider two possible synchronization approaches. In the first approach, referred to as first path (FP), we consider the integration starting point (synchronization point) defined by the first relevant path (10 dB below the maximum power value among the multipath components). In the second approach referred to as maximum energy (MAX), we consider the integration starting point (synchronization point) as the point which provides the maximum signal energy with the integration time T .⁹ Note that the simulations do not consider any particular pulse shape but they simply consider the integrated signal energy obtained from the channel realizations in an integration interval of duration T . The channel realization considers a sampling rate of 0.5 ns. The bandwidth of the signal is used to determine the amount of noise power. As depicted in Fig. 14(a) and Fig. 15(a), also in LOS conditions represented by CM1 and CM3, the first path component is not the best integration starting point. The FP approach requires a longer integration time than the MAX in order to achieve the lowest BEP. Furthermore, the MAX approach shows a small dependency on the value of T even for different E_b/N_0 . On the other hand, time synchronization based on the first relevant path shows a high sensitivity to the integration time. This can be attributed to the high diversity order of the UWB signals which leads to significant variation over small distances and times. In NLOS conditions, Fig. 14(b) and Fig. 15(b) for CM2 and CM4, respectively, the differences between the two synchronization approaches are also evident.

⁹The synchronization procedures are completely different in the two cases. In the first case, after locking on one of the received multipath component a search back algorithm is required in order to find the first multipath component. In the second case, after locking on the signal by searching an integration interval with significant energy, the synchronization is achieved by sliding the integration window around the locking point and searching for the one providing the maximum energy.

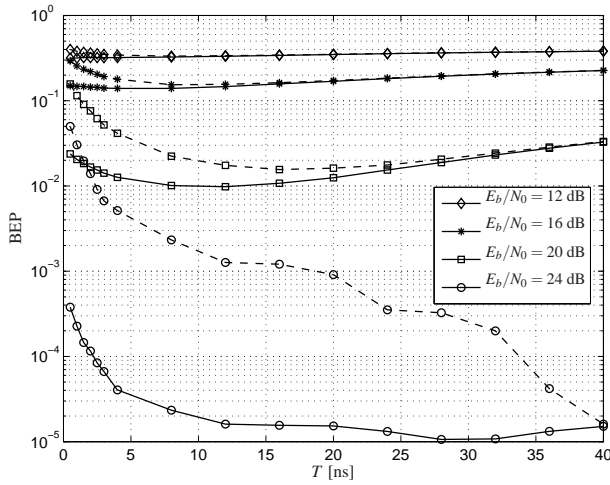


(a) IEEE802.15.4a CM1 (LOS, residential environment)

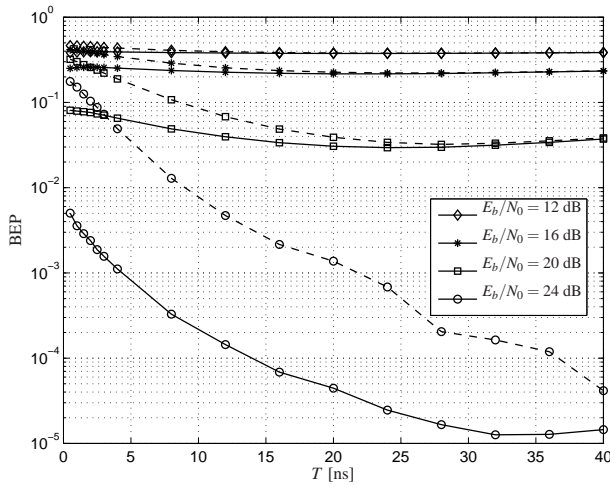


(b) IEEE802.15.4a CM2 (NLOS, residential environment)

Fig. 14. BER of the ED as a function of the signal integration time T for a bandwidth $W = 2$ GHz. The integration is repeated over 16 pulses. Solid line = MAX, dashed line = FP.



(a) IEEE802.15.4a CM3 (LOS, office environment)



(b) IEEE802.15.4a CM4 (NLOS, office environment)

Fig. 15. BER of the ED as a function of the signal integration time T for a bandwidth $W = 2$ GHz. The integration is repeated over 16 pulses. Solid line = MAX, dashed line = FP.

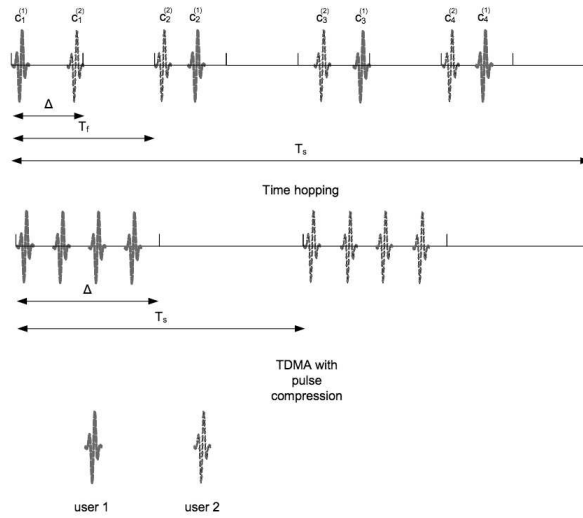
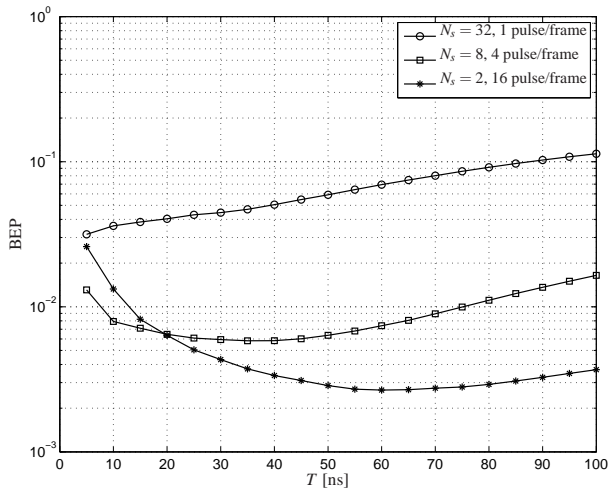


Fig. 16. TH and TDMA with pulse compression schemes.

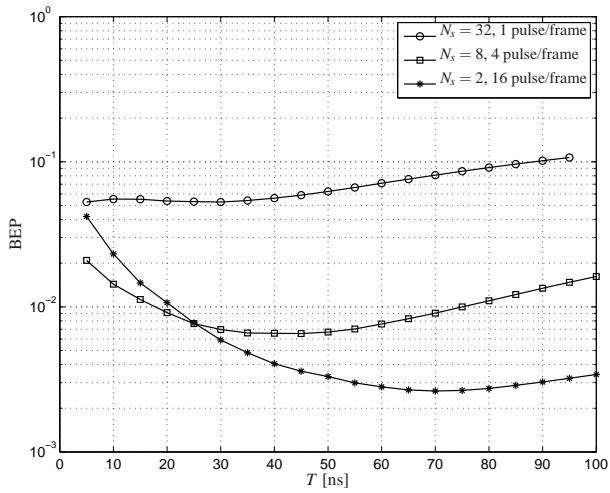
3.7.3 Pulse compression technique

To this point, we have considered the case that the pulse repetition frequency within the symbol interval is at least of the order of the maximum excess delay of the channel impulse response to avoid inter-pulse interference but also to allow the use of time hopping schemes. However, in order to transmit sufficient energy to support reasonable BEP values, each symbol is composed of a large number of pulses and when a non-coherent approach is implemented, the overall integrated noise energy increases with N_p . If the multiuser capabilities can be addressed by implementing a TDMA system (Fig. 16), it is then of interest to evaluate the performance of the ED detector receiver when the pulses are transmitted very close to each other reducing the overall integration time and consequently the integrated noise energy. In Fig. 17(a) and Fig. 17(b), the comparison among different pulse repetition structures is shown. In the case of multiple pulses per frame, the interval between pulses is 2 ns. As can be seen, there is a considerable gain which can be achieved by sending the pulses in a burst due to reduced integrated noise energy. The overlapping of the pulses creates a kind of shadowing effect which increases the variance of the received signal energy; however, the benefit is

guaranteed by the reduced noise energy. Another interesting point is that the BEP is now only weakly dependent on the type of channel impulse response since the temporal dispersion of the signal energy is smoothed because of the short intervals between transmitted pulses. Note that for the AcR the pulse compression technique requires very long delay lines which become very difficult to implement with sufficient accuracy. The IEEE802.15.4a physical layer is also based on the transmission of bursts composed of 4 pulses, 2 ns apart from each others. In the IEEE802.15.4a standard draft, the hopping code is applied at the burst level.



(a) IEEE802.15.4a CM1 (LOS, residential environment)



(b) IEEE802.15.4a CM2 (NLOS, residential environment)

Fig. 17. BER of the ED using the pulse compression technique as a function of the signal integration time T for $E_b/N_0 = 20$ dB, $T_p = 0.5$ ns and $W = 2$ GHz.

3.8 Conclusions

In this chapter we have compared several realizations of the AcR which differ in the way they combine the pulses belonging to the same symbols. The comparison among these realizations has been initially carried out in an AWGN channel. For AcR with TR-BPAM and the ED with BPPM, the comparison has then been extended to consider the presence of multipath fading channels. In this chapter we have shown that these two receiver structures have equal BEP performance in the absence of interference. The BEP performance results have been obtained by using closed-form expressions and by numerical integration. To complete the performance evaluation, we provided BEP curves in the presence of IEEE802.15.4a channel models including a discussion on the most appropriate synchronization procedure. Finally, we introduced the pulse compression techniques which can drastically improve the performance of UWB non-coherent receivers.

4 Coexistence and interference

4.1 Introduction

Due to its large transmission bandwidth and its operation in unlicensed spectrum, UWB systems may need to coexist and contend with many narrowband communication systems and with other UWB systems. In the previous chapter, one of the stated goals was to investigate low complexity transceiver structures. The receiver structures proposed and analyzed support the low-complexity objective; however, as a consequence they cannot rely on sophisticated algorithms to reduce the effect of the interference. As a result, it is important to analyze the performance of such receiver structures in the presence of multiple uncoordinated narrowband and UWB systems for successful deployment of UWB systems.

In this chapter, the BEP performance of two systems are compared. The first system is an AcR based on TR signaling and binary pulse amplitude modulation (TR-BPAM), and the second utilises an ED receiver based on a conventional square-law detector and binary pulse position modulation (BPPM). The comparison is made in multipath fading channels, in the presence of interference. We consider three cases: 1) single NBI source, where the interfering node is located at a fixed distance from the receiver, 2) multiple NBI sources and 3) multiple UWB interference sources, where the interfering nodes are scattered according to a spatial Poisson process.

This chapter is organized as follows: in Section 4.2, a brief review of stable distributions is given; Section 4.3.1 and Section 4.3.2 derive, respectively, the BEP expressions which consider multipath fading channels and account for the presence of single and multiple NBI. In Section 4.3.3, numerical results considering the effect of NBI are presented. Section 4.4 extends the analysis to the case of multiple UWB interferers by describing the multiple UWB interference system in Section 4.4.1 and proposing a statistical model for the aggregate interference in Section 4.4.3. In Section 4.4.4, BEP formulas for both AcR and ED are derived based on the proposed statistical model for multiple UWB interference and in Section 4.4.5 the numerical results in the presence of UWB interference are presented. Section 4.5 concludes this chapter.

4.2 Overview of stable distributions

Before starting the analysis of the performance of UWB non-coherent receivers in the presence of interference, we provide a short introduction to univariate and multivariate stable distributions since these will play an important role in the forthcoming analysis. As will be shown in the next sections, the usage of stable distributions to model the statistics allows us to account for the spatial distribution of the interference sources [102, 143]. As highlighted in [144, 149], in the absence of power control, stable distributions provide a good fitting of the heavy tail which characterizes the distribution of the aggregate interference signal and which cannot be modeled by using the Gaussian distribution. In both cases of NBI and UWB interference, the heavy tail depends on the fact that the received interference signal strength depends on the travelled distance R as $1/R^\nu$.

4.2.1 Univariate stable distribution

An univariate stable distribution of a variable X is conveniently described by its characteristic function

$$\psi(v) = \mathbb{E} \{ e^{jvX} \} = \begin{cases} \exp [-\gamma |v|^\alpha (1 - j\beta \text{sign}(v) \tan \frac{\pi\alpha}{2}) + jv\mu] & \alpha \neq 1 \\ \exp [-\gamma |v| (1 - j\beta \text{sign}(v) \ln |v|) + jv\mu] & \alpha = 1 \end{cases}, \quad (62)$$

where the four parameters present in (62) are defined as follows:

$\alpha \in (0, 2]$ Characteristic exponent, which controls the heaviness of the PDF tail. If $\alpha = 2$, then $X \sim \mathcal{N}(0, 2\gamma)$

$\beta \in [-1, 1]$ Skewness parameter. The cases where $\beta < 0$, $\beta = 0$, $\beta > 0$ correspond to a PDF which is skewed to the left, symmetric round the center μ , and skewed to the right, respectively.

$\gamma \in [0, \infty)$ Dispersion parameter, which behaves like the variance.

$\mu \in \mathbb{R}$ Location parameter, which behaves like the mean.

We will denote a stable distributed r.v. by $X \sim \mathcal{S}(\alpha, \beta, \gamma, \mu)$.¹⁰ If $\beta = -1$ or $\beta = 1$, the stable distribution is called totally skewed. When $\beta = 0$ the stable distribution is symmetric. Stable distributions symmetric about $\mu = 0$ with characteristic exponent α are called symmetric α -stable ($S\alpha S$) and their characteristic functions are in the form

$$\psi(v) = \exp(-\gamma|v|^\alpha). \quad (63)$$

Some of the properties of stable r.v.s which are used in this chapter are provided hereafter.

Scaling property Let $X \sim \mathcal{S}(\alpha, \beta, \gamma)$ with $\alpha \neq 1$, and let k be a non-zero real constant. Then,

$$kX \sim \mathcal{S}(\alpha, \text{sign}(k)\beta, |k|^\alpha \gamma). \quad (64)$$

Decomposition property Let $X \sim \mathcal{S}(\alpha, 0, \gamma)$. Then, X can be decomposed as

$$X = \sqrt{V}G, \quad (65)$$

where $V \sim \mathcal{S}(\frac{\alpha}{2}, 1, \cos \frac{\pi\alpha}{2})$ and $G \sim \mathcal{N}(0, 2\gamma^{2/\alpha})$.

The main problem of α -stable distributions is that no closed-form expressions exist for their PDF and CDF, except for the Gaussian ($\alpha = 2$), Cauchy ($\alpha = 1$), and Levy ($\alpha = 1/2$) distributions. However, these distributions are useful in the analysis proposed in the next sections since their CF is required. To offer an insight into the PDFs of α -stable distributions and the effect of the different parameters, several PDF curves are plotted in Figures 18-21. From Fig. 18 and Fig. 19, we notice the effect of the characteristic exponent on the PDF around its mean on the PDF tail. Lowering the values of α , the PDF tends to be more peaky around its mean with a heavier tail. From Fig. 20 we notice the effect of β on the skewness of the PDF. Fig. 21 shows the similarity between the effect of γ and the effect of the variance.

4.2.2 Multivariate stable distribution

The real r.v.s X_1, \dots, X_n are jointly α -stable, or the real random vector $\bar{X} = [X_1, \dots, X_n] \in \mathbb{R}^n$ is symmetric α stable if the joint characteristic function is of the form

$$\psi(\bar{v}) = \exp\left[-\int_S |\bar{v}^T \bar{s}|^\alpha \Gamma(ds) + j\bar{v}^T \bar{\mu}\right], \quad (66)$$

¹⁰Unless otherwise indicated, in this chapter we only deal with distributions where $\mu = 0$, and therefore use the notation $X \sim \mathcal{S}(\alpha, \beta, \gamma)$.

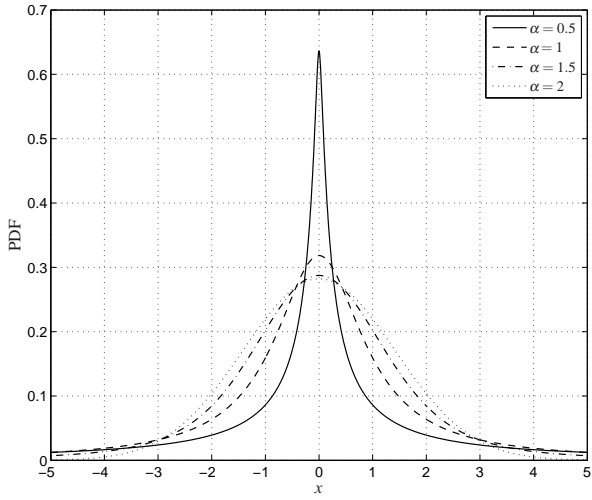


Fig. 18. Probability density functions of stable distributed r.v.s for varying characteristic exponents α , $\beta = 0$, $\gamma = 1$, and $\mu = 0$.

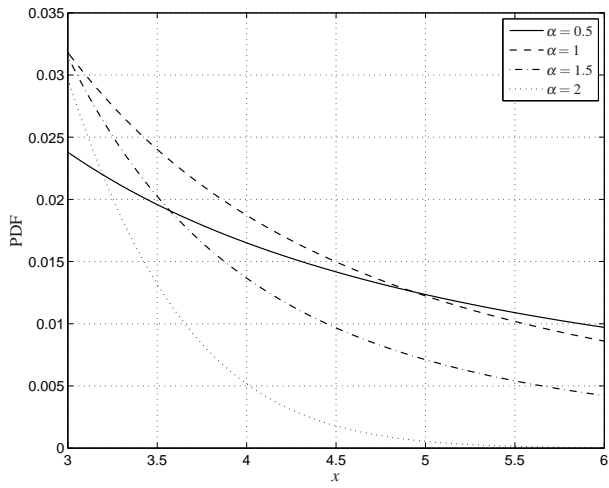


Fig. 19. Probability density function's tails for stable distributed r.v.s for varying characteristic exponents α , $\beta = 0$, $\gamma = 1$, and $\mu = 0$.

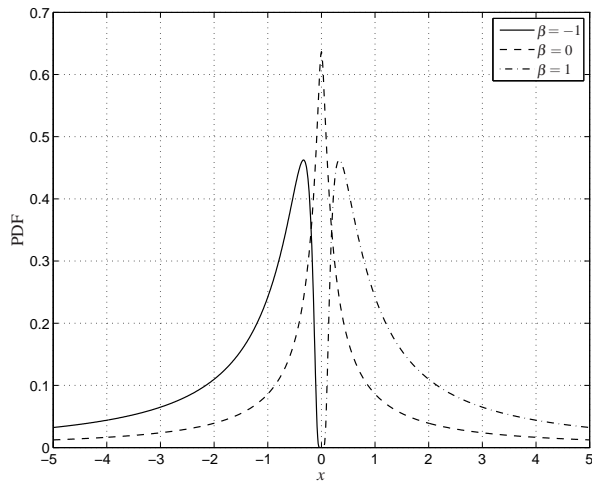


Fig. 20. Probability density function of stable distributed r.v.s for varying skewness parameters β , $\alpha = 0.5$, $\gamma = 1$, and $\mu = 0$.

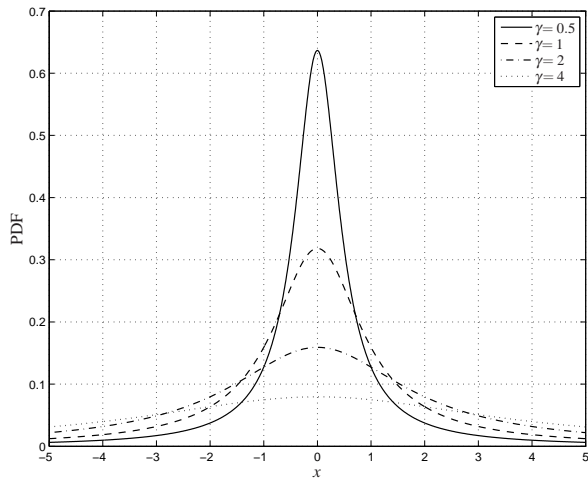


Fig. 21. Probability density function of stable distributed r.v.s for varying dispersion parameters γ , $\alpha = 1$, $\beta = 0$, $\gamma = 1$, and $\mu = 0$.

where the spectral measure $\Gamma(\cdot)$ is symmetric, i.e., $\Gamma(\bar{A}) = -\Gamma(\bar{A})$ for any measurable set on the unit sphere \mathcal{S} , and \bar{v} , $\bar{\mu}$, and \bar{s} are n dimensional real vectors. Among the classes of multivariate stable distributions we will make use of the sub-Gaussian distributions. These distributions can be described through their CF as follows:

$$\psi(\bar{v}) = \exp\left(-\frac{1}{2}\left|\sum_{i=1}^n \sum_{j=1}^n v_i v_j \bar{\Sigma}_{ij}\right|^{\alpha/2}\right), \quad (67)$$

where the $n \times n$ matrix $\bar{\Sigma}$ is positive definite. The decomposition property applies to this class of multivariate r.v.s as follows:

Decomposition property If the CF of a $S\alpha S$ vector \bar{X} is in the form of (67), then the vector \bar{X} can be decomposed as

$$\bar{X} = \sqrt{V}\bar{G}, \quad (68)$$

where $V \sim \mathcal{S}(\frac{\alpha}{2}, 1, \cos \frac{\pi\alpha}{2})$ and \bar{G} is the underlying Gaussian vector, independent of V , with covariance matrix $\bar{\Sigma}$.

4.3 BEP analysis in the presence of narrowband interference

In the following sections, for the BEP analysis in the presence of narrowband interference (NBI), we refer to the system model and receiver structures described in Section 3.5.

4.3.1 BEP analysis in the presence of a single NB interferer

For the case of a single NBI, it was shown in [145] that the NBI can be well approximated by a single-tone interference, i.e.,¹¹

$$\xi(t) = \sqrt{2J}\alpha_J \cos(2\pi f_J t + \theta), \quad (69)$$

where J is the average received power of the interference and f_J is the center frequency. The parameters α_J and θ represent the amplitude and the phase, respectively, of the

¹¹The following analysis is valid if we assume that the NB interfering signal does not saturate the amplification chain of the UWB receiver and so no higher order harmonics are generated in the receiver. In order this assumption to be realistic, a notch filter working at the interference frequency might be required. If the notch filter is present, J accounts for the filter attenuation.

fading associated with the NBI. We consider Rayleigh fading with $\mathbb{E}\{\alpha_j^2\} = 1$, which is a good model when using NB signals [146]. We assume the NBI to be within the band of interest of the signal.

4.3.1.1 Auto-correlation receiver (AcR)

If we incorporate in our analysis the NBI given in (69) and use the sampling expansion approach [147], (52) still holds with

$$\beta_{1,j,m} \triangleq \frac{1}{2\sqrt{2W}}(\eta_{2,j,m} + \xi_{2,j,m} + \eta_{1,j,m} + \xi_{1,j,m}), \quad (70)$$

and

$$\beta_{2,j,m} \triangleq \frac{1}{2\sqrt{2W}}(\eta_{2,j,m} + \xi_{2,j,m} - \eta_{1,j,m} - \xi_{1,j,m}), \quad (71)$$

where $\xi_{1,j,m}$ and $\xi_{2,j,m}$, for odd m (even m) are the real (imaginary) parts of the samples of the equivalent low-pass version of

$$\xi_{1,j}(t) \triangleq \sqrt{2J}\alpha_j \cos[2\pi(f_j t + j2T_f^{\text{TR}} + c_j T_p) + \theta], \quad (72)$$

and

$$\xi_{2,j}(t) \triangleq \sqrt{2J}\alpha_j \cos[2\pi(f_j t + j2T_f^{\text{TR}} + c_j T_p + T_r) + \theta], \quad (73)$$

respectively, sampled at Nyquist rate W over the interval $[0, T]$. Furthermore, by conditioning on θ , $\{c_j\}$, $\{a_j\}$, $\{h_l\}$, and α_j , the conditional variance σ_{TR}^2 of $\beta_{1,j,m}$ and $\beta_{2,j,m}$ is simply $\frac{N_0}{4}$, and the non-centrality parameters of $Y_{\text{TR},1}$ and $Y_{\text{TR},2}$ for $d_0 = +1$ are, respectively, given by [147]

$$\begin{aligned}
\mu_{Y_{\text{TR},1}}^{(\text{NBI})} &\triangleq \frac{1}{2\sigma_{\text{TR}}^2} \sum_{j=0}^{\frac{N_s}{2}-1} \int_0^T \left[w_j(t) + \frac{\xi_{1,j}(t) + \xi_{2,j}(t)}{2} \right]^2 dt \\
&\approx \underbrace{\frac{E_s^{\text{TR}}}{N_0} \sum_{l=1}^{L_{\text{CAP}}} h_l^2}_{\triangleq \mu_{\text{A,TR}}} + \underbrace{\frac{\alpha_j^2 N_s J T}{2N_0} [1 + \cos(2\pi f_j T_r)]}_{\triangleq \mu_{\text{B,TR}}^{(\text{NBI})}} \\
&\quad + \frac{4\alpha_j |\widehat{P}(f_j)| \sqrt{2E_p^{\text{TR}} J} \cos(\pi f_j T_r)}{N_0} \\
&\quad \times \underbrace{\sum_{j=0}^{\frac{N_s}{2}-1} a_j \sum_{l=1}^{L_{\text{CAP}}} h_l \cos(2\pi f_j (\tau_l + j2T_f^{\text{TR}} + c_j T_p + T_r/2) + \varphi)}_{\triangleq \mu_{\text{C,TR}}^{(\text{NBI})}}, \tag{74}
\end{aligned}$$

and

$$\mu_{Y_{\text{TR},2}}^{(\text{NBI})} \approx \frac{\alpha_j^2 N_s J T}{2N_0} - \frac{\alpha_j^2 N_s J T}{2N_0} \cos(2\pi f_j T_r), \tag{75}$$

where $|\widehat{P}(f_j)|$ is the magnitude of the frequency response of $p(t)$ at frequency f_j . The composite random phase is given by $\varphi \triangleq \arg\{\widehat{P}(f_j)\} + \theta$, where $\arg\{\widehat{P}(f_j)\}$ is the angle of the frequency response of $p(t)$ at frequency f_j , and φ is uniformly distributed over $[0, 2\pi)$. Using (55), (74) and (75), we invoke the approximate analytical method developed in [147] to obtain the approximate BEP conditioned on $d_0 = +1$ as follows:¹²

$$\begin{aligned}
P_{e,\text{TR}|d_0=+1}^{(\text{NBI})} &\simeq \frac{1}{2} + \frac{1}{\pi} \int_0^\infty \left(\frac{1}{1+v^2} \right)^{q_{\text{TR}}} \\
&\quad \Re \left\{ \frac{\Psi_{\mu_{\text{TR}}(\frac{-jv}{1+jv})} \Psi_J(g_{\text{TR},d_0=+1}(jv) \cdot J)}{jv} \right\} dv, \tag{76}
\end{aligned}$$

where $\Psi_J(jv)$ is the CF of α_j^2 and

$$g_{\text{TR}|d_0=+1}(jv) \triangleq \frac{-jv}{1+jv} \frac{N_s T}{2N_0} [1 + \cos(2\pi f_j T_r)] + \frac{jv}{1-jv} \frac{N_s T}{2N_0} [1 - \cos(2\pi f_j T_r)]. \tag{77}$$

¹²Under the approximate analytical method, the last term $\mu_{\text{C,TR}}^{(\text{NBI})}$ in (74) is considered to be negligible compared to the first two terms.

Similarly, the approximate BEP conditioned on $d_0 = -1$ is given by

$$P_{e,TR|d_0=-1}^{(NBI)} \simeq \frac{1}{2} + \frac{1}{\pi} \int_0^\infty \left(\frac{1}{1+v^2} \right)^{q_{TR}} \Re e \left\{ \frac{\Psi_{\mu_{TR}} \left(\frac{-jv}{1+jv} \right) \Psi_J (g_{TR,d_0=-1}(jv) \cdot J)}{jv} \right\} dv, \quad (78)$$

where

$$g_{TR|d_0=-1}(jv) \triangleq \frac{-jv}{1+jv} \frac{N_s T}{2N_0} \left[1 - \cos(2\pi f_j T_r) \right] + \frac{jv}{1-jv} \frac{N_s T}{2N_0} \left[1 + \cos(2\pi f_j T_r) \right]. \quad (79)$$

As a result, it follows that the BEP of the AcR for detecting TR signaling with BPAM in the presence of a single NBI is given by

$$P_{e,TR}^{(NBI)} = \frac{1}{2} \left(P_{e,TR,d_0=+1}^{(NBI)} + P_{e,TR,d_0=-1}^{(NBI)} \right). \quad (80)$$

4.3.1.2 Energy detector (ED)

Similar to the steps in Section 4.4.2.1, we incorporate the NBI given in (69) into (45) to obtain

$$Y_{ED,1} = \frac{1}{2\sigma_{ED}^2} \sum_{j=0}^{\frac{N_s}{2}-1} \sum_{m=1}^{2WT} \frac{(w_{1,j,m} + \xi_{1,j,m} + \eta_{1,j,m})^2}{2W},$$

$$Y_{ED,2} = \frac{1}{2\sigma_{ED}^2} \sum_{j=0}^{\frac{N_s}{2}-1} \sum_{m=1}^{2WT} \frac{(\xi_{2,j,m} + \eta_{2,j,m})^2}{2W}, \quad (81)$$

where $\xi_{1,j,m}$ and $\xi_{2,j,m}$ for odd m (even m) are the real (imaginary) parts of the samples of the equivalent low-pass version of

$$\xi_{1,j}(t) \triangleq \sqrt{2J} \alpha_j \cos[2\pi f_j(t + jT_r^{\text{ED}} + c_j T_p) + \theta], \quad (82)$$

and

$$\xi_{2,j}(t) \triangleq \sqrt{2J} \alpha_j \cos[2\pi f_j(t + jT_r^{\text{ED}} + c_j T_p + \Delta) + \theta] \quad (83)$$

respectively, sampled at Nyquist rate W over the interval $[0, T]$. The non-centrality parameter of $Y_{ED,1}$ in (81) conditioned on θ , $\{c_j\}$, $\{a_j\}$, $\{h_l\}$, α_j , and $d_0 = 0$ is given

by¹³

$$\begin{aligned}
\mu_{Y_{ED},1}^{(NBI)} &= \underbrace{\frac{1}{2\sigma_{ED}^2} \sum_{j=0}^{\frac{N_s}{2}-1} \int_0^T w_{1,j}^2(t) dt}_{\triangleq \mu_{A,ED}} \\
&\quad + \underbrace{\frac{1}{2\sigma_{ED}^2} \sum_{j=0}^{\frac{N_s}{2}-1} \int_0^T \xi_{1,j}^2(t) dt}_{\triangleq \mu_{B,ED}^{(NBI)}} + \underbrace{\frac{1}{\sigma_{ED}^2} \sum_{j=0}^{\frac{N_s}{2}-1} \int_0^T w_{1,j}(t) \xi_{1,j}(t) dt}_{\triangleq \mu_{C,ED}^{(NBI)}},
\end{aligned} \tag{84}$$

where $\mu_{A,ED}$, $\mu_{B,ED}^{(NBI)}$, and $\mu_{C,ED}^{(NBI)}$ denote the received signal energy term, the received interference energy term, and signal-interference cross term, respectively. Specifically, we have

$$\begin{aligned}
\mu_{A,ED} &= \frac{E_s^{ED}}{N_0} \sum_{l=1}^{L_{CAP}} h_l^2, \tag{85} \\
\mu_{B,ED}^{(NBI)} &= \frac{\alpha_f^2 J}{N_0} \sum_{j=0}^{\frac{N_s}{2}-1} \left[T + \frac{\sin(4\pi f_j(T + jT_f^{ED} + c_j T_p) + 2\theta)}{4\pi f_j} \right. \\
&\quad \left. - \frac{\sin(4\pi f_j(jT_f^{ED} + c_j T_p) + 2\theta)}{4\pi f_j} \right] \\
&\approx \frac{\alpha_f^2 N_s J T}{2N_0}, \tag{86}
\end{aligned}$$

where the approximation in (86) holds for UWB systems since $T \gg \frac{1}{4\pi f_j}$ and $|\sin(\phi)| \leq 1$. Finally, $\mu_{C,ED}^{(NBI)}$ can be written as

$$\begin{aligned}
\mu_{C,ED}^{(NBI)} &= \frac{2\alpha_f \sqrt{2E_p^{ED} J}}{N_0} \sum_{j=0}^{\frac{N_s}{2}-1} a_j \sum_{l=1}^{L_{CAP}} h_l \\
&\quad \times \int_{\tau_l}^{\tau_l + T_p} p(t) [\cos(2\pi f_j(t + \tau_l + jT_f^{ED} + c_j T_p) + \theta)] dt \\
&= \frac{2\alpha_f |\hat{P}(f_j)| \sqrt{2E_p^{ED} J}}{N_0} \sum_{j=0}^{\frac{N_s}{2}-1} a_j \sum_{l=1}^{L_{CAP}} h_l [\cos(2\pi f_j(\tau_l + jT_f^{ED} + c_j T_p) + \theta)].
\end{aligned} \tag{87}$$

¹³The statistical symmetry of Z_{ED} with respect to d_0 still holds even in the presence of interference, and hence we need to consider only the BEP conditioned on $d_0 = 0$.

Following the steps leading to (86), the non-centrality parameter of $Y_{\text{ED},2}$ in (81) when conditioned on θ , α_J , and $d_0 = 0$ is given by

$$\mu_{Y_{\text{ED},2}}^{(\text{NBI})} \approx \frac{\alpha_J^2 N_s J T}{2N_0}. \quad (88)$$

By invoking the approximate analytical method, we can obtain the approximate BEP of the ED receiver for detecting BPPM in the presence of a single NBI as follows:¹⁴

$$P_{\text{e,ED}}^{(\text{NBI})} \simeq \frac{1}{2} + \frac{1}{\pi} \int_0^\infty \left(\frac{1}{1+v^2} \right)^{q_{\text{ED}}} \Re \left\{ \frac{\Psi_{\mu_{\text{ED}}}\left(\frac{-jv}{1+jv}\right) \Psi_J(g_{\text{ED}}(jv) \cdot J)}{jv} \right\} dv, \quad (89)$$

where

$$g_{\text{ED}}(jv) = \frac{N_s T}{2N_0} \left(\frac{-jv}{1+jv} + \frac{jv}{1-jv} \right). \quad (90)$$

4.3.2 BEP analysis in the presence of multiple NB interferers

For the case of multiple NB interferers, we model the spatial distribution of the interferers according to a homogeneous Poisson point process in the two-dimensional plane [102, 104, 143, 148, 149]. The probability that k nodes lie inside region \mathcal{R} depends only on the area $A_{\mathcal{R}} = |\mathcal{R}|$, and is given by [150]

$$\mathbb{P}\{k \in \mathcal{R}\} = \frac{(\lambda A_{\mathcal{R}})^k}{k!} e^{-\lambda A_{\mathcal{R}}}, \quad (91)$$

where λ is the spatial density (in nodes per unit area). We assume that a large number (infinite number) of NB interferers are transmitting with the same carrier frequency within the band of interest. As a result, the aggregate interfering signal accumulated at the UWB receiver can be expressed as

$$\zeta(t) = \sum_{n=1}^{\infty} \zeta^{(n)}(t), \quad (92)$$

where $\zeta^{(n)}(t)$ denotes the interference signal from the n th NB interferer at the UWB receiver as given by

$$\zeta^{(n)}(t) = \sqrt{2I} \frac{e^{\sigma_1 G^{(n)}}}{(R^{(n)})^v} \alpha^{(n)} \cos(2\pi f_J(t - \tau^{(n)}) + \theta^{(n)}), \quad (93)$$

¹⁴As in the case for AcR, the last term $\mu_{\text{C,ED}}^{(\text{NBI})}$ in (84) is considered to be negligible compared to the first two terms.

where I is the average power at the border of the near-field zone of each interfering transmitter antenna¹⁵ and $\tau^{(n)}$ is a r.v. which accounts for the asynchronism between the interferers. The parameters $\alpha^{(n)}$ and $\theta^{(n)}$ denote the amplitude and phase, respectively, of the fading associated with the n th interferer. As for the single interferer, we consider Rayleigh fading for each of the multiple NBI, where $\mathbb{E}\{(\alpha^{(n)})^2\} = 1$ and $\phi^{(n)} = 2\pi f_j \tau^{(n)} + \theta^{(n)}$ can be modeled as uniform r.v. over $[0, 2\pi)$. The shadowing term $e^{\sigma_1 G^{(n)}}$ follows a log-normal distribution with shadowing parameter σ_1 and $G^{(n)} \sim \mathcal{N}(0, 1)$. According to the far-field assumption, the signal power decays as $1/(R^{(n)})^{2\nu}$, where $R^{(n)}$ is the distance between the n th NB node and the UWB receiver, and ν is the environmental dependent amplitude loss exponent.¹⁶ Note that $\phi^{(n)}$, $G^{(n)}$, and $\alpha^{(n)}$ are independent and identically distributed (i.i.d.) r.v.s in n for all interfering signals. We can equivalently write (93) as

$$\zeta^{(n)}(t) = \sqrt{2I}\Re\left\{ \frac{e^{\sigma_1 G^{(n)}}}{(R^{(n)})^\nu} \mathbf{X}^{(n)} e^{j2\pi f_j t} \right\}, \quad (94)$$

where $\mathbf{X}^{(n)} = X_1^{(n)} + jX_2^{(n)}$ is a circularly symmetric (CS) Gaussian r.v. with $X_1^{(n)} = \alpha^{(n)} \cos(\phi^{(n)})$, $X_2^{(n)} = \alpha^{(n)} \sin(\phi^{(n)})$. The aggregate interfering signal over the period T_s can be represented as

$$\zeta(t) = \sqrt{2I}\Re\{ \mathbf{A} e^{j2\pi f_j t} \}, \quad (95)$$

where $\mathbf{A} = A_c + jA_s$ such that $A_c \triangleq \sum_{n=1}^{\infty} \frac{e^{\sigma_1 G^{(n)}}}{(R^{(n)})^\nu} X_1^{(n)}$ and $A_s \triangleq \sum_{n=1}^{\infty} \frac{e^{\sigma_1 G^{(n)}}}{(R^{(n)})^\nu} X_2^{(n)}$.¹⁷ As shown in Appendix 2, the complex r.v. \mathbf{A} is characterized by a CS stable distribution¹⁸

$$\mathbf{A} \sim \mathcal{S}_c \left(\frac{2}{\nu}, 0, \lambda \pi C_{2/\nu}^{-1} e^{2\sigma_1^2/\nu^2} \mathbb{E} \left\{ |X_j^{(n)}|^{2/\nu} \right\} \right), \quad (96)$$

with C_x defined as

$$C_x \triangleq \frac{1-x}{\Gamma(2-x) \cos(\pi x/2)}, \quad (97)$$

¹⁵ I accounts for the near-field loss K .

¹⁶For NBI within the bandwidth of UWB signals, the far field assumption corresponds to a few tens of centimeters thus making the far field path-loss model a reasonable assumption. The parameter ν corresponds to a decay in *signal amplitude*, not in *signal power*. Experimental studies have shown [151] that it can approximately range from 0.8 (e.g. hallways inside buildings) to 4 (e.g. dense urban environment), where $\nu = 1$ corresponds to free space propagation.

¹⁷We consider the fading and the mobility of the interferers sufficiently low such that \mathbf{A} is constant within the period T_s .

¹⁸We use $\mathcal{S}_c(\alpha, \beta, \gamma)$ to denote a CS stable distribution of a complex r.v. with i.i.d. real and imaginary parts, each distributed as $\mathcal{S}(\alpha, \beta, \gamma)$.

where $\Gamma(\cdot)$ is the Gamma function. Interestingly, (95) and (96) imply that the aggregate interference can be thought as a single NBI with complex CS stable fading.¹⁹ Note that a single interference system working at the frequency f_j has been considered. However, the interference model can be easily extended to account for n systems with different parameters and transmitting at different frequencies. The aggregate interference in this case would be represented by n independent alpha-stable distributed r.v.s.

4.3.2.1 Auto-correlation receiver (AcR) in the presence of multiple NB interferers

Following the approach in Section 4.4.2.1, we derive the non-centrality parameters of $Y_{\text{TR},1}$ and $Y_{\text{TR},2}$ when conditioned on \mathbf{A} , $\{c_j\}$, $\{a_j\}$, $\{h_l\}$ and $d_0 = +1$ as follows:

$$\begin{aligned} \mu_{Y_{\text{TR},1}}^{(\text{NBIs})} &\approx \frac{E_s^{\text{TR}}}{N_0} \sum_{l=1}^{L_{\text{CAP}}} h_l^2 + \frac{|\mathbf{A}|^2 I T N_s}{2N_0} \left[1 + \cos(2\pi f_j T_r) \right] \\ &+ \frac{4|\widehat{P}(f_j)| \sqrt{2E_p^{\text{TR}} J}}{N_0} \sum_{j=0}^{N_s/2-1} a_j \sum_{l=1}^{L_{\text{CAP}}} h_l \\ &\times \left[A_c \cos(\pi f_j T_r) \cos \left(2\pi f_j (\tau_l + j2T_f^{\text{TR}} + c_j T_p + T_r/2) + \arg \left\{ \widehat{P}(f_j) \right\} \right) \right. \\ &\quad \left. - A_s \cos(\pi f_j T_r) \sin \left(2\pi f_j (\tau_l + j2T_f^{\text{TR}} + c_j T_p + T_r/2) + \arg \left\{ \widehat{P}(f_j) \right\} \right) \right], \end{aligned} \quad (98)$$

$$\mu_{Y_{\text{TR},2}}^{(\text{NBIs})} \approx \frac{|\mathbf{A}|^2 I T N_s}{2N_0} \left[1 - \cos(2\pi f_j T_r) \right], \quad (99)$$

where the derivation of (98) and (99) can be found in Appendix 3. Using the approximate analytical method, it follows from (55), (98), and (99) that the approximate BEP of the AcR for detecting TR signaling with BPAM conditioned on \mathbf{A} and $d_0 = +1$ is given by

$$\begin{aligned} P_{e,\text{TR}|\mathbf{A},d_0=+1}^{(\text{NBIs})} &\simeq \frac{1}{2} + \frac{1}{\pi} \int_0^\infty \left(\frac{1}{1+v^2} \right)^{q_{\text{TR}}} \\ &\Re \left\{ \frac{\Psi_{\mu_{\text{TR}}} \left(\frac{-jv}{1+jv} \right) \exp \left(g_{\text{TR},d_0=+1}(jv) \cdot I |\mathbf{A}|^2 \right)}{jv} \right\} dv. \end{aligned} \quad (100)$$

¹⁹Note that in the case of CS stable distribution the real and imaginary parts are uncorrelated but not necessarily independent.

Following Appendix 2, from (218), it follows that

$$|\mathbf{A}|^2 = 2\gamma^{2/\alpha}V(G_1^2 + G_2^2) = 2\gamma^{2/\alpha}VC, \quad (101)$$

where C is a central Chi-squared distributed r.v. with 2 degrees of freedom. Applying the scaling property,²⁰ $|\mathbf{A}|^2$ conditioned on C is a stable distributed r.v. with characteristic exponent $1/\nu$, skewness 1 and dispersion $(2C)^{1/\nu}\gamma\cos(\frac{\pi}{2\nu})$. The CF of $|\mathbf{A}|^2$ conditioned on C for $\nu > 1$ is given by²¹

$$\Psi_{|\mathbf{A}|^2|C}(j\nu) = \exp\left[-(2C)^{1/\nu}\gamma\cos\left(\frac{\pi}{2\nu}\right)|j\nu|^{1/\nu}\left(1 - \frac{j\nu}{|j\nu|}\tan\left(\frac{\pi}{2\nu}\right)\right)\right]. \quad (102)$$

The approximated BEP conditioned on C and $d_0 = +1$ can be written as

$$P_{e,\text{TR}|C,d_0=+1}^{(\text{NBIs})} \simeq \frac{1}{2} + \frac{1}{\pi} \int_0^\infty \left(\frac{1}{1+\nu^2}\right)^{q_{\text{TR}}} \Re\left\{\frac{\Psi_{\mu_{\text{TR}}}\left(\frac{-j\nu}{1+j\nu}\right)\Psi_{|\mathbf{A}|^2|C}(g_{\text{TR},d_0=+1}(j\nu)\cdot I)}{j\nu}\right\}d\nu, \quad (103)$$

where $g_{\text{TR},d_0=+1}(j\nu)$ is defined in (77). Similarly the approximated BEP conditioned on C and $d_0 = -1$ can be written as

$$P_{e,\text{TR}|C,d_0=-1}^{(\text{NBIs})} \simeq \frac{1}{2} + \frac{1}{\pi} \int_0^\infty \left(\frac{1}{1+\nu^2}\right)^{q_{\text{TR}}} \Re\left\{\frac{\Psi_{\mu_{\text{TR}}}\left(\frac{-j\nu}{1+j\nu}\right)\Psi_{|\mathbf{A}|^2|C}(g_{\text{TR},d_0=-1}(j\nu)\cdot I)}{j\nu}\right\}d\nu, \quad (104)$$

where $g_{\text{TR},d_0=-1}(j\nu)$ is defined in (79). The total approximated BEP conditioned on C can be expressed as

$$P_{e,\text{TR}|C}^{(\text{NBIs})} \simeq \frac{1}{2} \left(P_{e,\text{TR}|C,d_0=+1}^{(\text{NBIs})} + P_{e,\text{TR}|C,d_0=-1}^{(\text{NBIs})}\right). \quad (105)$$

²⁰The scaling property states that if $X \sim S(\alpha, \beta, \gamma)$, then $kX \sim S(\alpha, \text{sign}(k)\beta, |k|^\alpha\gamma)$ for any non-zero real constant k [152].

²¹For $\nu = 1$, $\Psi_{|\mathbf{A}|^2|C}(j\nu) = \exp[-2C\gamma\cos(\frac{\pi}{2})|j\nu|\ln|j\nu|] = 1$. In this case, A_c and A_s are independent Gaussian r.v.s. It follows that $|\mathbf{A}|^2 = 2\gamma C$ and $\Psi_{|\mathbf{A}|^2}(j\nu) = \frac{1}{1-4j\nu}$.

Compared to (100), we only need to numerically average over C , which is computationally more attractive. However, we can also avoid this averaging by approximating the CF of $|\mathbf{A}|^2$. We can approximate the expectation of (102) with respect to C as follows:

$$\psi_{|\mathbf{A}|^2}(j\nu) \simeq \left[1 + \Omega_\nu 2^{1/\nu} \gamma \cos\left(\frac{\pi}{2\nu}\right) |j\nu|^{1/\nu} \left(1 - \frac{j\nu}{|j\nu|} \tan\left(\frac{\pi}{2\nu}\right) \right) \right]^{-k\nu}, \quad (106)$$

where we have used the Gamma distribution to approximate the distribution of $C^{1/\nu}$. Notes on this approximation are provided in Appendix 4. Table 6 gives the different parameters for this approximation. Using (100) and (106), the approximate BEP of the AcR for detecting TR signaling with BPAM in the presence of multiple NBI conditioned on $d_0 = +1$ is given by

$$P_{e,\text{TR}|d_0=+1}^{(\text{NBIs})} \simeq \frac{1}{2} + \frac{1}{\pi} \int_0^\infty \left(\frac{1}{1+\nu^2} \right)^{q_{\text{TR}}} \Re \left\{ \frac{\Psi_{\mu_{\text{TR}}}\left(\frac{-j\nu}{1+j\nu}\right) \Psi_{|\mathbf{A}|^2}(g_{\text{TR},d_0=+1}(j\nu) \cdot I)}{j\nu} \right\} d\nu. \quad (107)$$

Similarly, the approximate BEP of TR signaling with AcR in the presence of multiple NBI conditioned on $d_0 = -1$ is given by

$$P_{e,\text{TR}|d_0=-1}^{(\text{NBIs})} \simeq \frac{1}{2} + \frac{1}{\pi} \int_0^\infty \left(\frac{1}{1+\nu^2} \right)^{q_{\text{TR}}} \Re \left\{ \frac{\Psi_{\mu_{\text{TR}}}\left(\frac{-j\nu}{1+j\nu}\right) \Psi_{|\mathbf{A}|^2}(g_{\text{TR}|d_0=-1}(j\nu) \cdot I)}{j\nu} \right\} d\nu. \quad (108)$$

As a result, it follows that the BEP of the AcR for detecting TR signaling with BPAM in the presence of multiple NBI is given by

$$P_{e,\text{TR}}^{(\text{NBIs})} = \frac{1}{2} \left(P_{e,\text{TR},d_0=+1}^{(\text{NBIs})} + P_{e,\text{TR},d_0=-1}^{(\text{NBIs})} \right). \quad (109)$$

4.3.2.2 Energy detector (ED) in the presence of multiple NB interferers

Following the approach in Section 4.3.1.2, we derive the non-centrality parameters of $Y_{\text{ED},0}$ and $Y_{\text{ED},1}$ conditioned on \mathbf{A} , $\{c_j\}$, $\{a_j\}$, $\{h_l\}$ and $d_0 = 0$ as follows:

$$\begin{aligned} \mu_{Y_{\text{ED},1}}^{(\text{NBIs})} &\approx \frac{E_s^{\text{ED}}}{N_0} \sum_{l=1}^{L_{\text{CAP}}} h_l^2 + \frac{|\mathbf{A}|^2 I T N_s}{2N_0} + \frac{2|\widehat{P}(f_j)| \sqrt{2E_p^{\text{ED}} I}}{N_0} \sum_{j=0}^{\frac{N_s}{2}-1} a_j \sum_{l=1}^{L_{\text{CAP}}} h_l \\ &\times \left[A_c \cos \left(2\pi f_j (\tau_l + jT_f^{\text{ED}} + c_j T_p) + \arg \left\{ \widehat{P}(f_j) \right\} \right) \right. \\ &\quad \left. - A_s \sin \left(2\pi f_j (\tau_l + jT_f^{\text{ED}} + c_j T_p) + \arg \left\{ \widehat{P}(f_j) \right\} \right) \right], \end{aligned} \quad (110)$$

$$\mu_{Y_{\text{ED},2}}^{(\text{NBIs})} \approx \frac{|\mathbf{A}|^2 I T N_s}{2N_0}, \quad (111)$$

where the derivation of (110) and (111) follows directly from Appendix 3. Similar to Section 4.3.2.1, the approximated BEP of the ED receiver for detecting BPPM conditioned on C in the presence of multiple NBI is given by

$$P_{e,\text{ED}|C}^{(\text{NBIs})} \simeq \frac{1}{2} + \frac{1}{\pi} \int_0^\infty \left(\frac{1}{1+v^2} \right)^{q_{\text{ED}}} \Re \left\{ \frac{\Psi_{\mu_{\text{ED}}} \left(\frac{-jv}{1+jv} \right) \Psi_{|\mathbf{A}|_C^2} (g_{\text{ED}}(jv) \cdot I)}{jv} \right\} dv, \quad (112)$$

where g_{ED} is defined in (90). Using the approximate CF derived in (106), we can then rewrite (112) as

$$P_{e,\text{ED}}^{(\text{NBIs})} \simeq \frac{1}{2} + \frac{1}{\pi} \int_0^\infty \left(\frac{1}{1+v^2} \right)^{q_{\text{ED}}} \Re \left\{ \frac{\Psi_{\mu_{\text{ED}}} \left(\frac{-jv}{1+jv} \right) \Psi_{|\mathbf{A}|^2} (g_{\text{ED}}(jv) \cdot I)}{jv} \right\} dv. \quad (113)$$

4.3.3 Numerical and simulation results

In this section, we evaluate the performance of both AcR with TR signaling and ED with BPPM signaling, in the presence of single and multiple NB interferers, based on the analysis developed in Sections 4.3.1 and 4.3.2. Note that all results shown are based on the approximate analytical method. We consider a bandpass UWB system with pulse duration $T_p = 0.5$ ns, symbol interval $T_s = 3200$ ns, and $N_s = 32$. For simplicity, T_r and Δ are set such that there is no ISI or isi in the system, i.e., $T_r = 2T_r^{\text{TR}} - T_g - N_h T_p$ and

$\Delta = T_f^{\text{ED}} - T_g - N_h T_p$. We consider a TH sequence of all ones ($c_j = 1$ for all j) and $N_h = 2$. For UWB channels, we consider a dense resolvable multipath channel, where each multipath component amplitude is Nakagami distributed with fading severity index m and average power $\mathbb{E}\{h_l^2\}$, where $\mathbb{E}\{h_l^2\} = \mathbb{E}\{h_1^2\} \exp[-\varepsilon(l-1)]$, for $l = 1, \dots, L$, are normalized such that $\sum_{l=1}^L \mathbb{E}\{h_l^2\} = 1$ [153]. For simplicity, the fading severity index m is assumed to be identical for all paths. The average power of the first arriving multipath component is given by $\mathbb{E}\{h_1^2\}$, and ε is the channel power decay factor. With this model, we denote the UWB channel characteristic by (L, ε, m) for convenience. For the NBI model, we assume that the NBI is within the band of interest and experiences flat Rayleigh fading, i.e., the CF of α_j is $\psi_f(j\nu) = 1/(1 - j\nu)$. To compare AcR and ED performance, we let $E_s^{\text{TR}} = E_s^{\text{ED}} = E_b$, with E_b denoting the energy per bit. We define the signal-to-interference ratios as $\text{SIR} \triangleq E_b/(JT_s)$ and $\text{SIR}_T \triangleq E_b/(IT_s)$ for the cases of single NBI and of multiple NBI respectively. The central frequencies of the NBI are chosen in order to provide an insight into the effect of the interference on the receiver structures that have been analyzed.

4.3.3.1 Performance with a single NB interferer

Figure 22 compares the BEP performance of both non-coherent receiver structures in the presence of a single NBI with $(L, \varepsilon, m) = (32, 0, 3)$, $WT = L$ for $E_b/N_0 = 16, 18, 20$ dB using (105) and (89). Interestingly, we see that the performance with AcR strongly depends on the operating frequency of the NBI. On the other hand, the performance with the ED is independent of the carrier frequency of the NBI since the non-centrality parameters are affected by the NBI independently of the value of f_j . Moreover, the ED-based system tends to be more robust to NBI compared to the AcR-based system in the interference-limited scenario. However, as the NBI becomes negligible, i.e., with SIR greater than 5 dB, both receiver structures yield similar performances since $E_s^{\text{ED}} = E_s^{\text{TR}}$.²²

²²This is consistent with the result derived in the absence of interference and shown in Chapter 3.

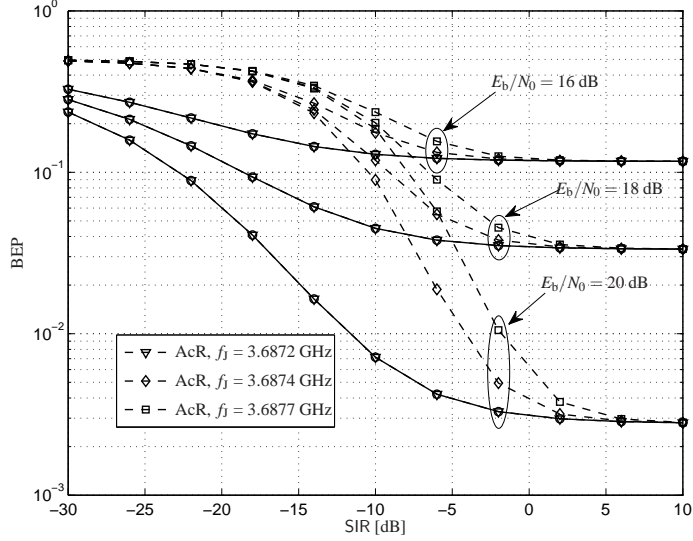


Fig. 22. BEP comparison of UWB non-coherent structures for UWB channel parameters $(L, \varepsilon, m) = (32, 0, 3)$ and integration time and bandwidth product $WT = L$, in the presence of a single NBI characterized by Rayleigh fading. The solid and dashed lines indicate ED receiver and AcR, respectively.

In Fig. 23, we show the validity of the approximation used in Sections 4.4.2.1 and 4.3.1.2 by comparing the BEP performance as a function of f_J with $(L, \varepsilon, m) = (32, 0.4, 3)$, $WT = L$, $E_b/N_0 = 20$ dB and $SIR = -10$ dB for both non-coherent receiver structures. We can see that the approximate analytical method is in good agreement with the quasi-analytical method.²³ In addition, we observe that the two systems have the same performance only when $f_J = n/4T_r$ for n odd. This can be intuitively explained by looking at how the interference modifies the received signal space. In the case of the AcR, the interference cross-term produces a DC component which is a function of $f_J T_r$ as shown in (77) and (79). As a result, the received signal space is no longer symmetric around zero for the case of TR signaling with BPAM. On the other hand, the symmetry of the received signal space for the case of BPPM is unaffected by the DC component related to the squaring of the interference signal in the ED receiver.

²³As a reminder, we say that the approximate analytical method assumes the signal-interference cross terms in the definition of the non centrality parameters negligible while the quasi-analytical method do not make this assumption.

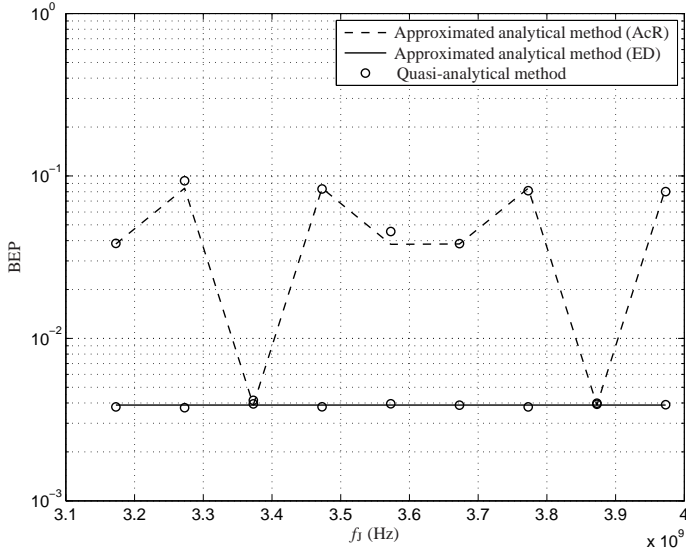


Fig. 23. BEP comparison of UWB non-coherent structures in the presence of a single NBI as a function of f_j for UWB channel parameters $(L, \varepsilon, m) = (32, 0, 3)$, $E_b/N_0 = 20$ dB, $SIR = -10$ dB and integration time and bandwidth product $WT = L$. The solid and dashed lines indicate the ED receiver and the AcR, respectively.

The effect of the integration interval T on the performance of both non-coherent receiver structures in the presence of single NBI at $f_j = 3.6872$ GHz with $(L, \varepsilon, m) = (32, 0.4, 3)$, and $E_b/N_0 = 20$ dB is shown in Fig. 24. We observe that the optimum T for the two non-coherent receiver structures are different. This is not surprising since the amount of interference energy accumulation for both receiver structures is different, and this amount also depends on the value of f_j for the case of the AcR. In addition, it is clear from Fig. 24 that the optimum T increases with SIR due to decreasing interference accumulation. As such, it is important that the integration interval is appropriately designed taking into consideration the type of non-coherent receiver structure, the operating carrier frequency of potential NBI, operating E_b/N_0 , and SIR.

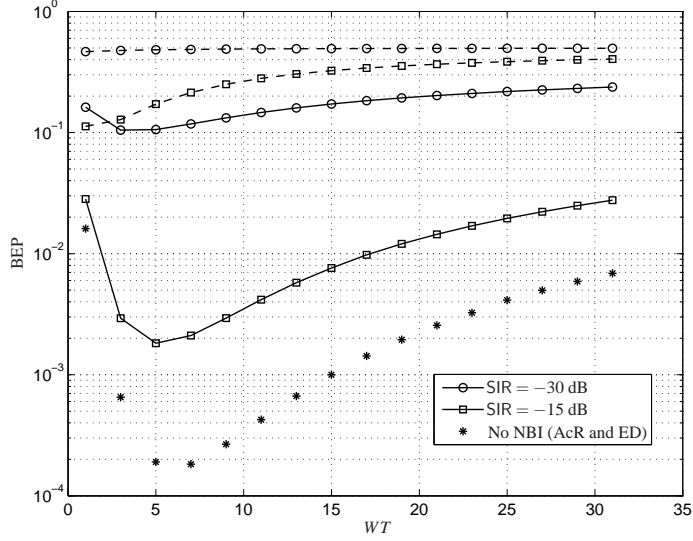


Fig. 24. BEP comparison of UWB non-coherent structures in the presence of single NBI for interference frequency $f_j = 3.6877$ GHz, for UWB channel parameters $(L, \varepsilon, m) = (32, 0.4, 3)$ and $E_b/N_0 = 20$ dB. The solid and dashed lines indicate the ED receiver and the AcR, respectively.

4.3.3.2 Performance with multiple NB interferers

First, we show the validity of the approximate analytical method for the case of multiple NBI. In Fig. 25, we show the BEP performance as a function of f_j with $(L, \varepsilon, m) = (32, 0, 3)$, $\lambda = 0.01$, $WT = L$, $E_b/N_0 = 20$ dB, and $\text{SIR}_T = -10$ dB for both non-coherent receiver structures. Similar to the single NBI case, the approximate analytical method is in good agreement with the quasi-analytical method. Next, we compare the results obtained with the approximated BEP formulas for AcR and ED receiver structures using the approximated CF of $|\mathbf{A}|^2$ in (106) with the semi-analytical results. Note that we still need to average the approximated conditional BEP expression in (105) and (112) over C . However, as apparent in the next plot, we see that this numerical averaging can be avoided by invoking an approximation on the CF of $|\mathbf{A}|^2$ using (106) to obtain (109) and (113) for both non-coherent receiver structures. In Figs. 26, we show the BEP performance of both non-coherent receiver structures as a function of WT with

$E_b/N_0 = 20$ dB, $(L, \varepsilon, m) = (32, 0.4, 3)$, $\lambda = 0.01$, $\nu = 1.5$, and $\sigma_1 = 1.2$ dB. We observe that by using the approximation in (106), we can obtain results that are in good agreement with the semi-analytical results. As seen in the single NBI case, the optimum T for the two receiver structures is different and the ED-based system performs better than the AcR-based when subject to multiple NBI.

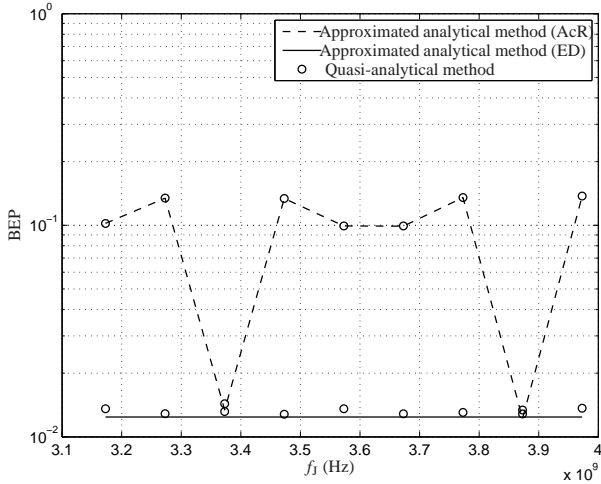


Fig. 25. BEP comparison of UWB non-coherent structures in the presence of multiple NBI as a function of the interference frequency f_j for UWB channel parameters $(L, \varepsilon, m) = (32, 0.4, 3)$, interferers spatial density $\lambda = 0.01$, $E_b/N_0 = 20$ dB, $SIR_T = -10$ dB and integration time and bandwidth product $WT = L$.

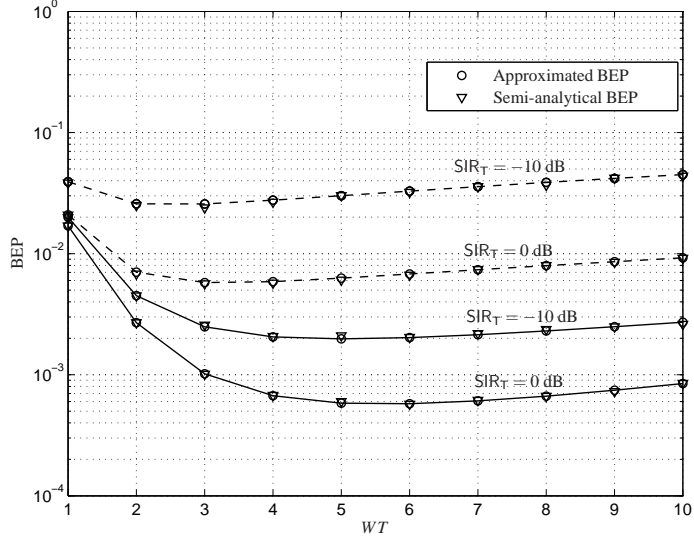


Fig. 26. BEP in the presence of multiple NBI as a function of the integration time and bandwidth product WT for $E_b/N_0 = 20$ dB, UWB channel parameters $(L, \varepsilon, m) = (32, 0.4, 3)$, interferers spatial density $\lambda = 0.01$, amplitude loss exponent $\nu = 1.5$, and interference signal shadowing parameter $\sigma_1 = 1.2$ dB. Comparison between the results obtained using approximate BEP formulas (109) and (113) and, semi-analytical BEP formulas (105) and (112) for the AcR (dashed lines) and the ED (solid lines), respectively.

In addition, in Figures 27 and 28, we show the effect of spatial density λ of the multiple NBI on the optimum T of ED-based and AcR-based systems with $E_b/N_0 = 20$ dB, UWB channel parameters $(L, \varepsilon, m) = (32, 0.4, 3)$, amplitude loss exponent $\nu = 1.5$, and interference signal shadowing parameter $\sigma_1 = 1.2$ dB, respectively. As λ increases, the aggregate interference becomes stronger and consequently, the optimum integration interval needs to be smaller to reduce the amount of interference energy accumulation. Similar to the single NBI results, we see that the performance of the AcR-based system strongly depends on the NBI carrier frequency.

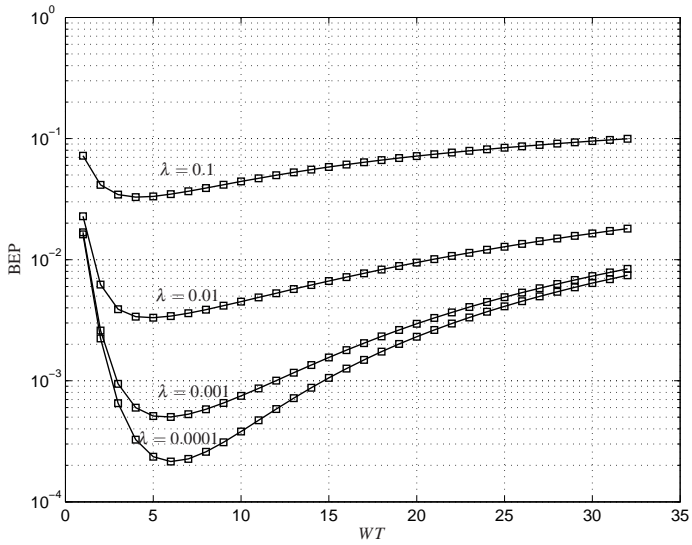


Fig. 27. Effect of the multiple NBI spatial density λ on the optimum integration time of the ED receiver for $E_b/N_0 = 20$ dB, $SIR_T = -10$ dB, UWB channel parameters $(L, \varepsilon, m) = (32, 0.4, 3)$, amplitude loss exponent $\nu = 1.5$, and interference signal shadowing parameter $\sigma_I = 1.2$ dB.

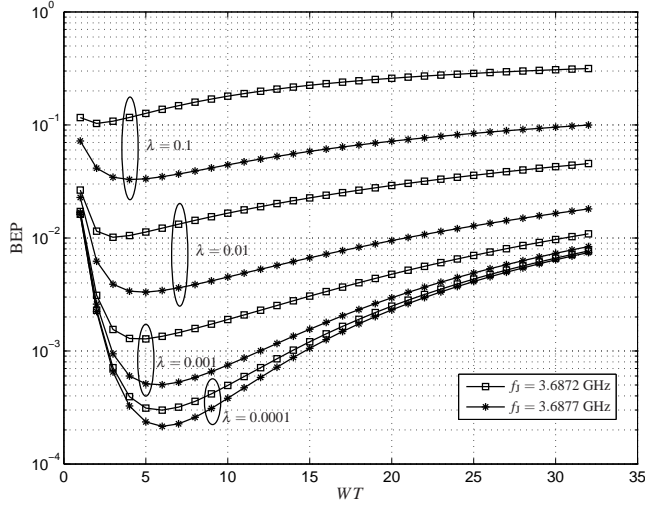


Fig. 28. Effect of the multiple NBI spatial density λ and of the NBI carrier frequency f_1 on the optimum integration time of the AcR for $E_b/N_0 = 20$ dB, $SIR_T = -10$ dB, UWB channel parameters $(L, \varepsilon, m) = (32, 0.4, 3)$, amplitude loss exponent $\nu = 1.5$, and interference signal shadowing parameter $\sigma_I = 1.2$ dB.

Lastly, we present a scenario demonstrating how our results can be useful for co-existence planning between UWB systems and multiple NBI systems. Specifically, in Fig. 29 we plot the BEP performance of the ED-based system as a function of E_b/N_0 for UWB channel parameters $(L, \varepsilon, m) = (32, 0, 3)$, $WT = L$, amplitude loss exponent $\nu = 1.5$, and interference signal shadowing parameter $\sigma_I = 1.2$ dB. We see that a reduction of 10 dB in the spatial density of the interferers allows the increase of the average individual interferer power by 15 dB. The relationship between the reduction of the spatial density Δ_λ^- and the increase of the average individual interferer power Δ_I^+ , both expressed in dB, can be derived from (112) and (102), where $\Delta_I^+ = \nu \Delta_\lambda^-$.

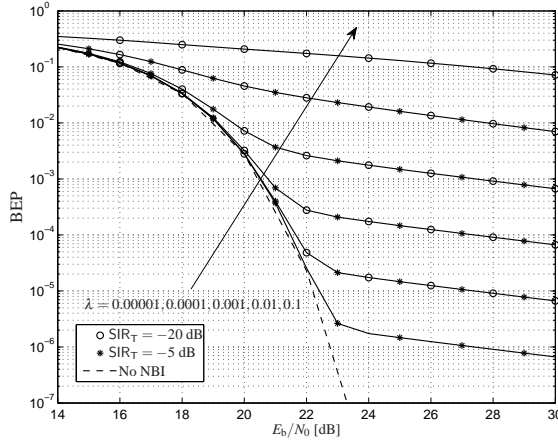


Fig. 29. Combined effect of the parameters λ and SIR_T on the BEP of the ED for $E_b/N_0 = 20$ dB, UWB channel parameters $(L, \varepsilon, m) = (32, 0, 3)$, integration time and bandwidth product $WT = L$, amplitude loss exponent $\nu = 1.5$, and interference signal shadowing parameter $\sigma_I = 1.2$ dB.

4.4 UWB interference

In this section we extend the BEP analysis to the case where UWB interference is present. We assume the sources of interference coming not from the users of the same network but coming from the neighboring UWB networks. It is quite realistic to consider that the low complexity of the schemes analyzed restricts the multi-user capability through the use of TDMA as no multiuser interference suppression is included in the receiver structures. Hence, it is a reasonable assumption to consider other UWB communication networks as a major source of UWB interference.

4.4.1 Multiple UWB interferers

In this framework we consider a single UWB system as the only source of interference. However, the study can be extended to the case of several networks with different parameters. As in the case of the NBI, we model the spatial distribution of the multiple UWB interferers according to a homogeneous Poisson point process in the two-dimensional

plane [102, 143, 148]. The probability that k nodes lie inside region \mathcal{R} depends only on the area $A_{\mathcal{R}} = |\mathcal{R}|$, and is given by [150]

$$\mathbb{P}\{k \in \mathcal{R}\} = \frac{(\lambda A_{\mathcal{R}})^k}{k!} e^{-\lambda A_{\mathcal{R}}}, \quad (114)$$

where λ is the spatial density (in nodes per unit area). In order to reduce the interference on other systems, the UWB devices are required to be active (transmitting) only for a small percentage a_f of time. In this framework, we consider that the density λ accounts for the activity factor such that $\lambda \triangleq \lambda_s a_f$, where λ_s is the density of active and inactive devices. The n th interferer transmitted signal can be expressed as

$$I^{(n)}(t) = \sqrt{P^I} \sum_i b_i^{(n)}(t - iN_s^I T_f^I), \quad (115)$$

where $b_i^{(n)}(t) \triangleq \sum_{j=1}^{N_s} e_i^{(n)} a_j^{(n)} p(t - jT_f - c_j^{(n)} T_p - d_i^{(n)} \Delta^I)$, $P^I \triangleq E_b^I / T_f^I N_s^I$ is the average power at the border of the near-field zone of each interfering transmitter antenna, and T_f^I is the pulse repetition period average which is common to the whole interferer system. The term $p(t)$ is a unit energy bandpass pulse with duration T_p and center frequency f_c , the term $e_i^{(n)} \in \{-1, 1\}$ is the i th data symbol for a BPAM modulation, $d_i^{(n)} \in \{0, 1\}$ is the i th data symbol for a BPPM modulation, Δ^I is the position modulation shift of the interfering system, $c_j^{(n)}$ is the j th element of the hopping sequence $\{c_j^{(n)}\}$ in the range $0 < c_j^{(n)} < N_h^I$, and N_h^I is the maximum shift associated with the hopping code. The bipolar amplitude sequence $\{a_j^{(n)}\} \in \{-1, 1\}$ is considered as a random process. The average pulse repetition interval is considered long enough in order to avoid isi and ISI. The interferer signals have the symbol duration $T_s^I = T_f^I N_s^I$. For notational convenience we define $\Psi^{(n)} = \{\{e_i^{(n)}\}, \{c_j^{(n)}\}, \{a_j^{(n)}\}, \{h_i^{(n)}\}\}$. We assume that the multiple interferers use the same pulse waveform as the desired signal so their signal is undistorted at the output of the BPZF. As a result, the aggregate interfering signal for a large (infinite) number of interferers at the output of the BPZF can be expressed as

$$\zeta(t) = \sum_{n=1}^{\infty} \zeta^{(n)}(t), \quad (116)$$

where $\zeta^{(n)}(t)$ denotes the signal from the n th interferer and it can be expressed as

$$\zeta^{(n)}(t) = \frac{e^{\sigma_1 G^{(n)}}}{(R^{(n)})^V} \sqrt{P^I_{V^{(n)}}} (t - D^{(n)}), \quad (117)$$

where σ_I , $G^{(n)}$, $R^{(n)}$ and v are defined as in the NBI case, $D^{(n)}$ is a uniformly distributed r.v. which accounts for the asynchronism of the interferers and

$$v^{(n)}(t) = \sum_i b_i^{(n)}(t - iN_s^I T_f^I) * h^{(n)}(t), \quad (118)$$

where $h^{(n)}(t) = \sum_{l=0}^{L-1} |h_l^{(n)}| e^{-j\phi_l^{(n)}} \delta(t - \tau_l^{(n)})$ is the channel impulse response of the n th interferer-receiver link defined similar to the case of the desired signal with maximum excess delay T_g^I . By using (117), we can rewrite (116) as

$$\zeta(t) = \sum_{n=1}^{\infty} \frac{e^{\sigma_I G^{(n)}}}{(R^{(n)})^v} \sqrt{P^I} v^{(n)}(t - D^{(n)}). \quad (119)$$

4.4.2 Received signals in the presence of UWB interference

4.4.2.1 Auto-correlation receiver (AcR)

If we incorporate in our analysis the UWB interference given in (119) and use the sampling expansion approach [147], (52) still holds with $\beta_{1,j,m} \triangleq \frac{1}{2\sqrt{2W}}(\eta_{2,j,m} + \zeta_{2,j,m} + \eta_{1,j,m} + \zeta_{1,j,m})$ and $\beta_{2,j,m} \triangleq \frac{1}{2\sqrt{2W}}(\eta_{2,j,m} + \zeta_{2,j,m} - \eta_{1,j,m} - \zeta_{1,j,m})$, where $\zeta_{1,j,m}$ and $\zeta_{2,j,m}$ for odd m (even m) are the real (imaginary) parts of the samples of the equivalent low-pass version of $\zeta_{1,j}(t) \triangleq \zeta(t + jT_f + c_j T_p)$ and $\zeta_{2,j}(t) \triangleq \zeta(t + jT_f + c_j T_p + T_f)$ respectively, sampled at Nyquist rate W over the interval $[0, T]$. Conditioning on $\{\Psi^{(n)}\}$, $\{c_j\}$, $\{a_j\}$, and $\{h_l\}$, the conditional variance σ_{TR}^2 of $\beta_{1,j,m}$ and $\beta_{2,j,m}$ is simply $\frac{N_0}{4}$, and the non-centrality parameters of $Y_{\text{TR},1}$ and $Y_{\text{TR},2}$ for $d_0 = +1$ are, respectively, given by

$$\begin{aligned} \mu_{Y_{\text{TR},1}}^{(\text{UWB})} &\triangleq \frac{1}{2\sigma_{\text{TR}}^2} \sum_{j=0}^{\frac{N_s}{2}-1} \sum_{m=1}^{2TW} \frac{1}{2W} \left[w_{j,m} + \frac{\zeta_{1,j,m} + \zeta_{2,j,m}}{2} \right]^2 \\ &= \underbrace{\frac{E_s^{\text{TR}}}{N_0} \sum_{l=1}^{L_{\text{CAP}}} h_l^2}_{\triangleq \mu_{\text{A,TR}}} + \underbrace{\sum_{j=0}^{\frac{N_s}{2}-1} \sum_{m=0}^{2TW} \frac{1}{2N_0} \frac{r_{1,j,m}^2}{2W}}_{\triangleq \mu_{\text{B,TR}}^{(\text{UWB})}} + \underbrace{\sum_{j=0}^{\frac{N_s}{2}-1} \sum_{m=1}^{2TW} \frac{1}{2N_0} \frac{r_{1,j,m} w_{j,m}}{2W}}_{\triangleq \mu_{\text{C,TR}}^{(\text{UWB})}}, \quad (120) \\ \mu_{Y_{\text{TR},2}}^{(\text{UWB})} &\triangleq \frac{1}{2\sigma_{\text{TR}}^2} \sum_{j=0}^{\frac{N_s}{2}-1} \sum_{m=0}^{2TW} \frac{1}{2W} \left[\frac{\zeta_{2,j,m} - \zeta_{1,j,m}}{2} \right]^2 \\ &= \sum_{j=0}^{\frac{N_s}{2}-1} \sum_{m=1}^{2TW} \frac{1}{2N_0} \frac{r_{2,j,m}^2}{2W}, \quad (121) \end{aligned}$$

where $r_{1,j,m} \triangleq \zeta_{1,j,m} + \zeta_{2,j,m}$ and $r_{2,j,m} \triangleq \zeta_{2,j,m} - \zeta_{1,j,m}$.

4.4.2.2 Energy detector (ED)

If we incorporate the interference in (45) and use the sampling expansion, conditioning on $\{\Psi^{(n)}\}$, $\{c_j\}$, $\{a_j\}$ and $\{h_l\}$, the non-centrality parameter of $Y_{\text{ED},0}$ and $Y_{\text{ED},1}$ for $d_0 = 0$ can be respectively expressed as

$$\begin{aligned} \mu_{Y_{\text{ED},0}}^{(\text{UWB})} &\triangleq \frac{1}{2\sigma_{\text{ED}}^2} \sum_{j=0}^{\frac{N_s}{2}-1} \sum_{m=1}^{2WT} \frac{(w_{1,j,m} + \zeta_{1,j,m})^2}{2W} \\ &= \underbrace{\frac{E_s^{\text{TR}}}{N_0} \sum_{l=1}^{L_{\text{CAP}}} h_l^2}_{\triangleq \mu_{\text{A,ED}}} + \underbrace{\sum_{j=0}^{\frac{N_s}{2}-1} \sum_{m=0}^{2TW} \frac{1}{N_0} \frac{\zeta_{1,j,m}^2}{2W}}_{\triangleq \mu_{\text{B,ED}}^{(\text{UWB})}} + \underbrace{\sum_{j=0}^{\frac{N_s}{2}-1} \sum_{m=1}^{2TW} \frac{2}{N_0} \frac{\zeta_{1,j,m} w_{j,m}}{2W}}_{\triangleq \mu_{\text{C,ED}}^{(\text{UWB})}}, \end{aligned} \quad (122)$$

$$\mu_{Y_{\text{ED},1}}^{(\text{UWB})} \triangleq \frac{1}{N_0} \sum_{j=0}^{\frac{N_s}{2}-1} \sum_{m=1}^{2WT} \frac{\zeta_{2,j,m}^2}{2W}, \quad (123)$$

where $\zeta_{1,j,m}$ and $\zeta_{2,j,m}$ for odd m (even m) are the real (imaginary) parts of the samples of the equivalent low-pass version of $\zeta_{1,j}(t) \triangleq \zeta(t + jT_f + c_j T_p)$ and $\zeta_{2,j}(t) \triangleq \zeta(t + jT_f + c_j T_p + \Delta)$ respectively, sampled at Nyquist rate W over the interval $[0, T]$.

4.4.3 Statistical characterization of the aggregate interference

Since the aggregate interference signal after the BPZF is band-limited and in practice is also power-limited, we can use the sampling expansion in order to derive a statistical model of the aggregate interference. We consider the complex vector $\bar{\zeta}_{1,j}$ composed of WT samples which are the sum of the interference low-pass equivalent signal samples.²⁴ The samples of the signal are taken at the Nyquist rate W in the interval $[0, T]$ within the j th signal frame of the bit 0 position. The vector $\bar{\zeta}_{1,j} = \{\zeta_{1,j,1}, \dots, \zeta_{1,j,2WT}\}$

²⁴In the interference model presented in the previous section we consider an infinite number of interference sources as an approximation of a realistic scenario with a large number of active UWB devices. The aggregate interference is the sum of a finite number of contributions and each contribution has finite power.

is defined as follows

$$\bar{\zeta}_{1,j} = \sum_{n=1}^{\infty} \frac{e^{\sigma_1 G^{(n)}}}{(R^{(n)})^\nu} \bar{\mathbf{v}}_{1,j}^{(n)}, \quad (124)$$

where $\bar{\mathbf{v}}_{1,j}^{(n)} = \{v_{1,j,1}, \dots, v_{1,j,2WT}\}$ is the vector of samples of the equivalent low-pass version of $v^{(n)}(t + c_j T_p + j T_f - D^{(n)})$. The complex samples $\mathbf{v}_{1,j,m}^{(n)}$ at the sampling instant m are a sequence of i.i.d. random variables in n . If the signal of the n th interferer is present at the sampling instant m , each sample can be written with a simplified notation as

$$\mathbf{v}_{1,j,m}^{(n)} = p \left(\tau^{(n)} \right) h_m^{(n)} \sqrt{\exp(-\varepsilon^I(m - T^{(n)}))} \Theta_m^{(n)}, \quad (125)$$

where $\tau^{(n)} \triangleq (D^{(n)} \bmod T_p)$ is a r.v. uniformly distributed over $[0, T_p)$, $T^{(n)}$ is a discrete r.v. uniformly distributed over $[0, 1, \dots, L - 1]$, $h_m^{(n)}$ is a r.v. with variance $1/\sum_{l=1}^L \exp(-\varepsilon^I(l))$ and distributed according to the small-scale fading, and $\Theta_m^{(n)} = \cos(\phi_m^{(n)}) - J \sin(\phi_m^{(n)})$ with $\phi_m^{(n)}$ uniformly distributed over $[0, 2\pi)$.²⁵ Considering that the complex r.v. $\Theta_m^{(n)}$ is CS then, similar to the multiple NBI case and as shown in Appendix 2, $\bar{\zeta}_{1,j,m}$ is described by a stable complex distribution as follows

$$\bar{\zeta}_{1,j,m} \sim S_c \left(\frac{2}{\nu}, 0, \gamma_{\text{UWB}} \right), \quad (126)$$

with $\gamma_{\text{UWB}} = \lambda \pi C_{2/\nu}^{-1} e^{2\sigma_1^2/\nu^2} \mathbb{E} \left\{ |\Re\{\mathbf{v}_{1,j,m}^{(n)}\}|^{2/\nu} \right\}$. We can write $\mathbb{E} \left\{ |\Re\{\mathbf{v}_{1,j,m}^{(n)}\}|^{2/\nu} \right\} = \frac{T_s^1}{T_f^1} \cdot M \cdot F \cdot P$ where the variables M, F, P are defined as follows

$$\begin{aligned} M &= \mathbb{E} \left\{ |h_m^{(n)}|^{2/\nu} \right\} \mathbb{E} \left\{ \left(\sqrt{\exp(-\varepsilon T^{(n)})} \right)^{2/\nu} \right\} \\ &= \begin{cases} \mathbb{E} \left\{ |h_m^{(n)}|^{2/\nu} \right\} \frac{e^{-\frac{\varepsilon(L-1)}{\nu}} (e^{\frac{\varepsilon L}{\nu}} - 1)}{(e^{-\frac{\varepsilon}{\nu}} - 1)^L} & \text{for } \varepsilon \neq 0 \\ \mathbb{E} \left\{ |h_m^{(n)}|^{2/\nu} \right\} & \text{for } \varepsilon = 0 \end{cases}, \quad (127) \end{aligned}$$

$$F = \mathbb{E}_n \left\{ |e_i^{(n)} a_j^{(n)}|^{2/\nu} \right\}, \quad (128)$$

²⁵As suggested in [36], since the low-pass equivalent version of a signal is complex, we considered the phase of each multipath component uniformly distributed over $[0, 2\pi)$.

and

$$P = \mathbb{E}\{|p(\tau^{(n)})|^{2/\nu}\} \mathbb{E}\{|\cos(\phi_m)|^{2/\nu}\}. \quad (129)$$

It was shown in [104] that the LePage series, for $\alpha < 2$ ($\nu > 1$) converge with a good approximation to a stable distribution already for a small number of interferers. This makes the stable distribution a good tool to model the effect of the aggregate interference produced by similar sources which are spatially distributed. Note that the components of the aggregate interference vector $\bar{\zeta}_{1,j}$ are identically distributed and the vector is symmetric alpha-stable ($S\alpha S$), which implies that all its components are dependent for $\alpha < 2$ [152].²⁶ In order to proceed with the analysis, we make the assumption that the $S\alpha S$ vector $\bar{\zeta}_{1,j}$ is spherically symmetric. Spherically symmetric vectors belongs to the category of sub-Gaussian $S\alpha S$ vectors which implies that they can be decomposed as

$$\bar{\zeta}_{1,j} = \sqrt{V} \bar{G}_{1,j}, \quad (130)$$

where $V \sim \mathcal{S}(\alpha/2, 1, \cos(\frac{\pi\alpha}{4}))$ and $\bar{G}_{1,j}$ is a multivariate Gaussian random variable with scalar cross-correlation matrix $\bar{\Sigma}$. Unfortunately, we can only mathematically prove that the resulting $S\alpha S$ vector is spherically symmetric for some models of the interference. For instance, as shown in Appendix 5, the $\bar{\zeta}_{1,j}$ is spherically symmetric and therefore sub-Gaussian if we consider Rayleigh fading with a flat power delay profile, uniform phase, and $T_g^I = T_f^I$. In this case, the spherical symmetry of the vector $\bar{\zeta}_{1,j}$ is ensured by the fact that the real and imaginary components of each vector $\bar{v}_{1,j}$ along the WT dimensions are spherically symmetric. The cross-correlation matrix $\bar{\Sigma}$ is scalar and it can be expressed as²⁷

$$\bar{\Sigma} = 2\gamma_{\text{UWB}}^{2/\alpha} \bar{I}_{2WT,2WT}. \quad (131)$$

The choice of a channel model with Rayleigh fading, flat PDP and unitary duty cycle would still offer insights on the aggregate UWB interference such as the time diversity introduced by the several multipath components; however, it would miss many characteristics of the UWB signal such as the duty cycle at the frame level,²⁸ the exponential

²⁶For the case of flat fading, ($L^I = 1$), the aggregate interference vector $\bar{\zeta}_{1,j}$ is composed by i.i.d. alpha-stable r.v.s.

²⁷ $\bar{I}_{2WT,2WT}$ represents the $2WT \times 2WT$ identity matrix. Note that in (130) we aligned real (odd m) and imaginary (even m) components in one dimension.

²⁸In this framework we consider the duty cycle as the ratio T_g^I/T_f^I .

power decay profile of the channel impulse response and a non-Rayleigh fading statistics. In order to ensure the spherical symmetry of the resulting aggregate interference vector, we can consider an alternative model for each received interference signal given by

$$v_{1,j}^{l(n)}(t) = z^{(n)} d_{\alpha}^{-\alpha} \sum_{m=1}^{WT_f^I} \mathbf{G}_{1,j,m}^{(n)} p(t - mT_p), \quad (132)$$

where $d_{\alpha}^{\alpha} = 2^{\alpha/2} \pi^{-1/2} (\Gamma(\frac{\alpha+1}{2}))^{-1}$ corresponds to $\mathbb{E}\{|\mathbf{G}_{1,j,m}^{(n)}|^{\alpha}\}$, $\{\mathbf{G}_{1,j,m}^{(n)}\}_{m=1}^{WT_f^I}$ is a sequence of i.i.d. complex Gaussian random variables with zero mean and unitary variance, and the variable $z^{(n)}$ is such that

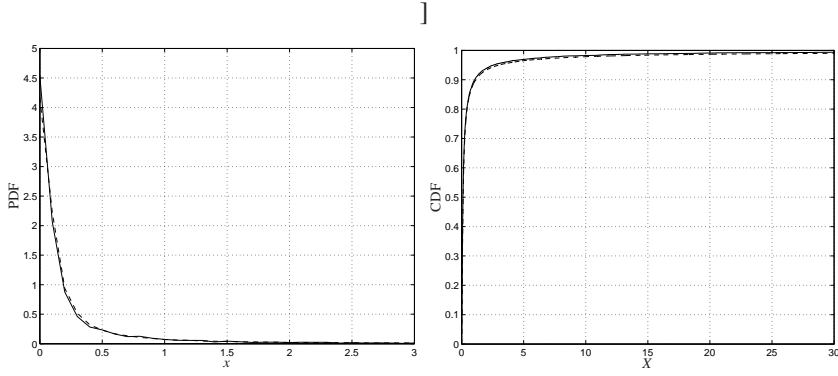
$$\begin{aligned} & \mathbb{E}\{|z^{(n)}|^{\alpha}\} \\ &= \frac{T_g^I}{T_f^I} \mathbb{E}\{|h_1^{(n)}|^{\alpha}\} \mathbb{E}\{|\exp(-\varepsilon(l - \delta^{(n)}))|^{\alpha}\} \mathbb{E}\{|\cos(\phi_m^{(n)})|^{\alpha}\}. \end{aligned} \quad (133)$$

Note that each interfering signal now covers the entire frame interval T_f^I . The effect of the duty cycle, of the channel fading, and of the PDP are now considered in the statistics of the variable $z^{(n)}$ which is zero with probability $1 - \frac{T_g^I}{T_f^I}$. The value $d_{\alpha}^{-\alpha}$ is such that the parameters of the Gaussian r.v. $\mathbf{G}_{1,j,m}^{(n)}$ do not affect the dispersion parameter γ_{UWB} of the $S\alpha S$ vector $\bar{\zeta}_{1,j}$.

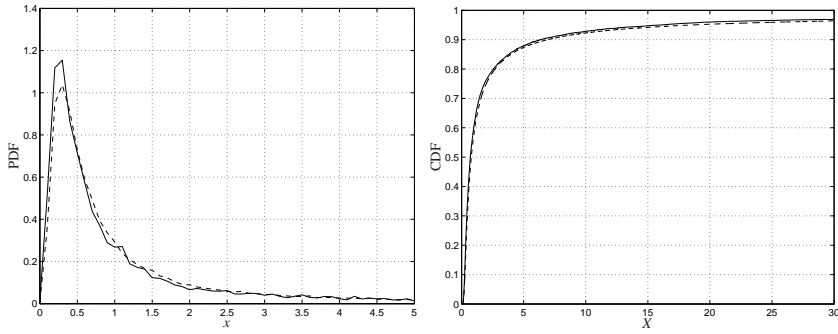
As will be shown in the next section, we are interested in the statistics of the integrated interference energy. It is important then to show how the statistics of the interference energy obtained with the sub-Gaussian assumption (as a result of (132)) are in close agreement with the statistics of the interference energy obtained by simulating the aggregate interference resulting from the original interference model represented by (124). To simulate this model, we consider a surface \mathcal{R} of area $A_{\mathcal{R}} = \pi R_s^2$ where UWB interferers are distributed according to a Poisson point process with spatial density λ . Each received interference signal is described by a simplified version of the original model omitting shadowing and pulse shape.²⁹ The multipath components are positioned within the pulse repetition interval of length T_f^I according to a delay $D^{(n)}$ which is uniformly distributed over T_f^I and includes a time shift due to the hopping sequence value and to the position modulation data. The amplitude attenuation of each

²⁹Shadowing and pulse shape are not of importance when testing the goodness of the sub-Gaussian approximation since they affect the dispersion parameter of the multivariate stable distribution but they do not affect the spherical symmetry of the distribution. As shown in (124) and (125), they are just multiplicative factors of each vector $\bar{\mathbf{v}}_{1,j}^{(n)}$.

received signal varies according to $1/(R^{(n)})^\nu$, where $R^{(n)}$ is the distance of the n th node consequent of the position of the node within \mathcal{R} . Figures 30, 31, and 32 plot the empirical PDFs and CDFs of the aggregate interference energy obtained from the statistical model described by the sub-Gaussian stable vector with dispersion parameter γ_{UWB} and from the aggregate interference energy obtained by 10000 simulations of the interference system model with $R_s = 50$ m, $\lambda = 0.1$, and $T_g^{\text{I}} = 16$ ns, for different values of T_f^{I} and ϵ^{I} . We consider the case of a single integration interval of duration $T = 5$ ns and the case of a total integration interval of $T = 30$ ns obtained considering two intervals of 15 ns belonging to two different pulse repetition periods. This second case is taken into consideration in order to evaluate the goodness of the statistical model where the aggregate interference vector over the whole symbol interval is considered sub-Gaussian. Figure 30 shows that in the case of a flat profile and $T_g^{\text{I}} = T_f^{\text{I}}$ there is good agreement among the interference statistical model described by the sub-Gaussian vector and the statistics of the aggregate interference obtained by simulations. In Fig. 31, we notice that in the case of an exponential PDP and $T_g^{\text{I}} = T_f^{\text{I}}$, the statistical model gives slightly less severe statistics for small values of interference energy, while there is still very good matching for the tail of the distribution. Comparing Fig. 31 with Fig. 30, it seems that in the statistical model described by the sub-Gaussian stable vector, the effect of ϵ^{I} is emphasized. Figure 32 shows that in the case of an exponential PDP and $T_g^{\text{I}} < T_f^{\text{I}}$, the statistical model correctly interprets the effect of the reduced duty cycle. A further discussion on the validity of the sub-Gaussian assumption is presented in Appendix 6.

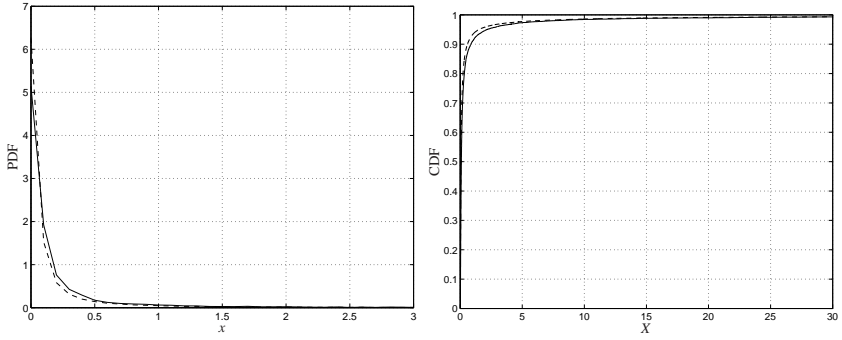


(a) $T = 5$ ns

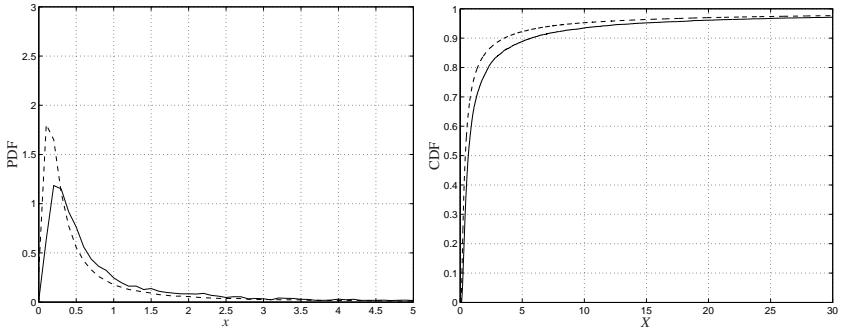


(b) $T = 30$ ns

Fig. 30. Comparison of the empirical PDFs and CDFs of the aggregate interference energy. The data are obtained by simulations of the sub-Gaussian vector (dashed line) and by simulations of the interference system (solid line) with $R_s = 50$ m, interferers spatial density $\lambda = 0.1$, pulse width $T_p = 0.5$ ns, pulse repetition period $T_f^I = 16$ ns, received signal duration $T_g^I = 16$ ns, fading parameter $m^I = 3$, and PDP exponent $\varepsilon^I = 0$.

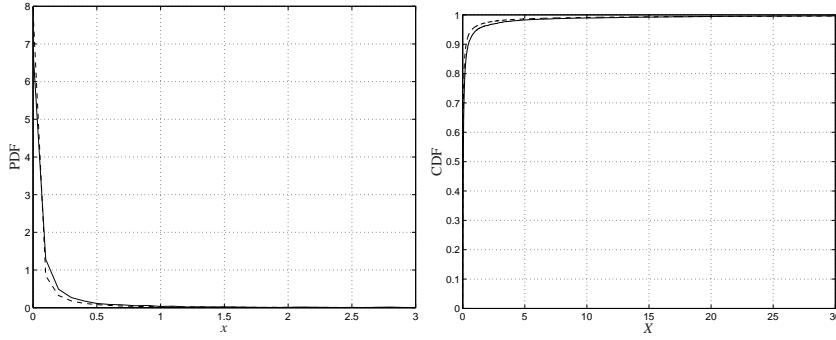


(a) $T = 5$ ns

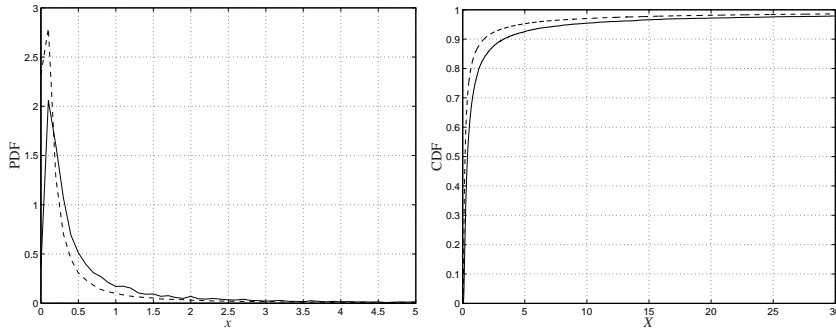


(b) $T = 30$ ns

Fig. 31. Comparison of the empirical PDFs and CDFs of the aggregate interference energy. The data are obtained by simulations of the sub-Gaussian vector (dashed line) and by simulations of the interference system (solid line) with $R_s = 50$ m, interferers spatial density $\lambda = 0.1$, pulse width $T_p = 0.5$ ns, pulse repetition period $T_f^1 = 16$ ns, received signal duration $T_{\text{eg}}^1 = 16$ ns, fading parameter $m^1 = 3$, and PDP exponent $\epsilon^1 = 0.4$.



(a) $T = 5$ ns



(b) $T = 30$ ns

Fig. 32. Comparison of the empirical PDFs and CDFs of the aggregate interference energy. The data are obtained by simulations of the sub-Gaussian vector (dashed line) and by simulations of the interference system (solid line) with $R_s = 50$ m, interferers spatial density $\lambda = 0.1$, pulse width $T_p = 0.5$ ns, pulse repetition period $T_f^I = 25$ ns, received signal duration $T_g^I = 16$ ns, fading parameter $m^I = 3$, and PDP exponent $\varepsilon^I = 0.4$.

4.4.4 BEP analysis in the presence of multiple UWB interferers

In the performance evaluation of both ED and AcR receivers, we consider two types of interference. The first type (Type 1) considers the aggregate interference signal to be periodic, such that the interference is the same in each modulation window for the BPPM and in the reference and modulated signal positions for the TR case. For the

second type (Type 2), more freedom is given to the aggregate interference signal.

4.4.4.1 Energy detector (ED) performance in the presence of Type 1 interference

In addition to the assumptions that the positions of the interferers, the shadowing and the channel impulse response of each interference signal do not change during the entire symbol duration T_s , we assume that each interfering transmitted signal is a train of pulses with a structure such that $n_1 T_f^I = \Delta$ and $n_2 T_f^I = T_f$, where n_1 and n_2 are integers and $n_2 > n_1$. No modulation is used ($e_i^{(n)} = 1(-1)$, $d_i^{(n)} = 0(1) \forall i$) and no random amplitude sequences and hopping code sequences are used ($a_j^{(n)} = 1(-1)$ and $c_j^{(n)} = 1 \forall j$). A simplified model representing Type 1 interference is given in Fig 33.

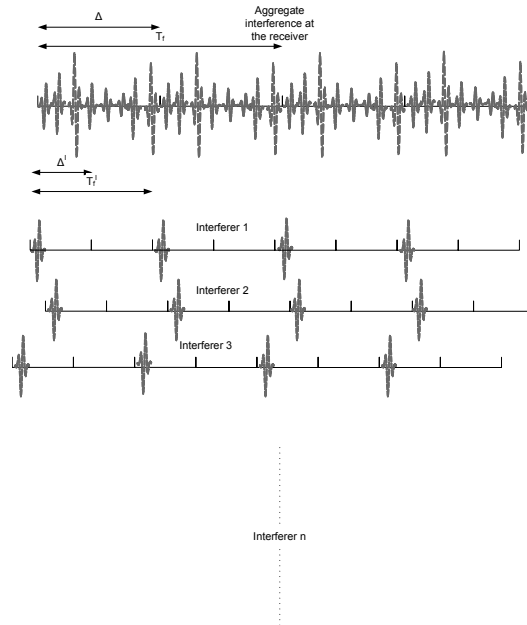


Fig. 33. Type 1 interference.

If the vector representing the aggregate interference can be expressed as in (130), the non-centrality terms of $Y_{ED,0}$ and $Y_{ED,1}$ for $d_0 = 0$ are given, respectively, by

$$\mu_{Y_{ED,0}}^{(UWB)} = \underbrace{\frac{E_s^{TR}}{N_0} \sum_{l=1}^{L_{CAP}} h_l^2}_{\triangleq \mu_{A,ED}} + \underbrace{\frac{P_1 N_s}{4WN_0} 2\gamma_{UWB}^v VC_1^{(1)}}_{\triangleq \mu_{B,ED}^{(UWB)}} + \underbrace{\sum_{j=0}^{\frac{N_s}{2}-1} \sum_{m=1}^{2WT} \frac{\zeta_{1,j,m} w_{j,m}}{2WN_0}}_{\triangleq \mu_{C,ED}^{(UWB)}}, \quad (134)$$

$$\mu_{Y_{ED,1}}^{(UWB)} = \mu_{B,ED}^{(UWB)}, \quad (135)$$

where $C_1^{(1)} = \sum_{m=1}^{2WT} G_{1,j,m}^2$ is a Chi-squared r.v. with $2WT$ degrees of freedom. Due to the transmitted interference signal model, the aggregate interference signal repeats itself at each interval Δ . As a result, the integrated energy has the same value for each integration interval. In order to evaluate the BEP of the ED for BPPM detection, we can use (55) and average the numerical integral over several realizations of the r.v.s which appear in (134) and (135). Alternatively we can use an approximated analytical approach, as in the NBI case, which considers $\mu_{C,ED}^{(UWB)}$ negligible compared with the others two terms in (134).³⁰ In this case, by defining $A^2 \triangleq VC_1^{(1)}$, the conditional BEP can be expressed as

$$P_{e,ED|A^2} \simeq \frac{1}{2} + \frac{1}{\pi} \int_0^\infty \left(\frac{1}{1+v^2} \right)^{q_{ED}} \Re \left\{ \frac{\Psi_{\mu_A^{ED}} \left(\frac{-jv}{1+jv} \right) \exp(g_{ED}^{(1)}(jv) 2\gamma_{UWB}^v A^2)}{jv} \right\} dv, \quad (136)$$

where

$$g_{ED}^{(1)}(jv) = \frac{P_1 N_s}{4WN_0} \left(\frac{-jv}{1+jv} + \frac{jv}{1-jv} \right). \quad (137)$$

Applying the scaling property, the r.v. A^2 conditioned on $C_1^{(1)}$ has a stable distribution with characteristic exponent $1/v$, skewness 1 and dispersion $(2C_1^{(1)})^{1/v} \gamma_{UWB} \cos(\frac{\pi}{2v})$. The CF of A^2 conditioned on $C_1^{(1)}$ for $v > 1$ is given by

$$\Psi_{A^2|C_1^{(1)}}(jv) = \exp \left[-(2C_1^{(1)})^{1/v} \gamma_{UWB} \cos \left(\frac{\pi}{2v} \right) |jv|^{1/v} \left(1 - \frac{jv}{|jv|} \tan \left(\frac{\pi}{2v} \right) \right) \right]. \quad (138)$$

³⁰As in the NBI case and also intuitively, the sum of the interference-signal cross-terms $\sum_{j=0}^{\frac{N_s}{2}-1} \sum_{m=1}^{2WT} \zeta_{1,j,m} w_{j,m}$ tends to give a marginal contribution to $\mu_{Y_{ED,0}}^{(UWB)}$ compared to the sum $\sum_{j=0}^{\frac{N_s}{2}-1} \sum_{m=1}^{2WT} w_{j,m}^2 + \sum_{j=0}^{\frac{N_s}{2}-1} \sum_{m=1}^{2WT} \zeta_{1,j,m}^2$ as the number of elements composing the sum increases.

Using (138), we can rewrite (136) as

$$P_{e,ED|C_1^{(1)}}^{(UWB)} \simeq \frac{1}{2} + \frac{1}{\pi} \int_0^\infty \left(\frac{1}{1+v^2} \right)^{q_{TR}} \Re \left\{ \frac{\Psi_{\mu_{ED}} \left(\frac{-jv}{1+jv} \right) \Psi_{A^2|C_1^{(1)}} \left(g_{ED}^{(1)}(jv) \right)}{jv} \right\} dv. \quad (139)$$

Compared to (136), we only need to numerically average over $C_1^{(1)}$, which is computationally much more attractive. However, similar to the NBI case, we can also avoid this average by approximating the CF of A^2 . We can approximate the expectation of (102) with respect to $C_1^{(1)}$ as follows:

$$\Psi_{A^2}(jv) \simeq \left[1 + \Omega_v \gamma_{UWB} \cos \left(\frac{\pi}{2v} \right) |jv|^{1/v} \left(1 - \frac{jv}{|jv|} \tan \left(\frac{\pi}{2v} \right) \right) \right]^{-k_v}, \quad (140)$$

where we have used the Gamma distribution to approximate the distribution of $(C_1^{(1)})^{1/v}$. Table 6 gives the different parameters for this approximation. Using (136) and (140), the approximate BEP of the ED for detecting BPPM in the presence of multiple UWB interference is given by

$$P_{e,ED}^{(UWB)} \simeq \frac{1}{2} + \frac{1}{\pi} \int_0^\infty \left(\frac{1}{1+v^2} \right)^{q_{ED}} \Re \left\{ \frac{\Psi_{\mu_{ED}} \left(\frac{-jv}{1+jv} \right) \Psi_{A^2} \left(g_{ED}^{(1)}(jv) \right)}{jv} \right\} dv. \quad (141)$$

4.4.4.2 Energy detector (ED) performance in the presence of Type 2 interference

With Type 2 interference, we still consider that the positions of the interferers and the shadowing terms do not change during the symbol but we remove all the other constraints of Type 1 interference. Due to the effect of the data modulation, of the hopping sequences and of the random amplitude sequences used by the interferers, the multipath components of each interferer signal change position and phase from one frame to another, even though the channel impulse response is constant over T_s . A simplified model representing Type 2 interference is given in Fig 34.

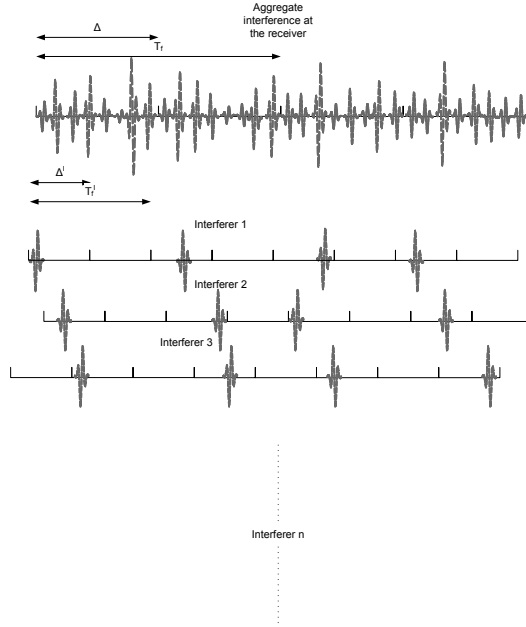


Fig. 34. Type 2 interference.

As a result, we can assume the vector $\bar{\zeta} = [\bar{\zeta}_{1,0}, \dots, \bar{\zeta}_{1, \frac{N_s}{2}-1}, \bar{\zeta}_{2,0}, \dots, \bar{\zeta}_{2, \frac{N_s}{2}-1}]$ to be sub-Gaussian, representing the aggregate interference signal along the entire symbol duration T_s . The cross-correlation matrix of the Gaussian vector $\bar{\zeta}$ is still scalar. The non-centrality terms of $Y_{ED,0}$ and $Y_{ED,1}$ for $d_0 = 0$ are given, respectively, by

$$\mu_{Y_{ED,0}}^{(UWB)} = \underbrace{\frac{E_s^{ED}}{N_0} \sum_{l=1}^{L_{CAP}} h_l^2}_{\triangleq \mu_{A,ED}} + \underbrace{\frac{P_I}{2WN_0} 2\gamma_{UWB}^V VC_1^{(2)}}_{\triangleq \mu_{B,ED}^{(UWB)}} + \underbrace{\sum_{j=0}^{\frac{N_s}{2}-1} \sum_{m=1}^{2WT} \frac{\zeta_{1,j,m} w_{j,m}}{2WN_0}}_{\triangleq \mu_{C,ED}^{(UWB)}}, \quad (142)$$

and

$$\mu_{Y_{ED,1}}^{(UWB)} = \frac{P_I}{2WN_0} 2\gamma_{UWB}^V VC_2^{(2)}, \quad (143)$$

where $C_1^{(2)}$ and $C_2^{(2)}$ are Chi-squared distributed with $\frac{N_s}{2} 2WT$ degrees of freedom. Dif-

ferently from Type 1 interference, the interference observed in the integration intervals related to bit 0 and bit 1 is no longer the same. Considering $\mu_{C,ED}^{(UWB)}$ to be negligible compared with the others two terms in (142), and considering

$$g_{ED|C_1^{(2)},C_2^{(2)}}^{(2)}(j\nu) = \frac{P_1}{2WN_0}V \left[C_1^{(2)} \frac{-j\nu}{1+j\nu} + C_2^{(2)} \frac{j\nu}{1-j\nu} \right], \quad (144)$$

the approximate BEP condition on $C_1^{(2)}$ and $C_2^{(2)}$ can be expressed as

$$P_{e,ED|C_1^{(2)},C_2^{(2)}}^{(UWB)} \simeq \frac{1}{2} + \frac{1}{\pi} \int_0^\infty \left(\frac{1}{1+\nu^2} \right)^{q_{ED}} \Re \left\{ \frac{\Psi_{\mu_{ED} \left(\frac{-j\nu}{1+j\nu} \right)} \Psi_V \left(g_{ED|C_1^{(2)},C_2^{(2)}}^{(2)}(j\nu) 2\gamma_{UWB}^V \right)}{j\nu} \right\} d\nu, \quad (145)$$

where $\Psi_V(j\nu)$ is the CF of the stable variable V . In this case, it is not possible to avoid the numerical average over $C_1^{(2)}$ and $C_2^{(2)}$; however, (145) is again computationally attractive.

4.4.4.3 Auto-correlation receiver (AcR) performance in the presence of Type 1 interference

We assume that $T_r = n_1 T_f^I$ and $T_f = n_2 T_f^I$ with n_1 and n_2 integer and $n_2 > n_1$ and we consider the transmitted signal to be composed of a train of pulses as in the ED case. Since the interference vector is periodic and repeats itself over each interval T_r for the entire symbol, we have $r_{1,j,m} = 2\sqrt{V}(G_{1,j,m})$ and $r_{2,j,m} = 0$. The non-centrality terms of the r.v.s $Y_{TR,1}$ and $Y_{TR,2}$ for $d_0 = +1$ can be expressed respectively as

$$\mu_{Y_{TR,1}}^{(UWB)} = \underbrace{\frac{E_s^{TR}}{N_0} \sum_{l=1}^{L_{CAP}} h_l^2}_{\mu_{A,TR}} + \underbrace{2\gamma_{UWB}^{2/\alpha} \frac{P^I N_s}{2WN_0} VC_1^{(1)}}_{\mu_{B,TR}^{(UWB)}} + \underbrace{\sum_{j=0}^{\frac{N_s}{2}-1} \sum_{m=0}^{2WT} \frac{r_{1,j,m} w_{j,m}}{2WN_0}}_{\mu_{C,TR}^{(UWB)}}, \quad (146)$$

and

$$\mu_{Y_{TR,2}}^{(UWB)} = 0, \quad (147)$$

where $C_1^{(1)}$ is a central Chi-squared distributed r.v. with $2TW$ degrees of freedom. In order to evaluate the BEP of the AcR for TR-BPAM detection, we can use (55) and average the numerical integral over several realizations of the r.v.s which appear in (146).

Otherwise we can use an approximate analytical approach which considers $\mu_{C,TR}^{(UWB)}$ negligible compared with the other two terms in (146), and the BEP conditioned on $C_1^{(1)}$ can be then written as

$$P_{e,TR|C_1^{(1)},d_0=+1}^{(UWB)} \simeq \frac{1}{2} + \frac{1}{\pi} \int_0^\infty \left(\frac{1}{1+v^2} \right)^{q_{TR}} \Re e \left\{ \frac{\Psi_{\mu_{TR}} \left(\frac{-jv}{1+jv} \right) \Psi_{A^2|C_1^{(1)}} \left(\frac{P^1 N_s}{2WN_0} \frac{-jv}{1+jv} \right)}{jv} \right\} dv, \quad (148)$$

where $\Psi_{A^2|C_1^{(1)}}(jv)$ is defined as in (138). Similarly for $d_0 = -1$, the BEP can be written as

$$P_{e,TR|C_1^{(1)},d_0=-1}^{(UWB)} \simeq \frac{1}{2} + \frac{1}{\pi} \int_0^\infty \left(\frac{1}{1+v^2} \right)^{q_{TR}} \Re e \left\{ \frac{\Psi_{\mu_{TR}} \left(\frac{-jv}{1+jv} \right) \Psi_{A^2|C_1^{(1)}} \left(\frac{P^1 N_s}{2WN_0} \frac{jv}{1-jv} \right)}{jv} \right\} dv. \quad (149)$$

Furthermore, considering the Gamma distribution as an approximation of the process $(C_1^{(1)})^{1/\nu}$, we have for $d_0 = +1$

$$P_{e,TR|d_0=+1}^{(UWB)} \simeq \frac{1}{2} + \frac{1}{\pi} \int_0^\infty \left(\frac{1}{1+v^2} \right)^{q_{TR}} \Re e \left\{ \frac{\Psi_{\mu_{TR}} \left(\frac{-jv}{1+jv} \right) \Psi_{A^2} \left(\frac{P^1 N_s}{2WN_0} \frac{-jv}{1+jv} \right)}{jv} \right\} dv, \quad (150)$$

and for $d_0 = -1$

$$P_{e,TR|d_0=-1}^{(UWB)} \simeq \frac{1}{2} + \frac{1}{\pi} \int_0^\infty \left(\frac{1}{1+v^2} \right)^{q_{TR}} \Re e \left\{ \frac{\Psi_{\mu_{TR}} \left(\frac{-jv}{1+jv} \right) \Psi_{A^2} \left(\frac{P^1 N_s}{2WN_0} \frac{jv}{1-jv} \right)}{jv} \right\} dv. \quad (151)$$

As a result, it follows that the BEP of the AcR using TR signaling with BPAM in the presence of UWB Type 1 interference is given by

$$P_{e,TR}^{(UWB)} = \frac{1}{2} \left(P_{e,TR,d_0=+1}^{(UWB)} + P_{e,TR,d_0=-1}^{(UWB)} \right). \quad (152)$$

4.4.4.4 Auto-correlation receiver (AcR) performance in the presence of Type 2 interference

As for the ED receiver, we consider the vector representing the aggregate interference over the entire symbol interval to be sub-Gaussian. As a result, we have $r_{1,j} \triangleq \zeta_{1,j,m} - \zeta_{2,j,m} \triangleq \sqrt{V}(G_{1,j,m} - G_{2,j,m})$ and $r_{1,j} \triangleq \zeta_{1,j,m} + \zeta_{2,j,m} = \sqrt{V}(G_{1,j,m} + G_{2,j,m})$. We can write the non-centrality parameter of $Y_{\text{TR},1}$ and $Y_{\text{TR},2}$ for $d_0 = +1$ as

$$\mu_{Y_{\text{TR},1}}^{(\text{UWB})} = \underbrace{\frac{E_s^{\text{TR}}}{N_0} \sum_{l=1}^{L_{\text{CAP}}} h_l^2}_{\mu_{\text{A,TR}}} + \underbrace{2\gamma_{\text{UWB}}^V \frac{P^{\text{I}}}{2WN_0} VC_1^{(2)}}_{\mu_{\text{B,TR}}^{(\text{UWB})}} + \underbrace{\sum_{j=0}^{\frac{N_s}{2}-1} \sum_{m=0}^{2WT} \frac{1}{N_0} \frac{r_{1,j,m} w_{j,m}}{2W}}_{\mu_{\text{C,TR}}^{(\text{UWB})}}, \quad (153)$$

and

$$\mu_{Y_{\text{TR},2}}^{(\text{UWB})} = 2\gamma_{\text{UWB}}^V \frac{P^{\text{I}}}{2WN_0} VC_2^{(2)}, \quad (154)$$

where $C_1^{(2)} = \sum_{j=0}^{\frac{N_s}{2}-1} \sum_{i=1}^{2WT} (G_{1,j,i} - G_{2,j,i})^2$ and $C_2^{(2)} = \sum_{j=0}^{\frac{N_s}{2}-1} \sum_{i=1}^{2WT} (G_{1,j,i} + G_{2,j,i})^2$. Note that $C_1^{(2)}$ and $C_2^{(2)}$ are independent and follow a central Chi-squared distribution with $\frac{N_s}{2} 2WT$ degrees of freedom. Considering $\mu_{\text{C,TR}}^{(\text{UWB})}$ negligible, the approximate BEP condition on $C_1^{(2)}$ and $C_2^{(2)}$ can be expressed as

$$P_{\text{e,TR}|C_1^{(2)},C_2^{(2)}}^{(\text{UWB})} \simeq \frac{1}{2} + \frac{1}{\pi} \int_0^\infty \left(\frac{1}{1+v^2} \right)^{q_{\text{TR}}} \Re \left\{ \frac{\Psi_{\mu_{\text{TR}}} \left(\frac{-jv}{1+jv} \right) \Psi_V \left(g_{\text{TR}|C_1^{(2)},C_2^{(2)}}(jv) 2\gamma_{\text{UWB}}^V \right)}{jv} \right\} dv, \quad (155)$$

where

$$g_{\text{TR}|C_1^{(2)},C_2^{(2)}}(jv) = \frac{P^{\text{I}}}{2WN_0} \left[C_1^{(2)} \frac{-jv}{1+jv} + C_2^{(2)} \frac{jv}{1-jv} \right]. \quad (156)$$

To solve the dependency, we only need to numerically average over $C_1^{(2)}$ and $C_2^{(2)}$. Note that in this case, the statistical symmetry with respect of d_0 is restored.

4.4.5 Numerical results

In this section, we evaluate the performance of both the AcR with TR signaling and the ED with BPPM signaling, in the presence of multiple UWB interferers considering the two types of interference described in the previous section. Note that all results shown are based on the approximate analytical method. For the desired signal, we consider a bandpass UWB system with pulse duration $T_p = 0.5$ ns, symbol interval $T_s = 3200$ ns, and $N_s = 32$. For simplicity, T_r and Δ are set such that there is no ISI or isi in the system, i.e., $T_r^{\text{TR}} = T_r$ with $T_r > T_g - N_h T_p$ and $T_f^{\text{ED}} = 2\Delta$ with $\Delta > T_g - N_h T_p$. We consider a TH sequence of all ones ($c_j = 1$ for all j) and $N_h = 2$. The desired signal is affected by a dense resolvable multipath channel, where each multipath amplitude is Nakagami distributed with fading severity index m and average power $\mathbb{E}\{h_l^2\}$, where $\mathbb{E}\{h_l^2\} = \mathbb{E}\{h_1^2\} \exp[-\varepsilon(l-1)]$, for $l = 1, \dots, L$, are normalized such that $\sum_{l=1}^L \mathbb{E}\{h_l^2\} = 1$. For simplicity, the fading severity index m is assumed to be identical for all paths. The average power of the first arriving multipath component is given by $\mathbb{E}\{h_1^2\}$, and ε is the channel power decay factor. With this model, we denote the channel characteristic of the desired signal by (L, ε, m) for convenience. For the UWB interferers we assume that they use the same waveform as the signal of interest and that the channel fading is also Nakagami with severity index m^I and average power $\mathbb{E}\{|h_l^I|^2\}$ defined as described above for the desirable signal. With this model, we denote the channel characteristic of the interference signals by $(L^I, \varepsilon^I, m^I)$. To compare the AcR and the ED, we let $E_s^{\text{TR}} = E_s^{\text{ED}} = E_b$, with E_b denoting the energy per bit. The signal to interference ratio (SIR_τ) is defined as $\text{SIR}_\tau = \frac{E_b}{N_s T_r P^I}$.

As shown in Section 4.4.3, for conditions that do not ensure the spherical symmetry of the aggregate interference vector, the aggregate interference energy statistics obtained by assuming the aggregate interference vector as sub-Gaussian is less severe than the statistics provided by simulation of the interference system. In this case, we can consider the BEP results as optimistic although they can still offer insights on the effect of the UWB interference.

4.4.5.1 Type 1 interference

Figure 35 compares the BEP performance of the AcR and the ED in the presence of Type 1 interference as a function of the integration time for UWB channel parameters $(L, \varepsilon, m) = (32, 0, 3)$ and UWB interference channel parameters $(L^I, \varepsilon^I, m^I) = (32, 0, 3)$.

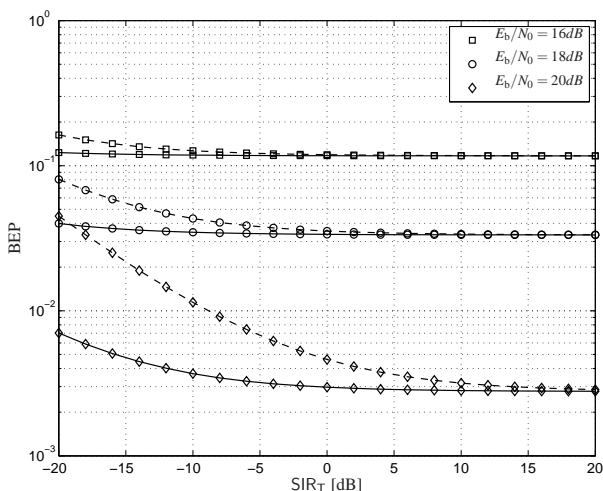


Fig. 35. BEP comparison of the AcR (dashed line) and the ED (solid line) in the presence of multiple UWB interferers (Type 1 interference) for UWB channel parameters $(L, \varepsilon, m) = (32, 0, 3)$, UWB interference channel parameters $(L^I, \varepsilon^I, m^I) = (32, 0, 3)$, pulse repetition interval $T_f^I = 50$ ns, interferers spatial density $\lambda = 0.01$, amplitude loss exponent $\nu = 1.5$, and interference signal shadowing parameter $\sigma_I = 1.6$ dB.

As in the case of NBI, the ED shows greater robustness than the AcR to this type of interference. In Fig. 36, the BEP is plotted versus the integration time for $E_b/N_0 = 20$ dB, $SIR_T = -20$ dB and $\lambda = 0.01$. It can be noticed that channel models characterized by a PDP, with higher ε^I have less effect on the performance of the receiver. This can be explained by the fact that with a steeper PDP, the interference signal energy is effectively concentrated in fewer multipath components which can be seen as a condition for a lower probability of collision. In Fig. 37 and Fig. 38, the effect of the pulse repetition T_f^I on the BEP is shown for both ED and AcR systems. A clear benefit, due to the lower probability of collision $\frac{T_g^I}{T_f^I}$, can be achieved if a lower pulse repetition rate is applied to the interference systems.

This type of periodic UWB interference is the result of very specific conditions which are unrealistic but together with the results obtained in the presence of NBI provide insight as to how the AcR can suffer from periodic interfering signals.

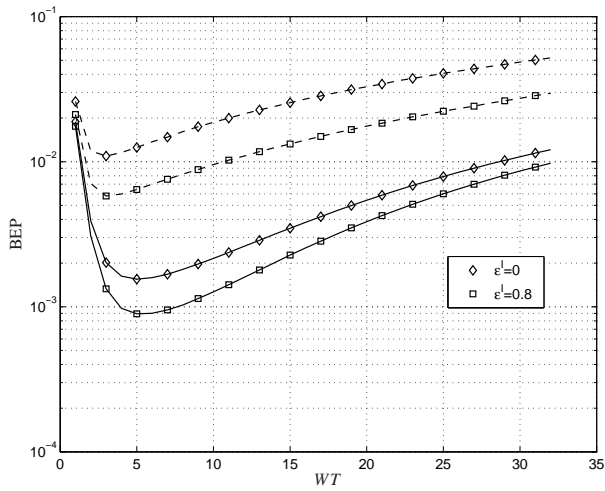


Fig. 36. BEP comparison of the AcR (dashed line) and the ED (solid line) in the presence of multiple UWB interferers (Type 1 interference) as a function of the integration time and bandwidth product WT for $E_b/N_0 = 20$ dB, $SIR_T = -20$ dB, UWB channel parameters $(L, \epsilon, m) = (32, 0.4, 3)$, UWB interference channel parameters $(L^I, \epsilon^I, m^I) = (32, \epsilon^I, 3)$, pulse repetition interval $T_f^I = 50$ ns, interferers spatial density $\lambda = 0.01$, amplitude loss exponent $\nu = 1.5$, and interference signal shadowing parameter $\sigma_I = 1.6$ dB.

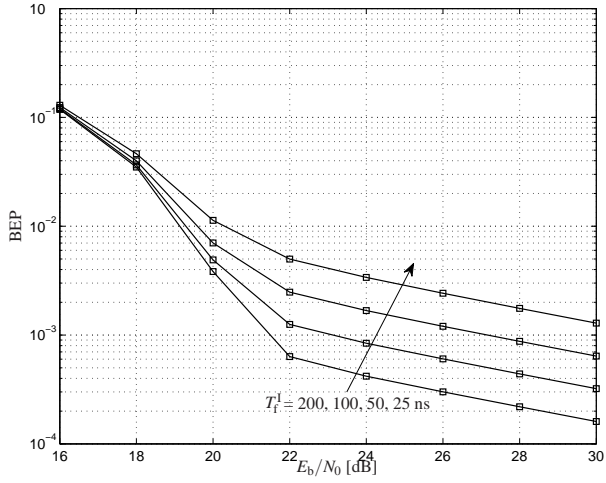


Fig. 37. Effect of the pulse repetition interval T_f^I on the BEP of the ED in the presence of multiple UWB interferers (Type 1 interference) for $E_b/N_0 = 20$ dB, $SIR_T = -20$ dB, UWB channel parameters $(L, \varepsilon, m) = (32, 0, 3)$, UWB interference channel parameters $(L^I, \varepsilon^I, m^I) = (32, 0, 3)$, interferers spatial density $\lambda = 0.01$, amplitude loss exponent $\nu = 1.5$, and interference signal shadowing parameter $\sigma_I = 1.6$ dB.

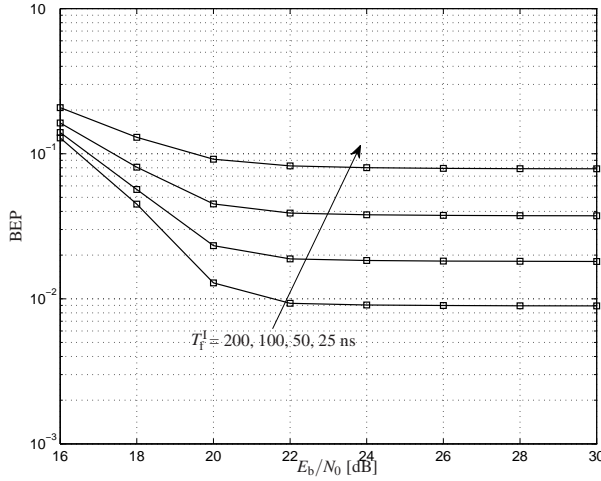


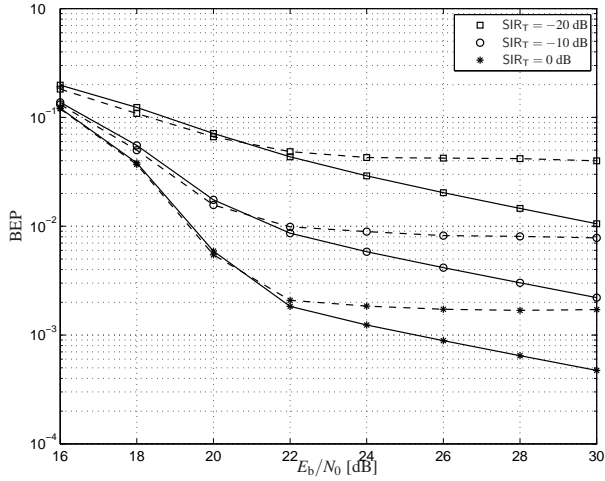
Fig. 38. Effect of the pulse repetition interval T_f^I on the BEP of the AcR in the presence of multiple UWB interferers (Type 1 interference) for $E_b/N_0 = 20$ dB, $SIR_T = -20$ dB, UWB channel parameters $(L, \varepsilon, m) = (32, 0, 3)$, UWB interference channel parameters $(L^I, \varepsilon^I, m^I) = (32, 0, 3)$, interferers spatial density $\lambda = 0.01$, amplitude loss exponent $\nu = 1.5$, and interference signal shadowing parameter $\sigma_I = 1.6$ dB.

4.4.5.2 Type 2 interference

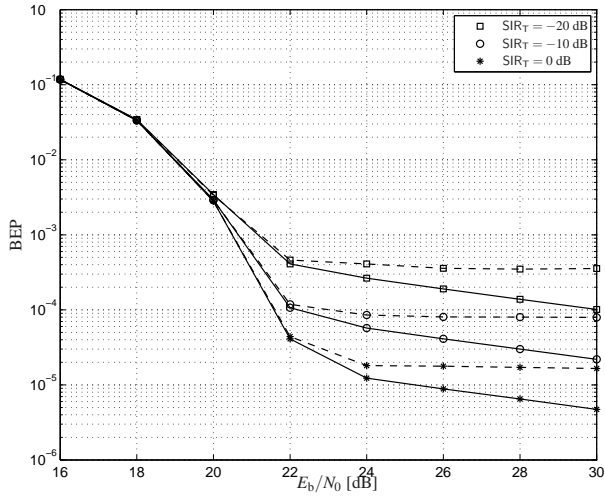
The numerical results obtained in this section are achieved by averaging over 5000 realizations of the variable $C_1^{(2)}$ and $C_2^{(2)}$. In Fig. 39(a) and Fig. 39(b) the performance of the ED receiver is presented for $\lambda = 0.1$ and $\lambda = 0.001$, respectively, in the presence of the two types of interference with channel parameters $(L, \varepsilon, m) = (32, 0, 3)$, $(L^I, \varepsilon^I, m^I) = (32, 0, 3)$, and $T_f^I = 50$ ns. It can be seen that when the effect of the interference becomes dominant, the Type 2 interference rapidly leads to saturation of the BEP curves at error floors which are much higher than the ones produced by the Type 1 interference. This can be explained by the fact that, in the case of Type 2 interference, the integrated interference energy in the bit positions 0 and bit positions 1 are no longer equivalent. This increases the BEP especially when the interference effect is dominant (large E_b/N_0).

In Figures 40(a) and 40(b), the performance of the AcR is compared in the presence of the two types of interference for $(L, \varepsilon, m) = (32, 0, 3)$, $(L^I, \varepsilon^I, m^I) = (32, 0, 3)$ and $T_f^I = 50$ ns. In this case, the Type 2 interference has much less effect on the BEP. The reason for this improvement is due to the fact that with Type 1 interference, the correlation among the aggregate interference signal at instant t and $t + T_f$ produces all positive values which help the detection of $d_0 = +1$ but makes the detection of $d_0 = -1$ impossible. With Type 2 interference, the correlation can give either positive or negative values reducing the effect of the interference on average. From Figures 39(a), 39(b) 40(a), and 40(b), in the presence of Type 2 interference, ED with BPPM and AcR with TR-BPAM detection perform equally.

For the NBI case, it is interesting to underline the relationship between the reduction of interference transmitted power and the density of the interferers. In the case of UWB interference, it is interesting to highlight the trade-off between pulse repetition interval T_f^I and spatial density λ . From the definition of μ_{ED} , we can see that there is an equivalent relation between T_f^I and λ . If, for instance, the density doubles, the pulse repetition interval should also double in order to avoid increasing the effect of the interference. Note that an increase of the pulse repetition interval is more effective than a reduction of the transmitted power to reduce the effect of the aggregate interference.

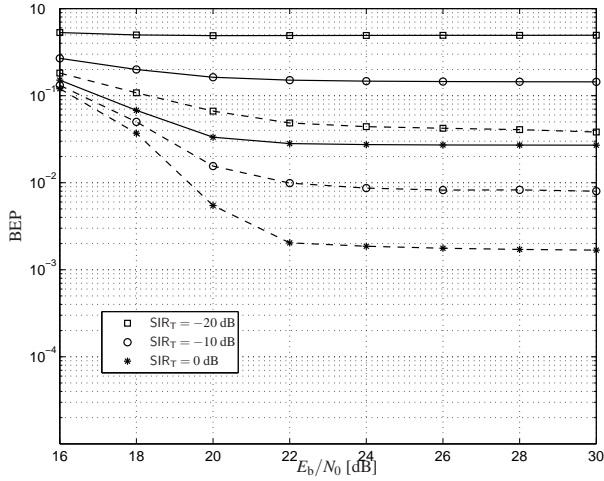


(a) spatial density $\lambda = 0.1$

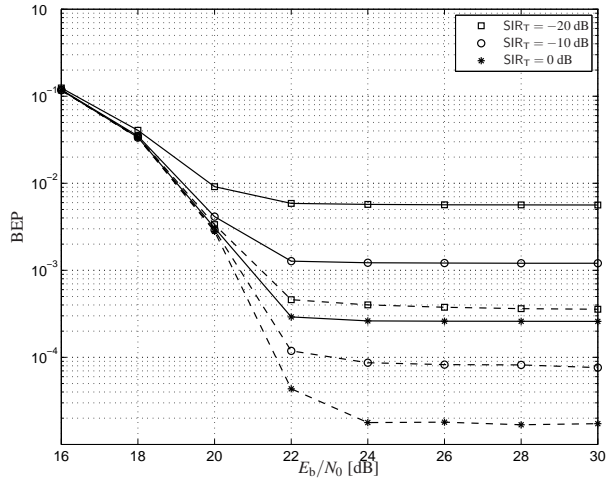


(b) spatial density $\lambda = 0.001$

Fig. 39. Comparison of the effect of the Type 1 interference (solid line) and Type 2 interference (dashed line) on the BEP performance of the ED receiver for UWB channel parameters $(L, \varepsilon, m) = (32, 0, 3)$, UWB interference channel parameters $(L^I, \varepsilon^I, m^I) = (32, 0, 3)$, pulse repetition interval $T_f^I = 50$ ns, amplitude loss exponent $\nu = 1.5$, and interference signal shadowing parameter $\sigma_I = 1.6$ dB.



(a) spatial density $\lambda = 0.1$



(b) spatial density $\lambda = 0.001$

Fig. 40. Comparison of the effect of the Type 1 interference (solid line) and Type 2 interference (dashed line) on the BEP performance of the AcR receiver for UWB channel parameters $(L, \varepsilon, m) = (32, 0, 3)$, UWB interference channel parameters $(L^I, \varepsilon^I, m^I) = (32, 0, 3)$, pulse repetition interval $T_f^I = 50$ ns, amplitude loss exponent $\nu = 1.5$, and interference signal shadowing parameter $\sigma_I = 1.6$ dB.

4.5 Conclusions

This chapter has focused on deriving BEP expressions in order to compare the performance of the AcR with TR-BPAM and the ED receiver with BPPM in the presence of NBI and UWB interference. Different from the no-interference case where the two schemes perform equally, it was shown that the ED-based system is more robust than the AcR-based system in the presence of NBI. The cases of single and multiple NBI are considered. In the multiple NBI case, we considered the interfering nodes to be scattered according to a spatial Poisson point random process and we showed that the aggregate interference can be represented by a single tone NBI with a CS complex-stable fading. Using a spatial Poisson point random process to describe the position of the interferers, the comparison of the two receiver schemes is extended considering the presence of multiple UWB interferers. It has been shown that the aggregate interference along the symbol interval can be represented by a symmetric alpha-stable vector. In order to proceed with our analysis, we assumed this vector to be spherically symmetric. This assumption turns out to be correct for channel models with flat PDP and unitary duty cycle while it leads to less severe aggregate interference in other conditions.

As a summary, the results demonstrate that the ED is more robust than the AcR to the interference. The AcR showed higher vulnerability to interfering signals which tend to be periodic with a period close to the delay between reference pulse and modulated pulse. It has been shown that, in the case of UWB interference, if the aggregate interference randomly changes along the symbol interval (i.e. no correlation between the aggregate interference in the reference pulse position and in the modulated pulse position for the AcR), the equivalence in terms of performance of the AcR and the ED is restored. Our framework is sufficiently simple to allow tractable analysis and can serve as a guideline for the design of heterogeneous networks where coexistence between UWB systems and NB systems is of importance.

5 Time of arrival estimation

5.1 Leading edge estimation problem

The very large bandwidth that characterizes UWB signals offers the possibility to transmit at very high data rates. It also provides very accurate temporal and spatial information that can be used for precise time-of-arrival (ToA) estimation. The unprecedented accuracy supported by the available bandwidth offers new possibilities in terms of synchronization, positioning and tracking [111, 112]. The capability to recover such information presents non-trivial implementation issues especially if the receiver structure is based on correlation and sampling. Using conventional digital signal processing techniques, the ultra-wide bandwidth requires a high sampling frequency and produces a complex received waveform which is difficult to reproduce at the receiver. The ToA estimation can be performed in different ways (i.e. one-way ranging, two-way ranging, etc.) and is based on the estimation of the signal leading edge within an uncertainty window in order to establish the propagation delay with respect to a temporal reference. Issues such as clock drift and clock jitter can affect the accuracy of the ToA. In this chapter, the focus is on the signal leading edge estimation. Prior works have analyzed the ranging problem in a dense multipath channel. As an example, in [109] the authors use a correlation based receiver under the assumption that the received waveform is a non-distorted replica of the transmitted signal. Applying a maximum likelihood estimation of unwanted parameters, the authors propose a generalized maximum likelihood estimator. In order to simplify the estimation of the parameters required for the ML estimation, a sub-optimal channel estimation technique based on a peak detection process is proposed in [154]. All these methods are based on the sampling of the signal at the Nyquist rate. This implies sampling rates of the order of several GHz which is not feasible for low-cost UWB devices. In [119], different transceiver types including stored reference, energy detection and transmitted reference are compared and several algorithms are exploited in the same framework. The result of this study proves that the stored reference receiver requires high sampling rates, while the energy detection receiver can achieve good results with a lower sampling rate. In [119], an intuitive ML estimator is proposed using integrator outputs. However, one of the main limitations of the ToA estimators based on energy detection presented in the literature is the minimum

integration time that can be implemented which defines the accuracy of the ToA estimation. Since a good integration circuit is characterized by a trade-off between linearity and power consumption, a limitation on the minimum integration time is imposed. In this chapter, the possibility of achieving accurate leading edge estimation independently of the integration length is analyzed. The proposed solutions are intended for analogue receivers with low signal sampling rate capabilities but can be extended to receivers with higher sampling rates and capable of more sophisticated digital signal processing. With the assumption that the distribution of the channel impulse response amplitudes is known, averaged maximum likelihood (AML) estimators are derived for different types of channel fading. As will be shown, this solution requires a weighting function that must be implemented in the RF stage. With the scope of a further simplification of the RF stage, a generalized maximum likelihood (GML) estimator is derived. Unlike previously proposed solutions based on energy detection, AML and GML estimators can achieve fine accuracy (i.e. the finest temporal granularity) even though they are based on relatively long integration windows. Because of the optimal estimators needed to identify LOS/NLOS, a simple but efficient identification test is proposed based on energy detection required by the ToA estimator. This capability to recognize LOS and NLOS conditions is also important in order to assess the confidence of the ToA estimation.

This chapter is organized as follow: in Section 5.2, the signal model used for leading edge estimation is presented; in Section 5.3, a brief review of commonly used leading edge estimators such as threshold crossing and maximum selection is given. In Section 5.4, the AML and GML estimators are presented. In Section 5.5, a channel state identification procedure based on energy detection is presented. In Section 5.6, the performance of the proposed algorithms is presented and compared.

5.2 Signal model for ToA

We use a signal model in which the transmitted signal for ToA estimation can be represented by a train of pulses as follows

$$s(t) = \sum_{j=1}^{N_p} \sqrt{\frac{E_p}{T_p}} p(t - jT_f), \quad (157)$$

where E_p is the energy per pulse, T_f is the pulse repetition period, and N_p is the number of pulses (frames) used for the estimation. The term $p(t)$ is a bandpass pulse with

duration T_p , center frequency f_c , and with $1/T_p \int_0^{T_p} p^2(t)dt = 1$. The term T_f is large enough in order to avoid inter-pulse interference. No multiuser interference is taken into consideration. The received signal containing the train of pulses assigned for ToA estimation occurs within a window of duration T_u that represents the uncertainty on the arrival time of the received signal (Fig. 41). This time window is identified by an earlier coarse synchronization process (e.g. [29]).

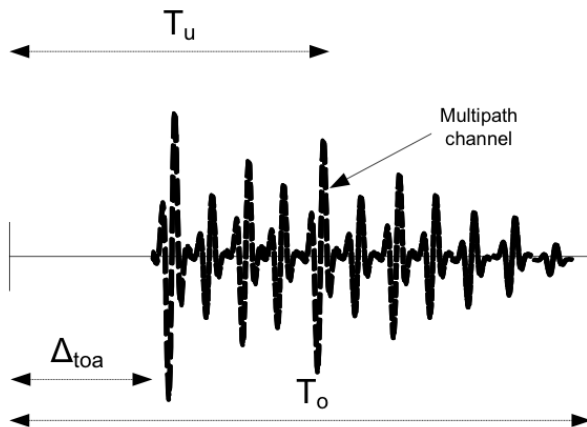


Fig. 41. ToA signal model.

The received signal can then be represented as follows

$$r(t) = w(t - \Delta_{\text{toa}}) + n(t), \quad (158)$$

where $n(t)$ represents a white Gaussian process with two-sided power spectral density $N_0/2$ and $\Delta_{\text{toa}} \triangleq \delta_{\text{toa}}T_p + \delta_p$ with δ_{toa} assuming integer values in the interval $[0, T_u/T_p - 1]$ with equal probability and δ_p uniformly distributed over the interval $[0, T_p)$. The value Δ_{toa} represents the delay of the received signal with respect to a temporal reference point. The term $w(t)$ is the convolution between the transmitted signal $s(t)$ and the channel impulse response $h(t)$ which is expressed as

$$h(t) = \sum_{i=0}^{L-1} \mathbf{p}_i h_i \delta(t - \tau_i), \quad (159)$$

where $\mathbf{p}_i = e^{-j\phi_i}$, h_i , and τ_i are phase, amplitude magnitude, and delay of the i th path, respectively. We consider a resolvable dense multipath channel, i.e., $|\tau_i - \tau_j| \geq T_p, \forall i \neq j$

j , where $\tau_i = \tau_1 + (i-1)T_p$, and $\{h_i\}_{i=1}^L$ are assumed to be statistically independent r.v.s. The value $T_d = \max\{\tau_i\}$ is the maximum excess delay of the channel and L is the number of paths composing the channel impulse response. Note that we implicitly assume that $W = 1/T_p$. The term $n(t)$ is a two-sided white Gaussian process with variance $N_0/2$. Let us consider that the received signal is filtered by a bandpass zonal filter of bandwidth W centered on f_c to limit the noise power. The filtered noise signal $\tilde{n}(t)$ is then characterized by the bandwidth W . The bandwidth of the filter is assumed to be large enough so that $w(t)$ is undistorted.

5.3 Threshold crossing and maximum selection algorithm

The Cramer-Rao bound of the arrival time estimate is defined as

$$\text{CRLB} = \frac{1}{2\beta^2 E_p / N_0}, \quad (160)$$

where β^2 is the second order moment of the spectrum $P(f)$ of a generic waveform $p(t)$ defined by

$$\beta^2 = \frac{\int_{-\infty}^{\infty} f^2 |P(f)|^2 df}{E_p}. \quad (161)$$

We can notice that the bound is inversely proportional to the signal energy, where the proportionality constant β^2 increases with the increase of the signal bandwidth. In the time domain, a larger bandwidth means that the energy is concentrated in a smaller time window allowing the reduction of the sampling/integration time and an increase of the accuracy of the estimation. However, when we pass from the theory to the implementation, several issues arise for very large bandwidth signals, specifically the very high sampling rate or very short integration time required. Low complexity leading edge estimation algorithms such as threshold crossing (TC) and maximum selection techniques (MAX) must also deal with implementation constraints which limit the time granularity of the observation of the received signal. For these algorithms, the uncertainty region is subdivided into M smaller windows of duration T_{small} and the above algorithms are applied using the signal energy values captured in each window. Considering the discrete signal model defined in the previous section, we can represent the TC algorithm as

$$\tilde{\delta}_{\text{toa}} = T_u / T_{\text{small}} \min\{n | x_n > \xi\}, \quad (162)$$

where $x_n = \int_n^{(n+1)T_{\text{small}}} r^2(t) dt$ and $n \in [0, T_u/T_{\text{small}} - 1]$, and ξ is a threshold which is typically set as a function of the early-detection (false-detection) and miss-detection probabilities. The decision of the MAX selection algorithm can be represented as follows:

$$\tilde{\delta}_{\text{toa}} = T_u/T_{\text{small}} \arg \max_n \{x_n\}. \quad (163)$$

When the TC algorithm is used, the first arrival path can be affected by a strong attenuation (low magnitude of the leading edge is possible also in LOS conditions) leading to late detection or miss-detection.³¹ This can be avoided by lowering the threshold; however, this leads to early detection (false alarm). Improved TC techniques base the threshold setting on the maximum integrated values in order to reduce the probability of incorrect detection. We can then expect an increase in the early leading edge estimations due to false alarm. The MAX algorithm tends to be affected by an increased number of late leading edge estimations due to the reduced power of the first path and due to the presence of stronger path components following the first. For a low complexity receiver, algorithms based on improved TC and MAX techniques have been proposed. For instance the *search back* algorithm makes use of both techniques by first finding a lock spot associated with the maximum integrated energy value and then performing a search back to locate the leading edge by using TC. Several studies have focused on the optimal/adaptive setting of the threshold in order to reduce estimation errors. However, all these efforts are limited by the integration (sampling) interval. Utilising a very short integration time requires an increase in complexity and power consumption.

5.4 Averaged maximum-likelihood (AML) and generalized maximum-likelihood (GML) estimators

If we consider an observation period T_o around the signal leading edge position for a single received pulse, the statistics of the observed signal conditioned on the multipath channel components $\{\{h_l\}, \{p_l\}\}$ and on the delay δ_{toa} can be represented as

$$P(r(t)|\{h_l\}, \{p_l\}, \Delta_{\text{toa}}) = \frac{1}{(\sqrt{2\pi N_0})^n} \exp \left\{ -\frac{\int_0^{T_o} [r(t) - w(t)]^2 dt}{N_0} \right\}, \quad (164)$$

³¹Especially in indoor environments the LOS might be partially blocked. As a result the first path (the one related to the LOS) is present but it might arrived with a magnitude lower than delayed multipath component caused by reflection of the transmitted waveform.

where n are the number of independent noise components for a bandwidth W and an observation time T_o . In order to simplify the derivation of the estimation algorithms, we consider a discrete representation of the received signal based on statistically independent signal samples which can be considered as the samples taken at rate $1/T_p$ of the correlator output which is matched to the shape $p(t)$. The probability function stripped of the unnecessary elements can be rewritten as

$$P(r(t)|\{h_l\}, \{p_l\}, \delta_{toa}) = \prod_{n=0}^{T_o/T_p-1} \exp \left\{ -\frac{[\mathbf{r}_n - \mathbf{w}_{n-\delta_{toa}} E_p]^2}{N_0} \right\}, \quad (165)$$

where \mathbf{r}_n are the samples of the correlator output and \mathbf{w}_n is the noise-free part of them. Depending on δ_{toa} , the sample of the correlator output \mathbf{r}_n is only noise if $n < \delta_{toa}$ and is signal plus noise if $n \geq \delta_{toa}$. Note that in order to simplify the model, we consider the receiver synchronized at the pulse level. This determines that $\mathbf{w}_i = h_i \mathbf{p}_i$. The leading edge estimation can be treated as a signal parameter estimation problem. This type of problem can be solved by using a maximum likelihood (ML) approach. Independent of the complexity of the receiver, accurate channel state information is typically not available at the ToA estimation stage. The terms $\bar{\mathbf{w}}$ are then unknown.

If we know the statistics of $\bar{\mathbf{w}} = [\mathbf{w}_0, \dots, \mathbf{w}_L]$, the problem can then be classified as a composite hypothesis problem. The r.v.s which produce the vector $\bar{\mathbf{w}}$ are defined as nuisance parameters that affect the decision related to the wanted parameter.

5.4.1 Averaged maximum-likelihood estimators (AML)

In order to perform the estimation, two solutions can be considered. The first is to maximize the likelihood function among different realizations of the vector $\bar{\mathbf{w}}$. This method is impractical for a large number of nuisance parameters. The second method is based on the knowledge of the nuisance parameter's distributions which can be used to average the likelihood function and solve the dependency. Often, the statistical characteristics of the fast fading are known for different conditions (indoor or outdoor). We will proceed to derive the averaged maximum likelihood (AML) estimator for different channel models. Note that the AML offers the optimal estimation in the presence of nuisance parameters [155, 156].

Extending the two hypotheses case considered in [157] to a T_u/T_p hypotheses case,

the averaged log-likelihood function for the j th hypothesis can be written as

$$\Lambda(j) = \log \left\{ \prod_{n=0}^{T_o/T_p-1} \int_{-\infty}^{\infty} \exp \left\{ -\frac{|\mathbf{r}_n - \mathbf{w}_{n-j}|^2}{N_0} \right\} P(\mathbf{w}_{n-j}) d\mathbf{w}_{n-j} \right\}. \quad (166)$$

Since all the possible leading edge positions must be considered in the observation window, we can say that T_o cannot be smaller than T_u . With the discrete model which has been used, the estimation of the leading edge position can be expressed as

$$\tilde{\delta}_{\text{toa}} = T_p \cdot \arg \max_{j \in \{0, T_u/T_p-1\}} \Lambda(j). \quad (167)$$

In the following analysis we first consider a complex Gaussian channel fading and then we extend the analysis considering log-normal and Nakagami fading with $\mathbf{p}_i = +1$ or -1 with equal probability (the derivations of the estimators are given in Appendix 7). The justification for considering these 3 types of fading is that the first model has been widely used for NB and WB systems and leads to a very simple estimator,³² the other two have been widely used to describe UWB channel models. When we consider the distribution of the channel impulse response $h(t)$ as complex Gaussian (Rayleigh fading with uniform phase), the real and imaginary parts of each multipath component are i.i.d. and Gaussian distributed with zero mean and normalized variance σ_i^2 such that $2 \sum_{i=0}^{L-1} \sigma_i^2 = 1$. With an exponential decay of the PDP, the variance values are such that $\sigma_i^2 = \mathbb{E} \{ |\mathbf{h}_0|^2 \} \exp(-\varepsilon i)$. The PDF of the real (imaginary) component can be expressed as

$$P(w_{1,i}) = \frac{1}{\sqrt{2\pi E_p \sigma_i^2}} e^{-\frac{w_{1,i}^2}{2E_p \sigma_i^2}}. \quad (168)$$

For the complex Gaussian fading, the averaged log-likelihood function is

$$\Lambda^G(j) = \sum_{n=j}^{T_o/T_p-1} \frac{2|\mathbf{r}_n|^2 E_p \sigma_{n-j}^2}{(1 + 2E_p \sigma_{n-j}^2)} - \log(\sqrt{1 + 2E_p \sigma_{n-j}^2}). \quad (169)$$

As shown in Fig. 42, the implementation of this estimator can be easily extended to the continuous time domain. This estimator turns out to be an energy detection receiver where the squared signal before integration is weighted by a function of the PDP and the integration result is shifted by a log function which is also dependent on the PDP.

³²Note that complex Gaussian fading has also been proposed to model the multipath fading of UWB channel [158].

Also note that in Fig. 42, there is no correlator at the receiver; however, we consider a BPF followed by a simple squaring block. Note that in the figure, the functions $c_G(n)$ and $l_G(n)$ are represented, respectively, by

$$c_G(n) = \frac{2E_p}{1 + 2E_p\sigma_n^2}, \quad (170)$$

and

$$l_G(n) = -\frac{1}{2} \log \left(\frac{1}{1 + 2E_p\sigma_n^2} \right). \quad (171)$$

An estimate of the received SNR is also required by this estimator. The observation time T_o corresponds to the integration time T_i .

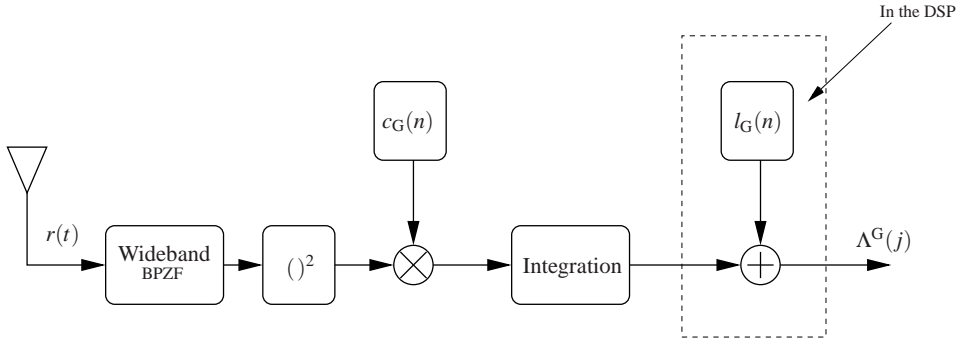


Fig. 42. Scheme of the AML estimator for complex Gaussian fading.

The estimators which are derived hereafter are difficult to implement using analogue techniques; however, they can be used as a reference in order to evaluate the performance of sub-optimal estimators in realistic UWB channel conditions. In the case of log-normal fading and $\mathbf{p}_i = 1$ or -1 with equal probability $\frac{1}{2}$, the PDF of h_i can be written as

$$P(h_i) = \frac{20}{\ln 10 \sqrt{2\pi\sigma_L^2} h_i} \exp \left\{ -\frac{(20 \log h_i - \mu_i)^2}{2\sigma_L^2} \right\}, \quad (172)$$

where $\mu_i = 10 \ln E_p \Omega_0 - \frac{10i\epsilon T_p}{\ln 10} - \frac{\sigma_L^2 \ln 10}{20}$ and $\Omega_0 = \mathbb{E}\{|h_0|^2\}$ is chosen in such a way that $\sum_{i=1}^L \Omega_0 \exp(-i\epsilon T_p) = 1$. The integration over the log-normal distribution, which is required to eliminate the dependency on the nuisance parameters, cannot be solved in

closed form. However, as shown in Appendix 7, the integral involved in the derivation of the estimator can be approximated using the Hermite-Gauss integral leading to the following average log-likelihood function

$$\Lambda^L(j) \approx \sum_{n=j}^{T_o/T_p-1} \log \left\{ \sum_{k=1}^N \frac{c_k}{\sqrt{\pi}} \exp(-10 \frac{\mu_n}{10} 10 \frac{\sigma_{Lz_k}}{10}) \cosh(10 \frac{\mu_n}{20} 10 \frac{\sigma_{Lz_k}}{20} r_n) \right\}. \quad (173)$$

The higher the value of N , the better the approximation given by the Hermite-Gauss integral. The performance of the estimator for different values of N is shown in Fig. 46. For the Nakagami fading, the PDF of the fading amplitude is expressed as

$$P(h_i) = \frac{2}{\Gamma(m)} \left(\frac{m}{\Omega_i} \right)^m h_i^{2m-1} \exp\left(-m \frac{h_i^2}{\Omega_i}\right), \quad (174)$$

where $\Gamma(\cdot)$ is the Gamma function, m is the fading parameter and Ω_i represent the average power of the i th multipath component $\Omega_i = E_p \Omega_0 \exp(-\varepsilon i T_p)$ with $\sum_{i=0}^{L-1} \Omega_0 \exp(-\varepsilon i T_p) = 1$. As shown in Appendix 7, the average over the Nakagami fading results in the following average log-likelihood function

$$\Lambda^N(j) = \sum_{n=j}^{T_o/T_p-1} \log \left\{ m^m (m + \Omega_{n-j})^{-m} {}_1F_1 \left(m; \frac{1}{2}; \frac{\Omega_{n-j} r_n^2}{(m + \Omega_{n-j})} \right) \right\}. \quad (175)$$

It can be noticed that for the case of log-normal and Nakagami fading, the estimators have a much higher complexity and they are not suitable for analogue receiver implementation. We remark here that these estimators are optimal under the assumption that the arrival time of the resolvable multipath components match perfectly with the timing of the weighting function of the estimators. Whilst this is an idealistic assumption, they provide a theoretical foundation to the intuitive idea of weighting the incoming signal according to the the PDP and they serve as a reference for evaluating the performance of sub-optimal solutions.

5.4.2 Suboptimal AML estimators

The complexity of the optimal estimator in the presence of log-normal fading depends on the value of N . As shown in the last section of this chapter, the performance degradation is very small even if N is small. We can consider the case of $N = 1$ which leads

to the estimator expressed by

$$\Lambda^L(j) = \sum_{n=j}^{T_o/T_p-1} -\left(10^{\frac{\mu_{n-j}}{10}}\right) + \log \left\{ \cosh \left(10^{\frac{\mu_{n-j}}{20}} r_n\right) \right\}. \quad (176)$$

A further simplification of the estimator proposed for the log-normal fading can be achieved considering that $\cosh(x) \approx \exp(|x|)/2$ leading to

$$\Lambda^L(\delta_i) = \sum_{n=j}^{T_oW-1} -10^{\frac{\mu_{n-j}}{10}} + 10^{\frac{\mu_{n-j}}{20}} |r_n| - \log(2). \quad (177)$$

The optimal estimator derived for Nakagami fading looks to be the most complex because of the presence of the hypergeometric function. If the fading parameter m is an integer, the hypergeometric function can be alternatively expressed with a finite series. For example for $m = 2$, equation (244) can be written as³³

$$\Lambda_n^N(i) = \log \left\{ \frac{2}{\Omega_i^3 \left(\frac{2+\Omega_i}{\Omega_i}\right)^{7/2}} \left(2\Omega_i \sqrt{\frac{2+\Omega_i}{\Omega_i}} r_n^2 \left(1 + e^{\frac{\Omega_i r_n^2}{2+\Omega_i}} \sqrt{\pi} \operatorname{erf} \left(\sqrt{\frac{\Omega_i r_n^2}{2+\Omega_i}} \right) \sqrt{\frac{\Omega_i r_n^2}{2+\Omega_i}} \right) \right. \right. \\ \left. \left. + \Omega_i \left(\frac{2+\Omega_i}{\Omega_i} \right)^{3/2} \left(2 + 3e^{\frac{\Omega_i r_n^2}{2+\Omega_i}} \sqrt{\pi} \operatorname{erf} \left(\sqrt{\frac{\Omega_i r_n^2}{2+\Omega_i}} \right) \sqrt{\frac{\Omega_i r_n^2}{2+\Omega_i}} \right) \right) \right\}. \quad (178)$$

We are primarily interested in the estimator derived for complex Gaussian fading since it is simple and offers reasonably good performance both in log-normal and Nakagami fading as shown in Section 5.6.1. We can then address simpler versions of this estimator. The log function which appears in (169) is present since that observation window does not change with the hypothesis and permits a fair comparison of the hypothesis. Moving the observation window according with the hypothesis would result in an estimator without the function $l_G(n)$ since the value of this function results equal for all the hypothesis. As a result, the estimator can be also implemented by a weighted sliding window. Another way to remove the log function without changing the observation window according to the hypothesis (leading edge positions) is to make the observation window sufficiently long so that the integrated signal energy tends to be the same for all the tested hypotheses and then l_G can be dropped. In this case, a simplified version of

³³This alternative expression drastically reduced the simulation time. However both log-likelihood functions expressed in (175) and (178) are based on tabled functions.

the estimator Λ_s^G is achieved. Other implementation issues are related to the knowledge of the channel impulse response and to the ability to shape the function $c_G(n)$ according to the PDP. We consider then an estimator Λ_{flat}^G with $\sigma_n^2 = \sigma^2 \forall n$. This is equivalent to simply considering the condition where only noise is received (before the leading edge) and the condition where signal plus noise are received (after the leading edge position). If no information is available on the PDP, the estimator Λ_s^G reduces to a simple energy detector with sliding window. Moreover, the estimation of the SNR is also required. We then consider the effect of the SNR estimate in the estimators referred to as $\Lambda_{\text{snrest}}^G$ and $\Lambda_{\text{snrest,flat}}^G$, respectively. A summary of the estimators examined is given in Table 1.

Table 1. Suboptimal AML estimators.

Estimator	$c_G(n)$	$l_G(n)$	Notes
Λ^G	$\frac{2E_p}{1+2E_p\sigma_n^2}$	$-\frac{1}{2} \log \left(\frac{1}{1+2E_p\sigma_n^2} \right)$	σ_n^2 based on PDP (known), E_p known
Λ_s^G	$\frac{2E_p}{1+2E_p\sigma_n^2}$	0	σ_n^2 based on PDP (known), E_p known, large T_o
Λ_{flat}^G	$\frac{2E_p}{1+2E_p\sigma^2}$	$-\frac{1}{2} \log \left(\frac{1}{1+2E_p\sigma^2} \right)$	σ^2 equal $\forall n$, E_p known
$\Lambda_{\text{snrest}}^G$	$\frac{2\tilde{E}_p}{1+2\tilde{E}_p\sigma_n^2}$	$-\frac{1}{2} \log \left(\frac{1}{1+2\tilde{E}_p\sigma_n^2} \right)$	σ_n^2 based on PDP (known), \tilde{E}_p estimated
$\Lambda_{\text{snrest,flat}}^G$	$\frac{2\tilde{E}_p}{1+2\tilde{E}_p\sigma^2}$	$-\frac{1}{2} \log \left(\frac{1}{1+2\tilde{E}_p\sigma^2} \right)$	σ^2 equal $\forall n$, \tilde{E}_p estimated

5.4.3 Generalized maximum-likelihood estimator (GML)

In the previous section, the derivation of the AML estimators was based on the knowledge of the multipath fading statistics and of the PDP. In this section the analysis of the leading edge estimation is extended to the case of no knowledge of the received signal fading statistics. In this case, the nuisance parameter $\bar{\mathbf{w}}$ in (166) is considered deterministic.

In order to estimate the leading edge position in the maximum likelihood sense,

we need an estimate of $\bar{\mathbf{w}}$. In order to perform the best possible estimate of δ_{toa} we must look for the $\hat{\bar{\mathbf{w}}}$ that maximizes the likelihood function. In this way we obtain the generalized maximum likelihood (GML). Considering the sampling expansion for the signals, the function for the j th hypothesis of the leading edge position can be expressed as follows

$$\Lambda(j) = \sum_{n=j}^{T_0 W - 1 + j} [2r_{1,n}w_{1,n} - w_{1,n}^2 + 2r_{2,n}w_{2,n} - w_{2,n}^2], \quad (179)$$

where $r_{1,n}$, $w_{1,n}$ are the real parts and $r_{2,n}$, $w_{2,n}$ the imaginary parts of the equivalent low-pass signals of $r(t)$ and $w(t)$ taken at the Nyquist rate in the interval $[0, T_0]$. Note that in this case the observation window moves when the hypothesis changes. The estimate $\bar{\mathbf{w}}$ in the ML sense is obtained by forcing the derivative of the likelihood function to zero. It follows that

$$\frac{d}{d\bar{w}_1 d\bar{w}_2} \Lambda(j) = 0, \quad (180)$$

if $\hat{w}_{1,n} = r_{1,n}$ and $\hat{w}_{2,n} = r_{2,n} \forall n$. Substituting the estimates $\hat{w}_{1,n}$ and $\hat{w}_{2,n}$ in (179), the generalized maximum log-likelihood function can be written in the continuous time domain as

$$\Lambda^{\text{GML}}(\tau) = \int_{\tau}^{\tau+T_i} r(t)^2 dt, \quad (181)$$

where $T_i = T_0$ is the integration time. In the absence of noise (or high SNR conditions), or for a flat channel PDP, the optimal integration time corresponds to the maximum delay spread of the channel T_d ; however, as shown in the Section 5.6, when the noise is present the optimal integration time is smaller or equal to T_d depending on the channel PDP and the E_p/N_0 . Following the maximization of the log-likelihood function, the selection can be written as

$$\hat{\delta}_{\text{toa}} = \arg \max_{\tau \in [0, T_u]} \{\Lambda^{\text{GML}}(\tau)\}. \quad (182)$$

The estimator described by (181) and (182) is implemented by using a sliding window (SW) and the accuracy of the leading edge position estimation depends on the time interval between consecutive integration starting points. In comparison with the MAX selection among integration values of adjacent integration windows, the sliding window approach is less affected by the possibility of having signal peaks that do not coincide with the leading edge position. Note that MAX selection corresponds to a particular case of sliding window with no overlapping windows.

5.4.4 Improved generalized maximum likelihood estimator (IGML)

The SW approach is very easy to implement due to its relative low complexity. However, in order to ensure good estimation accuracy, either a high number of integrators or a large number of pulses are required to cover the uncertainty period. A sub-optimal solution can be based on a trade-off between serial and parallel approaches where M integrations are performed in parallel and the integrations are done in shifted windows $T_u/T_p/M$ times in order to obtain the T_u/T_p observations.³⁴

A different approach is an estimator working with $M < T_u/T_p$ integration outputs and $T_{\text{step}} = T_u/M$ that can achieve an accuracy lower than T_{step} .

To derive this estimator, integration outputs are assumed to be statistically independent. As previously mentioned, this can occur when the integration corresponding to each window is performed over different blocks of pulses. Under this assumption, the joint probability of the integration variables involved in the observed vector \bar{y} conditioned on the leading edge position and on the channel impulse response can be written as follows

$$P(\bar{y}|\bar{h}, \delta_{\text{toa}}) = \prod_{n=1}^M P(y_n|\bar{h}, \delta_{\text{toa}}). \quad (183)$$

The vector \bar{y} is composed of M elements, where y_n is the integrated energy of the n th integration window and can be written for a single received pulse as follows

$$y_n = \sum_{j=0}^{N_p-1} \int_{(n-1)\Delta_s}^{(n-1)\Delta_s+T+jT_t} r^2(t) dt, \quad (184)$$

where $\Delta_s = T_{\text{step}}$. If we condition on \bar{h} , each integrator output is characterized by a Chi-squared distribution. For one single pulse (i.e for one integration window), conditioning on the channel impulse response, the integration results in the summation of $q = 2T/T_p$ statistically independent samples. Considering that for UWB channels the energy is spread over quite a large interval, the distribution of the integration output defined in (184) can be approximated by a Gaussian distribution as follows

$$P(y_n|\bar{h}, \delta_l) = \frac{1}{\sqrt{2\pi\sigma_n^2(\delta_{\text{toa}})}} e^{-\frac{(y_n - \mu_n(\delta_{\text{toa}}))^2}{2\sigma_n^2(\delta_{\text{toa}})}}, \quad (185)$$

³⁴We consider T_p as the smallest time granularity since we consider a discrete signal model.

where $\mu_n(\delta_{\text{toa}}) = qN_p\sigma_0^2 + N_p\xi_n(\delta_{\text{toa}})$, $\sigma_n^2(\delta_{\text{toa}}) = 2qN_p\sigma_0^4 + 4\sigma_0^2N_p\xi_n(\delta_{\text{toa}})$. The term $\xi_n(\delta_{\text{toa}})$ is the signal energy integrated in the n th integration window which depends on the leading edge position δ_{toa} and can be expressed as follows

$$\xi_n(\delta_{\text{toa}}) = \begin{cases} \sum_{i=(n-1)\Delta_s-\delta_i}^{q+(n-1)\Delta_s-\delta_i} E_p h_i^2 & (n-1)\Delta_s \geq \delta_{\text{toa}} \\ \sum_{i=1}^{q-(\delta_i-(n-1)\Delta_s)} E_p h_i^2 & (n-1)\Delta_s < \delta_{\text{toa}} \end{cases}. \quad (186)$$

To eliminate the dependency on the channel impulse response, the PDP is used so that the estimate $\tilde{h}_i^2 = \mathbb{E}\{h_i^2\}$. The noise variance $\tilde{\sigma}_0^2$ can be easily estimated and it will be assumed to be perfectly known. Once the noise variance is known, the estimate of the received signal energy \tilde{E}_p can then be estimated as described in the next section. Using estimated values, the estimator is obtained by maximizing the corresponding log-likelihood function which is

$$\Lambda(j)^{\text{IGML}} = \sum_{n=1}^M - \frac{\left(y_n - \left(qN_p\tilde{\sigma}_0^2 + N_p\tilde{\xi}_n(j) \right) \right)^2}{2qN_p\tilde{\sigma}_0^4 + 2\tilde{\sigma}_0^2\tilde{\xi}_n(j)} - \log(2qN_p\tilde{\sigma}_0^4 + 2\tilde{\sigma}_0^2N_p\tilde{\xi}_n(j)), \quad (187)$$

where the sequence of values $\{\tilde{\xi}_n(j)\}$ are estimates of the received signal energy function of the hypothesis j obtained by considering the PDP of the channel model $\{\tilde{h}_i\}$. This estimator moves some of the complexity from the RF part to the digital processing stage. The implementation of this estimator requires an analogue-to-digital converter with several bits of resolution in order to provide sufficient accuracy.

5.5 Channel model identification

Since some of the proposed leading edge estimators are based on the knowledge of the PDP, we require a procedure to determine which PDP should be used. The assumption here is that two PDPs are available, one for LOS conditions and one for NLOS conditions. Although it will be shown that good performance is achievable with no knowledge of the PDP, information about the channel condition can also be useful for positioning and tracking purposes. Localization and tracking algorithms can improve performance through the use of weights which define the accuracy of the ranging measurements [159–161]. Before proceeding with LOS/NLOS identification, we briefly describe the estimation of the noise variance and of the signal energy for energy detector receivers since they are required for some of the ToA estimators presented in the previous sections. The noise variance can be estimated during a common period with no

transmission by integrating the received signal in a signal-free time window of length T . The estimate is then obtained as follows

$$\tilde{\sigma}_0^2 = \frac{\int_T r^2(t) dt}{2TW}. \quad (188)$$

Considering the estimated noise variance $\tilde{\sigma}_0^2$, an estimation of the total received signal energy can be obtained by integrating the received signal over a reasonably long time interval as follows

$$\tilde{\xi}_p = \sum_{i=1}^{N_s} z_i - \tilde{\sigma}_0^2 N_p W T_1, \quad (189)$$

where z_i is the received signal plus noise energy in the i th time window of duration t_1 within the total integration time T_1 composed of $N_s = T_1/t_1$ consecutive integration windows. In (189) the energy is accumulated over N_p received pulses.

Some examples of LOS/NLOS identification algorithms are presented in the literature [162, 163]. However, they often base the identification on the statistics of ranging measurements. The scheme that we propose benefits from the nature of UWB channels and does not require ranging measurements. In LOS conditions, the channel energy tends to be concentrated in a few nanoseconds starting from the leading edge position. For NLOS conditions, the channel energy tends to be spread over several bursts making the delay spread of the channel longer in comparison with the LOS case. In order to proceed to LOS/NLOS identification, the maximum value among the N_s integrated energy values used in (189) is selected and divided by the total integrated energy giving

$$X_{CM} = \frac{\tilde{\xi}_{\max}}{\tilde{\xi}_p}, \quad (190)$$

where $\tilde{\xi}_{\max} = \max_{i \in \{1, \dots, M\}} \{z_i\} - \tilde{\sigma}_0^2 N_p W t_1$. The value X_{CM} is then compared to a threshold (Th) opportunely set and the decision is taken as follows

$$\begin{aligned} X_{CM} > Th &\rightarrow \text{LOS} \\ X_{CM} < Th &\rightarrow \text{NLOS} \end{aligned} \quad (191)$$

The scheme of the LOS/NLOS identification process is given in Fig. 43.

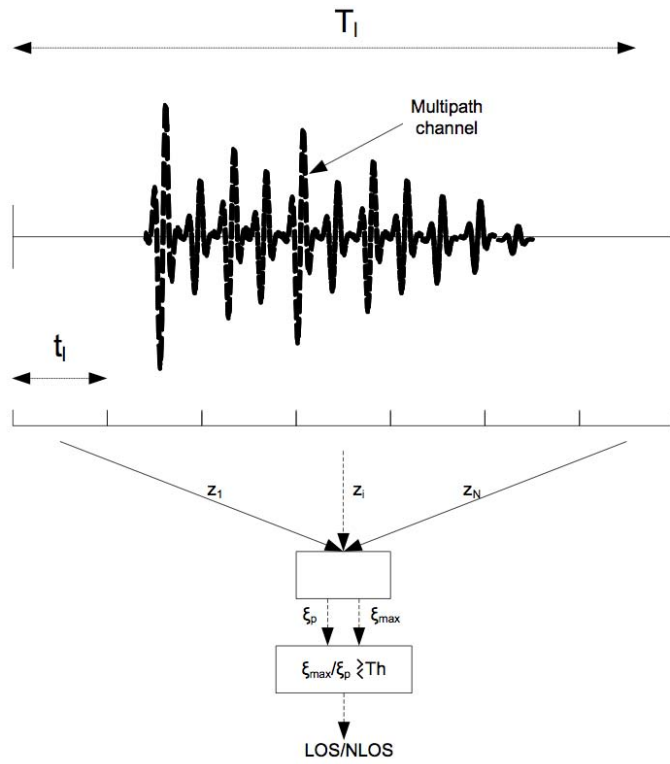


Fig. 43. Scheme of the LOS/NLOS identification process.

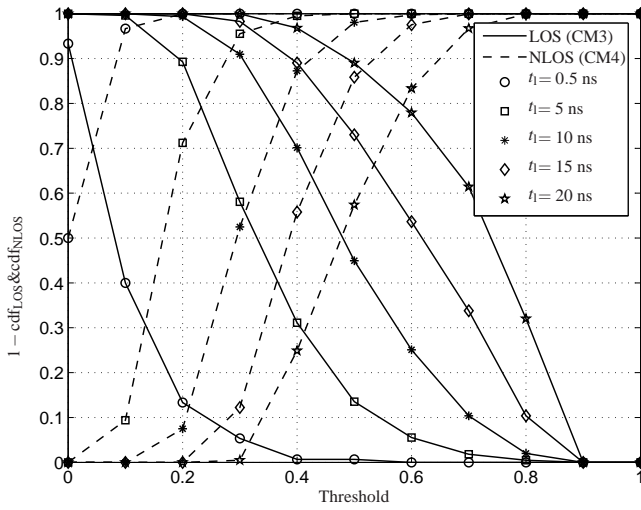


Fig. 44. Probability of correct LOS/NLOS identification for uncertainty-time interval $T_u = 20$ ns, and number of pulses $N_p = 1$.

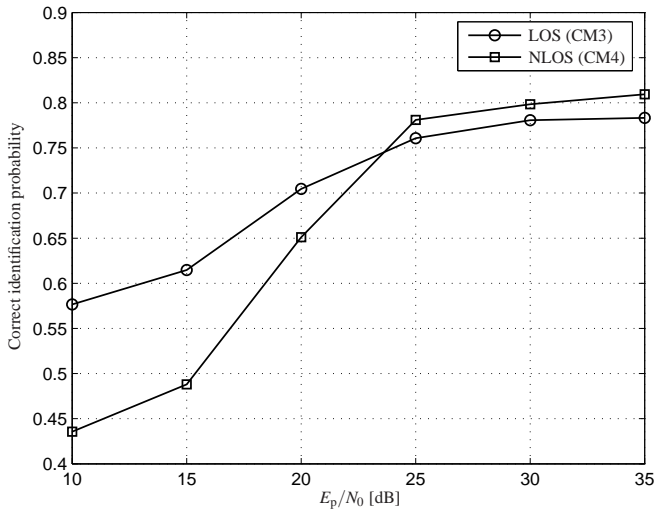


Fig. 45. Probability of correct channel identification for an uncertainty-time interval $T_u = 20$ ns and number of pulses $N_p = 1$.

In order to identify an opportune threshold, the complementary CDF of X_{CM} and the CDF of $1 - X_{\text{CM}}$ for NLOS and LOS channel conditions are respectively plotted in Fig. 44 versus the threshold value for 1000 channel realizations in the absence of noise for different t_1 values and $T_u = 20$ ns. The conditions of LOS and NLOS are, respectively, represented by the standard UWB channel models IEEE 802.15.4a CM3 and CM4. Setting for instance $Th = 0.6$ and considering $t_1 = 20$ ns, the correct detection is achieved for more than 80% of the evaluated cases. In Fig. 45 the performance of the identification of LOS and NLOS condition are plotted versus E_p/N_0 .

If more accurate LOS/NLOS information is required to improve the positioning accuracy, the channel identification procedure can be repeated after the time-of-arrival estimation has been carried out. Since the random offset due to propagation delay between the integration starting point and the starting point of the signal tends to smooth the difference between channel conditions, the knowledge of the starting point of the signal can be performed after the estimation of the leading edge in order to improve the performance of LOS/NLOS identification.

5.6 Simulation results

5.6.1 AML estimators

The simulation results shown consider an UWB signal based on the transmission of pulses with $T_p = 0.5$ ns. Using a tapped delay line channel model, the minimum time granularity is defined by T_p . The uncertainty region is characterized by $T_u = 20$ ns. The performance is evaluated in terms of root-mean-square error (RMSE). First, we show the performance of the AML estimators for simplified channel models. The models have the PDP of the multipath channel in common. The average power of the n th channel path component is given by $\mathbb{E}\{h_n^2\} = \mathbb{E}\{h_0^2\} \exp(-\varepsilon n T_p)$ with decay time constant $\varepsilon = 8.5$ 1/ns. We consider as a reference the log-normal fading defined by the PDF given in (172), which is characterized by $\sigma_L = 4.8/\sqrt{2}$, constant regardless of n and $L = 120$. In this case the performance of the AML estimator is given in Fig. 46 for different approximations of the Hermite-Gauss integral. It can be seen that for different values of N there is no appreciable difference in the estimator performance. Figure 47 shows the comparison between the simplified estimator expressed in (177) and the estimator given by $N = 1$. Degradation of the performance is appreciable for low values of E_p/N_0 . In Fig. 48, the performance of the optimal estimator for log-normal fading is

compared with the performance of the estimator Λ^G defined by (169). Although the estimator Λ^G provides degraded performance for high E_p/N_0 , the degradation is slight and has the benefit of low implementation complexity. Good performance is also provided by the estimator without knowledge of the PDP. In the case of Nakagami fading, the parameter m has been fixed to 2 since the fitting of the log-normal fading with parameters defined above, suggested a value of $m = 1.7 - 1.8$ for all the multipath components. This value has been rounded to 2 in order to obtain a finite series expression of the hypergeometric function. The performances of the optimal estimator defined in (175) and of Λ^G are plotted in Fig. 49. Also in this case, the simplest estimators offer quite good performance.

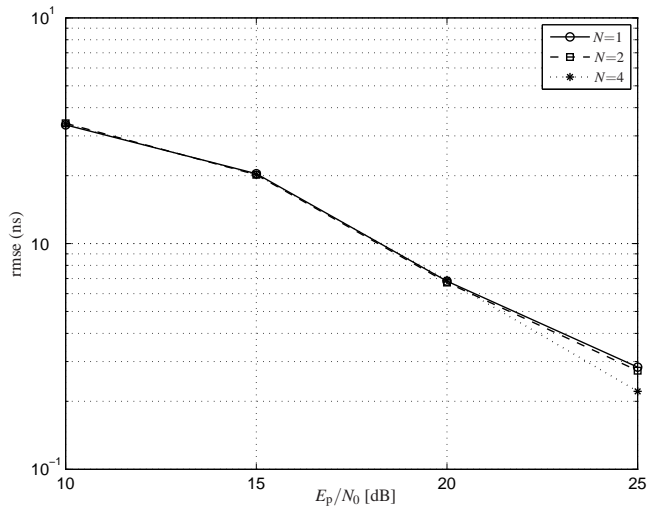


Fig. 46. Leading edge estimation error in log-normal fading. Comparison between different N values in the implementation of the optimal estimator.

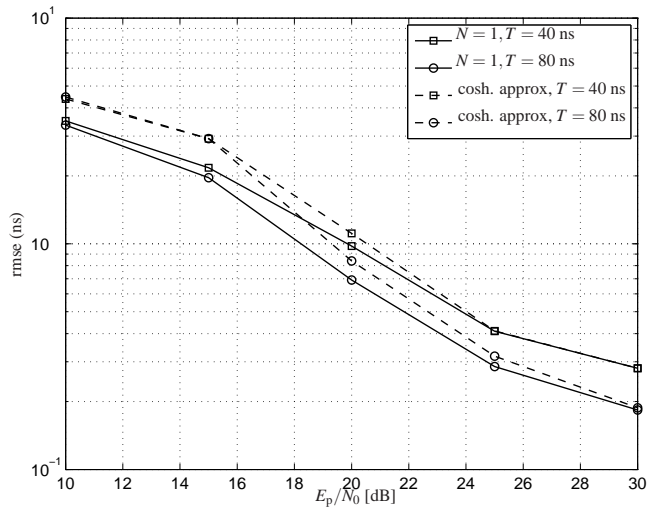


Fig. 47. Leading edge estimation error in log-normal fading. Comparison between optimal and sub-optimal estimators.

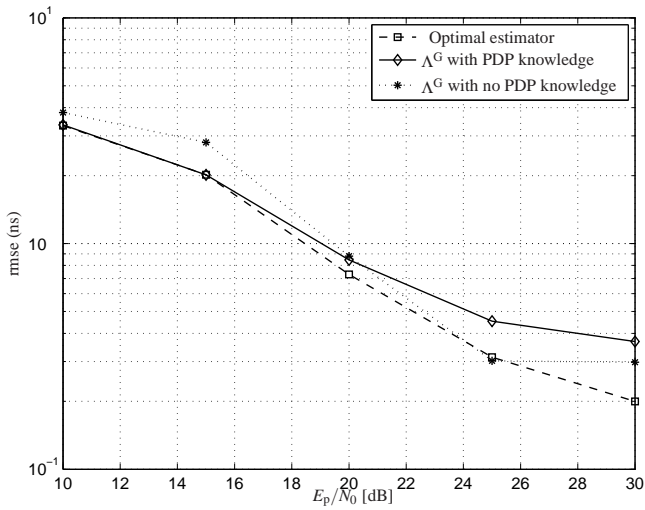


Fig. 48. Leading edge estimation error in log-normal fading. Comparison between optimal estimator and the estimator Λ^G .

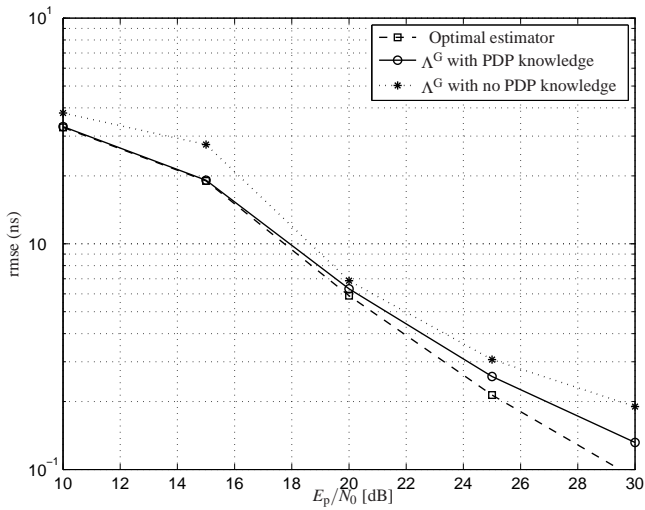


Fig. 49. Leading edge estimation error in Nakagami fading. Comparison between optimal estimator and the estimator Λ^G .

These results suggest that the estimator Λ^G is a good choice since it provides quite good performance in non-Gaussian fading channel (non-optimal conditions). Its implementation is simple and can be easily adopted by low-complexity receivers. In the next section, we evaluate the performance of the estimator Λ^G in the IEEE 802.15.4a channel models.

5.6.2 Simulation results for sub-optimal estimators in 802.15.4a channel models

Before evaluating the proposed sub-optimal ToA estimation algorithms, we briefly introduce another estimator based on energy detection, which has been presented in [119], referred to as (w_2 mess). The (w_2 mess) estimator can be represented as

$$\hat{\delta}_l = \arg \max_{j \in \{1, \dots, M\}} \left\{ \frac{\langle \mathbf{y}_j, \rho_{N_e} \rangle}{\hat{\mu}_j^{no} \cdot \hat{\sigma}_j^{no}} \right\}, \quad (192)$$

where \mathbf{y}_j is the vector of $N_e = T_d/T$ integrated noise plus signal energy values under the hypothesis j , ρ_{N_e} is the result of the integration of the PDP, $\hat{\mu}_j^{no}$ and $\hat{\sigma}_j^{no}$ are, respectively, the mean and the variance of the integration outputs obtained by integrating only noise.

In Fig. 50, the performance of the Λ^G estimator is plotted for CM3. It can be seen that the estimator performance is almost independent of the integration window length. Figure 51 shows the performance of the simplified version of the Λ^G estimator without the log function (Λ_s^G). If a long integration window is available, this simplified version can achieve a level of performance that is very close to that of the Λ^G . In Fig. 52, the performance of the SW estimator is given. The main drawback of this estimator is that the optimal integration window length is highly dependent on E_p/N_0 values. For low E_p/N_0 , a shorter integration window provides better results since the noise is dominant. Figure 53 compares the different Λ^G based estimators proposed in this chapter. It is interesting to note that the signal energy estimation ($\Lambda_{\text{snrest}}^G$) (performed as described in section 5.5) does not affect the performance of the leading edge estimator. Another interesting observation concerns the very good behaviour of the estimator in the case that no channel state information is available (Λ_{flat}^G). This estimator is also robust to SNR estimation errors ($\Lambda_{\text{snrest,flat}}^G$). In Fig. 54(a), the algorithm Λ^G is compared to the w_2 mess algorithm and to TC, MAX and Λ^{GML} (SW) algorithms. The Λ^G and w_2 mess algorithms have similar performance, drastically outperforming the others. The w_2 mess approach with $T_i = 0.5$ ns has performance similar to that of Λ^G . However, the

w_2 mess estimator can achieve smaller time granularity only with very short integration windows. The advantage of this estimator is that it can be widely implemented in the digital domain. Comparing the performance of $\Lambda_{\text{flat}}^{\text{G}}$ and Λ^{GML} , it is worth noting that both have no knowledge of the PDP; however, the $\Lambda_{\text{flat}}^{\text{G}}$ has much better performance. The difference is due to the fact that even with a coarse knowledge of the SNR, the performance of the ToA estimation can improve. In Fig. 54(b), the estimators are compared under NLOS channel conditions using multiple realizations of CM4. It can be seen that for a NLOS channel model, good results can also be achieved. As previously highlighted, the integrations for all the possible leading edge positions typically cannot be performed simultaneously. If M integrators are available, then the T_u/T_p observations can be performed over $T_u/(T_p M)$ different blocks of N_p pulses. In Fig. 55, the effect of the integration over successive blocks of N_p pulses are presented. These results show a small degradation of the performance due to the increased noise energy integrated.

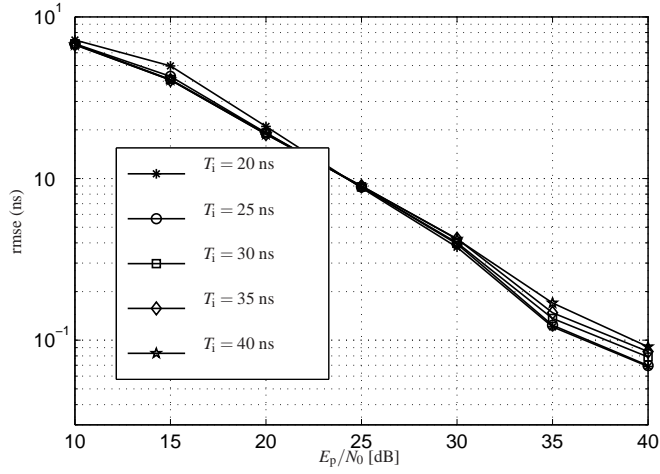


Fig. 50. Performance of the Λ^G ToA estimator considering different integration window lengths in IEEE 802.15.4a CM3 for number of pulses $N_p = 1$ and uncertainty-time interval $T_u = 20$ ns.

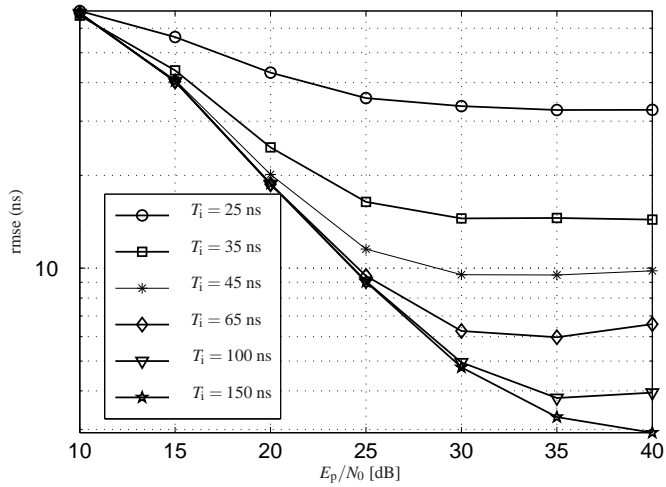


Fig. 51. Performance of the Λ_S^G ToA estimator considering different integration window lengths in IEEE 802.15.4a CM3 for number of pulses $N_p = 1$ and uncertainty interval time $T_u = 20$ ns.

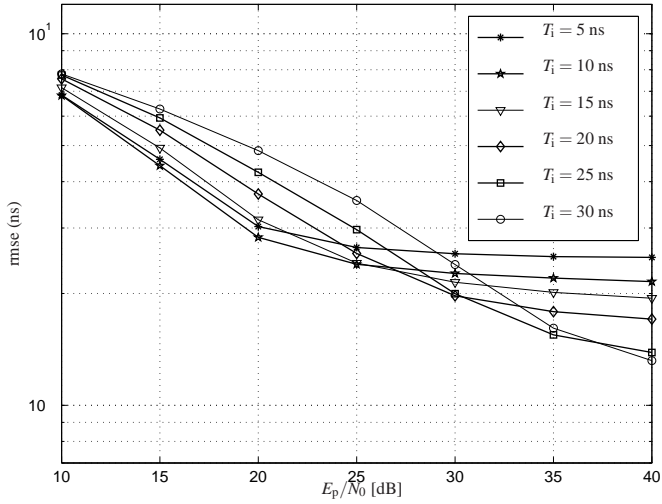


Fig. 52. Performance of the SW ToA estimator considering different integration window lengths in IEEE 802.15.4a CM3 for number of pulses $N_p = 1$ and uncertainty-time interval $T_u = 20$ ns.

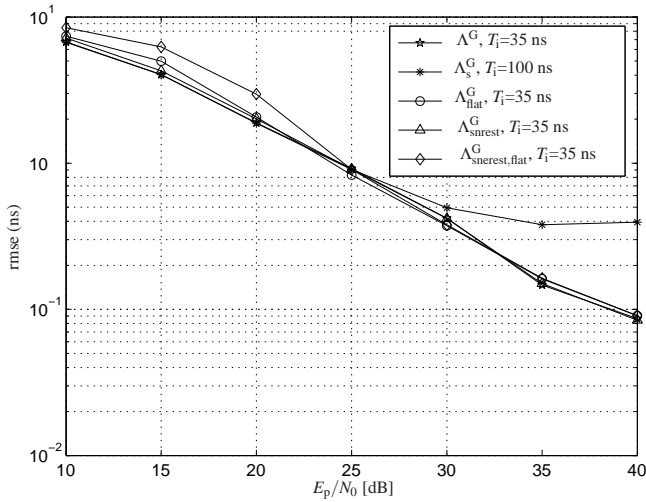
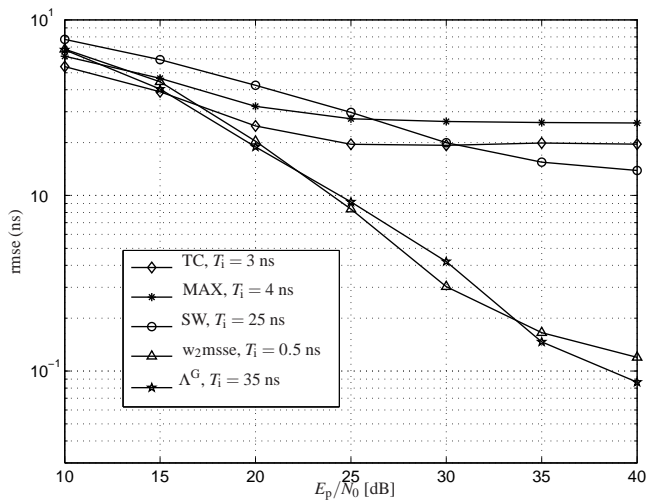
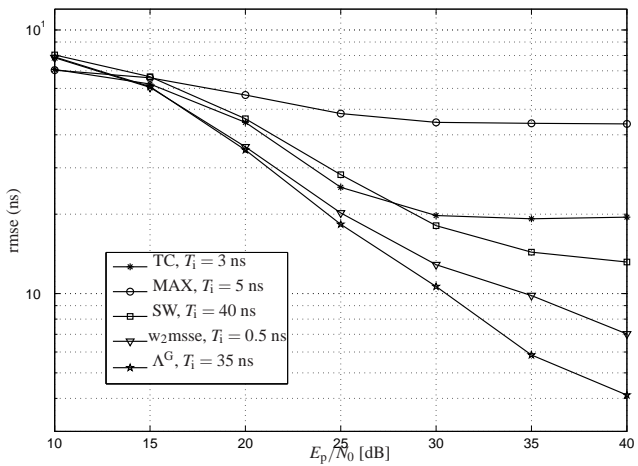


Fig. 53. Comparison of different ToA estimators in IEEE 802.15.4a CM3 for number of pulses $N_p = 1$ and uncertainty-time interval $T_u = 20$ ns.



(a) IEEE 802.15.4a CM3



(b) IEEE 802.15.4a CM4

Fig. 54. Comparison of the performance of several ToA estimators for number of pulses $N_p = 1$, uncertainty-time interval $T_u = 20$ ns. The probability of false alarm for the TC algorithm is set to $P_{fa} = 0.01$.

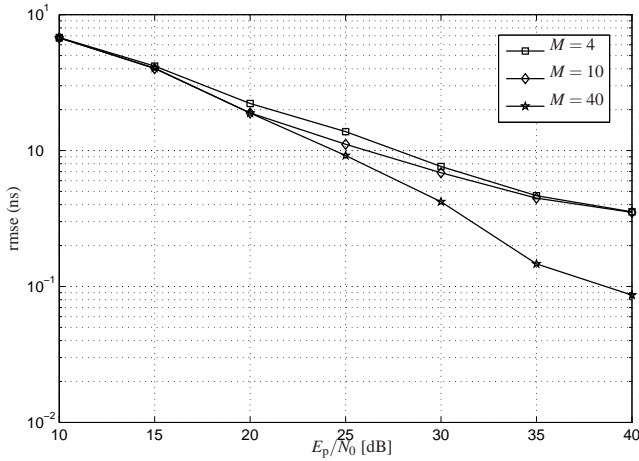


Fig. 55. Performance of the Λ_G estimator considering the observation performed over different blocks of bits for uncertainty-time interval $T_u = 20$ ns.

5.6.3 Simulation results for improved GML estimators

In the previous subsection we presented the performance of the SW estimator in comparison with the AML estimators. In Fig. 56, the performance of the GML receiver is shown. The curves present the performance for different implementations of the estimator depending on the number of available integrators M and the consequent $T_u/(T_p M)$ number of N_p blocks of pulses. For high E_p/N_0 , the accuracy degrades when the number of integrator decreases. This estimator has an optimal integration time that is dependent on the signal-to-noise ratio. Figure 58(a) compares the GML solution with the IGML one. In order to make a fair comparison between the GML and the IGML estimators, we consider that the estimation is done over the same number of pulses. If for $M = 4$ the GML estimator requires 10 pulses to cover the whole uncertainty region, then for the IGML the integration values are accumulated over $N_p = 10$ pulses. The results show that in CM3 the IGML based estimator with only 4 integration values outperforms the GML estimator working with the same or higher number of integrators. In Fig. 57, the performance of the IGML is plotted considering the effect of the received energy estimation. It can be noticed that the effect of a longer accumulation, for instance over

10 pulses, improves the performance for low E_p/N_0 values. A longer accumulation also improves the estimation of the received energy reducing the error contribution due to this estimate. For high values of the E_p/N_0 there is no benefit from accumulation since the error is only due to the difference between the signal impulse response \bar{h} and the PDP used as an approximation, and to the fact that large integration windows do not enable us to distinguish slightly different energetic contributions resulting from different path combinations (even in the case of favorable E_p/N_0). As reported in Fig. 58(b), in a channel model with a longer delay spread (e.g. CM4) the IGML estimator produces only slightly improved performance compared with the GML one. The comparison of the results shown in the previous subsection clearly show that AML based leading edge estimation algorithms outperform the GML based ones. GML based algorithms are penalized by the fact that the signal processing comes after the integration procedure which reduces the amount of information on the received multipath components.

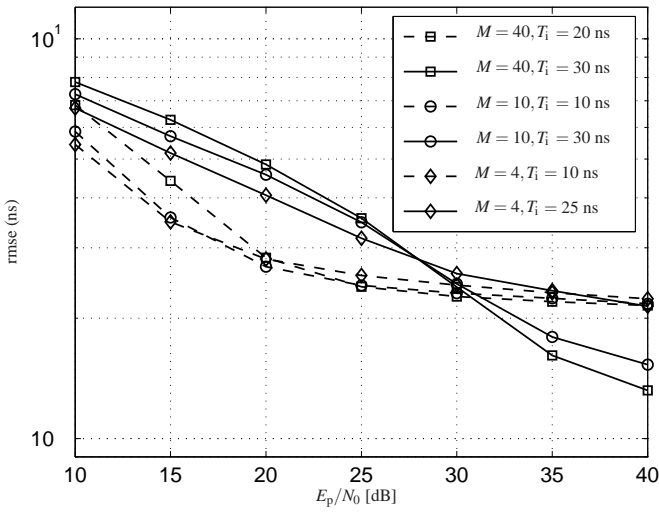


Fig. 56. Performance of the SW ToA estimator for different integration window lengths in IEEE 802.15.4a CM3 for number of pulses $N_p = 1$ and uncertainty-time interval $T_u = 20$ ns.

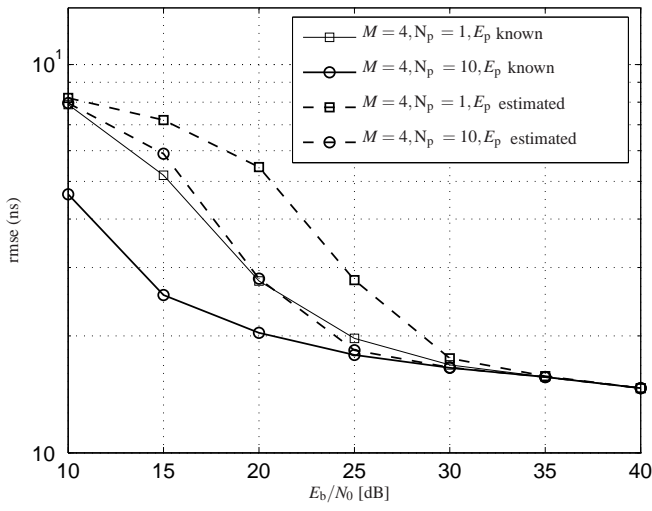
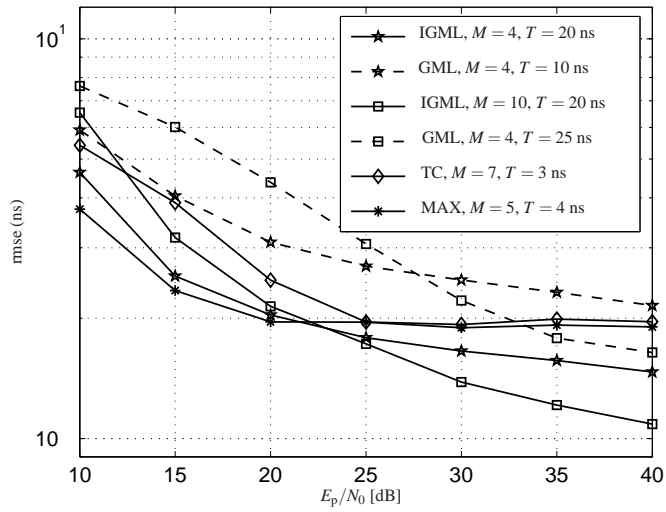
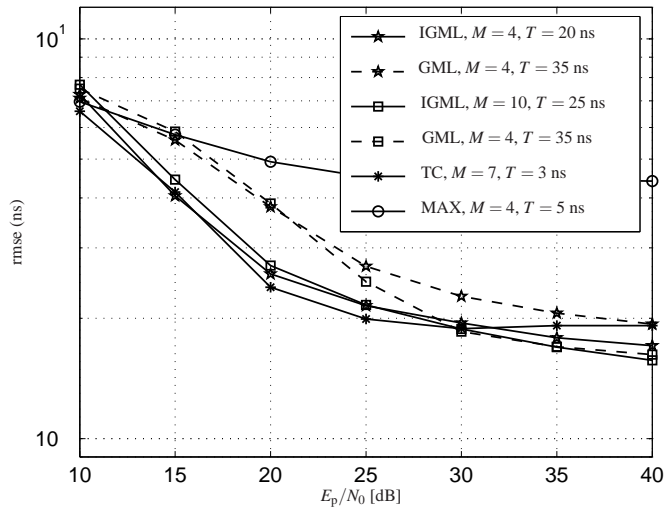


Fig. 57. Performance of the IGML estimator with received signal energy estimation in IEEE 802.15.4a CM3 for an uncertainty-time interval $T_u = 20$ ns.



(a) IEEE 802.15.4a CM3



(b) IEEE 802.15.4a CM4

Fig. 58. Comparison between different ToA estimators for uncertainty-time interval $T_u = 20$ ns. The probability of false alarm for the TC algorithm is set to $P_{fa} = 0.01$.

5.7 Conclusions

In this chapter we focused on low-complexity time-of-arrival estimators for UWB signals which can overcome the non-trivial implementation issues for receiver structures based on correlation and sampling. The investigation focused on performing accurate signal leading edge detection by using low-complexity receivers based on energy detection and was characterized by low sampling rates capability. We derived average maximum likelihood estimators for different types of channel fading. These estimators can be of high complexity and require knowledge of the channel PDP and of the received signal strength. The simplest estimator is the one derived in the case of Rayleigh fading, which can be based on an energy detector and simple analogue signal processing. We then considered sub-optimal implementations of this estimator which can operate with reduced or totally absent channel state information. If the implementation of these estimators is of high complexity, the approach based on the use of sliding window and energy detection can still produce acceptable performance. In addition, we also proposed a simple procedure to identify LOS and NLOS conditions by observing the distribution of the signal energy over the channel impulse response. This information can also be useful for positioning and tracking algorithms.

6 A practical implementation of a low-complexity transceiver for IR-UWB systems

6.1 Introduction

In the previous chapters we focused on low-complexity receiver solutions for UWB systems and developed tools useful to analyze the performance of such receivers. In this chapter we present a UWB sensor network concept which has been developed over the past 4 years at the Centre of Wireless Communication which is based on low-power and low-complexity devices. The system concept is targeted at recreational activities such as cross-country skiing, athletics and running. The devices are worn by the user and positioning and performance information rely on a peer-to-peer connection to fixed nodes. In a more advanced stage of this system concept, devices which are not in the range of fixed nodes will be able to send information using multi-hop techniques via intermediate nodes which act as relays. The communication system is based on IR-UWB. The main system features include the ability to support a large number of low-power devices; low-data-rate communications (up to 10kb/s per sensor); ad-hoc, peer-to-peer network topology; limited fixed infrastructure requirement; and a multi-hop architecture to extend the coverage of the system. The performance requirements of the system include the ability to support a target at a maximum distance of 50 m and mobile users with speed of few tens of km/h. The UWB devices themselves must be very low-power, very low-cost, lightweight, and wearable or embeddable.

6.2 UWB physical layer system model

6.2.1 *Transmitted signal*

The choice of receiver structure is the ED approach. As was underlined in previous chapters, the ED approach offers a good trade-off between complexity and performance. The non-coherent nature of the system does not require the generation of a local waveform and differs from the AcR in that the receiver does not require implementation of delay lines of the order of tens of nanoseconds, which are challenging to implement in

practice. Moreover, the ED demonstrated greater robustness against interference compared to the AcR. As presented in Chapter 3, in order to reduce the effect of noise, the transmitted signal is composed of a train of pulses and can be defined by

$$s(t) = \sum_k \sum_{j=1}^{N_p} \frac{E_b}{N_p T_p} a_j p(t - jT_f - d_k \Delta - kT_s), \quad (193)$$

where T_f is the pulse repetition interval, N_p is the number of pulses per symbol, $\Delta = N_p T_f$ is the modulation shift and $d_k \in 0, 1$ is the modulating data. The sequence $\{a_j\}$ is a pseudo-random amplitude sequence which is used for spectrum smoothing only. The term T_s is the symbol interval and in this case $T_s = 2\Delta$. Considering that $N_p = 30$ and $T_f = 4$ ns, the maximum data rate supported by the system is $R_d = 1/T_s \approx 4$ Mb/s.³⁵ Since the transmission scheme is very simple, the data rate can be easily scaled to increase the range of communication. The transmission of bursts of pulses does not allow the implementation of TH based on a random hopping of the pulses within a single symbol. However, if needed, hopping can be applied at the burst level with several bursts per symbol. In our design, we adopt a simple multiple access technique based on TDMA. Note that the absence of TH at pulse level reduces the spectral smoothing benefit which can be achieved. Consequently, amplitude randomization was adopted in order to reduce spectral lines in the transmitted signal and allow higher transmitted power.

6.2.2 Synchronization and data detection

Data detection is based on the difference of the received signal energy values integrated in the time window designated as bit 0 and as bit 1, respectively, and it can be written as

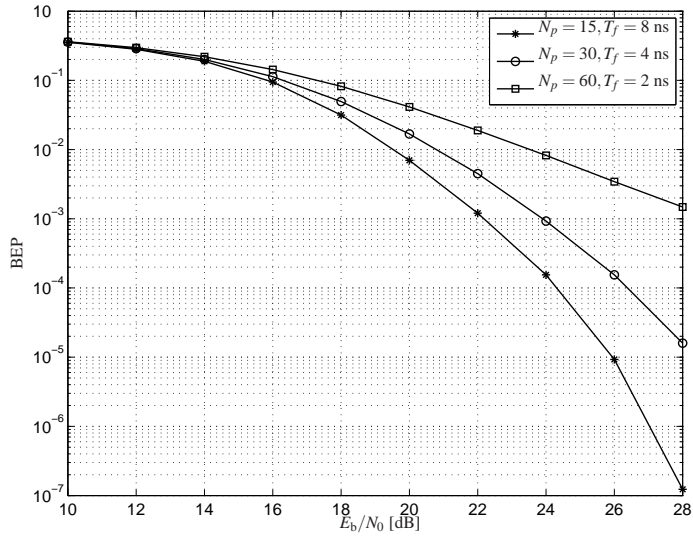
$$Z_{ED} = \int_{\tau_{\text{synch}}}^{\tau_{\text{synch}}+T} r^2(t) dt - \int_{\tau_{\text{synch}}+\Delta}^{\tau_{\text{synch}}+\Delta+T} r^2(t) dt, \quad (194)$$

where $T \leq \Delta$ is the integration time, τ_{synch} is the synchronization time instant and $r(t)$ is the received signal which is given by

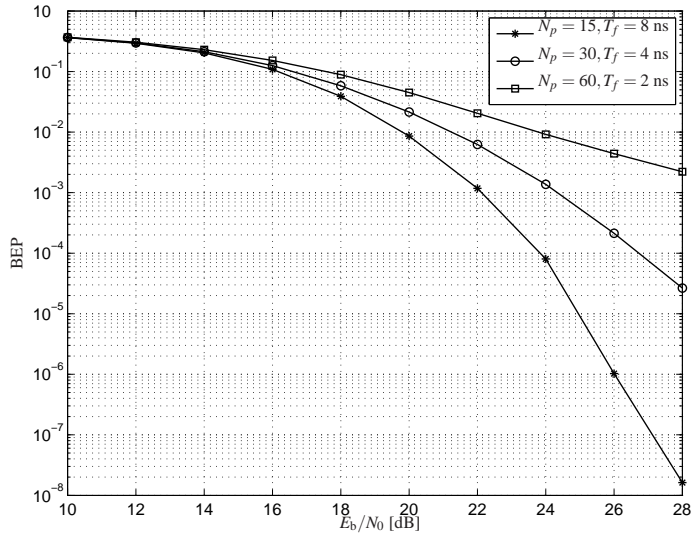
$$r(t) = s(t) * h(t) + n(t). \quad (195)$$

³⁵At present the current ASIC implementations supports $N_p = 60$ and $T_f = 2$ ns; however, the target for the next ASIC generation is to increase the transmitted power of each pulse in order to reduce the number of pulses required.

The term $h(t)$ represents the channel impulse response and $n(t)$ is a two-sided band-limited Gaussian process with auto-correlation function $\frac{N_0}{2}W \text{sinc}(t)$ determined by the BPZF used at the receiver to reduce the noise power. The necessary time information τ_{synch} for data demodulation is provided by a synchronization stage which is used to identify the beginning of the symbol interval and to adjust the integration related timing according to the delay spread of the received signal. As shown in Chapter 3, the positioning of the integration window according to the maximum received energy was shown to be a better choice from the prospective of BEP. More specifically, in our system we consider an integration time $T = N_p T_f$.



(a) IEEE 802.15.4a CM3



(b) IEEE 802.15.4a CM4

Fig. 59. BEP for different N_p values for integration time $T = \Delta = 120$ ns and bandwidth $W = 2$ GHz.

In Fig. 59(a) and Fig. 59(b), the BEP performance in IEEE 802.15.4a channels CM3 and CM4 for different numbers of pulses per symbol are presented. As discussed in Chapter 3, the pulse compression technique offers a considerable gain. However, considering a fixed integration period, it is beneficial to send fewer pulses and increase the time interval between them. The synchronization process is designed to provide the position of the integration window offering the maximum signal energy. The search for the maximum energy is performed by using a sequence of N_b bits which can be either all 0s or all 1s. This is simply a periodic signal with period T_s to which the receiver locks, similar to a classical NB system. The synchronization process is based on the integration of the received signal energy with a sliding window approach in order to find the lock spot. The i th observed variable for the synchronization process can be written as

$$Y_i = \sum_{k=1}^{N_b} \int_{(i-1)*\Delta_{\text{step}}}^{(i-1)*\Delta_{\text{step}}+T} r^2(t - \tau - kT_s) dt, \quad (196)$$

where τ is the delay referring to the time origin of the UWB devices. Note that for data detection purposes, τ might not be the estimated synchronization position since the synchronization is looking for the maximum energy window. Δ_{step} is the time interval which defines the granularity of the synchronization. The synchronization procedure is shown in Fig. 60.

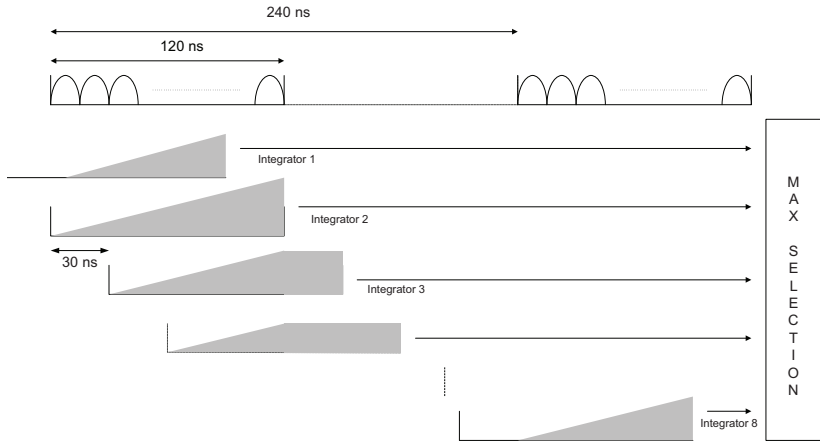
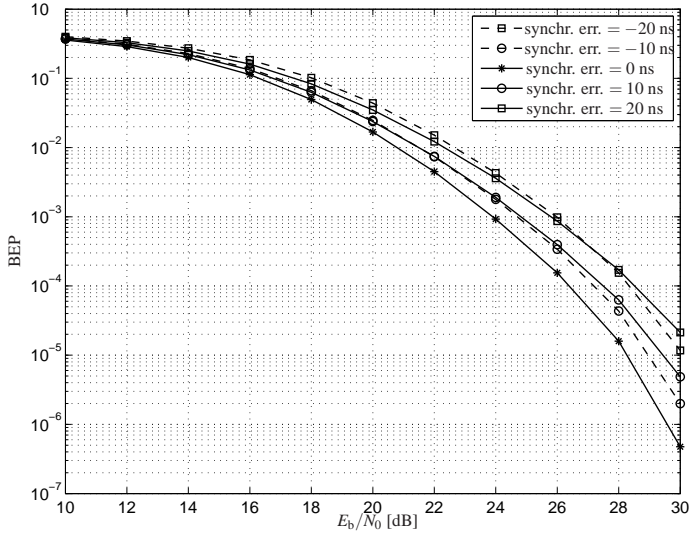


Fig. 60. Synchronization scheme.

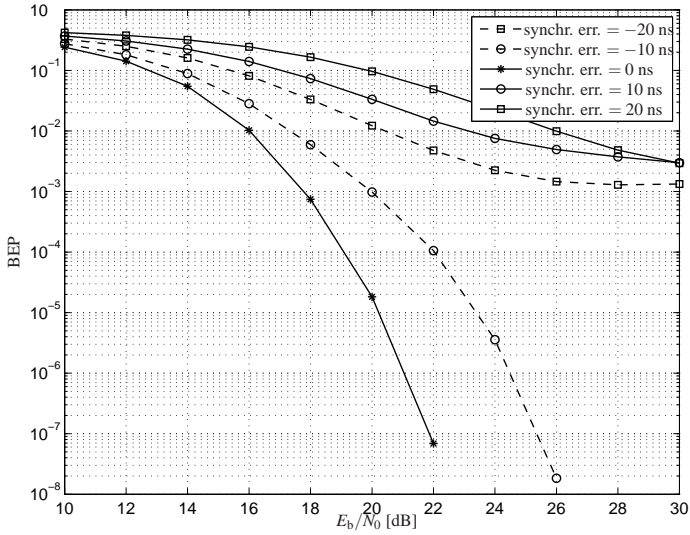
For a relatively low number of integration windows, a coarse synchronization time is given by

$$\tau_{\text{sync}} = \arg \max_{i \in \{1, \dots, M\}} Y_i, \quad (197)$$

where $M = T_s / \Delta_{\text{step}}$ is the number of observations used in the synchronization process. Once coarse synchronization is achieved, finer timing can be achieved by a refined search around the lock spot. In Fig. 61(a), the BEP is plotted considering different values of synchronization error using the pulse compression technique. If we compare Fig. 61(a) and Fig. 61(b) where we consider the case of $N_p = 1$, we can note that the pulse compression technique offers significant robustness to synchronization errors and allows synchronization on only a coarse level. For the single pulse case with an integration time of 30 ns, even if the integrated noise energy is much lower, a small error on the synchronization can drastically reduce the integrated signal energy leading to significant performance degradation. In this case the synchronization would require much more accuracy. The robustness to synchronization errors supports greater user mobility and/or allows an increase in the intervals between beacons.



(a) with pulse compression technique, for $T = \Delta = 120$ ns, $N_p = 30$, $T_f = 4$ ns



(b) without pulse compression technique, for $T = 30$ ns, $\Delta = 120$ ns, $N_p = 1$

Fig. 61. Effect of the synchronization error on the BEP in IEEE 802.15.4a CM3 with bandwidth $W = 2$ GHz.

6.2.3 Preamble detection and frame synchronization

As mentioned earlier, the synchronization is performed over a series of bits which are part of the beacon that each fixed node sends at different time intervals. The TDMA multiple access frame structure also supports UWB devices joining the network during a random-access interval. Other than synchronization, the beacon permits the UWB devices to join the network and to access the TDMA scheme controlled by the MAC protocol. The fixed nodes are divided a-priori into fixed node clusters that contain an arbitrary number of devices. The cluster strategy provides sufficient geographical coverage and limits the interference among clusters. The packet structure of a cluster frame is shown in Fig. 62. When an UWB device first joins the network, the sequence of bits used for synchronization is also used to perform beacon detection. The test used for beacon detection is based on the identification of the periodicity of the synchronization sequence. More specifically, the preamble detection procedure is run in parallel with the synchronization process by checking which integrator of the M provides the maximum at each period T_s . If the i th integrator consistently provides the maximum, we can consider preamble detection to be achieved.

Once preamble detection is achieved and the synchronization process identifies the integrators to be used for bit detection, a Barker sequence is used to perform frame synchronization. A description of the preamble structure is given in Fig. 63. The procedure to access the network is then completed by the request of a time slot within the super frame structure. This is achieved using the classical slotted ALOHA protocol.

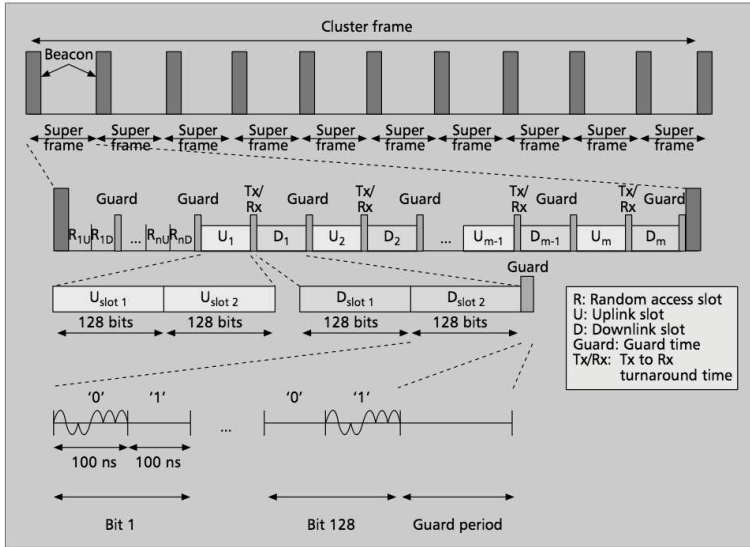


Fig. 62. Structure of the cluster packet.

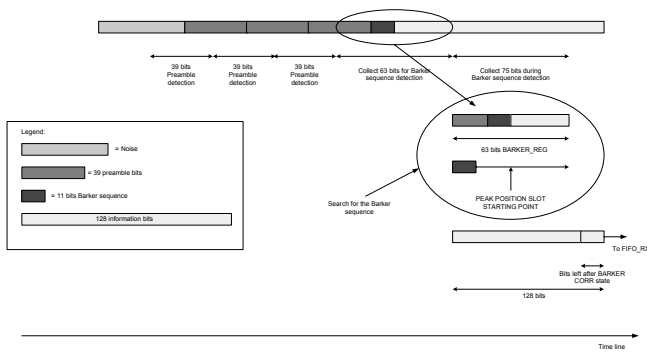


Fig. 63. Preamble detection and synchronization.

6.2.4 Time-of-arrival

As mentioned earlier, the large bandwidth the UWB signal can potentially support very high accuracy of the signal leading edge estimation. However, the receiver requirements to achieve such accuracy are demanding and cannot be considered for low-complexity and low-power solutions. In Chapter 5, we offered a statistical foundation to some low-complexity leading edge estimators. Among the proposed estimators, the technique selected for inclusion in the future design of our UWB transceiver is based on the sliding window approach since it is similar to the synchronization procedure and does not require significant redesign. It is clear that the use of a burst of pulses is not ideal for leading edge estimation since the transmission of consecutive pulses moves the point of maximum energy far from the leading edge point. For time-of-arrival estimation, it is then of interest to design the transmitter to have more powerful pulses and to send them with $T_f \geq T_g + T$, where T is a different integration time from the one used for data detection and is optimized for leading edge estimation purposes.

6.2.5 Link budget

In order to evaluate the parameters of the transceiver, which can ensure robust data communication, in this Section we develop a link budget formulation for the communication system described above. We use here a conventional link budget formula presented in [38]

$$P_{RX}(f) = P_{TX}(f) + G_{RX}(f) + G_{TX}(f) - 20\log_{10}\frac{4\pi c}{f} - 20\log_{10}d \text{ [dB]}, \quad (198)$$

where $P_{RX}(f)$, $P_{TX}(f)$, $G_{RX}(f)$, and $G_{TX}(f)$ are the frequency-dependent transmitted power, the received power, the receiver antenna gain and the transmitter antenna gain respectively. Frequency f is expressed in [Hz], d [m] is the distance between transmitter and receiver antenna and c is the speed of light in m/s. We target an uncoded system data rate of 4.25 Mbps, an implementation loss of 5 dB and a 3.6 dB noise figure for the receiver as acceptable design limits. The average transmitted power is -8.31 dBm. This value is obtained by integrating the transmitted spectral power within the 3.1-4.1 GHz band. The implementation loss takes into account the signal losses due to parasitics and reflections. Both the transmitter and receiver antenna are assumed to have a gain of 0 dBi. The path-losses at 1 (L_1) and 10 (L_2) meters have been calculated with the formulas presented in Table 2. Once the transmitted power and the path loss are known,

the received power $P_{RX}(f)$ can be obtained. Once the signal bandwidth and the noise figure of the receiver are known, the average noise power per bit N_{0bit} and the maximum supported average noise power P_N can be calculated.

Table 2. Link budgets in AWGN and in the IEEE 802.15.4a CM3.

Parameter	AWGN	CM3
Data rate (R_d)	4.25 Mbps	
Averaged TX power ($P_{TX}(f)$)	-8.31 dBm	
TX antenna gain ($G_{TX}(f)$)	0 dBi	
Central frequency (f_c)	3.6 GHz	
Path loss @ 1 m: $L_1 = 20\log_{10}(4\pi f_c)$	43.56 dB	
Path loss @ 10 m: $L_2 = 20\log_{10}d^{36}$	20 dB	
RX antenna gain $G_{RX}(f)$	0 dBi	
RX power (P_{RX})	-71.87 dBm	
Average noise power per bit: $N_{0bit} = -174 + 10\log_{10}(W)$	-84 dBm	
RX noise figure (NF)	3.6 dB	
Average noise power ($P_N = N_{0bit} + NF$)	-80.4 dBm	
Minimum E_b/N_0 (for $BEP = 10^{-3}$)	17 dB	24 dB
Implementation loss	5 dB	
Link margin	9.5 dB	2.5 dB
Minimum RX sensitivity level: $NF + N_{0bit} + E_b/N_0 - W/R_d$	-86.5 dBm	-79.5 dBm

For BPPM modulation, when $R_d = 4.25$ Mbps, $W = 1$ GHz, integration time $T = 120$ ns and the target BER is 10^{-3} , the receiver should operate with an E_b/N_0 of 17 dB. The minimum sensitivity level of the receiver provides the minimum signal level that can be detected at the receiver input. From the values obtained by the link budget calculation presented in Table 2, the LNA should be able to amplify a signal in the range of few μV in a 50Ω system.

6.3 Transceiver design and power consumption

Since oscillators and circuits for up-conversion and down-conversion are not needed and because of the simple signaling structure and detection procedure, the system described above supports the objective of very low power consumption. The design of the UWB transceiver is based on the use of a $0.35\ \mu\text{m}$ BiCMOS process. In Fig. 64, the transceiver block scheme is presented and the complete design of this transceiver can be found in [164].

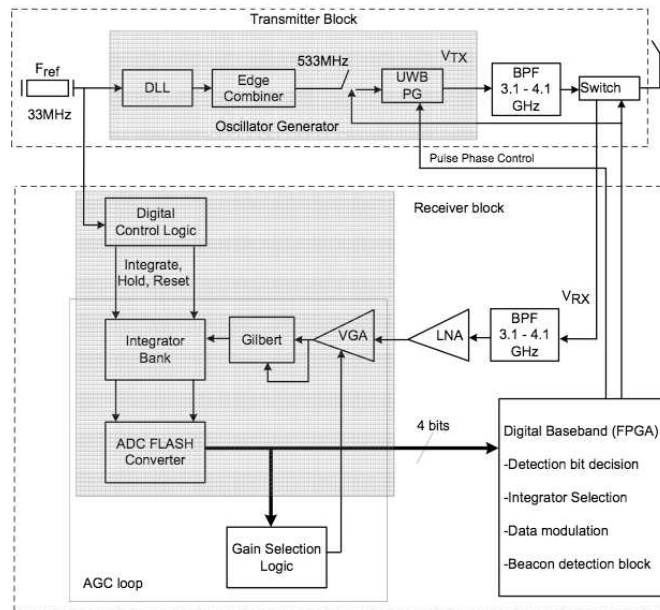


Fig. 64. Transceiver block scheme.

6.3.1 Transmitter

The input of the transmitter block is a low frequency 33 MHz signal which is multiplied by the multiplication stage to achieve a high frequency signal of 533 MHz required to trigger the pulse generator. Such a high frequency signal is needed in order to produce the burst of pulses used for the pulse compression technique. The output of the pulse generator is a Gaussian monocycle 340 ns long with a -10dB bandwidth of 4.7 GHz.

The design of the multiplication section is based on a frequency synthesizer and contains a delay locked loop (DLL) and a digital edge combiner. The DLL and digital edge combiner simplifies the frequency synthesizer's design due to the stability of the DLL, low generated noise, low die area and low-power consumption. The transmitter is implemented in standard CMOS technology. Operating continuously with 533 MHz pulse repetition frequency, the pulse transmitter achieves 20.48 mW to 35 mW total power consumption with a supply voltage of 3.3 V. With the transmitter operating at lower duty cycles, the power consumption will decrease accordingly.

6.3.2 Receiver

The receiver design is based on an ED structure. Compared with an AcR, the ED has a simplified implementation since the design of delay lines can be substituted by a Gilbert cell, which will be described later in this section, in order to produce the squaring operation. Figure 65 shows the effect on the BEP for the AcR of the jitter between delay line at the receiver and the delay line at the transmitter. A few picoseconds of jitter can produce a serious degradation of the performance. After the antenna, the signal is filtered by a BPF in order to reduce the noise power and then amplified by a low-noise amplifier (LNA) with a gain of 20 dB.

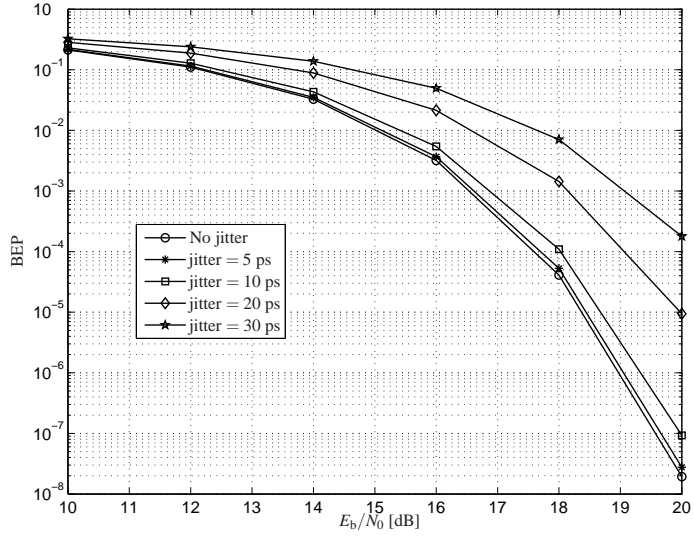


Fig. 65. Effect of the delay lines jitter for a single transmitted pulse in IEEE 802.15.4a CM3 with $T = 30$ ns.

Table 3. Amplification chain.

Stage	Gain	NF	Power
LNA	20 dB	2.5 dB	20 mW
VGA	15 dB	10 dB	10.56 mW
Gilbert	10 dB	13 dB	3.96 mW
Total	45 dB	3.6 dB	34.52 mW

Considering the noise enhancement effect associated with non-coherent data detection, the design of a good LNA is fundamental to providing high gain to increase the sensitivity and at the same time keep the noise figure low for large bandwidth. The receiver front-end chain implemented has a maximum overall gain of 45 dB with the overall power consumption of 117 mW with a voltage supply of 3.3 V. A LNA with a noise figure of 2 dB, and a forward gain of 18 dB in the 3.1 - 5 GHz band was designed

in a 0.35 μm BiCMOS process. After the LNA, the amplification chain is composed of a variable-gain amplifier (VGA) with variable gain between -5 and 15 dB.

The gain of the VGA is controlled by selection logic designed to keep the voltage output at an appropriate level to have the Gilbert cell behaving as a multiplier. In narrowband receivers, the Gilbert cell is often used as a modulator since a local oscillator is present. In the case of an impulse radio ED, the Gilbert cell multiplies the input signal by itself producing the squared signal. A summary of the performance of the amplification chain is given in Table 3. The output of the Gilbert cell is then integrated by a bank of 8 integrators which, after analogue-to-digital conversion, are used for synchronization and data detection purposes. The control signals of the integrator blocks are generated by on-chip digital control logic which is programmed to perform the sliding window synchronization. Because of the structure of the received signal, the analogue-to-digital converter (ADC) is required to operate at symbol rate rather than pulse repetition rate, which greatly reduces the power consumption of the receiver. Each integrator analogue output voltage is converted to digital format by a 4-bit parallel (FLASH) ADC architecture. The IR-UWB transceiver has resulted in an ASIC implementation for which the total consumed power is around 600 mW. Table 4 shows a summary of the power consumption of the different transceiver components.

Table 4. Transceiver power consumption.

Block	Value
Transmitter	20 mW
Receiver Front-end	117 mW
Baseband (FPGA)	450 mW
Total	587 mW

6.3.3 *Transceiver complexity*

The complexity can be evaluated both as quality and as quantity, where quantity means the number of gates for digital circuits and number of transistors for analogue circuits, both of them being translated into dice area. Based on the quantity it is straight forward to say that the analog part of an energy detector as it has been described in this Thesis

has a lower complexity than the analog part of a Rake receiver. The Rake receiver is based on the match filter concept, which requires several delay lines and correlators (working at high frequencies in the UWB case) in order to build the decision variable, while the ED does not have any delay line and requires only a Gilbert cell and few integrators. From the digital point of view, the Rake receiver is quite complex since for all its different implementations (All Rake, Partial Rake, Selective Rake), it requires channel estimation procedures and also precise synchronization in order to have high correlation value. On the other hand, the ED uses the digital circuit only for a coarse synchronization. The Rake receiver can also be fully digital. In this case due to the large bandwidth of the UWB signal a very high sampling rate is required and consequently a fast and precise A/D converter needs to be designed.

Quality means how well-known, reliable and well understood design issues are used in the transceiver blocks. For instance, in the case of the ED, the Gilbert cell is low complexity since it has been known already for a long time and its functionality can be easily described by circuit equations. As mentioned already in the Thesis, the disadvantage of the AcR is mainly due to the delay lines required for the correlation. The design of an analogue delay line with a delay of the order of few tens of nanosecond, with a very wide bandwidth, is very challenging.

6.4 Conclusions

In this chapter, an example implementation of an UWB transceiver for sensor networks based on low complexity and low-power consumption devices has been presented. The pulse compression technique based on the transmission of burst of pulses has been implemented as it reduces the effect of noise and also simplifies the synchronization procedure since the data detection becomes robust against synchronization error. The design of the transceiver based on this approach has resulted in an ASIC with low complexity and low-power consumption suiting the requirements of sensor network applications where low-cost and long battery life are important requirements.

7 Conclusions and future work

7.1 Summary and conclusions

Although impulse-radio based UWB communications were initially proposed for short range, high data rate systems, the implementation challenges moved the focus of attention to low data rate systems where the IR techniques offer viable solutions for the stringent requirements of low-cost and low-power consumption. This Thesis has proposed and evaluated solutions for low complexity UWB systems with application in sensor networks. Considering that AcR based receivers offer low-complexity and low-power consumption, this Thesis first analyzed the performance of different realizations of the AcR based on different transmission schemes and identified two possible solutions: the transmitted reference with BPAM; and the ED with BPPM. These two schemes offer the best trade-off of performance and complexity amongst the schemes reviewed. The analysis of the performance of the two selected schemes was then extended considering the performance over fading channel conditions. Closed form expressions for BEP and integrable BEP formulas have been derived for channel fading models which exhibit a closed form characteristic function. Using numerical averaging techniques, the performance of the selected schemes has been evaluated for the IEEE 802.15.4a standard channel models.

The low-power spectral density of UWB signals allows UWB transmission over spectrum regions where NB systems are allocated. Evaluation of the effect of NB interference, especially for low complexity, low-cost receivers where no interference mitigation techniques can be implemented, is therefore extremely important. In this Thesis we derived a statistical model based on the geographical distribution of multiple NB interferers. The aggregate interference is statistically modeled using a stable distribution and its effect on the performance of non-coherent receivers is included in the numerically integrable BEP formulations. Furthermore, since the UWB spectrum is unlicensed, we can expect that different UWB systems will interfere with each other. In order to include the effect of UWB interference, we extended the interference model derived for the multiple NBI case to the UWB case by using a multivariate stable distribution. The result allows us to include the effect of the aggregate UWB interference in numerically integrable BEP formulations. In both NB and UWB cases, the tools developed in the

This Thesis allows a quick evaluation of the effect of several interference parameters on the performance of non-coherent UWB receivers. For both the NB and UWB interference cases, we can conclude that the ED is more robust to interference, while the AcR was seen to be vulnerable to periodic interference signals with periods similar to the delay between reference pulse and modulated pulse.

In the Thesis, the time-of-arrival estimation problem for low complexity devices is also addressed and several different estimators with different levels of complexity and implementation issues were derived and compared. We have shown that accurate ranging is possible with devices which have a low sampling rate.

To conclude the Thesis, a realization of a UWB sensor network based on low complexity devices has been presented. Following the insights resulting from the theoretical work, the design of an IR-UWB transceiver has been described. The design layout proved that the choice of an ED allows a largely analogue transceiver implementation leading to a very low-power consumption design.

7.2 Future work

A significant improvement of the work presented in this Thesis could be gained from undertaking experimental studies to validate the statistical aggregate interference models developed in this Thesis. NB devices are already available at low-cost and UWB evaluation kits are also becoming more widely available. It is then feasible to carry out a large scale measurement campaign of the aggregate interference considering the geographical distribution and the mobility of the devices in different environments. Co-existence among UWB systems and between UWB and NB systems could then be more accurately examined exploring coordinated and uncoordinated systems.

The error probability tools developed in this Thesis can be practically applied in the case of uncoordinated networks. In order to ensure that interference remains at an acceptable level, each network should be able to sense the level of interference and apply the interference model to determine an acceptable density of active nodes inside the network and determine an acceptable data rate and transmitted power. Awareness of the environment (LOS / NLOS) where the network is active would also assist in opportunistically setting the parameters.

Regarding the transceiver design, a decrease of the minimum integration time together with faster and more accurate analogue-to-digital converters would permit the use of more sophisticated receiver algorithms that have been proposed for non-coherent

receivers in recent years. The ED process could be improved by utilising digital timing circuits with variable timing of control signals making the integrators more suitable for different applications (data detection, ranging, interference estimation). However, more advanced designs must always consider the trade-off between performance and power consumption, which is the key parameter for many sensor applications. Performance evaluation of the full IR-UWB energy detection transceiver in an experimental test environment would also be a significant step towards the final goal; the integrated software radio-based IR-UWB transceiver.

References

1. Intel (2005) Ultra-wideband (uwb technology), Enabling high-speed wireless personal area networks. URI: [http:// www.intel.com/technology/ultrawideband/downloads/Ultra-Wideband.pdf](http://www.intel.com/technology/ultrawideband/downloads/Ultra-Wideband.pdf).
2. Ross GF (1963) The transient analysis of multiple beam feed networks for array systems. Ph.D. thesis, Polytechnic Institute of Brooklyn, Brooklyn, NY.
3. Papoulis A (1962) The Fourier Integral and Its Applications. McGraw-Hill, New York.
4. Ross GF (1973). Transmission and reception system for generating and receiving base-band duration pulse signals without distortion for short base-band pulse communication system. US Patent 3,728,632.
5. Barrett TW (2000) History of ultra wideband (UWB) radar & communications: pioneers and innovators. Proc Progress in Electromagnetics Symp. Cambridge, MA, USA.
6. Nicholson AM & Ross GF (1975) A new radar concept for short-range application. Proc IEEE First Int Radar Conf Washington D.C., USA: 146–151.
7. Taylor JD (2001) Ultra-wideband radar technology. CRC Press, Boca Raton.
8. Fullerton LW (1987). Spread spectrum radio transmission system. US Patent 4,641,317.
9. Scholtz R (1993) Multiple access with time-hopping impulse modulation. Proc Military Commun Conf vol. 2: 447–450.
10. Win MZ, Scholtz RA & Fullerton LW (1996) Time-hopping SSMA techniques for impulse radio with an analog modulated data subcarrier. Proc IEEE Int Symp on Spread Spectrum Techniques & Applications vol. 1: 359–364.
11. Win MZ & Scholtz RA (1997) Comparisons of analog and digital impulse radio for wireless multiple-access communications. Proc IEEE Int Conf on Commun vol. 1: 91–95.
12. FCC (2002) First report and order in the matter of revision of part 15 of the commission's rules regarding ultra-wideband transmission systems. Technical report, FCC.
13. ECC (2007) On allowing the use of the radio spectrum for equipment using ultra-wideband technology in a harmonised manner in the community. Technical report, European Commission.
14. WiMedia. WiMedia Alliance. URI: <http://www.wimedia.org>.
15. IEEE (2007) P802.15.4a/D7, approved draft amendment to IEEE standard for information technology-telecommunications and information exchange between systems-PART 15.4: wireless medium access control (MAC) and physical layer (PHY) specifications for low-rate wireless personal area networks (LR-WPANs): Amendment to add alternate PHY (amendment of IEEE std 802.15.4).
16. IEEE (2003) IEEE 802.15 WPAN Low Rate Alternative PHY Task Group 4a (TG4a).
17. Rabbachin A & Oppermann I (2005) Comparison of UWB auto-correlation and transmitted reference schemes. Proc IEEE Int Conf on Ultra-Wideband. Zurich, Switzerland.
18. Rabbachin A & Oppermann I (2006) Comparison of UWB transmitted reference schemes. IEE Proc Commun 153(1): 136–142.
19. Rabbachin A, Quek TQ, Pinto PC, Oppermann I & Win MZ (2007) UWB energy detection in the presence of multiple narrowband interferers. Proc of IEEE Int Conf on Ultra Wideband: 857–862.
20. Rabbachin A, Quek TQ, Pinto PC, Oppermann I & Win MZ (2008) Effect of aggregate

- narrowband interference on the UWB autocorrelation receiver. Proc of IEEE Int Conf on Ultra Wideband. Submitted.
21. Rabbachin A, Quek TQ, Pinto PC, Oppermann I & Win MZ (2008) Non-coherent ultrawideband communications in the presence of multiple narrowband interferers. IEEE Trans Wireless Commun. Submitted.
 22. Rabbachin A, Oppermann I & Denis B (2006) GML ToA estimation based on low complexity UWB energy detection. Proc 17th IEEE Int Symp on Personal, Indoor and Mobile Radio Communications. Helsinki, Finland.
 23. Rabbachin A, Oppermann I & Denis B (2006) ML time-of-arrival estimation based on low complexity UWB energy detection. Proc of IEEE Int Conf on Ultra Wideband. Boston, USA.
 24. Oppermann I, Stoica L, Rabbachin A, Shelby Z & Haapola J (2004) UWB wireless sensor networks: UWEN-a practical example. IEEE Commun Mag 42(12): S27–S32.
 25. Rabbachin A, Stoica L, Tiuraniemi S & Oppermann I (2005) A low cost, low power UWB based sensor network. Proc of the Int Workshop on Wireless Ad-hoc Networks: 288–292.
 26. Rabbachin A, Tesi R & Oppermann I (2004) Bit error rate analysis for UWB systems with a low complexity, non-coherent energy collection receiver. IST Mobile & Wireless Telecommunications Summit. Lyon, France: 1 – 4.
 27. Stoica L, Rabbachin A & Oppermann I (2006) A low-complexity noncoherent IR-UWB transceiver architecture with TOA estimation. IEEE Trans Microwave Theory Tech 54(4 Part 2): 1637–1646.
 28. Stoica L, Rabbachin A, Repo HO, Tiuraniemi TS & Oppermann I (2005) An ultrawideband system architecture for tag based wireless sensor networks. IEEE Trans Veh Technol 54(5): 1632 – 1645.
 29. Rabbachin A & Oppermann I (2004) Synchronization analysis for UWB systems with a low-complexity energy collection receiver. IEEE Joint UWBST & IWUWBS: 288–292.
 30. Taylor JD, editor (1995) Introduction to Ultra-Wideband Radar Systems. CRC Press, Boca Raton, FL, first edition.
 31. Win MZ & Scholtz RA (1998) Impulse radio: how it works. IEEE Commun Lett 2(2): 36–38.
 32. Win MZ & Scholtz RA (1998) On the energy capture of ultrawide bandwidth signals in dense multipath environments. IEEE Commun Lett 2(9): 245–247.
 33. Win MZ & Scholtz RA (2000) Ultra-wide bandwidth time-hopping spread-spectrum impulse radio for wireless multiple-access communications. IEEE Trans Commun 48(4): 679–689.
 34. Win MZ, Scholtz RA & Barnes MA (1997) Ultra-wide bandwidth signal propagation for indoor wireless communications. Proc IEEE Int Conf on Commun vol. 1: 56–60.
 35. Molisch A (2005) Ultrawideband propagation channels-theory, measurement, and modeling. IEEE Trans Veh Technol 54(5): 1528–1545.
 36. Foerster J (2003). Channel modeling sub-committee report final. IEEE P802.15-02/490r1-SG3a.
 37. Saleh A & Valenzuela R (1987) A statistical model for indoor multipath propagation. IEEE J Select Areas Commun 5(2): 128–137.
 38. Molisch AF, Balakrishnan K, Chong CC, Emami S, Fort A, Karedal J, Kunisch J, Schantz H, Schuster U & Siwiak K (2004) IEEE 802.15.4a channel model. Final report. Technical report, IEEE. URI: <http://www.ieee802.org/15/pub/TG4a.html>.

39. Cassioli D, Win MZ & Molisch AF (2002) The ultra-wide bandwidth indoor channel: from statistical model to simulations. *IEEE J Select Areas Commun* 20(6): 1247–1257.
40. Kunisch J, Pamp J (2003) An ultra-wideband space-variant multipath indoor radio channel model. *Proc of IEEE Conf on Ultra Wideband Sys and Technol*: 290–294.
41. Keignart J & Daniele N (2002) Subnanosecond UWB channel sounding in frequency and temporal domain. *Proc of IEEE Conf on Ultra Wideband Sys and Technol*: 25–30.
42. Turin W, Jana R, Ghassemzadeh S, Rice C & Tarokh T (2002) Autoregressive modeling of an indoor UWB channel. *Proc of IEEE Conf on Ultra Wideband Sys and Technol*: 71–74.
43. Ghassemzadeh S, Jana R, Rice C, Turin W & Tarokh V (2002) A statistical path loss model for in-home UWB channels. *Proc of IEEE Conf on Ultra Wideband Sys and Technol*: 59–64.
44. Muqaibel A, Safaai-Jazi A, Attiya A, Bayram A & Riad S (2003) Measurement and characterization of indoor ultra-wideband propagation. *Proc of IEEE Conf on Ultra Wideband Sys and Technol*: 295–299.
45. Dohler M, Allen B, Armogida A, McGregor S, Ghavami M & Aghvami H (2004) A new twist on UWB pathloss modelling. *Proc 59th Annual Int Veh Technol Conf vol. 1*: 1999–2003.
46. Liu J, Dohler M, Allen B & Ghavami M (2006) Power loss modelling of short-range ultra wideband pulse transmissions. *IEE Proc Commun* 153(1): 143–152.
47. Fleming R, Kushner C, Roberts G & Nandiwada U (2002) Rapid acquisition for ultra-wideband localizers. *Proc of IEEE Conf on Ultra Wideband Sys and Technol*: 245–249.
48. Homier E (2004) Synchronization of ultra-wideband signals in the dense multipath channel. Ph.D. thesis, University of South California.
49. Homier E & Scholtz R (2002) Rapid acquisition of ultra-wideband signals in the dense multipath channel. *Proc of IEEE Conf on Ultra Wideband Sys and Technol*: 105–109.
50. Homier E & Scholtz R (2003) A generalized signal flow graph approach for hybrid acquisition of Ultra-Wideband signals. *Int J Wireless Info Networks* 10(4): 179–191.
51. Suwansantisuk W, Win M & Shepp L (2005) On the performance of wide-bandwidth signal acquisition in dense multipath channels. *IEEE Trans Veh Technol* 54(5): 1584–1594.
52. Soderi S, Inatti J & Hämäläinen M (2003) CLPDI algorithm in UWB synchronization. *Proc of the Int Workshop on Ultra Wideband Sys*.
53. Zhang J, Kennedy R & Abhayapala T (2005) Cramer-Rao Lower bounds for the synchronization of UWB signals. *EURASIP Journal on Applied Signal Processing* 2005(3): 426–438.
54. He N & Tepedelenlioglu C (2004) Performance analysis of non-coherent UWB receivers at different synchronization levels. *Proc IEEE Global Telecomm Conf vol. 6*.
55. Luo X & Giannakis G (2004) Low-complexity blind synchronization and demodulation for (ultra-) wideband multi-user ad hoc access. *IEEE Trans Commun* 5.
56. Carbonelli C & Mengali U (2005) Low complexity synchronization for UWB noncoherent receivers. *Proc 61st Annual Int Veh Technol Conf 2*.
57. Yang L & Giannakis G (2005) Timing ultra-wideband signals with dirty templates. *IEEE Trans Commun* 53(11): 1952–1963.
58. Ramirez-Mireles F (2001) On the performance of ultra-wide-band signals in Gaussian noise and dense multipath. *IEEE Trans Veh Technol* 50(1): 244–249.
59. Ramirez-Mireles F, Win MZ & Scholtz RA (1997) Performance of ultra-wideband time-shift-modulated signals in the indoor wireless impulse radio channel. *Proc Asilomar Conf*

- on Signals, Systems and Computers. vol. 1: 192–196.
60. Win MZ & Scholtz RA (1997) Energy capture vs. correlator resources in ultra-wide bandwidth indoor wireless communications channels. *Proc Military Commun Conf* vol. 3: 1277–1281.
 61. Mielczarek B, Wessman M & Svensson A (2003) Performance of coherent UWB Rake receivers with channel estimators. *Proc 58th Annual Int Veh Technol Conf.* vol. 3: 1880–1884.
 62. Lovelace WM & Townsend JK (2002) The effects of timing jitter and tracking on the performance of impulse radio. *IEEE J Select Areas Commun* 20(9): 1646–1651.
 63. Hoctor R & Tomlinson H (2002) Delay-hopped transmitted-reference rf communications. *Proc of IEEE Conf on Ultra Wideband Sys and Technol:* 265–269.
 64. Pierce JR & Hopper A (1952) Nonsynchronous time division with holding and with random sampling. *Proc IRE:* 1079–1088.
 65. Ghassemzadeh S, Jana R, Rice C, Turin W & Tarokh V (2004) Measurement and modeling of an ultra-wide bandwidth indoor channel. *IEEE Trans Commun* 52(10): 1786–1796.
 66. Kunisch J & Pamp J (2002) Measurement results and modeling aspects for the UWB radio channel. *Proc of IEEE Conf on Ultra Wideband Sys and Technol:* 19–23.
 67. Zasowski T, Althaus F, Stager M, Wittneben A & Troster G (2003) UWB for noninvasive wireless body area networks: channel measurements and results. *Proc of IEEE Conf on Ultra Wideband Sys and Technol:* 285–289.
 68. Torrieri DJ (1992) *Principle of Secure Communications Systems.* Artech House, Boston.
 69. Bharadwaj A & Townsend JK (2001) Evaluation of the covertness of time-hopping impulse radio using a multi-radiometer detection. *Proc Military Commun Conf* vol. 1: 128–134.
 70. Weisenhorn M & Hirt W (2004) Robust noncoherent receiver exploiting UWB channel properties. *Proc of the Joint IEEE Conf on Ultra Wideband Sys and Technol and Int Workshop on Ultra Wideband Sys:* 156–160.
 71. Quek T, Win M & Dardari D (2005) UWB transmitted reference signaling schemes-Part II: narrowband interference analysis. *Proc IEEE Int Conf on Ultra-Wideband:* 593–598.
 72. Quek TQS & Win MZ (2005) Analysis of UWB transmitted-reference communication systems in dense multipath channels. *IEEE J Select Areas Commun* 23(9): 1863–1874.
 73. Quek TQS, Win MZ & Dardari D (2007) Unified analysis of UWB transmitted-reference schemes in the presence of narrowband interference. *IEEE Trans Commun* 6: 2126–2139.
 74. Witralsal K, Leus G, Pausini M & Krall C (2005) Equivalent system model and equalization of differential impulse radio uwb systems. *IEEE J Select Areas Commun* 23(9): 1851–1862.
 75. Pausini M, Janssen GJM & Witralsal K (2006) Performance enhancement of differential UWB autocorrelation receivers under ISI. *IEEE J Select Areas Commun* 24(4): 815–821.
 76. Romme J & Witralsal K (2006) Transmitted-reference UWB systems using weighted autocorrelation receivers. *IEEE Trans Microwave Theory Tech* 54(4): 1754–1761.
 77. Paquelet S & Aubert L (2004) An energy adaptive demodulation for high data rates with impulse radio. *IEEE Radio and Wireless Conference:* 323–326.
 78. Paquelet S, Aubert L & Uguen B (2004) An impulse radio asynchronous transceiver for high data rates. *Proc of the Joint IEEE Conf on Ultra Wideband Sys and Technol and Int Workshop on Ultra Wideband Sys:* 1–5.
 79. Weisenhorn M & Hirt W (2005) ML receiver for pulsed UWB signals and partial channel state information. *Proc IEEE Int Conf on Ultra-Wideband.*

80. Chao YL & Scholtz RA (2004) Weighted correlation receivers for ultra-wideband transmitted reference systems. *Proc IEEE Global Telecomm Conf* vol. 1: 66–70.
81. Dubouloz S, Denis B, de Rivaz S & Ouvry L (2005) Performance analysis of LDR UWB non-coherent receivers in multipath environments. *Proc IEEE Int Conf on Ultra-Wideband*: 491–496.
82. Sahin ME, Guvenc I & Arslan H (2005) Optimization of energy detector receivers for UWB systems. *Proc 61st Annual Int Veh Technol Conf* vol. 2, 1386–1390.
83. Dubouloz S, de Rivaz S, Sambuq M & Ouvry L (2006) Effects of hard decision on the detection of preambles for uwb non-coherent communications. *Proc of IEEE Int Conf on Ultra Wideband*: 131–136.
84. Hämäläinen M, Hovinen V, Tesi R, Iinatti J & Latva-aho M (2002) On the UWB system coexistence with GSM900, UMTS/WCDMA, and GPS. *IEEE J Select Areas Commun* 20(9): 1712–1721.
85. Hämäläinen M, Iinatti J, Hovinen V & Latva-aho M (2001) In-band interference of three kinds of UWB signals in GPS L1 band and GSM900 uplink band. *Proc 12th IEEE Int Symp on Personal, Indoor and Mobile Radio Communications* vol. 1: D–76–D–80.
86. Hämäläinen M, Saloranta J, Makela JP, Oppermann I & Patana T (2003) Ultra wideband signal impact on IEEE802.11b and Bluetooth performances. *Proc 14th IEEE Int Symp on Personal, Indoor and Mobile Radio Communications* vol. 3: 2943–2952.
87. Hämäläinen M, Tesi R & Iinatti J (2004) UWB coexistence with IEEE 802.11a and UMTS in modified Saleh-Valenzuela channel. *Proc of the Joint IEEE Conf on Ultra Wideband Sys and Technol and Int Workshop on Ultra Wideband Sys*: 45–49.
88. Giuliano R, Guidoni G, Mazzenga F & Vatalaro F (2004) On the UWB coexistence with UMTS terminals. *Proc IEEE Int Conf on Commun* vol. 6: 3571–3575 Vol.6.
89. Giuliano R & Mazzenga F (2005) On the coexistence of power-controlled ultrawide-band systems with UMTS, GPS, DCS1800, and fixed wireless systems. *IEEE Trans Veh Technol* 54(1): 62–81.
90. Giuliano R, Mazzenga F & Vatalaro F (2003) On the interference between UMTS and UWB systems. *Proc of IEEE Conf on Ultra Wideband Sys and Technol*: 339–343.
91. Cassioli D, Persia S, Bernasconi V & Valent A (2005) Measurements of the performance degradation of UMTS receivers due to UWB emissions. *IEEE Commun Lett* 9(5): 441–443.
92. Bellorado J, Ghassemzadeh S, Greenstein L, Sveinsson T & Tarokh V (2003) Coexistence of ultra-wideband systems with IEEE-802.11 a wireless LANs. *Proc IEEE Global Telecomm Conf* vol. 1: 410–414.
93. Foerster J (2002) Interference modeling of pulse-based UWB waveforms on narrowband systems. *Proc 55th Annual Int Veh Technol Conf* vol. 4: 1931–1935.
94. Pinto P, Chong C, Giorgetti A, Chiani M & Win M (2006) Narrowband communication in a Poisson field of ultrawideband interferers. *Proc of IEEE Int Conf on Ultra Wideband*: 387–392.
95. Miller T, Potter L & McCorkle J (1997) RFI suppression for ultra wideband radar. *IEEE Trans Aerosp Electron Syst* 33(4): 1142–1156.
96. Choi J & Stark W (2002) Performance analysis of ultra-wideband spread-spectrum communications in narrowband interference. *Proc Military Commun Conf* vol. 2.
97. Giorgetti A & Dardari D (2005) The impact of OFDM interference on TH-PPM/BPAM transmission systems. *Vehicular Technology Conference, 2005. VTC 2005-Spring*. 2005

IEEE 61st. vol. 2.

98. Zhao L & Haimovich A (2002) Performance of ultra-wideband communications in the presence of interference. *IEEE J Select Areas Commun* 20(9): 1684–1691.
99. Taha A & Chugg K (2002) A theoretical study on the effects of interference UWB multiple access impulse radio. *Proc Asilomar Conf on Signals, Systems and Computers* vol. 1, 728–732.
100. Pausini M & Janssen G (2005) On the narrowband interference in transmitted reference UWB receivers. *Proc IEEE Int Conf on Ultra-Wideband*: 571–575.
101. Win M, Pinto P, Giorgetti A, Chiani M & Shepp L (2006) Error performance of ultrawide-band systems in a Poisson field of narrowband interferers. *Proc IEEE Int Symp on Spread Spectrum Techniques & Applications*: 410–416.
102. Pinto PC, Chong CC, Giorgetti A, Chiani M & Win MZ (2006) Narrowband communication in a Poisson field of ultrawideband interferers. *Proc of IEEE Int Conf on Ultra Wideband*. Waltham, MA: 387–392.
103. Sousa E (1992) Performance of a spread spectrum packet radio network link in a Poisson field of interferers. *IEEE Trans Inform Theory* 38(6): 1743–1754.
104. Ilow J, Hatzinakos D & Venetsanopoulos AN (1998) Performance of FH SS radio networks with interference modeled as a mixture of Gaussian and alpha-stable noise. *IEEE Trans Commun* 46(4): 509–520.
105. Kapoor R, Banerjee A, Tsihrintzis G & Nandhakumar N (1999) UWB radar detection of targets in foliage using alpha-stable clutter models. *IEEE Trans Aerosp Electron Syst* 35(3): 819–834.
106. Tsihrintzis G & Nikias C (1996) Fast estimation of the parameters of alpha-stable impulsive interference. *IEEE Trans Signal Processing* 44(6): 1492–1503.
107. Fontana R, Inc M & Germantown M (2002) An insight into UWB interference from a shot noise perspective. *Proc of IEEE Conf on Ultra Wideband Sys and Technol*: 309–313.
108. Fontana R & Gunderson S (2002) Ultra-wideband precision asset location system. *Proc of IEEE Conf on Ultra Wideband Sys and Technol*: 147–150.
109. Lee J & Scholtz R (2002) Ranging in a dense multipath environment using an UWB radio link. *IEEE J Select Areas Commun* 20(9): 1677–1683.
110. Mazzucco C, Spagnolini U, MulaS G (2004) A ranging technique for UWB indoor channel based on power delay profile analysis. *Proc 59th Annual Int Veh Technol Conf* vol. 5.
111. Denis B, Pierrot J & Abou-Rjeily C (2006) Joint Distributed synchronization and positioning in UWB Ad Hoc networks using TOA. *IEEE Trans Microwave Theory Tech* 54(4 Part 2): 1896–1911.
112. Gezici S, Tian Z, Giannakis G, Kobayashi H, Molisch A, Poor H & Sahinoglu Z (2005) Localization via ultra-wideband radios: a look at positioning aspects for future sensor networks. *IEEE Signal Processing Mag* 22(4): 70–84.
113. Dardari D, Chong C & Win M (2006) Improved lower bounds on time-of-arrival estimation error in realistic UWB channels. *Proc of IEEE Int Conf on Ultra Wideband*: 531–537.
114. Dardari D & Win M (2006) Threshold-based time-of-arrival estimators in UWB dense multipath channels. *Proc IEEE Int Conf on Commun* vol. 10: 4723–4728.
115. Sieskul B & Kaiser T (2005) Cramer-Rao bound for TOA estimations in UWB positioning systems. *Proc IEEE Int Conf on Ultra-Wideband*: 408–413.
116. Guvenc I & Sahinoglu Z (2005) Multiscale energy products for TOA estimation in IR-UWB systems. *Proc IEEE Global Telecomm Conf* vol. 1.

117. Guvenc I & Sahinoglu Z (2005) TOA estimation with different IR-UWB transceiver types. *Proc IEEE Int Conf on Ultra-Wideband*: 426–431.
118. Guvenc I, Sahinoglu Z, Molisch A & Orlik P (2005) Non-coherent TOA estimation in IR-UWB systems with different signal waveforms. *Proceedings of 1st IEEE/CreateNet International Workshop on Ultrawideband Wireless Networking (UWBNETS'05)*: 245–251.
119. Guvenc I, Sahinoglu Z & Orlik PV (2006) TOA estimation for IR-UWB systems with different transceiver types. *IEEE Trans Microwave Theory Tech* 54(4): 1876–1886.
120. Denis B, Keignart J & Daniele N (2003) Impact of NLOS propagation upon ranging precision in UWB systems. *Proc of IEEE Conf on Ultra Wideband Sys and Technol*: 379–383.
121. Lee J, Jo Y, Kang S, Kang A, Ha D & Yoon S (2006) Determination of the existence of LoS blockage and its application to UWB localization. *Proc Military Commun Conf* 1–4.
122. Pahlavan K, Li X & Mäkelä JP (2002) Indoor geolocation science and technology. *IEEE Commun Mag* 40(2): 112 – 118.
123. Althaus F, Troesch F & Wittneben A (2005) UWB geo-regioning in rich multipath environment. *Proc 62nd Annual Int Veh Technol Conf*.
124. Maravic I, Kusuma J & Vetterli M (2003) Low-sampling rate UWB channel characterization and synchronization. *Int. J of Commun Networks* 5(4): 319–327.
125. Maravic I, Vetterli M & Ramchandran K (2004) Channel estimation and synchronization with sub-Nyquist sampling and application to ultra-wideband systems. *Proc IEEE Int Symp on Circuit and Sys* vol. 5.
126. Navarro M, Prior S & Najar M (2006) Low Complexity frequency domain TOA estimation for IR-UWB Communications. *Proc 64th Annual Int Veh Technol Conf*: 1–5.
127. Schroeder J, Galler S & Kyamakyia K (2005) A low-cost experimental ultra-wideband positioning system. *Proc IEEE Int Conf on Ultra-Wideband*: 632–637.
128. Shannon CE (1949) Communication in the presence of noise. *Proc IRE* vol. 37, 10–21.
129. Dubouloz S, Denis B, de Rivaz S & Ouvry L (2005) Performance analysis of LDR UWB non-coherent receivers in multipath environments. *Ultra-Wideband, 2005 IEEE International Conference on (ICU)*: 491 – 496.
130. Pausini M & Janssen G (2004) Analysis and comparison of autocorrelation receivers for IR-UWB signals based on differential detection. *Proc IEEE Int Conf Acoustics, Speech, and Signal Processing*. iv–513 – iv 516.
131. Simon MK (1995) *Digital Communications Techniques*. Prentice-Hall, Englewood Cliffs, NJ.
132. Quek TQS & Win MZ (2004) Ultrawide bandwidth transmitted-reference signaling. *Proc IEEE Int Conf on Commun. Paris, FRANCE*, vol. 6: 3409–3413.
133. Kotelnikov VA (1933) On the carrying capacity of the ether and wire in telecommunications. *Material for the First All-Union Conf on Questions of Comm, Izd Red Upr Svyazi RKKA*.
134. Quek TQS & Win MZ (2005) Analysis of UWB transmitted-reference communication systems in dense multipath channels. *IEEE J Select Areas Commun* 23(9): 1863–1874.
135. Choi JD & Stark WE (2002) Performance of ultra-wideband communications with suboptimal receivers in multipath channels. *IEEE J Select Areas Commun* 20: 1754–1766.
136. Lindsey W (1964) Error probabilities for rician fading multichannel reception of binary and n-ary signals. *IEEE Trans Inform Theory* 10: 339–350.
137. Quek TQS & Win MZ (2004) Ultrawide bandwidth transmitted-reference signaling. *Proc IEEE Int Conf on Commun* vol. 6, 3409–3413.

138. Quek TQS & Win MZ (2005) Analysis of UWB transmitted-reference communication systems in dense multipath channels. *IEEE J Select Areas Commun* 9: 1863–1874.
139. Quek TQS, Win MZ & Dardari D (2005) UWB transmitted-reference signaling schemes - Part I: Performance analysis. *Proc IEEE Int Conf on Ultra-Wideband*: 587–592.
140. Simon MK & Alouini MS (2000) *Digital Communication over Fading Channels: A Unified Approach to Performance Analysis*. John Wiley & Sons, Inc., New York, NY, 10158, first edition.
141. Gil-Pelaez J (1951) Note on the inversion theorem. *Biometrika* 38(3/4): 481–482.
142. Cassioli D, Win M & Molisch A (2001) A statistical model for the UWB indoor channel. *Proc. 53th Annual Int Veh Technol Conf* vol. 2, 1159–1163.
143. Win MZ, Pinto PC, Giorgetti A, Chiani M & Shepp LA (2006) Error performance of ultra-wideband systems in a Poisson field of narrowband interferers. *Proc. IEEE Int Symp on Spread Spectrum Techniques & Applications*. Manaus, BRAZIL, 410–416.
144. Ilow J, Hatzinakos D & Venetsanopoulos AN (1998) Analytic alpha-stable noise modeling in a Poisson fields of interferers or scatters. *IEEE Trans. Signal Processing* 46(6): 1601–1611.
145. Giorgetti A, Chiani M & Win MZ (2005) The effect of narrowband interference on wide-band wireless communication systems. *IEEE Trans Commun* 53(12): 2139–2149.
146. Jakes WC Ed (1995) *Microwave Mobile Communications*. IEEE Press, Piscataway, New Jersey, 08855-1331, classic reissue edition.
147. Quek TQS, Win MZ & Dardari D (2007) Unified analysis of UWB transmitted-reference schemes in the presence of narrowband interference. *IEEE Trans Wireless Commun* 6(6): 2126–2139.
148. Pinto PC (2006) *Communication in a Poisson Field of Interferers*. Master's thesis, Department of Electrical Engineering and Computer Science, Massachusetts Institute of Technology, Cambridge, MA. Thesis advisor: Professor Moe Z. Win.
149. Sousa E (1992) Performance of a spread spectrum packet radio network link in a Poisson field of interferers. *IEEE Trans on Inform Theory* 38(6): 1743–1754.
150. Kingman J (1993) *Poisson Processes*. Oxford University Press, 1st edition.
151. Molisch AF Ed (2001) *Wideband Wireless Digital Communications*. Prentice Hall Publishers, Upper Saddle River, New Jersey 07458.
152. Samoradnitsky G & Taqqu MS (1994) *Stable Non-Gaussian Random Processes*. Chapman and Hall, 1st edition.
153. Cassioli D, Win MZ & Molisch AF (2002) The ultra -wide bandwidth indoor channel: from statistical model to simulations. *IEEE J Select Areas Commun* 20(6): 1247–1257.
154. Falsi C, Dardari D, Mucchi L & Win M (2006) Time of arrival estimation for UWB localizers in realistic environments. *EURASIP J Appl Signal Processing (Special Issue on Wireless Location Technologies and Applications)* 2006: Article ID 32082, 1–13.
155. Peterson W, Birdsall T & Fox W (1954) The theory of signal detectability. *IEEE Trans Inform Theory* 4(4): 171–212.
156. Selin I (1965) Detection of coherent radar returns of unknown Doppler shift. *IEEE Trans Inform Theory* 11(3): 396–400.
157. Van Trees HL (1968) *Detection, Estimation, and Modulation Theory*. John Wiley & Sons, Inc, New York, NY 10158-0012, first edition.
158. Schuster U, Bolcskei H & Durisi G (2005) Ultra-wideband channel modeling based on information-theoretic criteria. in *IEEE J Select Areas Commun*.

159. Destino G & Abreu G (2006) Localization from imperfect and incomplete ranging. Proc. 17th IEEE Int Symp on Personal, Indoor and Mobile Radio Communications.
160. Destino G & Abreu G (2006) Sensor Localization from WLS optimization with Closed-form Gradient and Hessian. Proc IEEE Global Telecomm Conf.
161. Destino G, Macagnano D & Abreu G (2007) Hypothesis testing and iterative WLS minimization for WSN localization under LOS/NLOS condition. Proc. Asilomar Conf on Signals, Systems and Computers.
162. Al-Jazzar S & Caffery J (2005) New algorithms for NLOS identification. 14th IST Mobile and Wireless Communication Summit. Dresden, Germany.
163. Gezici S, Kobayashi H & Poor H (2003) Nonparametric nonline-of-sight identification. Proc 58th Annual Int Veh Technol Conf vol. 4.
164. Stoica L (2007) Non-coherent Energy Detection Transceivers for Ultra Wideband Impulse Radio Systems. Ph.D. thesis, Department of Electrical and Information Engineering, University of Oulu, Oulu, Finland. Thesis advisors: Dr. Ian Oppermann and Prof. Matti Latva-aho.
165. Samoradnitsky G & Taqqu M (1994) Stable Non-Gaussian Random Processes. Chapman and Hall, 1st edition.
166. Pivato M & Seco L (2003) Estimating the spectral measure of a multivariate stable distribution via spherical harmonic analysis. Journal of Multivariate Analysis 87(2): 219–240.
167. Papoulis A (1984) Probability, Random Variables, and Stochastic Processes. McGraw-Hill, Inc., New York, NY, 10020, second edition.
168. Abramowitz M & Stegun IA (1970) Handbook of Mathematical Functions with Formulas, Graphs, and Mathematical Tables. United States Department of Commerce, Washington, D.C.
169. Gubner JA (2006) A New Formula for Lognormal Characteristic Functions. IEEE Trans Veh Technol 55(5): 1669.

Appendix 1 SNR_d derivations

This appendix presents the derivations of the SNR_d expressions of the receiver schemes presented in Fig. 3, Fig. 4, and Fig. 5. The SNR_d for the SR-BPPM cases (scheme 1 and scheme 2) can be expressed as follows:

$$(\text{SNR}_d)_{\text{SR-BPPM}} = \frac{(N_p - 1)^2}{N_p^2} (E'_b)^2 / \text{Var}\{Y_{d_0=0}^{\text{SR-BPPM}}\}. \quad (199)$$

Considering that all the noise terms in equation (19) are statistically independent the variance $\text{Var}\{Y_{d_0=0}^{\text{SR-BPPM}}\}$ can be expressed as follows:

$$\begin{aligned} \text{Var}\{Y_{d_0=0}^{\text{SR-BPPM}}\} &= \sum_{m=1}^{2TW} (N_p - 1)^2 \frac{E'_b}{N_p} w_m^2 \mathbb{E}\{n_{1,m}^2\} \\ &+ \sum_{j=0}^{N_p-2} \left(\frac{E'_b}{N_p} w_m^2 \mathbb{E}\{n_{3,j,m}^2\} + \mathbb{E}\{n_{1,m}^2 n_{3,j,m}^2\} \right. \\ &+ (1 - g_m) \left(\frac{E'_b}{N_p} w_m^2 \mathbb{E}\{n_{4,j,m}^2\} + \mathbb{E}\{n_{1,m}^2 n_{4,j,m}^2\} \right) \\ &\left. + g_m \mathbb{E}\{n_{2,m}^2 n_{4,j,m}^2\} \right) \\ &= \frac{E'_b}{N_p} \sigma_n^2 \left((N_p - 1)^2 + (2 - g_m) (N_p - 1) \right) \\ &+ 2TW 2(N_p - 1) \sigma_n^4. \end{aligned} \quad (200)$$

Since the channel does not change over the symbol period, the signal $w(t)$ remains the same over the symbol. As a result, we remove the index j related to the frame position from the samples of $w(t)$. Since there is statistical symmetry with respect to d_0 , the variable SNR_d can be expressed as

$$(\text{SNR}_d)_{\text{SR-BPPM}} = \frac{\frac{(N_p - 1) 2E'_b}{N_p} \frac{2E'_b}{N_0}}{\left(N_p + 1 - g_m + 2TW N_p \frac{N_0}{E'_b} \right)}. \quad (201)$$

The same approach can be followed for all the other structures.

For SR-BPAM structure (scheme 3), the variance $\text{Var}\{Y_{a_0=+1}^{\text{SR-BPAM}}\}$ can be expressed

as follows:

$$\begin{aligned}
\text{Var}\{Y_{a_0=+1}^{\text{SR-BPAM}}\} &= \sum_{m=1}^{2TW} (N_p - 1)^2 \frac{E'_b}{N_p} w_m^2 \mathbb{E}\{n_{1,m}^2\} \\
&\quad + \sum_{j=0}^{N_p-2} \frac{E'_b}{N_p} w_m^2 \mathbb{E}\{n_{3,j,m}^2\} + \mathbb{E}\{n_{1,m}^2 n_{3,j,m}^2\}. \\
&= \frac{E'_b}{N_p} \sigma_n^2 \left((N_p - 1)^2 + (N_p - 1) \right) + 2TW(N_p - 1) \sigma_n^4.
\end{aligned} \tag{202}$$

Since there is statistical symmetry with respect to a_0 , the variable SNR_d can be expressed as

$$(\text{SNR}_d)_{\text{SR-BPAM}} = \frac{\frac{(N_p-1)}{N_p} \frac{2E'_b}{N_0}}{(N_p + 2TW N_p \frac{N_0}{E'_b})}. \tag{203}$$

For the DB-BPPM structures (scheme 4 and scheme 5), the variance $\text{Var}\{Y_{d_0=0}^{\text{DB-BPPM}}\}$ can be expressed as follows:

$$\begin{aligned}
\text{Var}\{Y_{d_0=0}^{\text{DB-BPPM}}\} &= \sum_{m=1}^{2TW} \sum_{j=0}^{\frac{N_p}{2}-1} \frac{E'_b}{N_p} w_m^2 \mathbb{E}\{n_{1,j,m}^2\} + \frac{E'_b}{N_p} w_m^2 \mathbb{E}\{n_{3,j,m}^2\} \\
&\quad + \mathbb{E}\{n_{1,j,m}^2 n_{3,j,m}^2\} \\
&\quad + (1 - g_m) \left(\frac{E'_b}{N_p} w_m^2 \mathbb{E}\{n_{4,j,m}^2\} + \mathbb{E}\{n_{1,j,m}^2 n_{4,j,m}^2\} \right) \\
&\quad + g_m \mathbb{E}\{n_{2,j,m}^2 n_{4,j,m}^2\}.
\end{aligned} \tag{204}$$

Since there is statistical symmetry with respect to d_0 , the variable SNR_d can be expressed as

$$\begin{aligned}
(\text{SNR}_d)_{\text{DB-BPPM}} &= \frac{\frac{(E'_b)^2}{4}}{\left(\frac{3}{2} E'_b \sigma_n^2 (1 - g_m) + 2TW N_p \sigma_n^4 \right)} \\
&= \frac{\frac{2E'_b}{N_0}}{(6 - 2g_m + 2N_p 2TW \frac{N_0}{E'_b})}.
\end{aligned} \tag{205}$$

For the DB-BPAM structure (scheme 6), the variance $\text{Var}\{Y_{a_0=+1}^{\text{DB-BPAM}}\}$ can be ex-

pressed as follows:

$$\begin{aligned} \text{Var}\{Y_{a_0=+1}^{\text{DB-BPAM}}\} &= \sum_{m=1}^{2TW} \sum_{j=0}^{\frac{N_p}{2}} ((w_m^2 \mathbb{E}\{n_{1,j,m}^2\} + w_m^2 \mathbb{E}\{n_{3,j,m}^2\} \\ &\quad + \mathbb{E}\{n_{1,j,m}^2 n_{3,j,m}^2\})). \end{aligned} \quad (206)$$

Since there is statistical symmetry with respect to a_0 , the variable SNR_d can be expressed as

$$\begin{aligned} (\text{SNR}_d)_{\text{DB-BPAM}} &= \frac{\frac{(E'_b)^2}{4}}{(E'_b \sigma_n^2 + 2TW N_p \sigma_n^4)} \\ &= \frac{\frac{2E'_b}{N_0}}{(4 + 2TW N_p \frac{N_0}{E'_b})}. \end{aligned} \quad (207)$$

For the ALT-BPPM structure (scheme 7), the variance $\text{Var}\{Y_{d_0=0}^{\text{ALT-BPPM}}\}$ can be expressed as follows:

$$\begin{aligned} \text{Var}\{Y_{d_0=0}^{\text{ALT-BPPM}}\} &= \sum_{m=1}^{2TW} \left(\sum_{j=1}^{N_p-3} 4 \frac{E'_b}{N_p} w_m^2 \mathbb{E}\{n_{2,j+1,m}^2\} + \frac{E'_b}{N_p} w_m^2 \mathbb{E}\{n_{1,1,m}^2\} \right. \\ &\quad + \frac{E'_b}{N_p} w_m^2 \mathbb{E}\{n_{2,N_p,m}^2\} + \sum_{j=0}^{N_p-2} \mathbb{E}\{n_{1,j,m}^2 n_{1,j+1,m}^2\} \\ &\quad \left. + \mathbb{E}\{n_{2,j,m}^2 n_{2,j+1,m}^2\} \right) \\ &= \frac{E'_b}{N_p} \sigma_n^2 (4(N_p - 2) + 2) + 2TW 2(N_p - 1) \sigma_n^4. \end{aligned} \quad (208)$$

Since there is statistical symmetry with respect to d_0 , the variable SNR_d can be expressed as

$$(\text{SNR}_d)_{\text{ALT-BPPM}} = \frac{\frac{(N_p-1) 2E'_b}{N_p N_0}}{(4 \frac{N_p}{N_p-1} - \frac{6}{N_p-1} + N_p 2TW \frac{N_0}{E'_b})}. \quad (209)$$

For the ALT-BPAM structure (scheme 8), the variance $\text{Var}\{Y_{a_0,0=+1}^{\text{ALT-BPAM}}\}$ can be

expressed as follows:

$$\begin{aligned}
\text{Var}\{Y_{a_{0,0}=+1}^{\text{ALT-BPAM}}\} &= \sum_{m=1}^{2TW} \left(\sum_{j=1}^{N_p-3} 4 \frac{E'_b}{N_p} w_m^2 \mathbb{E}\{n_{2,j+1,m}^2\} \right. \\
&\quad + \frac{E'_b}{N_p} w_m^2 \mathbb{E}\{n_{1,1,m}^2\} + \frac{E'_b}{N_p} w_m^2 \mathbb{E}\{n_{2,N_p,m}^2\} \\
&\quad \left. + \sum_{i=0}^{N_p-2} \mathbb{E}\{n_{2,j,m}^2 n_{2,j+1,m}^2\} \right) \\
&= \frac{E'_b}{N_p} \sigma_n^2 (4(N_p - 2) + 2) + 2TW(N_p - 1) \sigma_n^4. \quad (210)
\end{aligned}$$

Since there is statistical symmetry with respect to $a_{0,0}$, the variable SNR_d can be expressed as

$$(\text{SNR}_d)_{\text{ALT-BPAM}} = \frac{\frac{(N_p-1)}{N_p} \frac{2E'_b}{N_0}}{\left(4 \frac{N_p}{N_p-1} - \frac{6}{N_p-1} + N_p TW \frac{N_0}{E'_b}\right)}. \quad (211)$$

$$(\text{SNR}_d)_{\text{ED-BPPM}} = (E'_b)^2 / \text{Var}\{Y_{d_0=0}^{\text{ED-BPPM}}\}. \quad (212)$$

For the ED-BPPM structure, the variance $\text{Var}\{Y_{d_0=0}^{\text{ED-BPPM}}\}$ can be expressed as follows:

$$\begin{aligned}
\text{Var}\{Y_{d_0=0}^{\text{ED-BPPM}}\} &= \sum_{m=1}^{2TW} \sum_{j=0}^{\frac{N_p}{2}} 4w_m^2 \mathbb{E}\{n_{2,j,m}^2\} + \mathbb{E}\{n_{1,j,m}^4\} + \mathbb{E}\{n_{2,j,m}^4\} \\
&\quad - 2\mathbb{E}\{n_{1,j,m}^2\} \mathbb{E}\{n_{2,j,m}^2\} \\
&= 4E'_b \sigma_n^2 + 4TWN_p \sigma_n^4. \quad (213)
\end{aligned}$$

Since there is statistical symmetry with respect to d_0 , the variable SNR_d can be expressed as

$$\begin{aligned}
(\text{SNR}_d)_{\text{ED-BPPM}} &= \frac{(E'_b)^2}{4E'_b \sigma_n^2 + 4TWN_p \sigma_n^4} \\
&= \frac{\frac{2E'_b}{N_0}}{\left(4 + 2N_p TW \frac{N_0}{E'_b}\right)}. \quad (214)
\end{aligned}$$

Appendix 2 LePage series representation of Alpha-stable distributions

To derive the distribution of \mathbf{A} given in (96), we start with the following LePage series representation of alpha-stable distributions. Let $\{\tau_i\}_{i=1}^{\infty}$ denote the arrival times of a one-dimensional Poisson process with rate λ ; let $\{\mathbf{Z}_i\}_{i=1}^{\infty}$ be a sequence of CS i.i.d. complex r.v.s $\mathbf{Z}_i = Z_{i1} + jZ_{i2}$, independent of the sequence $\{\tau_i\}$ and satisfying $\mathbb{E}\{|\mathbf{Z}_i|^\alpha\} < \infty$. If $0 < \alpha < 2$, then

$$\sum_{i=1}^{\infty} \frac{\mathbf{Z}_i}{\tau_i^{1/\alpha}} \stackrel{\text{a.s.}}{\sim} \mathcal{S}_c(\alpha, \beta = 0, \gamma = \lambda C_\alpha^{-1} \mathbb{E}\{|\mathbf{Z}_i|^\alpha\}), \quad (215)$$

where C_α is defined in (97). If a homogeneous Poisson point process in the plane has spatial density λ and $R^{(n)}$ denotes the distance of node i to the origin, then the sequence $\{R^{(n)}\}_{n=1}^{\infty}$ represents Poisson arrival times on the line with the constant arrival rate $\lambda\pi$. This can be easily shown by mapping the spatial Poisson process from Cartesian into polar coordinates, and then applying the mapping theorem [150]. Using this fact, we can then apply the above theorem to (95) and write

$$\begin{aligned} \mathbf{A} &= \sum_{n=1}^{\infty} \frac{e^{\sigma_1 G^{(n)}} \mathbf{X}^{(n)}}{(R^{(n)})^\nu} \\ &= \sum_{n=1}^{\infty} \frac{\overbrace{e^{\sigma_1 G^{(n)}} \mathbf{X}^{(n)}}^{\text{CS i.i.d.}}}{\underbrace{((R^{(n)})^2)^{\nu/2}}_{\tau_n}} \stackrel{\text{a.s.}}{\sim} \mathcal{S}_c\left(\alpha = \frac{2}{\nu}, \beta = 0, \gamma = \lambda\pi C_{2/\nu}^{-1} \mathbb{E}\{|e^{\sigma_1 G^{(n)}} X_j^{(n)}|^{2/\nu}\}\right), \end{aligned} \quad (216)$$

for $\nu > 1$. Note that $\mathbf{X}^{(n)}$ is CS due to the uniform phase $\phi^{(n)}$. As a result, $e^{\sigma_1 G^{(n)}} \mathbf{X}^{(n)}$ is also CS. Using the moment property of log-normal r.v.s, i.e., $\mathbb{E}\{e^{kG^{(n)}}\} = e^{k^2/2}$ with $G^{(n)} \sim \mathcal{N}(0, 1)$, (216) simplifies to

$$\mathbf{A} \stackrel{\text{a.s.}}{\sim} \mathcal{S}_c\left(\alpha = \frac{2}{\nu}, \beta = 0, \gamma = \lambda\pi C_{2/\nu}^{-1} e^{2\sigma_1^2/\nu^2} \mathbb{E}\{|X_j^{(n)}|^{2/\nu}\}\right), \quad (217)$$

for $\nu > 1$. This is the result in (96), and the derivation is complete. If \mathbf{A} is CS (isotropic) then it can be decomposed as follows [165]:

$$\mathbf{A} = \sqrt{V} \mathbf{G}, \quad (218)$$

with $V \sim \mathcal{S}(\alpha/2, 1, \cos(\frac{\pi\alpha}{4}))$ and $\mathbf{G} = G_1 + jG_2$, where G_1 and G_2 are i.i.d. Gaussian r.v.s with zero mean and variance $2\gamma^{2/\alpha}$, respectively. In addition, V and \mathbf{G} are independent. From (218), it follows that

$$|\mathbf{A}|^2 = 2\gamma^{2/\alpha}V(G_1^2 + G_2^2) = 2\gamma^{2/\alpha}VC, \quad (219)$$

where C is a central Chi-squared distributed r.v. with 2 degrees of freedom.

Appendix 3 Derivation of $\mu_{\text{TR},Y_1}^{(\text{NBIs})}$ and $\mu_{\text{TR},Y_2}^{(\text{NBIs})}$

The non-centrality parameter of $Y_{\text{TR},1}$ is defined as

$$\begin{aligned} \mu_{Y_{\text{TR},1}}^{(\text{NBIs})} &\triangleq \underbrace{\frac{1}{2\sigma_{\text{TR}}^2} \int_0^T w_j^2(t) dt}_{\mu_{\text{A,TR}}} + \underbrace{\frac{1}{2\sigma_{\text{TR}}^2} \int_0^T \frac{(\zeta_{1,j}(t) + \zeta_{2,j}(t))^2}{4} dt}_{\mu_{\text{B,TR}}^{(\text{NBIs})}} + \\ &\quad \underbrace{\frac{1}{2\sigma_{\text{TR}}^2} \int_0^T w_j(t) [\zeta_{1,j}(t) + \zeta_{2,j}(t)] dt}_{\mu_{\text{C,TR}}^{(\text{NBIs})}} \end{aligned} \quad (220)$$

The term $\mu_{\text{A,TR}}$ corresponds to (75) defined in the case of the single NBI. The term $\mu_{\text{B,TR}}^{(\text{NBIs})}$ can be derived with the expansion of all the terms as follows:

$$\begin{aligned} \frac{1}{2N_0} \sum_{j=0}^{\frac{N_s}{2}-1} \int_0^T \zeta_{1,j}^2(t) dt &= \\ \frac{A_c^2 I}{2N_0} \sum_{j=0}^{\frac{N_s}{2}-1} \left[T + \frac{\sin(4\pi f_j(T + j2T_f^{\text{TR}} + c_j T_p))}{4\pi f_j} - \frac{\sin(4\pi f_j(j2T_f^{\text{TR}} + c_j T_p))}{4\pi f_j} \right] & \\ + \frac{A_c A_s I}{N_0} \sum_{j=0}^{\frac{N_s}{2}-1} \left[\frac{\cos(4\pi f_j(T + j2T_f^{\text{TR}} + c_j T_p))}{4\pi f_j} - \frac{\cos(4\pi f_j(j2T_f^{\text{TR}} + c_j T_p))}{4\pi f_j} \right] & \\ + \frac{A_s^2 I}{2N_0} \sum_{j=0}^{\frac{N_s}{2}-1} \left[T - \frac{\sin(4\pi f_j(T + j2T_f^{\text{TR}} + c_j T_p))}{4\pi f_j} + \frac{\sin(4\pi f_j(j2T_f^{\text{TR}} + c_j T_p))}{4\pi f_j} \right] & \\ \approx \frac{|\mathbf{A}|^2 I T N_s}{4N_0}, & \end{aligned} \quad (221)$$

$$\frac{1}{2N_0} \sum_{j=0}^{\frac{N_s}{2}-1} \int_0^T \zeta_{2,j}^2(t) dt \approx \frac{|\mathbf{A}|^2 I T N_s}{4N_0}, \quad (222)$$

$$\frac{1}{N_0} \sum_{j=0}^{\frac{N_s}{2}-1} \int_0^T \zeta_{1,j}(t) \zeta_{2,j}(t) dt \approx \mu_{\text{D,TR}}^{(\text{NBIs})}. \quad (223)$$

The above approximations are obtained considering that $T \gg \frac{1}{4\pi f_j}$, $|\sin \phi| \leq 1$, $|\cos \phi| \leq 1$ and $|\mathbf{A}|^2 \geq |A_c A_s|$. In addition, $\mu_{\text{D}} = \frac{|\mathbf{A}|^2 I T N_s}{2N_0} \cos(2\pi f_j T_r)$ when $T \cos(2\pi f_j T_r) \gg \frac{1}{4\pi f_j}$.

Otherwise, $\mu_{D,TR}^{(NBIs)}$ is of the same order as $\frac{1}{4\pi f_j}$, which is negligible compared to the first term of $\mu_{B,TR}^{(NBIs)}$. As a result we can ignore the latter case and consider only the scenario when $T \cos(2\pi f_j T_r) \gg \frac{1}{4\pi f_j}$. The term $\mu_{B,TR}^{(NBIs)}$ can then be approximated as

$$\mu_{B,TR}^{(NBIs)} \approx \frac{|\mathbf{A}|^2 I T N_s}{2N_0} [1 + \cos(2\pi f_j T_r)]. \quad (224)$$

The third term $\mu_{C,TR}^{(NBIs)}$ can be derived as follows:

$$\begin{aligned} \mu_{C,TR}^{(NBIs)} &= \frac{2\sqrt{2E_p^{TR}} I A_c}{N_0} \sum_{j=0}^{\frac{N_s}{2}-1} a_j \sum_{l=1}^{L_{CAP}} h_l \int_0^{T_p} p(t) [\cos(2\pi f_j(t + \tau_l + j2T_f^{TR} + c_j T_p)) \\ &\quad + \cos(2\pi f_j(t + \tau_l + j2T_f^{TR} + c_j T_p + T_r))] dt \\ &\quad - \frac{2\sqrt{2E_p^{TR}} I A_s}{N_0} \sum_{j=0}^{\frac{N_s}{2}-1} a_j \sum_{l=1}^{L_{CAP}} h_l \int_0^{T_p} p(t) [\sin(2\pi f_j(t + \tau_l + j2T_f^{TR} + c_j T_p)) \\ &\quad + \sin(2\pi f_j(t + \tau_l + j2T_f^{TR} + c_j T_p + T_r))] dt \\ &= \frac{4|\hat{P}(f_j)|\sqrt{2E_p^{TR}} I}{N_0} \sum_{j=0}^{\frac{N_s}{2}-1} a_j \sum_{l=1}^{L_{CAP}} h_l \\ &\quad \times [A_c \cos(\pi f_j T_r) \cos(2\pi f_j(\tau_l + j2T_f^{TR} + c_j T_p + T_r/2) + \arg\{\hat{P}(f_j)\}) \\ &\quad - A_s \cos(\pi f_j T_r) \sin(2\pi f_j(\tau_l + j2T_f^{TR} + c_j T_p + T_r/2) + \arg\{\hat{P}(f_j)\})]. \end{aligned} \quad (225)$$

Substituting the expression of $\mu_{A,TR}$, $\mu_{B,TR}^{(NBIs)}$, and $\mu_{C,TR}^{(NBIs)}$ in (220), we obtain (98).

Using a similar approach leading to (224), the non-centrality parameter of $Y_{2,TR}$ be approximated as follows:

$$Y_{2,TR} \approx \frac{|\mathbf{A}|^2 I T N_s}{2N_0} [1 - \cos(2\pi f_j T_r)]. \quad (226)$$

Appendix 4 Gamma approximation

The process identified by the r.v $X = C^{1/\nu}$ where C is a central Chi-squared distributed r.v. with q degrees of freedom can be approximated by a Gamma random process for a wide range of ν values. The PDF of a Gamma random process can be written as

$$P_X(x) = \frac{x^{k_\nu-1} e^{-x/\Omega_\nu}}{\Omega_\nu^{k_\nu} \Gamma(k_\nu)}. \quad (227)$$

Figure 66 and Fig. 67 show the fit of the Gamma distribution over 100000 realizations of the r.v. X for different values of ν . It can be noticed that the Gamma distribution is a good approximation of the statistics of the r.v. X and that the quality of the approximation improves for large degrees of freedom q . Table 5 and Table 6 show the different value of the Gamma distribution parameters Ω_ν and k_ν for different values of ν and $q = 2$, and for different values of q and $\nu = 1.5$, used in the numerical results.

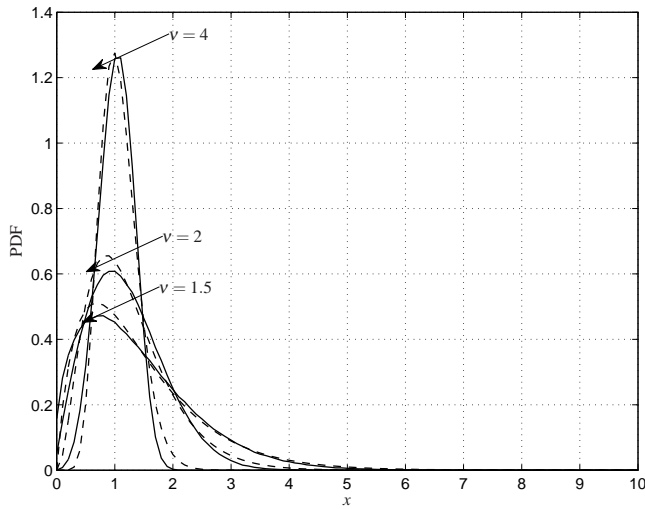


Fig. 66. Fitting of the random process $C^{1/\nu}$ (solid line) with the Gamma distribution (dashed line). The r.v. C is central Chi-squared distributed with $q = 2$ degrees of freedom.

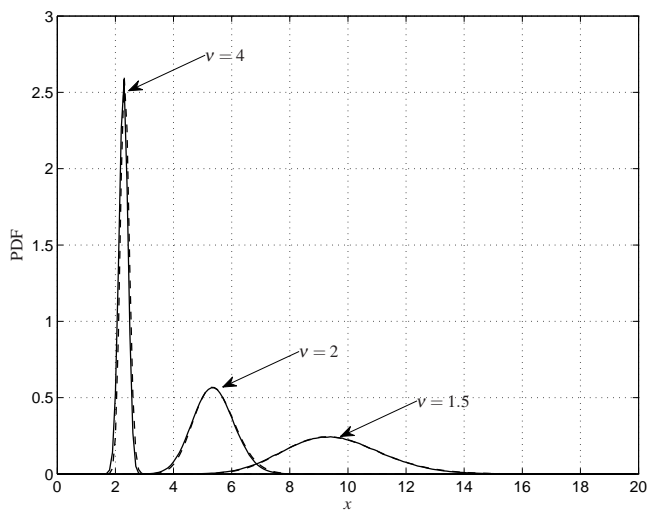


Fig. 67. Fitting of the random process $C^{1/v}$ (solid line) with the Gamma distribution (dashed line). The r.v. C is central Chi-squared distributed with $q = 30$ degrees of freedom.

Table 5. Ω_v and k_v parameters for $q = 2$.

v	k_v	Ω_v
1.1	1.1703	1.5464
1.2	1.3254	1.2657
1.3	1.5380	1.0305
1.4	1.7116	0.8923
1.5	1.9218	0.7442
1.6	2.1161	0.6473

Table 6. Ω_ν and k_ν parameters for $\nu = 1.5$.

q	k_ν	Ω_ν
2	1.9218	0.7442
4	4.1115	0.5821
6	6.3197	0.5042
8	8.5662	0.4555
10	10.8586	0.4179
12	13.0779	0.3935
14	15.3221	0.372
16	17.5096	0.3575
18	19.8196	0.3426
20	22.1347	0.3291
22	24.2554	0.3201
24	26.4512	0.3117
26	28.6136	0.3041
28	30.9042	0.2961
30	33.3568	0.2871
32	35.7055	0.2804
34	37.7489	0.2764
36	40.2499	0.2691
38	42.3876	0.2651
40	44.4482	0.2616
42	46.9090	0.2562
44	48.8983	0.2537
46	51.2296	0.2494
48	53.5560	0.2455
50	55.5253	0.2434
52	57.8969	0.2396
54	60.1846	0.2364
56	62.4032	0.2335
58	64.8374	0.2303
60	67.1983	0.2272
62	69.3940	0.2249
64	71.8425	0.2219

Appendix 5 Derivation of the spherical symmetric vector $\bar{\zeta}_{1,j}$

We first prove that the samples of the band-pass signal $v^{(n)}(t)$ taken at the Nyquist rate are uncorrelated. We start from the fact that the process $X(t) = v^{(n)}(t)$ is WSS stochastic then $X(t) = X(t - D^{(n)})$. The auto-correlation function of the process $X(t)$ can be written as

$$R_{X(t)}(\tau) = \lim_{T \rightarrow \infty} \frac{1}{2T} \mathbb{E} \left\{ \int_{-T}^T v^{(n)}(\tau) v^{*(n)}(t + \tau) dt \right\}. \quad (228)$$

Considering the random behaviour of the amplitude sequence and of the amplitude modulation data we have $\mathbb{E}\{a_j^{(n)} a_k^{(n)}\} = 0 \forall j \neq k$ and $\mathbb{E}\{e_i^{(n)} e_l^{(n)}\} = 0 \forall i \neq l$, respectively. Due to the random amplitude sequence the effect of the hopping code on the auto-correlation function vanishes. Similarly, due to the amplitude modulation, the effect of the position modulation also vanishes. Furthermore, we also have $\mathbb{E}\{h_l h_k\} = 0 \forall i \neq l$. As a result, the auto-correlation function can be written as

$$R_{X(t)}(\tau) = \mathbb{E}\{e_i^2\} \sum_{j=1}^{N_s^I} \mathbb{E}\{a_j^2\} \sum_{l=0}^{L-1} \mathbb{E}\{|h_l|^2\} R_{p(t)}(\tau). \quad (229)$$

The correlation function $R_{X(t)}(\tau)$ is then determined by the correlation function of the pulse waveform $R_{p(t)}(\tau)$. Since the sampling rate is $1/W$ and $W = 1/T_p$ where $[0, T_p)$ is the support of the waveform, we can conclude that the samples of the process $v^{(n)}(t)$ taken at the Nyquist rate are uncorrelated. As a result, considering a flat PDP, a Rayleigh fading for each channel component and $T_g^I = T_f^I$, the vectors $\bar{X}_1^{(n)} = \Re\{v_{1,j}^{(n)}\}$ and $\bar{X}_2^{(n)} = \Im\{v_{1,j}^{(n)}\}$ are composed by independent Gaussian r.v.s. As a result the vectors are spherically symmetric. The aggregate interference vector is then a sum of spherically symmetric vectors and, therefore, is spherically symmetric [144]. Since from Appendix 2 we have that the complex r.v. $\zeta_{1,j,m}$ is circularly symmetric, it follows from (67) and (68) that the aggregate interference can be represented as in (130).

Appendix 6 Test of the spherical symmetry of the interference vector

In order to test if the vector $\bar{\zeta}_{1,j}$ is sub-Gaussian with cross-correlation matrix as expressed in (131) we should check for its spherical symmetry. A multivariate stable distribution is considered spherically symmetric if its spectral measure is uniform. The estimation of the spectral measure is not an easy task for multivariate stable distribution. A way of estimating the spectral measure is presented in [166] and it is based on the sum of spherical harmonics. We limit our test here by considering the ratio of two components of the aggregate interference vector defined as follows

$$X \triangleq \frac{\zeta_{1,j,m}}{\zeta_{1,j,n}}. \quad (230)$$

where $\zeta_{1,j,m}$ and $\zeta_{1,j,n}$ are elements of the stable random vector $\bar{\zeta}_{1,j}$. If the vector is sub-Gaussian and the cross-correlation matrix of the multivariate Gaussian variable expresses in (130) is scalar, the variable X is the ratio of two i.i.d. Gaussian r.v.s with zero mean and unit variance, which corresponds to the standard Cauchy distribution which is characterized by the following PDF

$$P_X(x) = \frac{1}{\pi(1+x^2)}. \quad (231)$$

From Figures 68-70, we can have a qualitative idea on the spherical symmetry of the interference vector by observing the difference between the Cauchy distribution and the distribution of X obtained by simulating the interference system. As shown in Appendix 5, for $T_g^I = T_f^I$, flat PDP and Rayleigh fading, the aggregate interference is spherically symmetric. As a result, in Fig. 68 we can see that X is Cauchy distributed. We notice from Fig. 69 that, although for $T_g^I = T_f^I$, flat PDP and Nakagami fading, the vector $\Re\{\bar{\mathbf{v}}_{1,j}^{(n)}\}$ ($\Im\{\bar{\mathbf{v}}_{1,j}^{(n)}\}$) is not spherically symmetric,³⁷ the distribution of X is in good agreement with the Cauchy distribution allowing us to assume that the aggregate interference vector is spherically symmetric. From Fig. 68 -Fig. 70, we also see that the ratio among two aggregate interference samples belonging to two different time frames defined as $X = \frac{\zeta_{1,j,m}}{\zeta_{1,i,n}}$ follows the Cauchy distribution. Note that in the case $T_g^I = T_f^I$ the

³⁷In the case of independent random variables, only identically Gaussian random distributed variables are spherically symmetric[167].

received signal covers the entire pulse repetition interval and consequently there is no room for the hopping code. As a result, the multipath components of different interfering signals always maintain the same position in different frames. We can conclude that the random amplitude sequences used by each interferer are sufficient to ensure the aggregate interference vector to be spherically symmetric and therefore sub-Gaussian in the case of flat PDP. In the case of $T_g^I < T_f^I$, the distribution of the r.v. X does not follow a Cauchy distribution meaning that the aggregate interference vector is no longer spherically symmetric.

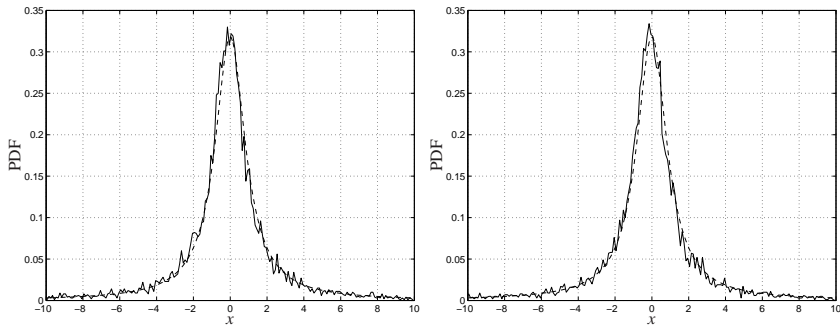


Fig. 68. Comparison of the standard Cauchy distribution PDF (solid line) and the empirical PDF of the variable X obtained by simulation of the interference system (dashed line) for $A_{\mathcal{R}} = 50$ m, interferers spatial density $\lambda = 0.1$, received signal duration $T_g^I = 16$ ns, pulse width $T_p = 0.5$ ns, pulse repetition interval $T_f^I = 16$ ns, $m^I = 1$, and $\varepsilon^I = 0$. The left figure considers two elements belonging to the same time frame and the right figure considers two elements belonging to two different time frames.

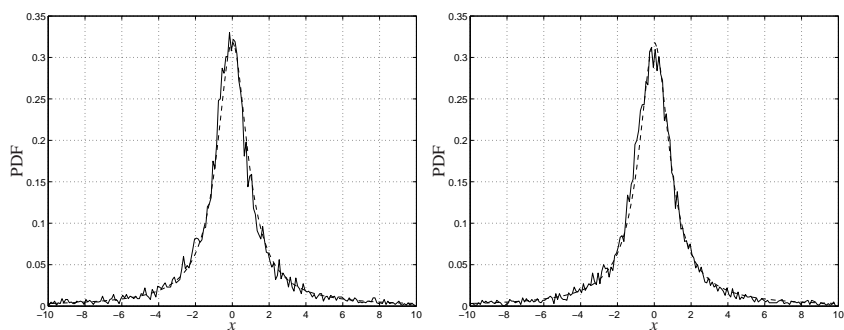


Fig. 69. Comparison of the standard Cauchy distribution PDF (solid line) and the empirical PDF of the variable X obtained by simulation of the interference system (dashed line) for $A_{\mathcal{R}} = 50$ m, interferers spatial density $\lambda = 0.1$, received signal duration $T_g^I = 16$ ns, pulse width $T_p = 0.5$ ns, pulse repetition interval $T_f^I = 16$ ns, $m^I = 1$, and $\varepsilon^I = 0$. The left figure considers two elements belonging to the same time frame and the right figure considers two elements belonging to two different time frames.

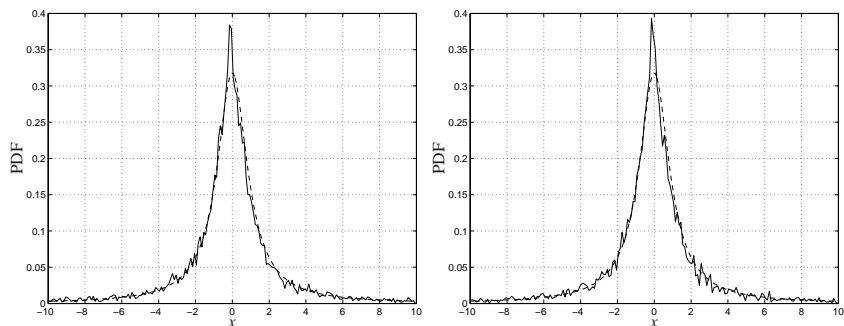


Fig. 70. Comparison of the standard Cauchy distribution PDF (solid line) and the empirical PDF of the variable X obtained by simulation of the interference system (dashed line) for $A_{\mathcal{R}} = 50$ m, interferers spatial density $\lambda = 0.1$, received signal duration $T_g^I = 16$ ns, pulse width $T_p = 0.5$ ns, pulse repetition interval $T_f^I = 25$ ns, $m^I = 3$, and $\varepsilon^I = 0.4$. The left figure considers two elements belonging to the same time frame and the right figure considers two elements belonging to two different time frames.

Appendix 7 Derivation of averaged maximum likelihood estimators

The derivation of the AML estimators expressed by the log-likelihood functions is related to the solution of the integral

$$\int \exp(r_n h_{n-j} - h_{n-j}^2) P(h_{n-j}) dh_{n-j}. \quad (232)$$

Complex Gaussian fading

We derive here the estimator expressed by (169).

Considering $\mathbf{w}_{n-j} = w_{1,j} + jw_{2,j}$ as complex Gaussian and taking out the unnecessary values the n th component of the log-likelihood function for the j th hypothesis can be rewritten as

$$\Lambda_n^G(j) = \log \left\{ \int_{-\infty}^{\infty} \exp(2r_{1,n}w_{1,n-j} - w_{1,n-j}^2) \frac{1}{\sqrt{2\pi\sigma_{n-j}^2}} \exp\left(\frac{w_{1,n-j}^2}{2\sigma_{n-j}^2}\right) dw_{1,n-j} \int_{-\infty}^{\infty} \exp(2r_{2,n}w_{2,n-j} - w_{2,n-j}^2) \frac{1}{\sqrt{2\pi\sigma_{n-j}^2}} \exp\left(\frac{w_{2,n-j}^2}{2\sigma_{n-j}^2}\right) dw_{2,n-j} \right\}. \quad (233)$$

The integrals in (233) have a closed form solution. The n th component of the log-likelihood function can be expressed as

$$\Lambda_n^G(j) = \frac{2|\mathbf{r}_n|^2\sigma_{n-j}^2}{(1+2\sigma_{n-j}^2)} - \log(\sqrt{1+2\sigma_{n-j}^2}). \quad (234)$$

The optimal estimator in the case of complex Gaussian distributed fading can be expressed as

$$\Lambda^G(j) = \sum_{n=j}^{T_0W-1} \Lambda_n^G(j). \quad (235)$$

Log-normal fading and $\mathbf{p}_{n-j} \in \{1, -1\}$

We derive here the estimator expressed by (173) following the derivation presented in [80].

Using the change of variable $x_{n-j} = 20 \log_{10}(h_{n-j})$, the n th component of the log-likelihood function for the j th hypothesis can be written as

$$\Lambda_{n|\mathbf{p}_{n-j}}^L(j) = \log \left\{ \int_{-\infty}^{+\infty} \exp \left(2r_n \mathbf{p}_{n-j} 10^{\frac{x_{n-j}}{20}} - 10^{\frac{x_{n-j}}{10}} \right) \frac{1}{\sqrt{2\pi\sigma_L^2}} \exp \left[- \left(\frac{x_{n-j} - \mu_{n-j}}{\sqrt{2\sigma_L^2}} \right)^2 \right] dx_{n-j} \right\}. \quad (236)$$

With the further change of variable $y_{n-j} = (x_{n-j} - \mu_{n-j}) / (\sqrt{2\sigma_L})$, and considering that $\mathbf{p}_{n-j} = 1$ or -1 ($\phi_{n-j} = 0$ or π) with equal probability $\frac{1}{2}$, the integral in (236) can be expressed as

$$\begin{aligned} & \int_{-\infty}^{+\infty} \exp \left(2\mathbf{p}_{n-j} r_n 10^{\frac{x_{n-j}}{20}} - 10^{\frac{x_{n-j}}{10}} \right) \frac{1}{\sqrt{2\pi\sigma_L^2}} \exp \left[- \left(\frac{x_{n-j} - \mu_{n-j}}{\sqrt{2\sigma_L^2}} \right)^2 \right] dx_{n-j} \\ &= \int_0^{\infty} \left[\frac{\exp \left(r_n 10^{\frac{\sqrt{2}\sigma_L y_{n-j} + \mu_{n-j}}{20}} \right)}{2} + \frac{\exp \left(-r_n 10^{\frac{\sqrt{2}\sigma_L y_{n-j} + \mu_{n-j}}{20}} \right)}{2} \right] \\ & \quad \exp \left(-10^{\frac{\sqrt{2}\sigma_L y_{n-j} + \mu_{n-j}}{10}} \right) \exp(-y_{n-j}^2) dy_{n-j} \\ &= \int_{-\infty}^{\infty} \cosh \left(r_n 10^{\frac{\sqrt{2}\sigma_L y_{n-j} + \mu_{n-j}}{20}} \right) \exp \left(-10^{\frac{\sqrt{2}\sigma_L y_{n-j} + \mu_{n-j}}{10}} \right) \exp(-y_{n-j}^2) dy_{n-j}. \end{aligned} \quad (237)$$

There is no closed form solution for this integral. Since the function to be integrated is in the form $\exp(-x^2)f(x)$ we can use the Hermite-Gauss integral which is defined as follow [168, 169]

$$\int_{-\infty}^{\infty} \exp(-x^2) f(x) dx = \sum_{k=1}^N c_k f(z_k) + R_N, \quad (238)$$

where c_k are the weights defined as

$$c_k = \frac{2^{N-1} N! \sqrt{\pi}}{N^2 H_{N-1}^2(z_k)}, \quad (239)$$

and z_k is the k th the zero of the Hermite polynomial $H_N(x)$. Considering the residual part R_N negligible, the n th element of the log-likelihood function can be approximated as

$$\Lambda_n^L(j) \approx \log \left\{ \sum_{k=1}^N c_k \exp \left(-10 \frac{\sqrt{2}\sigma_L z_k + \mu_{n-j}}{10} \right) \cosh \left(r_n 10 \frac{\sqrt{2}\sigma_L z_k + \mu_{n-j}}{20} \right) \right\}. \quad (240)$$

The optimal estimator in the case of log-normal distributed fading can be expressed as

$$\Lambda^L(j) = \sum_{n=j}^{T_0 W - 1} \Lambda_n^L(j). \quad (241)$$

Nakagami fading and $\mathbf{p}_{n-j} \in \{1, -1\}$

We derive here the estimator expressed by (175). The n th component of the log-likelihood function for the j th hypothesis can be written as

$$\begin{aligned} \Lambda_{n|\mathbf{p}_{n-j}}^N(j) &= \log \left\{ \int_0^\infty \exp(2h_{n-j}(r_n \mathbf{p}_{n-j}) - h_{n-j}^2) \right. \\ &\quad \left. \frac{2}{\Gamma(m)} \left(\frac{m}{\Omega_{n-j}} \right)^m h_{n-j}^{2m-1} \exp \left(\frac{m h_{n-j}^2}{\Omega_{n-j}} \right) dh_{n-j} \right\}. \end{aligned} \quad (242)$$

The integral in (242) has a closed form solution. The integral in (242) can be expressed in terms of the Kummer confluent hypergeometric function ${}_1F_1(a; b; z)$ as follows

$$\begin{aligned} &\int_0^\infty \exp(2(r_n \mathbf{p}_{n-j}) h_i - h_{n-j}^2) \frac{2}{\Gamma(m)} \left(\frac{m}{\Omega_{n-j}} \right)^m h_{n-j}^{2m-1} \exp \left(\frac{m h_{n-j}^2}{\Omega_{n-j}} \right) dh_{n-j} \\ &= \frac{1}{\Gamma(m)} m^m (m + \Omega_{n-j})^{-m} \left[\Gamma(m) {}_1F_1 \left(m; \frac{1}{2}; \frac{\Omega_{n-j} (r_n \mathbf{p}_{n-j})^2}{(m + \Omega_{n-j})} \right) + \right. \\ &\quad \left. \frac{(r_n \mathbf{p}_{n-j}) \Gamma(\frac{1}{2} + m)}{\sqrt{\frac{m + \Omega_{n-j}}{\Omega_{n-j}}}} {}_1F_1 \left(m; \frac{1}{2}; \frac{\Omega_{n-j} (r_n \mathbf{p}_{n-j})^2}{(m + \Omega_{n-j})} \right) \right]. \end{aligned} \quad (243)$$

Considering now the $\mathbf{p}_{n-j} = 1$ or -1 ($\phi_{n-j} = 0$ or π) with equal probability $\frac{1}{2}$, the n th component of the log-likelihood function can be written as

$$\Lambda_n^N(i) = \log \left\{ m^m (m + \Omega_i)^{-m} {}_1F_1 \left(m; \frac{1}{2}; \frac{\Omega_i r_n^2}{(m + \Omega_i)} \right) \right\}. \quad (244)$$

The optimal estimator in the case of Nakagami distributed fading can be expressed as

$$\Lambda^N(j) = \sum_{n=j}^{T_0 W - 1} \Lambda_n^N(j). \quad (245)$$

281. Hamada, Atef Saad (2007) Manufacturing, mechanical properties and corrosion behaviour of high-Mn TWIP steels
282. Rahtu, Esa (2007) A multiscale framework for affine invariant pattern recognition and registration
283. Kröger, Virpi (2007) Poisoning of automotive exhaust gas catalyst components. The role of phosphorus in the poisoning phenomena
284. Codreanu, Marian (2007) Multidimensional adaptive radio links for broadband communications
285. Tiikkaja, Esa (2007) Koneäköä soveltavan kuituanalysoittorin ja virtauskenttäfraktioaattorin mittausten yhteydet kuumahierteen paperitekniisiin ominaisuuksiin. Kokeellinen tutkimus
286. Taparugssanagorn, Attaphongse (2007) Evaluation of MIMO radio channel characteristics from TDM-switched MIMO channel sounding
287. Elsilä, Ulla (2007) Knowledge discovery method for deriving conditional probabilities from large datasets
288. Perkkiö, Miia (2007) *Utilitas* restauroinnissa. Historiallisen rakennuksen käyttötarkoituksen muutos ja funktionaalinen integriteetti
289. Nissilä, Mauri (2008) Iterative receivers for digital communications via variational inference and estimation
290. Toivonen, Tuukka (2007) Efficient methods for video coding and processing
291. Lyöri, Veijo (2007) Structural monitoring with fibre-optic sensors using the pulsed time-of-flight method and other measurement techniques
292. Stoica, Lucian (2008) Non-coherent energy detection transceivers for Ultra Wideband Impulse radio systems
293. Koski, Anna (2008) Applicability of crude tall oil for wood protection
294. Gore, Amol (2008) Exploring the competitive advantage through ERP systems. From implementation to applications in agile networks
295. Kirillin, Mikhail (2008) Optical coherence tomography of strongly scattering media
296. Tölli, Antti (2008) Resource management in cooperative MIMO-OFDM cellular systems

Book orders:
OULU UNIVERSITY PRESS
P.O. Box 8200, FI-90014
University of Oulu, Finland

Distributed by
OULU UNIVERSITY LIBRARY
P.O. Box 7500, FI-90014
University of Oulu, Finland

S E R I E S E D I T O R S

A
SCIENTIAE RERUM NATURALIUM
Professor Mikko Siponen

B
HUMANIORA
Professor Harri Mantila

C
TECHNICA
Professor Hannu Heusala

D
MEDICA
Professor Olli Vuolteenaho

E
SCIENTIAE RERUM SOCIALIUM
Senior Researcher Eila Estola

E
SCRIPTA ACADEMICA
Information officer Tiina Pistokoski

G
OECONOMICA
Senior Lecturer Seppo Eriksson

EDITOR IN CHIEF
Professor Olli Vuolteenaho

EDITORIAL SECRETARY
Publications Editor Kirsti Nurkkala

ISBN 978-951-42-8799-2 (Paperback)

ISBN 978-951-42-8800-5 (PDF)

ISSN 0355-3213 (Print)

ISSN 1796-2226 (Online)

